# Experimental Realization of Quantum Gates and the Deutsch-Jozsa Algorithm with Trapped $^{40}Ca^{+}$ Ions

Dissertation

zur Erlangung des Doktorgrades an der
naturwissenschaftlichen Fakultät
der Leopold-Franzens-Universität Innsbruck

vorgelegt von

**Stephan Timo Gulde**

durchgeführt am Institut für Experimentalphysik
unter der Leitung von
o. Univ. Prof. Dr. R. Blatt

Innsbruck
März 2003

## Abstract

This thesis reports on the experimental realization of quantum gates and algorithms with an ion trap quantum information processor. $^{40}Ca^{+}$ ion strings are stored in a linear Paul trap. The ions are cooled and excited by laser light, and observed by detection of their fluorescence on a photomultiplier and on a CCD camera. The motion of a string (or a single trapped ion) can be described by vibrational modes (i.e. normal modes of the ion crystal). The $S_{1/2}$ ground state and the metastable $D_{5/2}$ state are used to encode one quantum bit in each ion (internal qubits). The lowest two quantum states of a selected vibrational mode are identified as an additional qubit (vibrational qubit).

A new linear ion trap is designed and built based on experiences made with previous traps. Resonant photoionization as a new trap loading technique is investigated using a setup of two blue laser diodes. This technique presents many advantages over traditional electron impact ionization in terms of trap operation and electric stray field compensation. Strings of up to three ions are spectroscopically investigated. Further experimental prerequisites for ion trap quantum computation such as motional ground state cooling, optical addressing and laser phase control are implemented.

For *quantum phase control*, a compensation method for unwanted AC-Stark shifts is developed and the technique of composite pulses is adapted from NMR technology. The composite pulse technique allows the implementation of arbitrary rotations of the vibrational qubit. This enables the use of a single trapped ion together with a vibrational qubit as a *universal* two-qubit quantum information processor. With the help of these techniques, the Deutsch-Jozsa algorithm is implemented. This represents the first complete quantum algorithm realized with an ion trap quantum computer. Moreover, a novel method based on off-resonant laser-ion coupling is employed to implement a universal quantum gate between internal and vibrational qubit. The type of coupling is dispersive, i.e. it creates conditional phase shifts but leads to no population transfer. Finally, preliminary experiments on the realization of a two-ion controlled-NOT gate according to Cirac and Zoller are carried out.

## Zusammenfassung

Diese Dissertation berichtet über die experimentelle Realisierung von Quantengattern und -algorithmen mit einem Ionenfallen-Quanteninformationsprozessor. $^{40}Ca^{+}$ Ionenketten werden in einer linearen Paulfalle gespeichert. Die Ionen werden mit Laserlicht gekühlt und angeregt und ihre Fluoreszenz wird mit Hilfe eines Photomultipliers sowie einer CCD-Kamera beobachtet. Die Bewegung einer Ionenkette (oder auch eines einzelnen gefangenen Ions) kann durch Vibrationsmoden (d.h. Normalmoden des Ionenkristalls) beschrieben werden. Der $S_{1/2}$-Grundzustand und der metastabile $D_{5/2}$-Zustand werden verwendet, um ein Quantenbit (Qubit) in jedes Ion einzuschreiben (interne Qubits). Die untersten zwei Quantenzustände einer ausgewählten Vibrationsmode werden als ein zusätzliches Qubit identifiziert (Vibrationsqubit).

Auf der Grundlage von Erfahrungen mit früheren Ionenfallen wird eine neue lineare Falle entworfen und gebaut. Resonante Photoionisation als eine neue Technik zum Laden einer Ionenfalle wird untersucht. Dafür wird ein Aufbau aus zwei blauen Laserdioden verwendet. Diese Methode zeigt verschiedene Vorteile gegenüber der traditionellen Ionisation durch Elektronenstoß bezüglich Fallenbetrieb und der Kompensation elektrischer Streufelder. Ketten von bis zu drei Ionen werden spektroskopisch untersucht. Weitere experimentelle Voraussetzungen für einen Ionenfallen-Quantenrechner wie z.B. Bewegungs-Grundzustandskühlung, optische Adressierung and Kontrolle der Laserphase werden implementiert.

Ein entscheidendes Element bei der Implementierung eines Quantencomputers ist die gezielte Kontrolle über Quantenphasen. Dazu wird eine neue Methode zur Kompensation unerwünscher AC-Stark-Verschiebungen entwickelt sowie die Methode zusammengesetzter Pulse aus der Kernspinresonanztechnik übernommen. Mit Hilfe zusammengesetzter Pulse ist es möglich beliebige Rotationen des Vibrationsqubits zu implementieren. Das wiederum erlaubt es, ein einzelnes gefangenes Ion zusammen mit einem Vibrationsqubit als einen *universellen* zwei-Qubit-Quantenrechner zu verwenden. Mit Hilfe dieser Techniken wird der Deutsch-Jozsa-Algorithmus implementiert. Dies stellt die erste Realisierung eines vollständigen Quanten-Algorithmus mit einem Ionenfallen-Quantenrechner dar. Darüber hinaus wird eine neuartige Methode, welche auf nichtresonanter Laser-Ion-Kopplung basiert, verwendet, um ein universelles Quantengatter zwischen internem und Vibrationsqubit zu implementieren. Es handelt sich hier um eine dispersive Kopplung welche konditionelle Phasenverschiebungen erzeugt jedoch zu keinem Populationstransfer führt. Schließlich werden vorbereitende Experimente zur Realisierung eines zwei-Ionen controlled-NOT-Gatters nach Cirac und Zoller durchgeführt.

# Contents


**1 Introduction** **1**

**2 Quantum Gates** **5**
2.1 Single Qubits . . . . . 5
2.2 Multi-Qubit Operations . . . . . 8

**3 Ion Trapping and Interaction with Light** **11**
3.1 Linear Paul Traps . . . . . 11
3.2 Linear Ion Crystals . . . . . 14
3.2.1 Equilibrium Positions . . . . . 14
3.2.2 Normal Modes . . . . . 15
3.2.3 Stability of a Linear String . . . . . 18
3.3 Spectroscopy . . . . . 19
3.3.1 Level Scheme and Laser Manipulation of $^{40}Ca^{+}$ . . . . . 19
3.3.2 Laser-Ion Interaction . . . . . 20
3.3.3 Lamb-Dicke Regime . . . . . 21
3.3.4 Generalizations of the Model . . . . . 23
3.3.5 The Quadrupole Transition . . . . . 24
3.3.6 Non-resonant Interactions . . . . . 26

**4 Quantum Computation with Trapped Ions** **31**
4.1 General Concepts . . . . . 31
4.2 Single Ion Gates and Composite Pulse Techniques . . . . . 32
4.3 The Deutsch-Jozsa Algorithm with a Single Ion . . . . . 37
4.3.1 The Algorithm . . . . . 37
4.3.2 Adaptation for an Ion Trap Quantum Processor . . . . . 40
4.4 Quantum Computation With Two and More Ions . . . . . 43

**5 Experimental Setup** **47**
5.1 Design of the New Linear Trap . . . . . 47
5.2 Laser Systems for $^{40}Ca^{+}$ . . . . . 53
5.3 Frequency and Phase Control at 729 nm . . . . . 54
5.4 Vacuum Vessel and Optical Access . . . . . 56
5.5 Addressing Optics . . . . . 59

**6 Operating the Trap** **61**
6.1 Trap Loading . . . . . 61

6.2 Compensation of Micromotion . . . . . 63
6.3 Patch effects . . . . . 67
6.4 A New Trap Loading Scheme by Photoionization . . . . . 68

**7 Experimental Results: Prerequisites** **71**
7.1 Spectroscopy on the Qubit Transition . . . . . 71
7.2 Laser Cooling . . . . . 76
7.2.1 Doppler Cooling . . . . . 76
7.2.2 Sideband Cooling . . . . . 78
7.3 Coherence on the Qubit Transition . . . . . 81
7.4 Individual Ion Addressing and Read-Out . . . . . 85
7.5 Switching the Laser Phase . . . . . 91
7.6 AC-Stark Shift Measurement and Compensation . . . . . 93
7.7 Testing the $-1$ Phase of a Sideband $2\pi$ Rabi Rotation . . . . . 98

**8 Experimental Results: Quantum Gates and Algorithms** **103**
8.1 Sideband Induced Stark Shifts - a Dispersive Phase Gate . . . . . 103
8.2 The Deutsch-Jozsa Algorithm . . . . . 111
8.3 The Cirac-Zoller Gate - First Results . . . . . 115

**9 Summary and Outlook** **119**

**A Appendix** **121**
A.1 Coupling Strengths on the Quadrupole Transition . . . . . 121
A.2 Radio-frequency trap drive . . . . . 122
A.3 Standard Configurations of the Experiment . . . . . 125

**Bibliography** **128**

# 1 Introduction

The foundations of quantum mechanics were laid at the beginning of the twentieth century [1]. From that time until the 1970s, approaches to quantum mechanics were based on *observations* of the behaviour of nature. During that time, practical applications obeying quantum mechanics typically involved bulk devices containing an enormous number of quantum systems, none of them directly accessible (e.g. the laser [2] and the semiconductor transistor [3]). Over the last thirty years, the idea of *quantum state control and quantum engineering* [4, 5], has emerged. The question "How can we achieve complete control over single quantum systems and how can we make use of this control?" is asked. Around the same time, the concept of *quantum computation* emerged from similar thinking. The important question to ask was "How can information processing be accomplished using quantum mechanical systems and can this new type of information processing be more efficient than computers based on the classical laws of physics?". These questions are conceptually new compared to earlier approaches since here quantum mechanical features of nature (such as entanglement [4]) are regarded as *resources* which may be exploited to tackle unsolved problems [6, 7]. The first steps towards quantum computation were taken in 1982 by Richard Feynman [8] when he observed that a simulation of a system's quantum dynamics on a classical computer will grow exponentially in terms of computational effort with the size of the quantum system. He pointed out that another quantum system which is under sufficient control concerning its preparation, unitary evolution and measurement (something which we would call a quantum computer today) could be used to mimic and thus simulate the dynamics of the given quantum system (see also [9]). In this case the number of required computational resources grows only linearly with the size of the system to be simulated. Soon after, David Deutsch [10, 11] gave an explicit model of quantum computation by defining quantum Turing machines and quantum circuits. Since then, a large field of quantum information research, both theoretical and experimental, has grown with various sub-disciplines such as quantum computation and quantum communication [12]. For an overview, see the book of Nielsen and Chuang [13], or [14]. The following introduction focuses on quantum computation and its practical implementation.

The basic element of quantum information is the *quantum bit*, or *qubit*, which replaces the *bit* of classical computer science. A physical qubit is simply a two-level system, i.e. a spin-1/2 system. The two quantum states are identified as the logic "0" and "1" of binary information and are therefore denoted $|0\rangle$ and $|1\rangle$ here. A crucial difference to the classical bit is that a qubit can be in a *superposition* of its two logic states. A certain set of qubits form the computational space, quantum mechanically speaking, the Hilbert space, in which all operations take place. The set of qubits is referred to as the qubit register. A general quantum computation consists of

- *Preparation* of the qubit register in a well defined, pure initial state.

- Application of a sequence of *unitary transformations* in this Hilbert space which, analogous to logic gates in classical computer science, are called quantum gates.
- Readout of the final result. This corresponds to a *measurement* of the qubit register. In certain quantum algorithms only a subset of the qubit register needs to be read out.

The demands on a physical implementation of a quantum computer are:

- The proposed implementation must feature a suitable set of two-level systems and be scalable.
- There must be experimental procedures at hand to implement the above operations - preparation, general unitary transformation, measurement - with sufficient fidelity.
- *Coherence* must be preserved during the course of the computation. Note that on top of the coherent properties of the freely evolving qubit register there is also decoherence introduced by coupling to the system (which is necessary to implement quantum gates).

DiVincenzo [15, 16] was the first to assemble such a list of criteria. Note that a (projective) measurement procedure for the individual qubits may also serve as a preparation tool.

The advantage of quantum algorithms over their classical counterparts lies in "quantum parallelism", i.e. the possiblity to run the quantum computer with superpositions as input states. This feature can be utilized to solve certain computational problems more efficiently than is possible on a classical computer. Quantum algorithms which outperform their classical counterparts will be referred to as *efficient quantum algorithms.*

It has been shown that there exist two-qubit gates which, in combination with single-qubit operations, allow the generation of arbitrary unitary transformations [17] (see also section 2.2). These gates are called *universal*, the controlled-NOT gate (the quantum analogy of the XOR gate) being a prominent example.

The first efficient quantum algorithm was presented by David Deutsch in his 1985 paper [10] and is known today as the **Deutsch-Jozsa algorithm** [13]. The underlying problem is to find out if a given Boolean function $f$ is constant (has always the same output, independent of the input) or balanced (has both 0 and 1 as possible outputs). While classically *two* evaluations of $f$ are necessary, Deutsch's algorithm can yield the result in just *one* evaluation. Several modifications of the problem have been developed [18, 19]. Details of the Deutsch-Jozsa algorithm and its history are given in section 4.3.

Another type of efficient quantum computations are **Quantum search algorithms**, the most well-known being the Grover algorithm [20]. It concerns the search of a data base for a particular entry. The "travelling salesman" problem also falls into this class of algorithms: imagine you are given a map containing many cities, and wish to determine the shortest route passing through all cities of the map. For a data base of magnitude $N$, a classical search procedure requires $\mathcal{O}(N)$ steps while the quantum algorithms find the correct entry after $\mathcal{O}(\sqrt{N})$ operations.

One of the most spectacular efficient quantum algorithm is the **Shor algorithm** [21]. It allows one to factor a large integer number $N$ into its prime factors in polynomial time. This means that the number of computational steps scales polynomially with the number of digits of $N$. In classical computation the only known procedure is to try one prime number after

the other and check if it is a divisor of $N$. The number of steps that this procedure requires grows exponentially with the number of digits of $N$. Shor's finding is of great relevance to cryptography because most public key encryption systems in use (in particular the most widely developed, the RSA cryptosystem [22]) rely on the fact that prime factorization of large numbers is exponentially difficult. There are other public key cryptosystem which are based on the difficulty of (classically) solving the discrete logarithm problem [23]. Also for this problem, Peter Shor presented an efficient (i.e. polynomial time) quantum solution in his 1994 paper [21].

Finally, quantum computers can be used for **simulations of quantum dynamics**. Since Feynman's seminal work [8], several procedures have been developed to efficiently simulate systems on a quantum computer, with no known efficient counterpart on a classical computer. The proposal of Abrams and Lloyd [24] for simulating many-body Fermi systems is just one example. To cite Nielsen and Chuang: "It is very likely that one of the major applications of quantum computers in the future will be performing simulations of quantum mechanical systems too difficult to simulate on a classical computer, a problem with profound scientific and technological implications".

There are a large variety of proposals for the *physical implementation* of a quantum computer. These include

- Photon quantum computers [25, 26].
- Cavity QED [27, 28].
- NMR [17].
- Josephson junctions [29, 30].
- Electrons floating on helium [31].
- Quantum dots [32].
- Spin-1/2 nuclei in a semiconductor matrix [33].
- Ion traps [34].

This list and the given references, which point to seminal works in the respective fields, are by no means exhaustive. The requirements defined above set very high technological demands and consequently all experimental attempts face considerable challenges. Until recently, complete quantum algorithms have only been realized with NMR techniques [35–37]. It should be noted that there is certain criticism about to what extent present day NMR quantum computation fulfils the specified requirements completely [38–41]. These concerns relate mainly to scalability and the fact that the system is in a highly thermal, separable state.

In ion trap quantum computers, quantum information is stored in two long-lived internal states $|g\rangle$ and $|e\rangle$ of trapped ions. In this way each ion contains one qubit. Under the influence of an external trapping potential in combination with the mutual Coulomb repulsion, the ions, if cooled, freeze into a crystal-like structure. In a *linear* Paul trap, the trapping potential is cigar-shaped and for strong radial trap confinement the crystal structure is a linear string of ions. This configuration is particularly suitable for the manipulation of the ion qubits with external laser fields. The ion string exhibits normal modes of motion (vibrational modes). Two-qubit operations are mediated by one selected vibrational mode (the quantum bus mode). The proposal of Cirac & Zoller [34] requires the quantum bus mode to be prepared in its lowest quantum state and is based on resonant excitations of optical transitions. Several other schemes have been proposed which also utilize a common vibrational mode to implement quantum gates between ion qubits [42, 43], [44], [45]. Moreover, ion trap quantum

computation schemes exist where the two-qubit coupling is mediated differently. One example is an array of microtraps, each trap containing one ion [46]. In this proposal two-qubit gates are mediated by the Coulomb interaction between ions in neighboring microtraps. In another proposal the ion qubits are coupled via a mode of the electromagnetic field of an optical resonator [47].

Over recent years a great deal of progress has been made in *experimental ion trap quantum computation*, in particular in the group of D.J. Wineland at NIST in Boulder. A fundamental quantum gate, the controlled-NOT between a single trapped ion and a vibrational mode, has been demonstrated [48]; two ions [49] and subsequently four ions [50] (the latter employing the methods of [42]) have been entangled.

In our group, several prerequisites for quantum computation, such as motional ground state cooling, individual ion addressing and elementary coherent manipulations have been previously demonstrated [51], [52], [4]. Recently, we have experimentally realized the Deutsch-Jozsa algorithm [53]. This represents the first implementation of an efficient quantum algorithm on an ion trap quantum computer and the first such implementation outside NMR. The Deutsch-Jozsa experiment represents the main achievement of this thesis. Preliminary results on a two-ion controlled-NOT gate are also reported. Besides several technical improvements, these experiments followed the methods proposed by Cirac & Zoller. We also realized a novel type of quantum gate, reported in section 8.1, where purely dispersive laser-ion coupling (off-resonant coupling which induces no population transfer) was employed to implement a universal quantum gate.

The thesis is structured as follows: Chapter 2 introduces the formalism of the basic quantum operations required for a quantum computer, i.e. single qubit rotations and two-qubit logic gates. Chapter 3 focuses on the theoretical foundations of the experiment, i.e. the function of Paul traps, the mechanics of a (linear) ion crystal and the interaction of ions with light. Special attention is paid to $^{40}Ca^{+}$, which is the ion used in our experiments, and to the effect of non-resonant interactions. Chapter 4 describes how quantum computation can be performed in ion traps. Chapter 5 is concerned with the various elements of the experimental setup. This chapter includes a description of the design process of the current trap based on the experiences made with previous trap constructions. Chapter 6 deals with the technicalities of operating the trap. In this context a new trap loading scheme by photoionization, which has significantly improved on the trap performance, is presented. In chapter 7 experimental achievements such as motional ground state cooling, optical addressing and laser phase control which represent prerequisites for our ion trap quantum computer are discussed. Chapter 8 discusses the major results of this thesis, i.e. the implementation of quantum gates and algorithms. Finally, chapter 9 summarizes the work presented here and gives an outlook on future goals.

# 2 Quantum Gates

## 2.1 Single Qubits

The most general state of a qubit reads

$$|\psi\rangle = e^{i\gamma}\left(\cos\frac{\alpha}{2}|0\rangle + e^{-i\beta}\sin\frac{\alpha}{2}|1\rangle\right). \tag{2.1}$$

Note that normalization to 1 is already included in this representation. In a pure spin-1/2 system, the overall phase $\gamma$ has no observable effect and can thus be ignored. Consequently the state vector can be rewritten as

$$|\psi\rangle = \left(\cos\frac{\alpha}{2}|0\rangle + e^{-i\beta}\sin\frac{\alpha}{2}|1\rangle\right). \tag{2.2}$$

A sometimes useful visualization of the qubit state of eqn. (2.2) is the Bloch vector. The latter is defined by a point on the unit sphere, the Bloch sphere, corresponding to the 3D angles $\alpha$ and $\beta$, as shown in Fig. 2.1.

A state $|\psi\rangle = a|1\rangle + b|0\rangle$ (with complex coefficients $a$ and $b$) of a qubit can also be written as a vector

$$[\psi] = \begin{bmatrix} a \\ b \end{bmatrix}.$$

Quantum operations in this single qubit space are represented by matrices, for example the quantum $NOT$ which flips the qubit state,

$$NOT = X = \begin{bmatrix} 0 & 1 \\ 1 & 0 \end{bmatrix}.$$

The X-matrix is in fact one of three fundamental matrices which are particularly useful in the description of a two-level system, the other two being

$$Y = \begin{bmatrix} 0 & -i \\ i & 0 \end{bmatrix} \quad \text{and} \quad Z = \begin{bmatrix} 1 & 0 \\ 0 & -1 \end{bmatrix}.$$

These are the three Pauli matrices which, outside quantum information, are normally denoted

$$\sigma_x = X, \quad \sigma_y = Y \text{ and } \sigma_z = Z.$$

There are two important theorems concerning unitary transformations in the two-level Hilbert space [13]:
1) An *arbitrary* unitary operation $U$ in the single qubit space can *always* be expressed as a

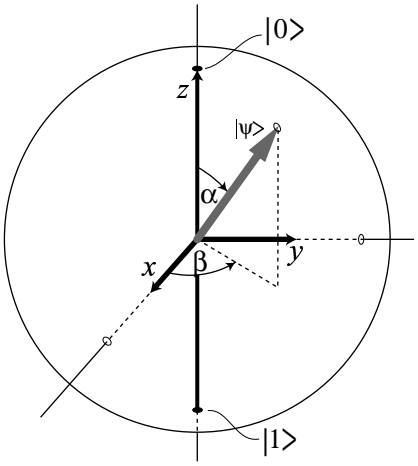


Figure 2.1: Bloch sphere representation of a qubit state $|\psi\rangle$.

rotation about a certain axis $\widehat{n}$ in the Bloch sphere by a certain angle $\theta$, modulo a possible global phase $\kappa$:

$$U = e^{i\kappa} R_{\widehat{n}}(\theta).$$

2) Given two non-colinear axes $\widehat{n}_1$ and $\widehat{n}_2$, an *arbitrary* rotation can always be decomposed into a series of rotations about $\widehat{n}_1$ and $\widehat{n}_2$.

In physical realizations of qubits, the two levels typically have different energies and single qubit operations are resonant excitations between these energy levels. The excitation pulse is typically some electromagnetic wave. The "static" qubit representation from above (see for example eqn. (2.2)) is obtained by a transformation into the rotating frame. In ion trap experiments qubits are normally encoded into two long-lived internal levels of each ion. Transitions between these energy levels are optically driven with laser radiation.

Independent of the precise physical qubit realization, the unitary transformation describing the action of a pulse of an electromagnetic wave resonant to the qubit transition (e.g. see section 3.3.3) reads

$$R(\theta, \phi) = e^{i\frac{\theta}{2}(e^{i\phi}\sigma^+ + e^{-i\phi}\sigma^-)}, \tag{2.3}$$

where

$$\sigma^+ = (\sigma_x + i\sigma_y)/2 = \begin{bmatrix} 0 & 1 \\ 0 & 0 \end{bmatrix}, \text{ and } \quad \sigma^- = (\sigma_x - i\sigma_y)/2 = \begin{bmatrix} 0 & 0 \\ 1 & 0 \end{bmatrix}$$

are the raising and lowering operators, respectively. $R(\theta, \phi)$ can be written as

$$R(\theta, \phi) = \begin{bmatrix} \cos\frac{\theta}{2} & ie^{i\phi}\sin\frac{\theta}{2} \\ ie^{-i\phi}\sin\frac{\theta}{2} & \cos\frac{\theta}{2} \end{bmatrix}.$$

It turns out that such a resonant excitation $R(\theta, \phi)$ corresponds to a rotation[1] of the Bloch vector about an axis $\widehat{n}_c$ which lies in the $x$-$y$ plane, see Fig. 2.2. The parameter $\phi$ defines the

[1] To within a possible global phase which does not directly show up in the Bloch sphere picture.

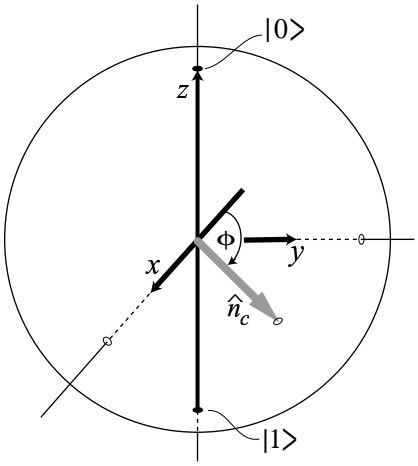


Figure 2.2: A resonant (carrier) excitation $R(\theta, \phi)$ corresponds to a rotation of the qubit state about an axis $\widehat{n}_c$ which lies in the $x$-$y$ plane; the angle $\phi$ defines the position of $\widehat{n}_c$ within that plane.

position of this axis within the $x$-$y$ plane as shown in Fig. 2.2. Experimentally, $\phi$ is defined by the phase of the exciting radiation. Experimental control of $\phi$ will be discussed in section 5.3. The parameter $\theta$ represents the pulse strength, defined as Rabi frequency times the duration of the pulse (cf. section 3.3.3). In the Bloch sphere picture, $\theta$ is the angle by which a given state vector gets rotated (about $\widehat{n}_c$).

The phases $\phi = \pi$ and $\phi = \pi/2$ correspond to rotations about the $x$-axis and the $y$-axis respectively. The corresponding matrices read:

$$R_x(\theta) := R(\theta, \pi) = e^{-i\frac{\theta}{2}X} = \begin{bmatrix} \cos\frac{\theta}{2} & -i\sin\frac{\theta}{2} \\ -i\sin\frac{\theta}{2} & \cos\frac{\theta}{2} \end{bmatrix} \tag{2.4}$$

and

$$R_y(\theta) := R(\theta, \pi/2) = e^{-i\frac{\theta}{2}Y} = \begin{bmatrix} \cos\frac{\theta}{2} & -\sin\frac{\theta}{2} \\ \sin\frac{\theta}{2} & \cos\frac{\theta}{2} \end{bmatrix}. \tag{2.5}$$

A rotation about the $z$-axis has the matrix form

$$R_z(\theta) = e^{-i\frac{\theta}{2}Z} = \begin{bmatrix} e^{-i\frac{\theta}{2}} & 0 \\ 0 & e^{i\frac{\theta}{2}} \end{bmatrix}. \tag{2.6}$$

Lower indices $\overline{x}, \overline{y}, \overline{z}$ (as opposed to $x, y, z$) denote the negative axes (or, equivalently, rotations in the opposite sense).

According to the above statement regarding the decomposition of an arbitrary rotation, any unitary single qubit transformation can be implemented as a series of $R_x(\theta)$ and $R_y(\theta)$ operations. Carrier laser pulses with the appropriate phases thus represent a *complete* single qubit toolbox. Example: a $\pi/2$-rotation about the $z$-axis,

$$R_z(\pi/2) = \begin{bmatrix} e^{-i\frac{\pi}{4}} & 0 \\ 0 & e^{i\frac{\pi}{4}} \end{bmatrix},$$

can be realized as

$$R_z(\pi/2) = R_{\overline{y}}(\pi/2)\ R_x(\pi/2)\ R_y(\pi/2).$$

Note that throughout this thesis concatenated operations are written down in the standard notation of matrix multiplication, i.e. chronologically sequences of operations like the above must be read from right to left. The operations $X$ and $Y$ correspond to $-iR_x(\pi)$ and $-iR_y(\pi)$, respectively.

## 2.2 Multi-Qubit Operations

Consider the composite system of $n$ qubits. It has been proven that an arbitrary unitary operator in the combined $2^n$ dimensional Hilbert space can be expressed as a product of *pairwise* and single qubit operations [17, 54–57]. This requires the availability of *universal* two-qubit gates on which the rest of this section will concentrate. A set of operators in a two-qubit computational space is called universal if any arbitrary operator in that space can be expressed as a product of them. It follows from the above that a "universal" two-qubit set is also universal for the whole $n$-qubit space. Note, however, that this statement says nothing about effciency, i.e. how many (polynomially or exponentially many) gates must be composed in order to create a given unitary transform.

An important two-qubit gate is the controlled-not gate ($CNOT$). The $CNOT$ operation flips one of the two qubits (the *target* qubit) if the other one (the *control* qubit) is in state $|1\rangle$ and leaves the target qubit unchanged if the control qubit is in $|0\rangle$. An example for a $CNOT$ is given by the matrix

$$CNOT = \begin{bmatrix} 1 & 0 & 0 & 0 \\ 0 & 1 & 0 & 0 \\ 0 & 0 & 0 & 1 \\ 0 & 0 & 1 & 0 \end{bmatrix},$$

where the notation of the matrix (just like all following two-qubit matrices) refers to the basis order $\{|0,0\rangle, |1,0\rangle, |0,1\rangle, |1,1\rangle\}$. In case of this $CNOT$, the second qubit (right in the bra-ket notation) controls the $NOT$-operation on the first. It can be shown that the $CNOT$ gate in combination with single qubit operations, forms a universal set of operators. In this sense the $CNOT$ is called a *universal two-qubit gate.*

The $CNOT$ itself can be decomposed as

$$CNOT = H_1\ \Phi\ H_1 \tag{2.7}$$

where $H$ denotes Hadamard gates which are single qubit operations, given by

$$H = \frac{1}{\sqrt{2}} \begin{bmatrix} 1 & 1 \\ 1 & -1 \end{bmatrix}.$$

The lower index 1 denotes that the matrix is extended to the composite space and that the gate acts on the *first* qubit. In the 2-qubit Hilbert space it thus reads

$$H_1 = \frac{1}{\sqrt{2}} \begin{bmatrix} 1 & 1 & 0 & 0 \\ 1 & -1 & 0 & 0 \\ 0 & 0 & 1 & 1 \\ 0 & 0 & 1 & -1 \end{bmatrix}.$$

$\Phi$ is a *phase gate* reading

$$\Phi = \begin{bmatrix} 1 & 0 & 0 & 0 \\ 0 & 1 & 0 & 0 \\ 0 & 0 & 1 & 0 \\ 0 & 0 & 0 & -1 \end{bmatrix}. \tag{2.8}$$

Consequently $\Phi$ (sometimes called a controlled-$Z$ gate) also represents a universal two-qubit gate.

It should be mentioned that the Hadamard gate, although frequently used in the literature, is not particularly well suited for a physical implementation: It has been stated above that any unitary operation can be expressed as a rotation $U = e^{i\kappa} R_{\widehat{n}}(\theta)$. In case of $H$, the rotation axis $\widehat{n}$ is the diagonal of the $x$-$z$-plane, namely $(x, y, z) = 1/\sqrt{2}(1, 0, -1)$ and the rotation angle $\theta$ is $\pi$. Consequently, it does not correspond to a resonant excitation of the qubit which is always a rotation about an axis lying in the $x$-$y$-plane (see above). $H$ can therefore not be implemented by a single resonant (laser) pulse. However, it can be decomposed, into a series of $x$-$y$-rotations, for example:

$$H = i \cdot R_x(\pi)\ R_y(\pi/2), \text{ or } \ H = -i \cdot R_y(\pi/2)\ R_x(\pi),$$

which correspond to a total of three rotations by $\theta = \pi/2$. Note that if the matrix is extended to a multi-qubit space the phase factor of $i$ remains global, and is thus of no physical importance. In other words, a Hadamard gate acting on qubit number 1 in a Hilbert space composed of arbitrarily many qubits can be written as

$$H_1 = -i \cdot R_{y1}(\pi/2)\ R_{x1}(\pi).$$

Fortunately, three $\pi/2$-pulses are not normally needed to implement a Hadamard gate appearing in some given algorithm; the overall sequence can typically be compiled into a shorter one. For example, $\Phi$ can be transformed into a $CNOT$ also by the sequence

$$CNOT = R_{y1}(\pi/2)\ \Phi\ R_{\bar{y}1}(\pi/2).$$

Thus, the Hadamard gates of eqn. (2.7) can be replaced by suitable single $\pi/2$ laser pulses.

Note that $\Phi$ itself is symmetric with respect to an exchange of the qubits. Only the surrounding (single qubit) pulses specify which one is the target qubit (here: number 1).

Various (universal) phase gates exist. The $-1$ of the gate $\Phi$ can, for example, be anywhere on the diagonal and the gate will still serve essentially the same purpose: If the gate is sandwiched between two Hadamard gates as in eqn. (2.7), then varying the positioning of the $-1$ on the diagonal of the phase gate will, at most, invert the role of $|0\rangle$ and $|1\rangle$ of the control qubit, thus resulting in a zero-controlled-not

$$0-CNOT = \begin{bmatrix} 0 & 1 & 0 & 0 \\ 1 & 0 & 0 & 0 \\ 0 & 0 & 1 & 0 \\ 0 & 0 & 0 & 1 \end{bmatrix}.$$

$0-CNOT$ and $CNOT$ can always be transformed into each other by two $NOT$ operations on the control qubit:

$$0-CNOT = NOT_2\ CNOT\ NOT_2.$$

Another phase gate which we have actually implemented experimentally ($\Phi(\tau_0)$ of section 8.1) reads

$$\Phi^* = \begin{bmatrix} 1 & 0 & 0 & 0 \\ 0 & 1 & 0 & 0 \\ 0 & 0 & i & 0 \\ 0 & 0 & 0 & -i \end{bmatrix}.$$

This clearly deviates from the "classical" phase gate $\Phi$ but it is still a universal two-qubit gate: The equation

$$\Phi = -i \cdot R_{z2}(\pi/2)\ \Phi^*,$$

which is easy to verify, shows that $\Phi^*$ can be directly transformed into $\Phi$ by a $\pi/2$ rotation of qubit 2 around the $z$-axis. This proves the universality of $\Phi^*$, as it can be transformed into a well known universal two-qubit gate using only a single qubit rotation. The $\Phi^*$ gate can also be transformed into a universal gate $C$ similar to the well known $CNOT$ using the sequence

$$C = R_{x1}(\pi/2)\ \Phi^*\ R_{\bar{x}1}(\pi/2) = \begin{bmatrix} 1 & 0 & 0 & 0 \\ 0 & 1 & 0 & 0 \\ 0 & 0 & 0 & -1 \\ 0 & 0 & 1 & 0 \end{bmatrix}.$$

It is important to note that, while quantum algorithms are often written down using "standard" gates like $CNOT$, they can always be rearranged to instead incorporate (for example) $C$ or $C'$.

Finally, an intriguing feature of a driven two-level system, namely its $4\pi$ periodicity, shall be discussed. A look at equations (2.3) through (2.5) shows that it is the angle $\frac{\theta}{2}$ instead of $\theta$ which appears in the functions. Consequently their true period is $\triangle\theta = 4\pi$. Rotations by $\theta = 2\pi$ bring any state vector back to itself on the Bloch sphere, but a phase factor of $-1$ is acquired: $R(2\pi, \phi) = -I$, where $I$ is the identity operator.

This $-1$ on a first view is a global phase factor and it has been argued above (cf. eqn. (2.1)) that it can be dropped. This is in general only true if the two coupled states form a pure and separate two-level system, the Hilbert space of which will be denoted by $\mathcal{H}_1$. If this system is combined with others $\mathcal{H}_2, \mathcal{H}_3, \ldots$ (which could be two-level systems as well, or also larger systems) the composite system is discribed by the Hilbert space

$$\mathcal{H} = \mathcal{H}_1 \otimes \mathcal{H}_2 \otimes \mathcal{H}_3 \otimes \ldots$$

It is clear that the $-1$ phase factor in this case is global in $\mathcal{H}_1$ and also in an arbitrarily large extension $\mathcal{H}$.

If, however, $\mathcal{H}_1$ contains more than two levels or if transitions are driven selectively between certain level pairs of the combined system $\mathcal{H}$, then the acquired phases are, in general, not global any more. Such non-global phases are made use of for the implementation of quantum logic with trapped ions, see section 4.2. Note that the Bloch sphere picture does not directly display the two-level global phase.

# 3 Ion Trapping and Interaction with Light

## 3.1 Linear Paul Traps

According to the Laplace equation $\Delta\Phi = 0$, confinement of a charged particle in three dimensions with *static* electric fields alone is not possible. Take for example an electric quadrupole field $\mathbf{E} = -\nabla\Phi$ which originates from a quadratic potential

$$\Phi = \alpha_x x^2 + \alpha_y y^2 + \alpha_z z^2.$$

Applying the Laplace equation yields $\alpha_x + \alpha_y + \alpha_z = 0$. Consequently, at least one of the three coefficients must be negative which corresponds to a repulsive potential in this direction. Paul traps and mass filters make use of time-dependent, oscillating fields to confine charged particles in all three dimensions.

Paul mass filters are based on two dimensional quadrupole fields, i.e. $\alpha_z = 0$. This potential shape can be experimentally realized by an electrode structure as depicted in Fig. 3.1. The Laplace eqation in this case gives $\alpha_x = -\alpha_y$ which means that $\Phi$ can be written as

$$\Phi_s(\mathbf{r}) = V\frac{x^2 - y^2}{2r_0^2}\ , \tag{3.1}$$

where $\mathbf{r} = (x, y, z)$. A trap structure as in Fig. 3.1 where the minimum distance from the trap axis to an electrode is $r_0$ and where voltages $V_{1,2} = \pm V/2$ are applied to diagonally opposite rods respectively, produces exactly this potential if the inner electrode surfaces are hyperbolically shaped[1].

For radial confinement of charged particles, the potential $\Phi_s$ is modulated sinusoidally:

$$\Phi(\mathbf{r}, t) = \Phi_s(\mathbf{r})\cos(\Omega t)\ ,$$

where $\Omega$ typically is in the radiofrequency range of several MHz. This means experimentally that an RF voltage $V_1(t) = V\cos(\Omega t)$ must be applied to one pair of diagonally opposite electrodes and a 180° phase shifted voltage $V_2(t) = -V_1(t)$ to the other pair (see Fig. 3.1). This configuration was actually the starting point of all radiofrequency traps, and was invented by Wolfgang Paul in 1953 as a mass filter. Only a few years later it was realized that the same setup could serve as a trap for charged particles [58], by adding DC-electrodes which confine the axial motion. When used as a mass filter, typically an additional offset DC voltage is applied to one of the diagonally opposite rod pairs. In the experiments presented here such an

[1] The situation is essentially the same if, as in our experiments, a voltage $V_1 = V$ is applied to one of the diagonally opposite rod pairs, while the other pair is held at ground potential ($V_2 = 0$)

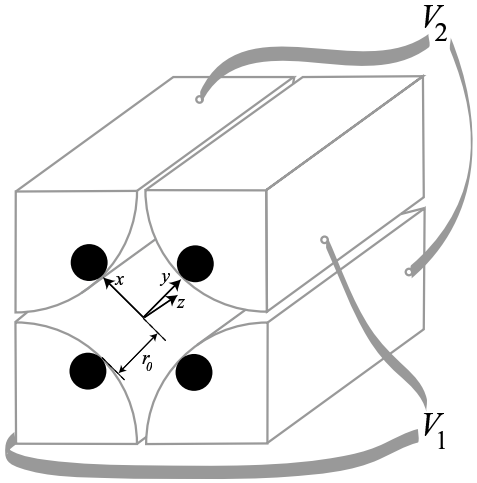


Figure 3.1: Schematic diagram of a quadrupole mass filter. Hyperbolically shaped inner surfaces (grey contours) guarantee a pure quadrupole potential inside the electrode structure. For better optical access, rod-shaped electrodes (black circles) are usually chosen.

offset voltage was never used and therefore will not be taken into account in this treatment.

The classical equations of motion for an ion of mass $M$ and charge $e$ in the potential $\Phi(\mathbf{r}, t)$ are $\mathbf{F} = -e\nabla\Phi = M\ddot{\mathbf{r}}$. They are special versions of the *Mathieu equations* and can be written in the following simple form:

$$\begin{aligned} \frac{d^2x}{d\tau^2} - 2q\cos(2\tau)x &= 0 \\ \frac{d^2y}{d\tau^2} + 2q\cos(2\tau)y &= 0 \\ \frac{d^2z}{d\tau^2} &= 0 \end{aligned}$$

where

$$\tau = \frac{1}{2}\Omega t \quad \text{and} \quad q = \frac{2eV}{Mr_0^2\Omega^2}\,. \tag{3.2}$$

These equations have stable solutions for $0 < q < 0.908$ [59]. In this parameter range the ion is confined radially, i.e. in $x$ and $y$, and moves freely along $z$.

In the experiments presented here, a high degree of optical access from many directions is desirable, in particular because single ion addressing and read out is required. Therefore, electrodes with smaller cross sections are chosen. They could for example be blade- or rod-shaped (Fig. 3.1). In this case, the assumption that the electric potential is quadrupole-like is only valid in a region near the trap axis. Further away from the trap axis, higher order multipole contributions must be taken into account to describe the actual potential. These multipole potentials lead to nonlinear resonances [60] which can cause trapping instabilities for values $0.5 \lesssim q < 0.908$. The exact pattern of nonlinear resonances and their strength strongly

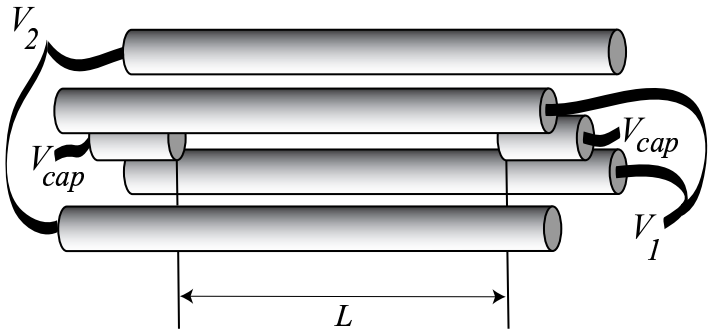


Figure 3.2: A linear Paul trap for charged particles. RF-voltages $V_1$ and $V_2$ produce radial confinement while the end-cap voltages $V_{cap}$ confine the axial motion.

depends on the individual trap design. The resonances become more densely spaced towards larger $q$-values near 0.908 [60]. The higher the order of a multipole causing a resonance, the smaller the effect near the trap center. Consequently, the instability problem is reduced if, as in our experiments, the ions are cooled close to their motional ground state because then the ions' wavefunctions only extend about ten nanometers from the trap axis. If a trap like ours, with non-hyperbolic electrodes, is still perfectly machined in a four-fold mirror symmetry and potentials $+V$ and $-V$ are applied to diagonally opposite pairs, then the first (lowest) multipole correction which occurs is a 16-pole (hexadecapole) [60]. Geometric imperfections on the other hand, also lead to lower order contributions.

For full 3D confinement the Paul mass filter is turned into a *linear Paul trap* by additional electrodes, called "end-caps", to which DC-voltages are applied. Fig. 3.2 shows a possible linear trap configuration where the end-caps are rod-shaped and placed on the trap axis. Such end-cap geometries have been experimentally realized [61] but also other end-cap configurations such as ring-shaped end-caps around the RF-rods [62] or segmented RF-rods [63–65]. It will be shown that axial confinement by DC-voltages has a defocusing effect on the radial confinement. The new equations of motion near the trap center are given by [66] :

$$\frac{d^2x}{d\tau^2} + (b - 2q\cos(2\tau))x = 0 \tag{3.3}$$

$$\frac{d^2y}{d\tau^2} + (b + 2q\cos(2\tau))y = 0 \tag{3.4}$$

$$\frac{d^2z}{d\tau^2} + 2bz = 0 \tag{3.5}$$

where

$$b = \frac{e\alpha V_{cap}}{mL^2\Omega^2} \tag{3.6}$$

(see Fig. 3.2) with a numerical factor $\alpha$ which depends on the geometry of the trap configuration. It is straightforward to show that the axial motion is harmonic with a frequency (in real time t)

$$\omega_z = \sqrt{\frac{b}{2}}\Omega = \sqrt{\frac{e\alpha V_{cap}}{2mL^2}}\,. \tag{3.7}$$

An analysis [59], [66] of the Mathieu equations (3.3) & (3.4) for the radial motion shows that an ion's motion in this potential separates into a slow *secular motion* around the trap center and a faster driven oscillation called *micromotion* at the frequency $\Omega$ around the trajectory of the secular motion. Moreover, for $b, q \ll 1$ the secular motion is harmonic. In other words the ions can then be considered to move in a harmonic quasi-potential which is produced by the RF-drive. This treatment holds even in the quantum mechanical limit [67], i.e. the harmonic oscillator of the secular motion can be quantized just as in a normal (non-quasi) potential. The frequency of this secular radial motion is

$$\omega_r = \omega_x = \omega_y = \frac{\Omega}{2}\sqrt{\frac{1}{2}q^2 - b}$$

This shows the previously mentioned defocussing effect of the axial confinement on the radial trapping: when operating a linear trap at a certain RF-drive power, i.e. a certain RF-amplitude $V$, and at very low end-cap voltages $V_{cap}$ ($\Rightarrow b \approx 0$) one finds the "pure" radial frequency

$$\omega_{r0} = \frac{q\Omega}{2\sqrt{2}} \tag{3.8}$$

and by increasing the end-cap voltages, i.e. increasing the axial frequency $\omega_z$, the radial frequency is reduced to

$$\omega_r = \sqrt{\omega_{r0}^2 - \frac{1}{2}\omega_z^2}\,.$$

It can be seen from this equation that for $\omega_z \ll \omega_{r0}$ the defocussing is negligible. In the other limit however, where $b \ll 1$ no longer holds, it has effects on trapping stability and the configuration of ion crystals (see also section 3.2.2). In fact, the $b$-$q$-stability diagram [66] shows that with axial confinement, i.e. for non-zero $\omega_z$
a) $\omega_r$ can no longer be arbitrarily low.
b) $q$ can be above the limit for a linear mass filter without end-caps (0.908). Moreover, for high enough $\omega_z$ in principle arbitrarily high radial frequencies could be reached. In this limiting case, however, the parameter range for stable trapping becomes increasingly narrow and furthermore the axial frequency always has to be larger than the radial frequency which is not suitable for trapping linear ion strings as necessary for the type of experiments presented here.

## 3.2 Linear Ion Crystals

### 3.2.1 Equilibrium Positions

The potential energy of $N$ ions of mass $M$ and charge $e$ confined in the 3-dimensional harmonic trap potential with (angular) frequencies $\omega_x, \omega_y$ and $\omega_z$ is given by [67]

$$U = \frac{M}{2}\sum_{n=1}^{N}(\omega_x^2 x_n^2 + \omega_y^2 y_n^2 + \omega_z^2 z_n^2) + \frac{e^2}{8\pi\epsilon_0}\sum_{\substack{n,m=1 \\ m\neq n}}^{N}\frac{1}{|\mathbf{r}_n - \mathbf{r}_m|}\,, \tag{3.9}$$

where $\mathbf{r}_n = (x_n, y_n, z_n)$ is the position vector of the $n$th ion. The first term is the trap potential, while the second describes the mutual Coulomb interactions. In a linear trap where $\omega_z$ denotes the axial frequency, the two radial frequencies are degenerate if the trap construction is perfectly symmetric:

$$\omega_x = \omega_y = \omega_r \ .$$

The following treatment of equilibrium positions assumes a linear ion chain configuration. This is true only if the radial confinement is sufficiently stronger than the axial confinement and if the number of ions N is not too large, otherwise the ions will assume a zig-zag or even more complicated 3-dimensional geometric configurations. The exact conditions for the transition from linear to zig-zag configuration will be discussed in section 3.2.3. A linear configuration implies that $x_n^{(0)} = y_n^{(0)} = 0$, where the upper index $^{(0)}$ denotes the ions' equilibrium positions. The axial equilibrium positions $z_n^{(0)}$ are then determined by the following equation:

$$\left[\frac{\partial U}{\partial z_n}\right]_{z_n=z_n^{(0)},\ x_n=y_n=0} = 0 \ .$$

For $N = 2$ and $N = 3$, they can be solved analytically [67,68]:

$$\begin{aligned} N=2: &\quad z_1 = -(1/2)^{2/3}\ l,\ z_2 = (1/2)^{2/3}\ l \\ N=3: &\quad z_1 = -(5/4)^{1/3}\ l,\ z_2 = 0,\ z_3 = (5/4)^{1/3}\ l \ , \end{aligned} \tag{3.10}$$

where

$$l = \left(\frac{e^2}{4\pi\epsilon_0 M\omega_z^2}\right)^{1/3} \tag{3.11}$$

represents the natural length scale of the problem. The experiments presented here work with axial trap frequencies on the order of $\omega_z = 2\pi \cdot 1$ MHz. For $^{40}Ca^+$ ions this amounts to inter-ion-separations of $\triangle z = 5.6\ \mu$m and $\triangle z = 4.8\ \mu$m for $N = 2$ and $N = 3$, respectively. For more than three ions the problem must be solved numerically. The spacing between adjacent ions then increases in size from the center to the outside of the string, hence the minimum separation $\triangle z_{min}$ in the crystal occurs between the central ions. Numerical simulations yield [68]

$$\triangle z_{min} \simeq 2.0\ l N^{-0.57} \ .$$

This approximation remains accurate for the entire ion number range of interest and even up to $N \simeq 1000$. For quantum computing purposes individual ion addressing is required. This addressing is obviously most difficult for the most closely spaced central ions.

### 3.2.2 Normal Modes

For small oscillations around the equilibrium positions ($y_n^{(0)} = 0,\ x_n^{(0)} = 0,\ z_n^{(0)}$) the Lagrangian $L = T - U$ of the system ($T$ being the kinetic energy) takes the form [69]

$$L = \frac{M}{2} \sum_{i=x,y,z} \left( \sum_{n=1}^{N} (\dot{\varrho}_{i|n}^2) - \omega_z^2 \sum_{n,m=1}^{N} (C_{n,m}^i \varrho_{i|n} \varrho_{i|m}) \right) \ ,$$

where $\varrho_{x|n}$, $\varrho_{y|n}$ and $\varrho_{z|n}$ are the displacements of the $n$th ion from its equilibrium position in $x$, $y$ and $z$ direction, respectively. The coupling matrices are given by

$$C^z_{n,m} = \begin{cases} 1 + 2 \sum\limits_{\substack{p=1 \\ p \neq m}}^{N} \frac{l^3}{\left|z^{(0)}_m - z^{(0)}_p\right|^3} & \text{if } n = m \ , \\ \frac{-2l^3}{\left|z^{(0)}_m - z^{(0)}_n\right|^3} & \text{if } n \neq m \end{cases}$$

and

$$C^x_{n,m} = C^y_{n,m} = \left(\frac{1}{\alpha} + \frac{1}{2}\right)\delta_{n,m} - \frac{1}{2}C^z_{n,m} \ ,$$

where $\delta_{n,m}$ is the Kronecker delta and $\alpha = (\omega_z/\omega_r)^2$ is a parameter describing the anisotropy of the trap potential. It can be seen that the motions in $x$, $y$ and $z$ direction are coupled. The radial directions $x$ and $y$ are assumed to be degenerate. As a consequence, the solutions of the problem, obtained by diagonalization of the $C^x$, $C^y$ and $C^z$ matrices, are two independent sets of normal modes. One set contains normal modes in the axial direction, the other in the radial direction, the latter being two-fold degenerate corresponding to $x$- and $y$-directions. There are $N$ axial and $2N$ radial modes.

The principal mode of the *axial modes* is the center-of-mass mode in which all ions move parallel in the axial direction with the same amplitude. This will be called the axial COM mode, and has the frequency $\omega_z$ (the axial frequency of a single ion). Higher order axial modes always have higher frequency. The second axial mode is the breathing mode, where the ions oscillate with amplitudes proportional to their distance from the trap center - in magnitude as well as in sign. This means that for uneven ion numbers the center ion stands still in the breathing mode. The frequency of the breathing mode is $\sqrt{3}\omega_z$, independent of the number of ions in the chain. The motional behaviour of higher order modes is described by more complicated eigenvectors. The frequencies of these modes have to be determined numerically and depend slightly on the total ion number. This dependence, however, is so weak that, for example, for all $N \leq 10$ the axial mode frequencies are described with very high accuracy by the list $\{1,\ \sqrt{3},\ \sqrt{29/5},\ 3.051,\ 3.671,\ 4.272,\ 4.864,\ 5.443,\ 6.013,\ 6.576\}$ in units of $\omega_z$ [68]. The spatial extension of the ions' wavepackets is described by the standard deviation of the Gaussian ground state probability distribution of the axial COM mode, which is given by

$$\delta z_{com} = \sqrt{\frac{\hbar}{2NM\omega_z}} \ .$$

This estimate is only reasonable, if the ions are cooled very close to the ground state, which, however, is possible in our experiment (as will be shown in chapter 7.2). For two $^{40}Ca^+$ ions and $\omega_z = 2\pi \cdot 1$ MHz one finds $\delta z_{com} = 7.9$ nm which is three orders of magnitude smaller than the separation between the two ions.

The principal *radial mode* is again the center-of-mass mode, all ions oscillating radially in phase and with equal amplitude at the frequency $\omega_r$. This mode is referred to as the radial COM mode. In contrast to the axial modes, however, every higher order mode is at a *lower* frequency [69]. The eigenvectors of the radial modes point radially instead of in the $z$-direction but are otherwise formally identical to the eigenvectors of the axial modes. As with the axial

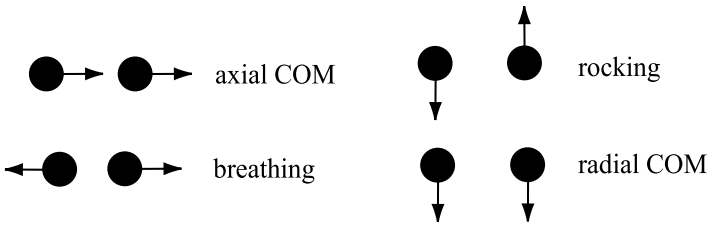


Figure 3.3: Normal modes of a two-ion crystal. The frequencies are: axial COM $\omega_z$, breathing $\sqrt{3}\omega_z$, radial COM $\omega_r$, rocking $\sqrt{\omega_r^2 - \omega_z^2}$.

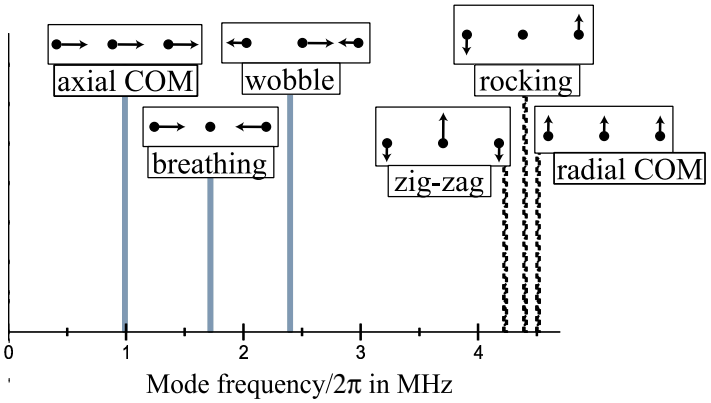


Figure 3.4: Mode frequency spectrum of a crystal of three $^{40}Ca^+$ ions in a linear trap with $\omega_r = 2\pi \cdot 4.5$ MHz and $\omega_z = 2\pi \cdot 1$ MHz (which are typical parameters for the experiments presented here). The frequencies are $\omega_{axialCOM} = 2\pi \cdot 1$ MHz, $\omega_{breathing} = 2\pi \cdot 1.73$ MHz, $\omega_{wobble} = 2\pi \cdot 2.41$ MHz, $\omega_{zig-zag} = 2\pi \cdot 4.22$ MHz, $\omega_{rocking} = 2\pi \cdot 4.39$ MHz and $\omega_{radialCOM} = 2\pi \cdot 4.5$ MHz. The modes are labeled with schematic pictures of their eigenvectors.

modes, the frequency of the second, often called rocking, mode can be determined analytically and does not depend on the number of ions in the chain:

$$\omega_{rock} = \sqrt{\omega_r^2 - \omega_z^2}\ .$$

The frequencies of higher order modes must be calculated numerically and again depend only very slightly on $N$.

The normal modes of two ions are depicted in Fig. 3.3, while Fig. 3.4 shows the mode structure[2] of a linear three-ion crystal in a trap potential typical for our present experiment.

[2]There is no clear convention for the naming of higher order modes; the names chosen here (in particular "wobble mode", "zig-zag mode") are descriptive of the motional behaviour.

### 3.2.3 Stability of a Linear String

One method to characterize the tranisition from a linear ion chain to a zig-zag crystal are numerical molecular dynamics simulations of the equilibrium crystalline configurations as done by Schiffer [70]. An alternative approach, offering a more physical picture of the process, is a stability analysis of the radial oscillations [69]: The radial mode of highest order (and therefore lowest frequency) is always the zig-zag mode where each ion moves in the opposite direction of its neighbor(s). The frequency of this mode decreases with increasing $N$ and with increasing anisotropy parameter $\alpha$. An instability occurs when $\omega_{zig\text{-}zag} = 0$, i.e. the corresponding oscillation freezes out and the new equilibrium configuration is a zig-zag.

For the critical anisotropy parameter where the transition occurs a power-law scaling $\alpha_{crit} = cN^{\gamma}$ is accurate for ion numbers of up to 1000 [68]. Of the two approaches mentioned above, molecular dynamics simulations have been performed more extensively, i.e. on a greater set of values, and therefore their results for the constants $c$ and $\gamma$ are probably the most reliable[3]:

$$\left(\frac{\omega_z}{\omega_r}\right)^2_{crit} = 2.53N^{-1.73}. \tag{3.12}$$

This scaling for the transition from linear to zig-zag configuration has been investigated experimentally by Enzer *et al.* [69].

Quantum computational applications must have the ions in a linear chain since in a zig-zag configuration they would encounter too much micromotion. This would, for example, lead to excessive motional heating. Typical parameters of our experiment are far from such a geometric transition. This can be seen for example in Fig. 3.4 from the fact that the zig-zag mode frequency is still far from zero. Eqn. (3.12) can be used to calculate the maximum ion number before the crystal becomes zig-zag-shaped for those trap frequencies and the result is $N < 10$. In practice, however, one is limited to smaller ion numbers. This is mainly related to the fact that the Lamb-Dicke parameter decreases with the number of ions (cf. section 4.4).

[3] The values of the parameter $c$ in Schiffers paper [70] appear to be misprinted as the reciprocals of their true values.

## 3.3 Spectroscopy

### 3.3.1 Level Scheme and Laser Manipulation of $^{40}Ca^{+}$

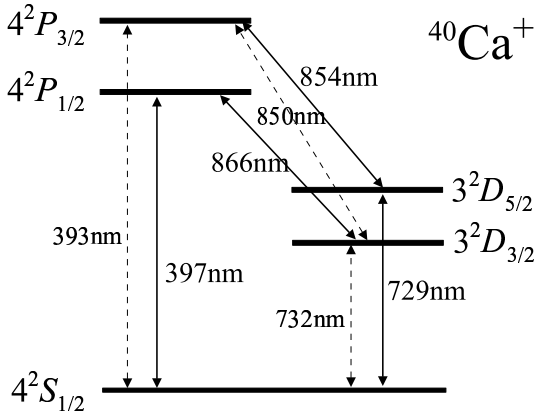


Figure 3.5: Electronic levels of $^{40}Ca^{+}$. The transitions indicated by solid line arrows are actively driven by laser radiation in the experiments. Note that all states indicated here split up into several Zeeman-substates.

The ion of choice for our quantum computing experiments is $^{40}Ca^{+}$. Fig. 3.5 shows all levels which ever get populated in the experiment. In the following, the first two terms of the spectroscopic notation (electronic shell quantum number and the multiplicity) are omitted. The 729 nm transition will be used for coherent manipulations. In other words, the levels $S_{1/2}$ and $D_{5/2}$ will be associated with the logic states of a qubit. To be more specific, one of the Zeeman substates $m = \{-1/2, +1/2\}$ of $S_{1/2}$ is selected as the logic $|0\rangle$, and one of the Zeeman substates $m = \{-5/2, -3/2, -1/2, +1/2, +3/2, +5/2\}$ of $D_{5/2}$ as the logic $|1\rangle$. The optical transition between the two states is an electric quadrupole transition (dipole-forbidden). Accordingly, the $D_{5/2}$ state has a rather long lifetime ($\approx$ 1 s) which ensures coherence of the qubit over this time scale. The particular features of this transition will be discussed in section 3.3.5. The qubit is coherently manipulated by narrow bandwidth laser radiation at 729 nm (cf. chapter 4).

A quantum computing protocol also requires a qubit *measurement* procedure. For this, the dipole transition at 397 nm is employed which connects to only one of the qubit states, namely $S_{1/2}$. Therefore we can apply an *electron shelving* technique [4] to measure the qubit state: Suppose the ion is in a superposition of $S_{1/2}$ and $D_{5/2}$. Light at 397 nm is applied, driving the $S_{1/2} \leftrightarrow P_{1/2}$ transition, and thereby projecting the atomic state to either $S_{1/2}$ or $D_{5/2}$. No fluorescence is detected if the ion is in the $D_{5/2}$ state, while in the opposite case light is scattered on the $S_{1/2} \leftrightarrow P_{1/2}$ transition. By repeatedly preparing the ion in the same state and measuring the fluorescence as described, the $D_{5/2}$ state occupation can be determined. Details of this electron shelving procedure have been discussed previously [4]. The detection efficiency is limited only by the finite lifetime of the $D_{5/2}$ state and can be as high as 99.9% with the present experimental setup.

The $S_{1/2} \leftrightarrow P_{1/2}$ transition is additionally used for Doppler cooling (cf. section 7.2.1) by red-detuning the laser at 397 nm by about half a linewidth. Whenever resonant light is scattered on this transition (for state detection or for Doppler cooling) the ion sometimes decays from $P_{1/2}$ into the $D_{3/2}$ state. Therefore a repumping laser at 866 nm is always applied along with the 397 nm light. The branching ratio is 15:1 between the $P_{1/2} \rightarrow S_{1/2}$ and the $P_{1/2} \rightarrow D_{3/2}$ decay.

Finally, a laser at 854 nm can be used to repump a possible $D_{5/2}$ population to the $S_{1/2}$ state or to quench the $D_{5/2}$ level if required. Quenching is necessary for sideband cooling on the $S_{1/2} \leftrightarrow D_{5/2}$ transition (cf. section 7.2.2).

In the following, the interaction of a harmonically trapped two-level atom (or ion) with light will be discussed and the $S_{1/2} \leftrightarrow D_{5/2}$ qubit transition will by analysed.

### 3.3.2 Laser-Ion Interaction

The following two sections are based on the discussion of laser-ion interaction in the PhD thesis of Christian Roos [4]. A main difference here is that the relative phase $\phi$ between the laser field and the atomic polarization is included throughout the discussion.

An ion trapped in a harmonic potential with frequency $\omega$, interacting with the travelling wave of a single mode laser tuned close to a transition that forms an effective two-level system, is described by the Hamiltonian [71, 72]

$$\begin{aligned} H &= H_0 + H_1 && (3.13)\\ H_0 &= \frac{p^2}{2m_0} + \tfrac{1}{2} m_0 \omega^2 x^2 + \tfrac{1}{2}\hbar\omega_a \sigma_z && (3.14)\\ H_1 &= \tfrac{1}{2}\hbar\Omega(\sigma^+ + \sigma^-)\left(e^{i(kx-\omega_l t+\phi)} + e^{-i(kx-\omega_l t+\phi)}\right) , && (3.15) \end{aligned}$$

where $k$ is the wave number, $\omega_l$ the frequency and $\phi$ the phase of the laser radiation; see section 2.1 for a definition of the matrices $\sigma_z, \sigma^+$ and $\sigma^-$. Finally, $m_0$ is the mass of the ion. The part $H_0$ of the Hamiltonian describes the state of the ion while the laser-ion interaction is contained in $H_1$, its strength being given by the coupling constant $\Omega$. Here it has been assumed that only a single transition ($\omega_a$ being the atomic transition frequency) is close to resonance and that the laser is directed along the x-axis to the ion. The Pauli operators act on the internal atomic states, $|S\rangle$ and $|D\rangle$. Defining the Lamb-Dicke parameter[4],

$$\eta = k\sqrt{\frac{\hbar}{2m_0\omega}} , \qquad (3.16)$$

the ion's external degrees of freedom, i.e. its harmonic oscillation, can be expressed in terms of creation and annihilation operators as

$$\begin{aligned} H_0 &= \hbar\omega(a^\dagger a + \tfrac{1}{2}) + \tfrac{1}{2}\hbar\omega_a\sigma_z && (3.17)\\ H_1 &= \tfrac{1}{2}\hbar\Omega\left(e^{i\eta(a+a^\dagger)}\sigma^+ e^{-i(\omega_l t+\phi)} + e^{-i\eta(a+a^\dagger)}\sigma^- e^{i(\omega_l t+\phi)}\right) . && (3.18) \end{aligned}$$

[4] If the laser is at an angle $\beta$ to the oscillation axis, the definition has to be replaced by $\eta = k\cos\beta\sqrt{\hbar/2m\omega}$.

Here, the rotating wave approximation [73] has been made. In the interaction picture defined by $U = e^{iH_0 t/\hbar}$ the Hamiltonian $H_I = U^\dagger H U$ takes the form

$$H_I = \tfrac{1}{2}\hbar\Omega\left(e^{i\eta(\hat{a}+\hat{a}^\dagger)}\sigma^+ e^{i\phi}e^{-i\Delta t} + e^{-i\eta(\hat{a}+\hat{a}^\dagger)}\sigma^- e^{-i\phi}e^{i\Delta t}\right) , \tag{3.19}$$

with $\hat{a} = ae^{i\omega t}$ and $\Delta = \omega_l - \omega_a$. The laser couples the state $|S,n\rangle$ to all states $|D,n'\rangle$, where $n, n'$ are vibrational quantum numbers. If the laser is tuned close to resonance of a transition $|S,n\rangle \leftrightarrow |D,n+m\rangle$ with fixed $m$ and $n = 0,1,2,3,...$ (which corresponds to $(\omega_l - \omega_a) \approx m\omega$), coupling to other levels can be neglected, provided the laser intensity is sufficiently low ($\Omega \ll \omega$). This assumption is valid for all experiments presented in this thesis[5]. In that case, the laser induces a pairwise coupling between the levels $|S,n\rangle$ and $|D,n+m\rangle$. The time evolution of the state $\Psi(t) = \sum_k (c_k(t)|S,k\rangle + d_k(t)|D,k\rangle)$ is governed by the Schrödinger equation $i\hbar\partial_t\Psi = H\Psi$ which is equivalent to the set of coupled equations

$$\dot{c}_n = -i^{(1-|m|)}e^{i\delta t}e^{-i\phi}\,(\Omega_{n+m,n}/2)\,d_{n+m} \tag{3.20}$$

$$\dot{d}_{n+m} = -i^{(1+|m|)}e^{-i\delta t}e^{i\phi}\,(\Omega_{n+m,n}/2)\,c_n\ . \tag{3.21}$$

$\delta = \Delta - m\omega$ accounts for a detuning of the laser from the transition, the constant

$$\Omega_{n+m,n} := \Omega\|\langle n+m|e^{i\eta(a+a^\dagger)}|n\rangle\| \tag{3.22}$$

is called Rabi frequency. Solutions to these equations show an oscillatory and complete exchange of population between the coupled levels. On resonance, this oscillation takes place with a frequency equal to the Rabi frequency $\Omega_{n+m,n}$. When the laser is detuned from resonance, the population transfer is no longer complete (amplitude $\Omega^2_{n+m,n}/(\delta^2 + \Omega^2_{n+m,n})$), yet it takes place at a higher frequency ($= \sqrt{\delta^2 + \Omega^2_{n+m,n}}$) [4].

Transitions that do not change the number of vibrational quanta ($\leftrightarrow m = 0$) are called *carrier* transitions. A transition is termed *blue sideband* if an absorption process is accompanied by an increase in the motional quantum number ($\leftrightarrow m = +1$) while it is termed *red sideband* if it decreases upon absorption ($\leftrightarrow m = -1$).

### 3.3.3 Lamb-Dicke Regime

For a given Lamb-Dicke parameter $\eta$, the coupling strengths $\Omega_{n,n}$, $\Omega_{n-1,n}$ and $\Omega_{n+1,n}$ of carrier, red and blue sideband, respectively, as a funtion of $n$ can be calculated [4] using eqn. (3.22) , see Fig. 3.6. This calculation considerably simplifies in the so-called Lamb-Dicke regime defined by the condition $\eta^2(2n+1) \ll 1$. In this regime, the atomic wavepacket is confined to a space much smaller than the wavelength of the transition. A first order Taylor expansion in eqn. (3.22) is then a very good approximation:

$$e^{i\eta(a^\dagger + a)} = 1 + i\eta(a^\dagger + a) + \mathcal{O}(\eta^2)\ .$$

[5] In principle, with our setup conditions could be reached, where $\Omega$ and $\omega$ are on the same order. The particular properties of this regime are made use of in the proposal by Jonathan, Plenio & Knight [44] for a special type of quantum gate.

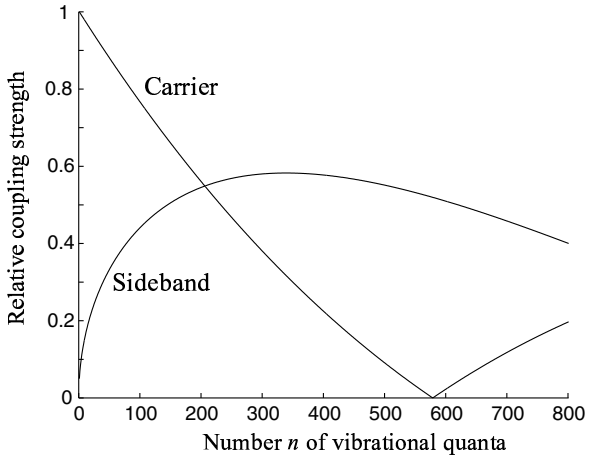


Figure 3.6: Relative coupling strength $\Omega_{n+m,n}/\Omega$ for $\eta = 0.05$ on carrier and first and second sideband (from [4]). The value of $\eta = 0.05$ represents a typical order of magnitude for our experiments. On the scale of this graph the difference between red and blue sideband is so small that it is not visible. The Lamb-Dicke regime corresponds to the region of low $n \lesssim 100$ where the carrier coupling is considerably stronger than all sideband couplings.

Explicitly, the coupling strength on the carrier is well approximated by

$$\Omega_{n,n} = (1 - \eta^2 n)\Omega \tag{3.23}$$

On resonance, the interaction Hamiltonian (3.19) reduces to

$$H_I = \tfrac{1}{2}\hbar\Omega_{n,n}(\sigma^+ e^{i\phi} + \sigma^- e^{-i\phi}) \; .$$

Note that in the resonant case the time dependence of $H_I$ vanishes. If the laser is pulsed, then this interaction is only on for a certain pulse duration $t$. The action of such a carrier pulse is described by the unitary operator

$$R(\theta, \phi) = e^{iH_I t/\hbar} = e^{i\frac{\theta}{2}(e^{i\phi}\sigma^+ + e^{-i\phi}\sigma^-)},$$

where $\theta = \Omega_{n,n}t$. This is the unitary operator representing an elementary single qubit rotation which has already been introduced in section 2.1 (eqn. (2.3)).

Sideband Coupling is given by

$$\Omega_{n-1,n} = \eta\sqrt{n}\Omega \tag{3.24}$$

on the red sideband and

$$\Omega_{n+1,n} = \eta\sqrt{n+1}\Omega \tag{3.25}$$

on the blue sideband. On the red sideband ($|S, n\rangle \leftrightarrow |D, n-1\rangle$), the Hamiltonian takes the form

$$H_I = \tfrac{1}{2}\hbar\eta\Omega(a\sigma^+ e^{i\phi} - a^\dagger\sigma^- e^{-i\phi}) \; , \tag{3.26}$$

which can also be written as

$$H_I = \tfrac{1}{2}\hbar\Omega_{n-1,n}(a_r\sigma^+ e^{i\phi} - a_r^\dagger\sigma^- e^{-i\phi})$$

with the "normalized" creation and annihilation operators $a_r = a/\sqrt{n}$ and $a_r^\dagger = a^\dagger/\sqrt{n}$. This definition ensures that the operators $a_r\sigma^+$ and $a_r^\dagger\sigma^-$ do not change the norm of a state vector. Accordingly, the matrix of a resonant laser pulse of duration $t$ on the red sideband is given by

$$R^-(\theta,\phi) = e^{i\frac{\theta}{2}(e^{i\phi}\sigma^+ a_r - e^{-i\phi}\sigma^- a_r^\dagger)}, \tag{3.27}$$

where $\theta = \Omega_{n-1,n}t$.

On the blue sideband ($|S,n\rangle \leftrightarrow |D,n+1\rangle$)

$$H_I = \tfrac{1}{2}\hbar\eta\Omega(a^\dagger\sigma^+ e^{i\phi} - a\sigma^- e^{-i\phi})\ .$$

By the same argument as for red sideband coupling, this Hamiltonian can be rewritten as

$$H_I = \tfrac{1}{2}\hbar\Omega_{n+1,n}(a_b^\dagger\sigma^+ e^{i\phi} - a_b\sigma^- e^{-i\phi})\ ,$$

where $a_b = a/\sqrt{n+1}$ and $a_b^\dagger = a^\dagger/\sqrt{n+1}$. A resonant laser pulse on the blue sideband is given by

$$R^+(\theta,\phi) = e^{i\frac{\theta}{2}(e^{i\phi}\sigma^+ a_b^\dagger - e^{-i\phi}\sigma^- a_b)}, \tag{3.28}$$

where $\theta = \Omega_{n+1,n}t$.

### 3.3.4 Generalizations of the Model

**Three-dimensional potential:** For the sake of notational simplicity, the previous discussion was limited to the simple case of an ion confined in a one-dimensional harmonic potential. Generalization to the case of a three dimensional harmonic potential is straightforward and only amounts to replacing $kx$ by the scalar product $\mathbf{k}\cdot\mathbf{r}$. The operator $\exp(i\eta(a^\dagger + a))$ is then replaced by $\exp(i\mathbf{k}\cdot\mathbf{r}) = \prod_m \exp(i\eta_m(a_m^\dagger + a_m))$, thereby allowing processes that change the quantum numbers of two or even all three oscillators simultaneously.

**Multi-ion crystal:** A similar calculation can be performed in the case of an crystal of $N$ ions. In this case the interaction Hamiltonian $H_1$ is given in the Schrödinger picture by

$$H_1 = \tfrac{1}{2}\sum_j \hbar\Omega_j\sigma_j^+ \exp\left(i\sum_m \eta_m^j(a_m^\dagger + a_m)\right)\exp(-i(\omega_l t - \phi_j)) + h.c.\ , \tag{3.29}$$

where $a_m^\dagger$ and $a_m$ are the creation and annihilation operators for the normal modes of oscillation labeled by $m$, while the index $j = \{1,\ldots,N\}$ refers to the individual ions. Note that the phases $\phi_j$ and coupling strengths $\Omega_j$ for the different ions are not necessarily equal.

In the *two-ion case*, the modulus of the Lamb-Dicke factors $|\eta_m^j| =: \eta_m$ depends only on the mode ($m$), while the sign of $\eta_m^j$ in general depends on $j$. The $\eta_m$ are given by

$$\eta_m = k\cos\beta\sqrt{\frac{\hbar}{2m_c\omega_m}}\ , \tag{3.30}$$

where $m_c = 2m_0$; $\omega_m$ denotes the frequency of the respective mode, cf. eqn. (3.16). As mentioned, $\beta$ is the angle between the addressing laser beam and the oscillation axis $\overrightarrow{e}$ of the ion. Note that in a linear crystal, $\overrightarrow{e}$ points in axial direction for all axial modes and in radial direction for all radial modes, independent of which ion in the string is addressed. In general, the Lamb-Dicke factors scale with the square root of the total mass $m_c = N \cdot m_0$ of the crystal. This property can pose problems when an ion trap quantum processor is to be scaled up in ion number. In the two-ion experiments presented here, typically only one of the two ions is optically addressed at one time. Consequently, to a good approximation, the sum over $j$ can be dropped.

Note that for more than two ions the modulus $|\eta_m^j|$ in general depends on both the mode $(m)$ and the ion $(j)$ [67], depending on the eigenvector of the mode (cf. section 3.2.2).

### 3.3.5 The Quadrupole Transition

The model for laser-ion interaction developed in the previous sections (3.3.2 to 3.3.4) is now applied to the qubit transition: In the experiments presented here a quadrupole transition, from the ground state to the $D_{5/2}$ state in $^{40}Ca^+$ at 729 nm, was chosen for coherent quantum manipulations. The induced electric-quadrupolar moment $\hat{Q}$ couples to the gradient of the electromagnetic field:

$$H_I = \hat{Q} \nabla E(t)$$

This type of interaction takes the shape of eqn. (3.15) when the Rabi frequency is defined as [67]

$$\Omega = \left| \frac{eE_0}{2\hbar} \langle S, m | (\boldsymbol{\epsilon} \cdot \mathbf{r})(\mathbf{k} \cdot \mathbf{r}) | D, m' \rangle \right| , \tag{3.31}$$

where $E_0$ is the electric field amplitude, $\mathbf{r}$ is the operator describing the position of the valence electron relative to the atomic centre of mass and $m$, $m'$ indicate the magnetic quantum number[6]. In a quadrupole transition, changes in the magnetic quantum number from $\Delta m := m' - m = 0$ up to $\Delta m = \pm 2$ are allowed. In our case, going from the $S_{1/2}$ ground state with two Zeeman-sublevels $m = \pm 1/2$ to the $D_{5/2}$ state with six sublevels $m' = -5/2, \ldots, +5/2$, this selection rule leaves a total of ten quadrupole allowed transitions. In principle any of these transitions could be used for coherent manipulations of the ion's quantum state. These various transitions have different coupling strengths $\Omega$ which depend on the $(m, m')$ combination and on the geometry, i.e. on the relative directions of the magnetic field, the polarization $\boldsymbol{\epsilon}$ and the wave vector $\mathbf{k}$ of the laser. The following equation for $\Omega$ represents a suitable formulation for our case (derived in Appendix A.1):

$$\begin{aligned} \Omega &= \left| \frac{eE_0}{2\hbar} \langle S_{1/2}, m | (\boldsymbol{\epsilon} \cdot \mathbf{r})(\mathbf{k} \cdot \mathbf{r}) | D_{5/2}, m' \rangle \right| \\ &= \kappa E_0 \sqrt{\frac{A}{k^3}} \Lambda(m, m') g^{(\Delta m)}(\phi, \gamma) , \end{aligned} \tag{3.32}$$

with

$$\kappa = \frac{e}{2\hbar} \left( \frac{15}{c\alpha} \right)^{1/2} = 3.089 \times 10^{12} \mathrm{V}^{-1} (\mathrm{sm})^{-1/2} ,$$

[6] For the sake of notational simplicity, possible lower indices $_j$, indicating that the magnetic quantum numbers refer to the total angular momentum $J$, are dropped, writing $m$ and $m'$ instead of $m_j$ and $m'_j$.

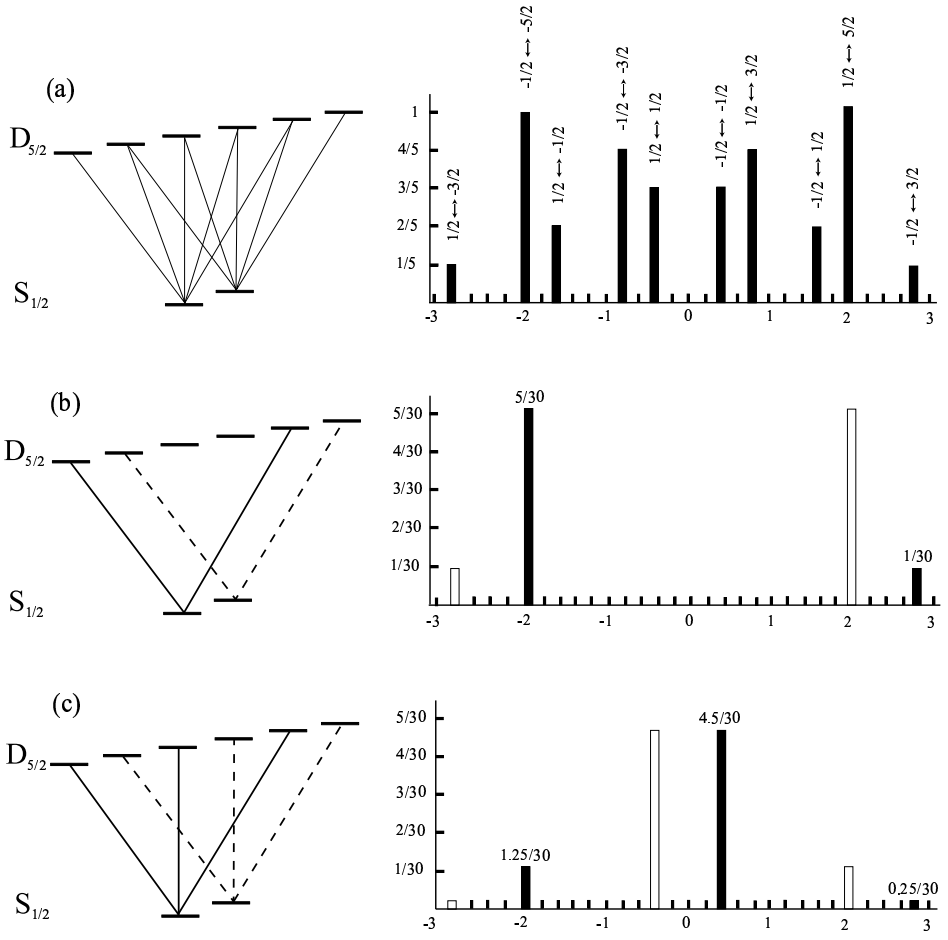


Figure 3.7: Zeeman substructure of the $S_{1/2} \leftrightarrow D_{5/2}$ transition (from [4]). (a) In a non-zero magnetic field the $S_{1/2} \leftrightarrow D_{5/2}$ quadrupole transition splits into ten components. The corresponding spectral positions are drawn in units of $\mu_B B/\hbar$ (where $\mu_B$ is Bohr's magneton). The height of the bars represents the specific Clebsch-Gordan coefficients $\Lambda^2$. (b) Allowed transitions in the case $\boldsymbol{\epsilon} \perp \boldsymbol{B} \perp \boldsymbol{k}$ ($\phi = \gamma = 90°$). The height of the bars indicates the relative line strengths $(\Lambda g^{(\Delta m)})^2$ (c) Same as (b) but for the geometry $\phi = 45°, \gamma = 0°$.

where $A$ is the spontaneous decay rate of the $D_{5/2}$ state. The specific Clebsch-Gordan coefficients $\Lambda(m, m')$ are shown in Fig. 3.7 (a) (respectively their squares) and listed in the appendix A.1. The functions $g^{(\Delta m)}$ contain the geometry-dependence of $\Omega$, where $\phi$ is the angle between the laser beam and the magnetic field and $\gamma$ the angle between the polarization and the magnetic field vector projected into the plane of incidence. They are listed in the Appendix A.1. It is thus possible to suppress some of the transitions by a proper choice of the geometry. Additionally, in the experiment $\sigma^-$ polarized light on the dipole transition at 397 nm is used to pump the ion into the $m = -1/2$ substate prior to coherent manipulations

on the quadrupole transition[7]. The following two configurations are particularly useful [4].
$\phi = 90°, \gamma = 90°$: If the polarization, the beam axis and the direction of magnetic field are mutually orthogonal, only the $\Delta m = \pm 2$ components are excited.
$\phi = 45°, \gamma = 0°$: In this configuration, the $\Delta m = 0$ transitions are excited most strongly while the $\Delta m = \pm 1$ transitions do not couple to the laser.
Figs. 3.7(b)&(c) show the relative line strengths ($\propto \Omega^2$) of the various transitions in the two cases. In fact, all experimental results presented in this thesis have been obtained in one of these two configurations. The first configuration offers the simples spectrum with the smallest possible number of allowed transitions. It has, however, the disadvantage that the allowed transition are far outside in the spectrum, hence their frequencies depend strongly on the magnetic field. Magnetic field noise shifts the resonance frequencies randomly, thus contributing to decoherence. This effect is five times weaker on the $S_{1/2}(m = -1/2) \leftrightarrow D_{5/2}(m' = -1/2)$ transition. As magnetic field fluctuations are an issue in the present setup (see section 7.3), all experiments directly related to quantum computing employ the states $S_{1/2}(m = -1/2)$ and $D_{5/2}(m' = -1/2)$ to represent the internal qubit. For notational simplicity, these two states will usually be denoted

$$\begin{aligned} |S\rangle &:= S_{1/2}(m = -1/2) \\ |D\rangle &:= D_{5/2}(m' = -1/2) \end{aligned}$$

throughout the rest of this thesis.

An experimental challenge for quantum computation is the availability of an appropriate light source. In our case the lifetime $1/A$ of the metastable $D_{5/2}$ level is 1.17 s [61]. The coherence time of our experiments, however, is not as long as that, which is due to several mechanisms such as fluctuations of the magnetic field. In our present experiment it turns out that the sum of all contributions amounts to a coherence time of at about 600 $\mu$s (see section 7.3). The laser at 729 nm must have a linewidth of 100 Hz or less in order to maintain coherence over that time scale.

### 3.3.6 Non-resonant Interactions

So far, all non-resonant processes have been neglected, assuming that their coupling strength $\Omega_i$ is much smaller than the detuning. It turns out that in our experiments, especially in the Lamb-Dicke regime and when the laser excites sideband transitions, off-resonant coupling to the carrier has to be considered. Two different processes can be distinguished and will be discussed in the following: population transfer and light shifts. Taking those effects into account is particularly important in the "design" of quantum algorithms and in the evaluation of their limits.

**Population Transfer** There is always a small transfer of population to the non-resonantly coupled levels. If, for example, the sideband transition $|S, 0\rangle \leftrightarrow |D, 1\rangle$ is driven with all the population initially in $|S, 0\rangle$, then the populations of the levels $|D, 0\rangle$ and $|S, 1\rangle$ oscillates

[7] Pumping into $m = +1/2$ with $\sigma^+$-light is equally possible.

quickly at a frequency of $\sqrt{\Omega^2 + \Delta^2}$ (off-resonant Rabi oscillations) with an amplitude of [73]

$$p = \left(\frac{\Omega}{\Delta}\right)^2$$

(for $\Delta \gg \Omega$). Hence, $p$ is a measure for off-resonant excitations. If the sideband transition is driven resonantly, the detuning $\Delta$ from the carrier is $\Delta = \omega_m$, where $\omega_m$ is the frequency of the corresponding vibrational mode, thus off-resonant carrier excitations are given by

$$p = \left(\frac{\Omega}{\omega_m}\right)^2 .$$

According to eqn. (3.25), the Rabi frequency $\Omega_S = \Omega_{1,0}$ of the sideband transition ($|S,0\rangle \leftrightarrow |D,1\rangle$) is

$$\Omega_S = \eta\Omega .$$

In quantum computation with trapped ions, sideband transitions are an essential ingredient (cf. section 2.1 and chapter 4). In view of a limited coherence time, which is always given in real systems (cf. section 7.3), it is of interest to drive these sideband transitions as fast as possible, in order to accomplish as many gate operations as possible within the coherence time. The upper limit for the sideband Rabi frequency $\Omega_S$ is set by off-resonant excitations. In other words, for a sufficient quality of the quantum gate operations, off-resonant excitations are required to be smaller than some value $p_0$, which is typically on the order of a few percent: $p < p_0$. The limit for $\Omega_S$ is therefore given by the inequality

$$p = \left(\frac{\Omega_S}{\eta\omega_m}\right)^2 < p_0 ,$$

which can be rewritten as

$$\Omega_S < \eta\omega_m\sqrt{p_0} . \tag{3.33}$$

Moreover, the Lamb-Dicke factor is proportional to the inverse square root of the vibrational frequency, $\eta \propto (\omega_m)^{-1/2}$ (see equations (3.16) and (3.30)). Consequently, if we assume the ion number, the beam geometry ($\beta$) and the maximum allowed off-resonant excitation $p_0$ to be fixed (constant), inequality 3.33 can be written as

$$\Omega_S < \text{const.} \cdot \sqrt{\omega_m} . \tag{3.34}$$

This means that the maximum allowed sideband Rabi frequency increases with $\sqrt{\omega_m}$. Consequently, if there is a choice between several vibrational modes which can be employed for quantum computation, it is advantageous to chose the mode with the highest frequency $\omega_m$.

**Light shifts** In general, any two atomic levels (with an energy difference $E = \hbar\omega$) are shifted by the dynamic Stark effect if (off-resonant) light of frequency $\omega_l$ is shone onto the atom (respectively ion) [73]. In this case, the energetically lower level is shifted[8] by $\Omega^2/4\Delta$ and the upper level by $-\Omega^2/4\Delta$, where $\Delta = \omega_l - \omega$ and $\Omega$ denotes the Rabi frequency of

[8] All level shifts are given in units of angular frequency.

the transition between the two levels (if the transition was driven resonantly with light of the same intensity and polarization). If, for example, the light is red-detuned, i.e. $\Delta < 0$, then the lower level is shifted down, while the upper level is shifted up. This picture holds only in a regime where the detuning $\Delta$ is large enough so that very little population transfer takes place, i.e. for $\Delta \gg \Omega$.

In the case of trapped ions in the Lamb-Dicke regime, usually only light shifts due to coupling to carrier transitions must be taken into account while sideband transitions produce only minor light shifts as their $\Omega$ is relatively small. However at specially chosen detunings and if the AC-Stark shift due to the carriers is compensated for, sideband-induced level shifts can be experimentally detected. The corresponding experiments are presented in section 8.1.

In a typical spectroscopy experiment on our qubit transition(s) the AC Stark effect appears, for example, in a shift of the observed sideband resonance frequency: Let us assume that we have cooled an ion to its motional ground state and then try to drive the blue sideband $|S,0\rangle \leftrightarrow |D,1\rangle$ resonantly by setting the detuning $\Delta = \omega_l - \omega_a$ to the vibrational mode frequency $\omega_m$ (note that $\omega_a$ is the frequency of a *carrier* transition). The $|S,0\rangle$ level is then Stark shifted *up* due to off-resonant coupling to the carrier transition $|S,0\rangle \leftrightarrow |D,0\rangle$ by $\delta_1 = \Omega_{0,0}^2/4\Delta$, while coupling to the carrier $|S,1\rangle \leftrightarrow |D,1\rangle$ shifts the $|D,1\rangle$ level *down* by $\delta_2 = \Omega_{1,1}^2/4\Delta$. In the Lamb-Dicke regime, $\Omega_{1,1} \approx \Omega_{0,0} = \Omega$ and the total shift of the sideband transition becomes $\delta_0 = -(\delta_1 + \delta_2) = -\Omega^2/2\Delta$. In general, sidebands are always shifted *towards the carrier*, meaning that red sidebands are shifted up while blue sidebands are shifted down in frequency. In the example above, the laser light would be detuned from the sideband resonance by $\delta_0$ although $\Delta$ is set exactly to the vibrational mode frequency $\omega_m$.

So far only the strongest source of level shifts, i.e. coupling to the nearest carrier of the Zeeman-manifold is taken into account. In reality, every carrier contributes to the overall level shift with its respective coupling strength $\Omega_q$ and detuning $\Delta_q$. Moreover, coupling to the $S_{1/2} - D_{5/2}$ quadrupole transition(s) is not the only source of level shifts: dipole transitions, to which the detuning is much larger (when working (near) resonantly on the $S_{1/2} - D_{5/2}$ transition) compensate this by approximately seven orders of magnitude stronger coupling (in terms of $\Omega^2$).

In the experiment, we can use a Ramsey-type spectroscopic method (see section 7.6) to measure AC-Stark shifts. This method probes the relative shift $\delta_{AC}$ of two atomic levels A and B which is produced by off-resonant light at a laser frequency $\omega^s$ shone onto the ion. In other words,

$$\delta_{AC} = \tfrac{1}{\hbar}\big[(E_A^s - E_B^s) - (E_A - E_B)\big], \tag{3.35}$$

where $E_A$ and $E_B$ are the energies of the two levels for the isolated, unperturbed atom/ion, while $E_A^s$ and $E_B^s$ are the AC-Stark shifted energy levels under the influence of laser radiation at frequency $\omega^s$.

In the following, a formula for $\delta_{AC}$ will be developed. In the experiment as it has been carried out, the first level (A) was $|S\rangle$ $(= S_{1/2}, m = -1/2)$. It will be assumed that $\omega^s$ is near resonant to the $S_{1/2} \leftrightarrow D_{5/2}$ transition(s) but at the same time far enough from any resonance so that no population transfer takes place. Moreover, the geometric configuration $\phi = 45°, \gamma = 0°$ (cf. section 3.3.5) was chosen. This means that only transitions to the states $D_{5/2}, m' = \{-5/2, -1/2, +3/2\}$ (which will be denoted here as $|D_{-5}\rangle, |D_{-1}\rangle$ and $|D_{+3}\rangle$,

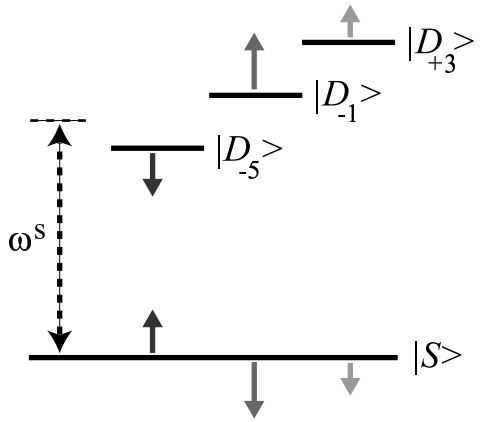


Figure 3.8: AC-Stark shifts of individual atomic levels in $^{40}Ca^{+}$ (see also text) induced by off-resonant light at frequency $\omega^s$. Individual shifts are indicated by grey arrows. Each grey-scale corresponds to the shifts induced by coupling to one of the three optical transitions. In the experiment, the relative level shift $\delta_{AC}$ between $|D_{-1}\rangle$ (level A) and $|S\rangle$ (level B) is probed. Consequently, the experiment is double sensitive to the shifts indicated by medium grey arrows, which accounts for the factor of 2 in eqn. (3.36). In practice there are also motional sidebands to each of the three carrier transitions but these can be neglected here as they are relatively weak.

respectively[9]) are allowed. The state $|D_{-1}\rangle$ was chosen as the second level (B). The situation is depicted in Fig. 3.8. The notation $\Omega_q$ is used for the coupling (in terms of Rabi frequency) of the off-resonant light ($\omega^s$) to the $|S\rangle \leftrightarrow |D_q\rangle$ transition. Accordingly, $\Delta_q$ denotes the detuning of $\omega^s$ from the $|S\rangle \leftrightarrow |D_q\rangle$ resonance at $\omega_q$, thus $\Delta_q = \omega^s - \omega_q$. The light of frequency $\omega^s$ now shifts all levels involved in different ways: off-resonant coupling to the $|S\rangle \leftrightarrow |D_{-5}\rangle$ transition, for example, shifts $|S\rangle$ by $\Omega_{-5}^2/4\Delta_{-5}$ and the state $|D_{-5}\rangle$ by $-\Omega_{-5}^2/4\Delta_{-5}$. Note however, that our probe method is sensitive only to shifts of the $|S\rangle \leftrightarrow |D_{-1}\rangle$ resonance. Moreover, coupling to various dipole transitions will also shift the levels $|S\rangle$ and $|D_{-1}\rangle$, each dipole transition contributing with a shift proportional to $\Omega_{dip,i}^2/\Delta_{dip,i}$. The index $i$ counts *all* dipole transitions. The respective coupling strengths $\Omega_{dip,i}$ are, just like each $\Omega_q$ of the quadrupole transitions, proportional to the light intensity. Consequently, each $\Omega_{dip,i}^2$ is proportional to, for example, $\Omega_{-1}^2$. Under the conditions of our experiment, where we always work near the $S_{1/2} - D_{5/2}$ resonance(s) to within a several MHz, we can assume the detunings $\Delta_{dip,i}$ to be constant. Taking all this into account, we can write the *total* light shift between $|S\rangle$ and $|D_{-1}\rangle$ as

$$\delta_{AC} = \frac{\Omega_{-1}^2}{4}\left(d - \frac{a_{-5}}{\Delta_{-5}} - \frac{2}{\Delta_{-1}} - \frac{a_{+3}}{\Delta_{+3}}\right) , \tag{3.36}$$

where the $a_q$ are the squares of the relative coupling strengths with respect to the probe transition $|S\rangle \leftrightarrow |D_{-1}\rangle$, which for the given geometry read $a_{-5} = 0.278$ and $a_{+3} = 0.0556$

[9]Note that the state $|D\rangle$ which has been defined in section 3.3.5, is denoted $|D_{-1}\rangle$ here for the sake of clarity.

($a_{-1}$ being one by definition), cf. Fig. 3.7(c). The constant $d$ contains the (squared) *relative* coupling strengths of, as well as the detunings to, *all* dipole transitions. Note that $d$ really is a constant because the sum of relative line strengths of a transition's Zeeman-manifold does *not* depend on the geometry. Therefore $d$ in principle is a direct function of fundamental constants - a complicated one, however.

In practice the beam geometry is never perfectly realized, i.e. $a_{-5}$ and $a_{+3}$ will differ slightly from their theoretical values. The Ramsey-type measurement for $\delta_{AC}$ mentioned above, where now the frequency $\omega^s$ is varied over a wide range, allows one to map eqn. (3.36). As mentioned, the corresponding experiment is described in section 7.6. A fit to these data yields values for $d$, $a_{-5}$ and $a_{+3}$. Knowledge of these three parameters then allows one to predict and "engineer" level shifts.

This is particularly important for the levels $|S\rangle$ and $|D\rangle = |D_{-1}\rangle$ which are used to encode a qubit. A level which is AC-Stark shifted in frequency by $\delta$ for a time $t$, acquires a phase factor $e^{i\delta \cdot t}$. In the implementation of quantum algorithms such phase factors cannot be tolerated (unless they are well controlled) as the quantum phase is the essential carrier of quantum information.

If, for example, the blue sideband of the $|S\rangle \leftrightarrow |D\rangle$ transition is driven resonantly, then this shifts the $|S\rangle \leftrightarrow |D\rangle$ resonance according to eqn. (3.36). Problems due to unwanted AC-Stark shifts exist also in precision spectroscopy [74] and with optical clocks [75, 76]. Our solution for the **compensation of** such unwanted **AC-Stark shifts** consists of simultaneously applying an additional light field. The detuning and intensity of the latter is chosen such that the additional field produces the opposite AC-Stark shift (i.e. opposite in sign and equal in magnitude) and thus nulls the overall shift. The detuning is chosen far from any resonance so that no additional population transfer occurs. Our method is related to [77], where the inhomogenous broadening of a hyperfine transition of $^{85}$Rb-atoms was suppressed using a bichromatic dipole trap.

# 4 Quantum Computation with Trapped Ions

## 4.1 General Concepts

As mentioned before, in our experiment two Zeeman-sublevels $|S\rangle$ and $|D\rangle$ (see section 3.3.5) are chosen as the two internal qubit states of a $^{40}Ca^{+}$ ion. Section 2.1 discussed how arbitrary rotations of this *internal qubit* can be accomplished by resonant excitations $R(\theta, \phi)$ and section 3.3.3 showed how the latter can be implemented by (addressed) carrier pulses (eqn. (3.3.3)). The trick to make efficient ion trap quantum computation possible proposed by Cirac and Zoller [34] is to employ one of the vibrational modes, more precisely its lowest two quantum states $|n = 0\rangle$ and $|n = 1\rangle$, as an additional qubit, the *vibrational qubit*. The situation is illustrated in Fig. 4.1. In this way even a *single* trapped ion in combination with a vibrational mode represents a *two*-qubit quantum information processor. Section 4.2 discusses in detail how universal two-qubit gates between internal and vibrational qubit can be implemented using laser pulses on the red sideband $R^{-}(\theta, \phi)$ (eqn. (3.27)) and on the blue sideband $R^{+}(\theta, \phi)$ (eqn. (3.28)) in addition to carrier pulses. Section 4.3 discusses the Deutsch-Jozsa algorithm and how it can be implemented on such a two-qubit quantum computer.

Section 4.4 shows how the quantum computation scheme can be extended to a string of trapped ion qubits.

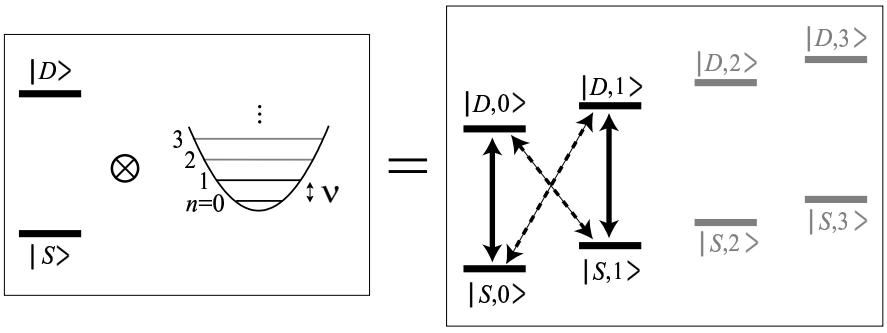


Figure 4.1: The elementary two-qubit system - the internal (electronic) degree of freedom of an individual ion, combined with a vibrational mode. The mode represents a harmonic oscillator (frequency $\nu$). Its two lowest levels $|n = 0\rangle$ and $|n = 1\rangle$ are identified as the *vibrational qubit*. The computational basis states of the combined system (drawn in black on the right hand side) will be denoted like $|S, n\rangle$. Dashed arrows: red and blue sideband transitions; Solid arrows: carrier transitions.

## 4.2 Single Ion Gates and Composite Pulse Techniques

This section deals with a single ion coupled to a vibrational mode. Note, however, that the same formalism applies if the ion is part of a string and the mode is a common vibration of the entire crystal - as long as only this one ion is optically addressed.

Using a *single* trapped ion as a complete two-qubit quantum computer requires a universal set of quantum gates (cf. section 2.2). This includes single qubit rotations of the *vibrational* qubit. Such rotations of the vibrational qubit pose certain problems arising from the fact that the mode has many *equidistant* oscillator levels, not just the qubit levels $|n = 0\rangle$ and $|n = 1\rangle$. These rotations cannot be directly driven by resonant radiation (which would be in the radiofrequency range of a few MHz): Such a resonant excitation would, for example, not only excite the $|S, 0\rangle \leftrightarrow |S, 1\rangle$ transition, but the $|S, 1\rangle$ population would simultaneously be transferred on to $|S, 2\rangle$, $|S, 3\rangle$ and so on. In other words, the computational space would not be conserved.

Single qubit operations on the *internal* state, on the other hand, can be efficiently performed by carrier pulses. Thus, a natural approach is to swap the internal and vibrational qubit information, then perform the desired operation on the internal qubit and finally swap back. The desired swap operation should interchange the populations of $|D, 0\rangle$ and $|S, 1\rangle$ and leave the populations of the other two computational basis states ($|S, 0\rangle$ and $|D, 1\rangle$) unaffected. Accordingly, the corresponding matrix in the basis order $\{|S, 0\rangle, |D, 0\rangle, |S, 1\rangle, |D, 1\rangle\}$ reads

$$SWAP = \begin{bmatrix} 1 & 0 & 0 & 0 \\ 0 & 0 & 1 & 0 \\ 0 & 1 & 0 & 0 \\ 0 & 0 & 0 & 1 \end{bmatrix}.$$

A red sideband $\pi$-pulse $R^-(\pi, \phi)$ would interchange the populations of $|D, 0\rangle$ and $|S, 1\rangle$ as desired (modulo certain phase factors which depend on $\phi$). However, such an operation would also (partially) transfer a possible $|D, 1\rangle$ state population (which is supposed to be unaffected) to the $|S, 2\rangle$ state. Again the problem is the conservation of computational space. The task of implementing a $SWAP$ operation, which may seem impossible at first, can in fact be fulfilled by the technique of *composite pulses*, which in the framework of NMR have been in use for several years [78, 79]. This technique takes advantage of the fact that the Rabi frequency of a sideband transition depends strongly on the motional quantum number, cf. eqn. (3.24). In particular, the $|D, 1\rangle \leftrightarrow |S, 2\rangle$ Rabi frequency is larger by a factor of $\sqrt{2}$ than the Rabi frequency of the $|D, 0\rangle \leftrightarrow |S, 1\rangle$ transition (cf. Fig. 4.2). Using this, it is possible to construct a series of pulses which fulfills the above requirements:

$$R_{swap}(\phi_0) = R^-(\frac{\pi}{\sqrt{2}}, \phi_0)\ R^-(\frac{2\pi}{\sqrt{2}}, \phi_0 + \phi_{swap})\ R^-(\frac{\pi}{\sqrt{2}}, \phi_0), \tag{4.1}$$

with $\phi_{swap} = \arccos(\cot^2(\frac{\pi}{\sqrt{2}})) \simeq 0.303\pi$ [80]. The meaning of $\phi_0$ will be explained below. The rotation angles $\theta$ here refer to the $|D, 0\rangle \leftrightarrow |S, 1\rangle$ transition. The same light pulse sequence corresponds to the operation

$$R'_{swap}(\phi_0) = R^-(\pi, \phi_0)\ R^-(2\pi, \phi_0 + \phi_{swap})\ R^-(\pi, \phi_0),$$

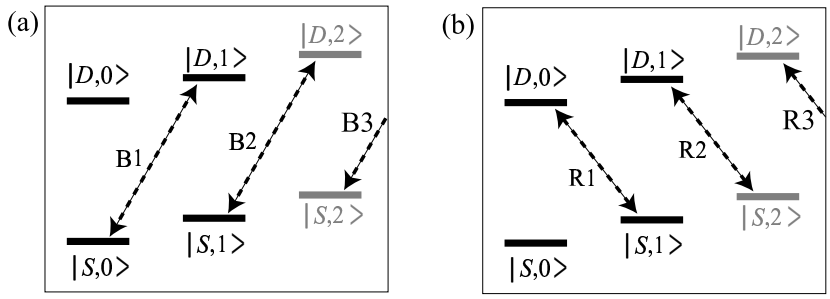


Figure 4.2: (a) Blue sideband coupling. (b) Red sideband coupling. The Rabi frequencies of the lowest sideband transitions B1 and R1 are equal, while the Rabi frequencies of B2 and R2 are bigger by a factor of $\sqrt{2}$ (see section 3.3.3).

on $|D,1\rangle \leftrightarrow |S,2\rangle$, where the rotation angles $\theta$ are larger by $\sqrt{2}$. The Bloch sphere trajectories of the state vector are depicted in Fig. 4.3. It is important to note that a sideband transition does not correspond to a single qubit rotation, rather a pairwise coupling between certain levels of the combined system $\mathcal{H}$ composed of the internal qubit and the motional states $|n\rangle$. Red sideband operations between $|D,1\rangle \leftrightarrow |S,2\rangle$ as depicted in Fig. 4.3 (right), for example, change both motional and internal degree of freedom. According to the concluding remark of section 2.2, if the quantum dynamics of such a subsystem ($|D,1\rangle$ and $|S,2\rangle$) is calculated, phase factors which appear global in the subsystem can not be dropped as they are not global in the complete system $\mathcal{H}$. The Bloch sphere picture directly displays only relative phases. The complete quantum phase evolution due to a series of rotations can be revealed by multiplying the matrices of the individual rotations.

In the case of our swapping pulse sequence, varying only the angle $\phi_0$ rotates the whole trajectories about the $z$-axis of the Bloch spheres. This changes nothing in the $|D,1\rangle \leftrightarrow |S,2\rangle$ subspace: the overall sequence $R'_{swap}$ always acts like an effective $4\pi$ pulse, hence like the identity operation $I$. In fact, any pulse sequence $R' = R^-(\pi,\phi_1)R^-(2\pi,\phi_2)R^-(\pi,\phi_1)$ with arbitrary $\phi_1$ and $\phi_2$ meets this requirement. On the $|D,0\rangle \leftrightarrow |S,1\rangle$ transition, $\phi_0$ plays a similar role as $\phi$ in a single $\pi$-pulse $R^-(\pi,\phi)$. As in that case, no angle $\phi$ exists which would correspond to a perfect swapping operation. Choosing $\phi_0 = \frac{1}{\sqrt{2}}\pi \simeq 0.707$ yields a "good approximation" [80], i.e.

$$|D,0\rangle \mapsto -|S,1\rangle \quad \text{and} \quad |S,1\rangle \mapsto |D,0\rangle \ ,$$

so that the complete matrix of this $SWAP$ operation reads

$$SWAP(\frac{1}{\sqrt{2}}\pi) = \begin{bmatrix} 1 & 0 & 0 & 0 \\ 0 & 0 & 1 & 0 \\ 0 & -1 & 0 & 0 \\ 0 & 0 & 0 & 1 \end{bmatrix} .$$

Note that the notation $SWAP(\phi_0)$ for the overall operation as a function of $\phi_0$ has been introduced. The unwanted minus sign in $SWAP(\frac{1}{\sqrt{2}}\pi)$ could, in principle, be compensated for by

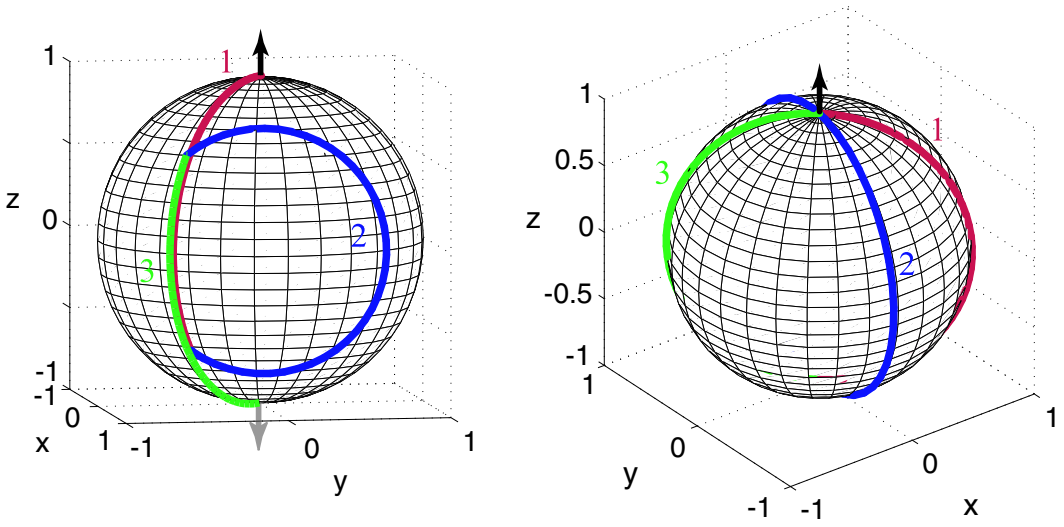


Figure 4.3: Bloch sphere trajectories for the composite $SWAP$ operation with $\phi_0 = 0.707\pi$. **Left**: Bloch sphere of the quasi-two-level-system $|D,0\rangle \leftrightarrow |S,1\rangle$. The initial state is assumed to be $|D,0\rangle$, which is marked by the black arrow. Pulse number 1 of the sequence $(R^-(\frac{\pi}{\sqrt{2}}, 0.707\pi))$ rotates the state vector more than half way down. Pulse number 2 brings it back up to its mirror image about the $x$-$y$-plane. The angle $\phi_{swap} = \arccos(\cot^2(\frac{\pi}{\sqrt{2}}))$ is precisely chosen to accomplish this. Clearly, pulse number 3 then rotates the state vector all the way down to the bottom of the sphere. The final state (grey arrow) thus is $|S,1\rangle$, times some phase factor which is not visible in the Bloch sphere picture. **Right**: The same laser pulse sequence and its action on the $|D,1\rangle \leftrightarrow |S,2\rangle$ subspace. All individual pulses of $R'_{swap}(\phi_0)$ are multiples of $\pi$ in length. It is easy to understand that the overall sequence brings the state vector back to its starting point (black arrow; say $|D,1\rangle$ for example) and that the acquired phase factors cancel out. In other words, the sequence here corresponds to a true identity operation.

an appropriate series of single qubit rotations added before and after $SWAP(\phi_0)$. As in the case of implementing Hadamard gates (see section 2.1), there is a simpler, "compiled" version: In the complete sequence of an algorithm, the $SWAP$ operation will typically appear in pairs. The problem of the unwanted phase factor $-1$ is solved by swapping the two qubits first with some arbitrary $\phi_0$ (for example $SWAP(0)$) and swapping back later with a $\phi_0$ different by $\pi$ ($SWAP(\pi)$). With the help of the composite $SWAP$ operation it is possible to perform *all* single qubit rotations in our computational space.

The last missing building block to make our single ion quantum gate toolbox complete is a *universal two-qubit gate* between internal and vibrational qubit. This will typically be a universal phase gate (like $\Phi$ of section 2.2). At present in our experiment, there are three different methods at hand to implement universal phase gates:

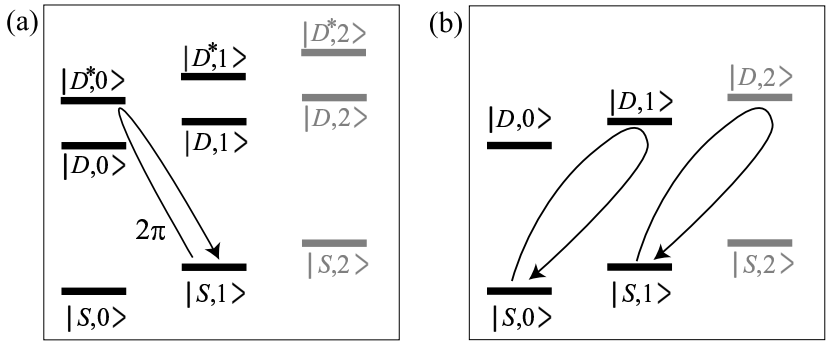


Figure 4.4: Two different methods to implement a phase gate experimentally. (a) The auxiliary level method requires an additional internal level $D^*$. A single $2\pi$ pulse on the red sideband of the auxiliary transition applies the phase factor of $-1$ to the state $|S,1\rangle$. (b) A composite sequence of pulses can be found which effectively acts like a $2\pi$ pulse on *both* blue sideband transitions B1 and B2, cf. Fig. 4.2.

- The method employed in the Cirac-Zoller proposal [34] based on using an *auxiliary level*, which will be discussed in the following.
- The *composite pulse* technique, which will also be detailed below.
- The method of *quantized AC-Stark shifts* which will not be discussed here but in section 8.1 along with its experimental realization.

The **auxiliary level** scheme is depicted in Fig. 4.4(a). The $-1$ phase on one of the basis states is acquired by a $2\pi$ rotation on the red sideband of an auxiliary transition. Only the $|S,1\rangle$ state population undergoes a transition, while $|S,0\rangle$, $|D,0\rangle$ and $|D,1\rangle$ are not affected (if off-resonant excitations are negligible). The method requires, of course, the availability of an auxiliary level. In our case, auxiliary levels are readily at hand in form of other Zeeman sublevels of the $D_{5/2}$ state. Note, however, that magnetic sublevels other than $|D\rangle$ are more sensitive to magnetic field fluctuations as detailed in section 3.3.5.

How can a phase gate be implemented with the help of **composite pulses**? Fig. 4.4 shows that a pulse sequence which effectively corresponds to a $2\pi$ rotation, i.e. to $-1 \cdot I$, on the $|S,0\rangle \leftrightarrow |D,1\rangle$ *and* on the $|S,1\rangle \leftrightarrow |D,2\rangle$ transition (despite the difference in Rabi frequency by a factor $\sqrt{2}$) would do the trick. The states $|S,0\rangle$, $|S,1\rangle$ and $|D,1\rangle$ then acquire a $-1$ sign, while $|D,0\rangle$ remains unaffected. The corresponding matrix reads

$$\Phi' = \begin{bmatrix} 1 & 0 & 0 & 0 \\ 0 & -1 & 0 & 0 \\ 0 & 0 & 1 & 0 \\ 0 & 0 & 0 & 1 \end{bmatrix}.$$

Note that a phase factor of $-1$, which is global in the computational space, has been dropped. A composite pulse sequence which meets these requirements is

$$R_{phase} = R^+(\pi, \frac{\pi}{2})\ R^+(\frac{\pi}{\sqrt{2}}, 0)\ R^+(\pi, \frac{\pi}{2})\ R^+(\frac{\pi}{\sqrt{2}}, 0) \tag{4.2}$$

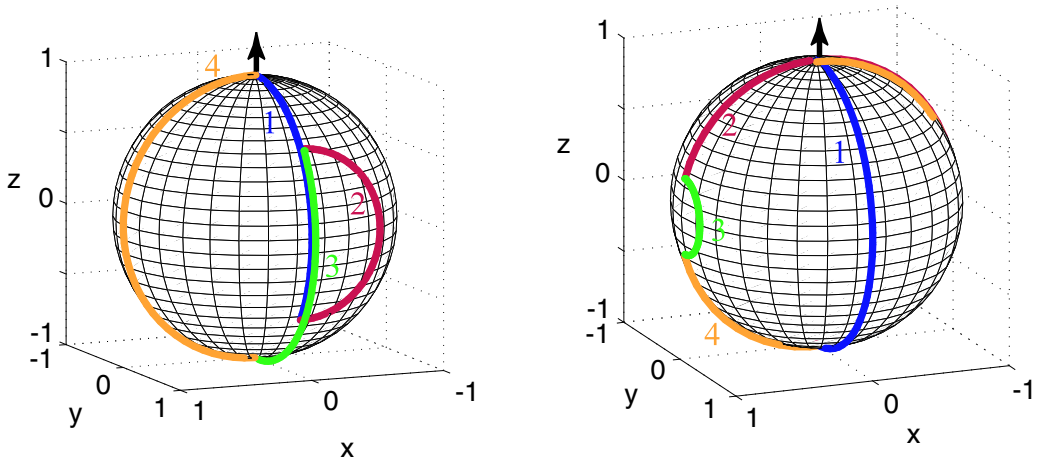


Figure 4.5: Bloch sphere trajectories for the composite phase operation $\Phi'$. **Left**: Bloch sphere of the quasi-two-level-system $|S,0\rangle \leftrightarrow |D,1\rangle$. The initial state is assumed to be $|S,0\rangle$, which is marked by the black arrow. The pulse sequence is $R_{phase}$. Pulse number 1 of the sequence $(R^+(\frac{\pi}{\sqrt{2}},0))$ rotates the state vector about the $x$-axis by $\frac{\pi}{\sqrt{2}}$. Pulse number 2 accomplishes a $\pi$-rotation about the $y$-axis. It therefore transforms the state to its mirror image about the $x$-$y$-plane. Consequently, laser pulse number 3, which is identical to number 1, rotates the state vector all the way down to the bottom of the sphere. Pulse number 4, just like number 2, represents a $\pi$-rotation about the $y$-axis. The final state thus is identical to the initial one, modulo some phase. It turns out that the acquired phase factor of the overall operation is $-1$, hence the sequence acts like a single $2\pi$-rotation: $|S,0\rangle \mapsto -|S,0\rangle$ and $|D,1\rangle \mapsto -|D,1\rangle$. **Right**: The same laser pulse sequence and its action on the $|S,1\rangle \leftrightarrow |D,2\rangle$ subspace. It is easy to understand that the overall sequence brings the state vector back to its starting point (black arrow) modulo some phase. Multiplying the matrices of the individual pulses reveals that the acquired phase is again $-1$. Thus, $R'_{phase}$ also acts like a single $2\pi$-rotation: $|S,1\rangle \mapsto -|S,1\rangle$ and $|D,2\rangle \mapsto -|D,2\rangle$.

on the $|S,0\rangle \leftrightarrow |D,1\rangle$ (blue) sideband. On the $|S,1\rangle \leftrightarrow |D,2\rangle$ subspace it reads

$$R'_{phase} = R^+(\sqrt{2}\pi, \frac{\pi}{2})\ R^+(\pi,0)\ R^+(\sqrt{2}\pi, \frac{\pi}{2})\ R^+(\pi,0).$$

Fig. 4.5 illustrates the sequences in the Bloch sphere picture. No auxiliary level is required, which makes the method more universal. The sequence takes a total of $3.4\pi$ of sideband rotations. A technical difficulty of the composite pulse technique consists in the controlled switching of the laser phases, see section 5.3.

## 4.3 The Deutsch-Jozsa Algorithm with a Single Ion

### 4.3.1 The Algorithm

In the beginning of this section, the underlying problem of the Deutsch-Jozsa algorithm is presented. The problem has first been defined by Deutsch [10] and is therefore commonly referred to as "Deutsch's problem".

Consider an unknown Boolean function $f(a)$ which accepts one (classical) bit as input and produces one (classical) bit as output. There exist four such functions altogether, which are described by the truth table

| $a$ | $f_1(a)$ | $f_2(a)$ | $f_3(a)$ | $f_4(a)$ |
|---|---|---|---|---|
| 0 | 0 | 1 | 0 | 1 |
| 1 | 0 | 1 | 1 | 0 |

The first two functions, $f_1$ and $f_2$, yield always the same output, independent of the input $a$ and are therefore be called *constant*. Each one of the other two, $f_3$ and $f_4$, has both 0 and 1 as a possible output. They are called *balanced* functions. The problem is now to determine which class (constant or balanced) a given unknown function belongs to; how many computational steps are needed? Note that we are not asking for the particular values $f_i(0)$ and $f_i(1)$ but for a global property of $f_i$.

The classical version of the problem can be formulated as follows: Given a one-bit computer as a "black box" which calculates one of the functions $f_i$ (the software) but it is not known which. The goal is to determine, which type of program (i.e. which type of function, constant or balanced) is running on the computer. With a *classical* computer the function must always be evaluated twice (the program must be run twice) to find out: If, for example, the input 1 is chosen and the output turns out to be 0, then the function could be $f_1$ (constant) or $f_4$ (balanced). A second evaluation, this time with 0 as input, is necessary to determine if the function is constant or balanced.

It will now be shown how with a simple quantum computer the symmetry (constant or balanced) of an unknown function is obtained in just one run. The quantum procedure outlined in the following was proposed by Cleve, Ekert, Macchiavello and Mosca [19] (for a history of the Deutsch-Jozsa algorithm, see the end of this section). The quantum problem requires adaptation of the functions. This is necessary as not all functions of the set $f_1$-$f_4$ are unitary, when they are read as operations which map from one *qubit* to one qubit. In particular, the constant functions are not. The generic procedure to adapt such non-unitary classical operations for quantum computation is to add an ancilla qubit [13,19]. The computational space thus consists of two qubits, their quantum state will be denoted $|a, w\rangle$. It will be shown that a suitable way to extend the functions $f_i$ to the two-qubit space is to replace them by *unitary* transformations $U_i$ which are defined by the map

$$U_i \ : \quad |a, w\rangle \mapsto |a, w \oplus f_i(a)\rangle, \tag{4.3}$$

where $\oplus$ indicates addition modulo two. Equivalently to the classical case, the quantum problem can now be expressed as follows: Given a (black box) two-qubit quantum computer on which one of the "programs" $U_i$ is implemented and it is not known which. The goal is to determine in only one run of the quantum computer if the program corresponds to a

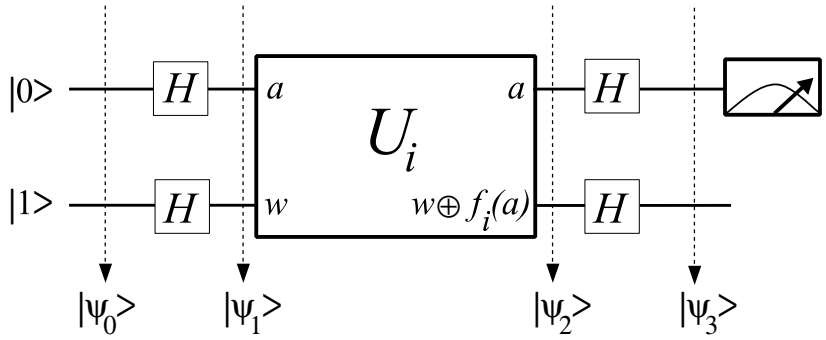


Figure 4.6: Quantum circuit representation of the Deutsch-Jozsa algorithm.

constant or a balanced $f_i$. A key feature of the algorithm is to evaluate $U_i$ with the two qubits in superpositions at the input, this way allowing quantum interference of different computational paths [19]. More precisely, the procedure starts with the state $|a, w\rangle = |0, 1\rangle$ and then the sequence of operations

$$U_{DJ} = H_1 \; H_2 \; U_i \; H_2 \; H_1 \tag{4.4}$$

is applied. The first two Hadamard gates create the superpositions, while the two Hadamard gates after $U_i$ serve to recombine different paths and make them interfere. The complete algorithm is depicted in Fig. 4.6. Let us follow the quantum state of the system through the algorithm. The input state $|\psi_0\rangle = |0, 1\rangle$ is transformed by the first two Hadamard gates into

$$\begin{aligned} |\psi_1\rangle &= \left[\frac{|0\rangle + |1\rangle}{\sqrt{2}}\right] \otimes \left[\frac{|0\rangle - |1\rangle}{\sqrt{2}}\right] \\ &= \frac{1}{2}\left[|0,0\rangle - |0,1\rangle + |1,0\rangle - |1,1\rangle\right]. \end{aligned}$$

Now $U_i$ is applied, resulting in the state

$$\begin{aligned} |\psi_2\rangle &= \frac{1}{2}\left[|0\rangle|f_i(0)\rangle - |0\rangle|f_i(0) \oplus 1\rangle + |1\rangle|f_i(1)\rangle - |1\rangle|f_i(1) \oplus 1\rangle\right] \\ &= \frac{1}{2}\left[(-1)^{f_i(0)}|0\rangle(|0\rangle - |1\rangle) + (-1)^{f_i(1)}|1\rangle(|0\rangle - |1\rangle)\right] \\ &= \left[\frac{(-1)^{f_i(0)}|0\rangle + (-1)^{f_i(1)}|1\rangle}{\sqrt{2}}\right] \otimes \left[\frac{|0\rangle - |1\rangle}{\sqrt{2}}\right] \end{aligned}$$

The last two single qubit rotations yield the final state before the measurement:

$$\begin{aligned} |\psi_3\rangle &= \left[\frac{(-1)^{f_i(0)}(|0\rangle + |1\rangle) + (-1)^{f_i(1)}(|0\rangle - |1\rangle)}{2}\right] \otimes |1\rangle \\ &= \left[\frac{(-1)^{f_i(0)} + (-1)^{f_i(1)}}{2}|0\rangle + \frac{(-1)^{f_i(0)} - (-1)^{f_i(1)}}{2}|1\rangle\right] \otimes |1\rangle. \end{aligned}$$

A closer look at the final state of the first qubit reveals that (modulo a possible (global) factor of $-1$) it reads $|0\rangle$ if $f_i(0) \oplus f_i(1) = 0$, which is the case if (and only if) $f_i$ constant. On the other hand the first qubit's state reads $|1\rangle$ if $f_i(0) \oplus f_i(1) = 1$, which is the case if (and only if) $f_i$ balanced. This is the desired result: The value of the first qubit (qubit $a$) at the end of the sequence is $|0\rangle$ or $|1\rangle$ depending on the symmetry of $f_i$. Accordingly, the algorithm finishes with a measurement of the first qubit. The result of this measurement indicates with certainty wether $f_i$ is constant or balanced. Note that in this protocol the function $f_i$ is evaluated only once, unlike in the classical case. In addition, only one qubit measurement is necessary, while the classical protocol requires two measurements.

The last Hadamard operation on the second qubit ($H_2$) is not required for the performance of the algorithm but was introduced here for reasons of symmetry. This will simplify the translation of the algorithm into laser pulses acting on a trapped ion.

The above algorithm represents an improved version [13, 19] of the original quantum algorithm proposed by Deutsch [10], which represents only a probablistic solution: In the original algorithm the function $f_i$ is evaluated only once but there are three possible outcomes: "constant", "balanced" and "inconclusive". For any $f_i$, the algorithm will output with a probability of 50% either "constant" or "balanced" and the output then correctly describes $f_i$. In these cases, the symmetry of $f_i$ is obtained in a single evaluation, which can not be accomplished by classical computation. In the other 50% of cases, i.e. when the output is "inconclusive", no information is obtained.

There exists an extension of Deutsch's problem, which was first presented by Deutsch and Jozsa [18]: Given a function $F(a)$ which accepts a string of $n$ input bits, i.e. a number from 0 to $2^n - 1$, and produces one bit as output. Moreover, $F$ is of one of two kinds; either $F(a)$ is *constant* for all values of $a$, or else $F(a)$ is *balanced*, that is, equal to 1 for exactly half of all possible $a$, and 0 for the other half. In their first proposal Deutsch and Jozsa present a quantum algorithm which requires two evaluations of $F$. Also in this case Cleve, Ekert, Macchiavello and Mosca [19] have found an improved quantum algorithm. The latter requires only a *single* evaluation of $F$ and a *single* measurement (this time of an $n$-qubit register) to reveal the global symmetry property of $F$. A direct comparison of performance with the classical solution is, however, more difficult than for Deutsch's original problem: Clearly, a classical computation will require $2^{n-1} + 1$ evaluations (each evaluation including a single-bit measurement) to prove with certainty that the unknown function is constant. Hence, the classical solution scales exponentially with $n$. In the best case, however, two evaluations are enough (i.e. if the first two evaluations of $F$ with two randomly chosen $a$ yield 0 and 1, hence $F$ is known to be balanced). A probabalistic classical computer which evaluates $F(a)$ for a few randomly chosen $a$, could quickly determine with high probability if $F$ is constant or balanced.

Although, as presented, improved versions of the original proposals exist, all quantum algorithms discussed here are commonly referred to as "Deutsch-Jozsa" algorithms [13] in honour of the crucial discoveries contained in the original papers: Deutsch's algorithm was the first concrete demonstration that a quantum computer could do something faster than a classical computer; the extension by Deutsch and Jozsa was the first example of a scalable problem where the quantum algorithm outperforms the classical solution regarding the scaling of the time required to solve the problem (at least for suitably chosen criteria of comparison).

### 4.3.2 Adaptation for an Ion Trap Quantum Processor

In this section the Deutsch-Jozsa algorithm is translated of into a series of laser pulses acting on a *single* trapped ion, which according to section 4.2 represents a two-qubit quantum processor.

It has been outlined in section 2.2 that Hadamard gates are not particularly well suited for a physical implementation but that they can typically be translated into suitable $\pi/2$ rotations. Accordingly, in the case of the Deutsch-Jozsa algorithm, the sequence of eqn. (4.4) can be translated into

$$U'_{DJ} = R_{\overline{y}1}(\pi/2)\ R_{\overline{y}2}(\pi/2)\ U_i\ R_{y2}(\pi/2)\ R_{y1}(\pi/2). \tag{4.5}$$

It can be easily verified that this sequence (with the same input $|\psi_0\rangle = |0,1\rangle$) yields the same final result as the sequence of eqn. (4.4).

Next, the matrices of the transformations $U_i$ are calculated according to their definition (4.3) and translated into suitable operations which can be implemented in our experiment: $U_1$ is the identity

$$U_1 = \begin{bmatrix} 1 & 0 & 0 & 0 \\ 0 & 1 & 0 & 0 \\ 0 & 0 & 1 & 0 \\ 0 & 0 & 0 & 1 \end{bmatrix} = I,$$

i.e. $U_1$ can be implemented by "doing nothing".

$$U_2 = \begin{bmatrix} 0 & 0 & 1 & 0 \\ 0 & 0 & 0 & 1 \\ 1 & 0 & 0 & 0 \\ 0 & 1 & 0 & 0 \end{bmatrix}.$$

A closer look at this matrix shows that $U_2$ is a $NOT$ operation on the second qubit, hence $U_2 = -iR_{x2}(\pi)$ (cf. section 2.1).

$$U_3 = \begin{bmatrix} 1 & 0 & 0 & 0 \\ 0 & 0 & 0 & 1 \\ 0 & 0 & 1 & 0 \\ 0 & 1 & 0 & 0 \end{bmatrix},$$

$U_3$ obviously represents a $CNOT$ operation controlled by the first qubit, which according to section 2.2 can be written as $U_3 = R_{y2}(\pi/2)\ \Phi\ R_{\overline{y}2}(\pi/2)$.

$$U_4 = \begin{bmatrix} 0 & 0 & 1 & 0 \\ 0 & 1 & 0 & 0 \\ 1 & 0 & 0 & 0 \\ 0 & 0 & 0 & 1 \end{bmatrix}.$$

$U_4$ turns out to be a *0-CNOT* operation, again controlled by the first qubit. It can thus be written as $U_4 = R_{x1}(\pi)\ R_{y2}(\pi/2)\ \Phi\ R_{\overline{y}2}(\pi/2)\ R_{x1}(\pi)$.

The next step is to identify the qubits. The first qubit ($a$) is the one that has to be measured. Clearly, the internal qubit is preferably used for this task as our electron shelving technique precisely distinguishes between $|S\rangle$ and $|D\rangle$. A direct read-out of the vibrational qubit on the

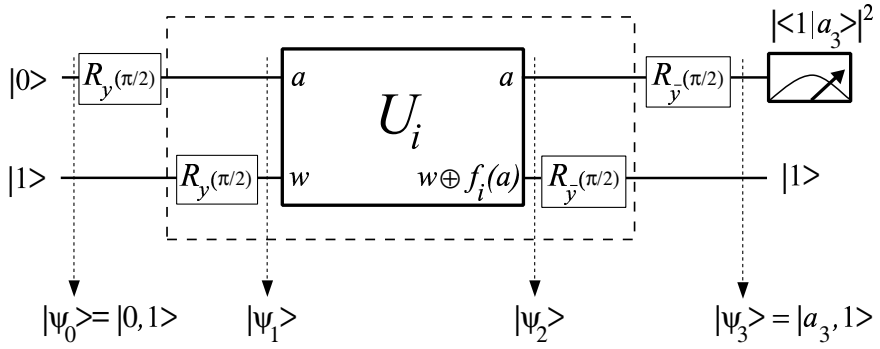


Figure 4.7: The complete Deutsch-Jozsa algorithm adapted for the experiment.

other hand is not possible in a single shot measurement. The algorithm requires the input $|0\rangle$ for the first qubit and the ion naturally is in the $|S\rangle$ state at the beginning of a sequence. Therefore the levels are identified as follows: $|S\rangle \equiv |0\rangle$ and $|D\rangle \equiv |1\rangle$. The vibrational qubit then has to be taken as the second qubit ($w$) of the algorithm. $w$ is supposed to be in the logic state $|1\rangle$ at the beginning of the sequence. The vibrational mode at this point (after sideband cooling) is in the $|n = 0\rangle$ state. It therefore comes naturally to make the association $|n = 1\rangle \equiv |0\rangle$ and $|n = 0\rangle \equiv |1\rangle$.

A slight modification of the algorithm is made by specifying the black box as being slightly larger than $U_i$. The new black box corresponds to the dashed box in Fig. 4.7 such that it includes the two $\pi/2$ pulses on the second qubit. This is just a conceptual change made to simplify the overall sequence. This change corresponds to a $U_i$ which on the second qubit operates in the $(|0\rangle + |1\rangle), (|0\rangle + |1\rangle)$ basis, rather than in the $|0\rangle, |1\rangle$ basis.

The two $\pi/2$ rotations of the first qubit in the overall sequence (eqn. (4.5)), $R_{y1}(\pi/2)$ and $R_{\overline{y}1}(\pi/2)$, can conveniently be implemented as carrier pulses with the appropriate laser phases. What remains are the four different (black box) operations $R_{\overline{y}2}(\pi/2)\ U_i\ R_{y2}(\pi/2)$, which can be implemented as follows:

- $\underline{i = 1}$ : $R_{\overline{y}2}(\pi/2)\ U_1\ R_{y2}(\pi/2) = R_{\overline{y}2}(\pi/2)\ I\ R_{y2}(\pi/2) = I$ is the identity operator.

- $\underline{i = 2}$ : $R_{\overline{y}2}(\pi/2)\ U_2\ R_{y2}(\pi/2) = R_{\overline{y}2}(\pi/2)\ R_{x2}(\pi)\ R_{y2}(\pi/2)$ modulo an irrelevant global phase $(-i)$. This is a series of single qubit rotations, which may seem easy to implement. We are, however, concerned with rotations of the second, that is, the *vibrational* qubit. The way to implement this has been outlined in section 4.2: operations on the vibrational qubit are achieved by sandwiching the operation, applied to the internal qubit, between two $SWAP$ operations with well defined relative phase, i.e.

  $$R_{\overline{y}2}(\pi/2)\ U_2\ R_{y2}(\pi/2) = SWAP(\pi)\ R_{\overline{y}1}(\pi/2)\ R_{x1}(\pi)\ R_{y1}(\pi/2)\ SWAP(0).$$

  The corresponding series of laser pulses reads

  $$R_{swap}(\pi)\ R_{\overline{y}1}(\pi/2)\ R_{x1}(\pi)\ R_{y1}(\pi/2)\ R_{swap}(0).$$

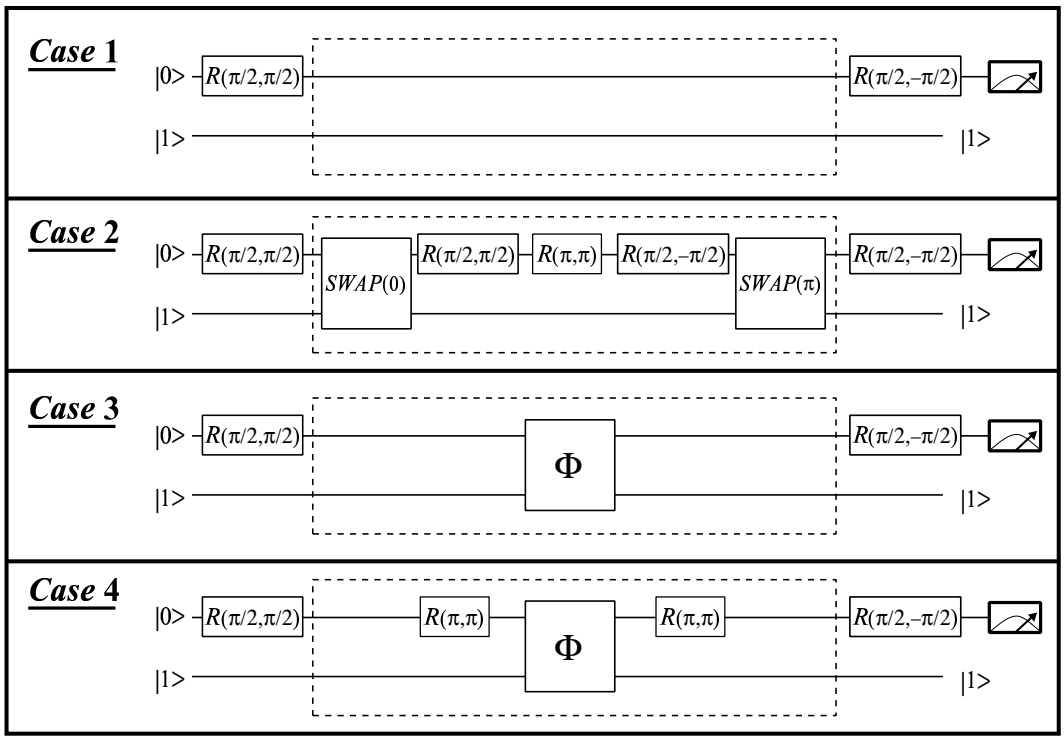


Figure 4.8: Complete sequence for all four cases $i = 1 \ldots 4$ of the Deutsch-Jozsa algorithm.

- $\underline{i = 3}$ : $R_{\overline{y}2}(\pi/2)\ U_3\ R_{y2}(\pi/2) = R_{\overline{y}2}(\pi/2)\ R_{y2}(\pi/2)\ \Phi\ R_{\overline{y}2}(\pi/2)\ R_{y2}(\pi/2) = \Phi$. So the black box corresponds to a phase gate.

- $\underline{i = 4}$ : $R_{\overline{y}2}(\pi/2)\ U_4\ R_{y2}(\pi/2) = R_{\overline{y}2}(\pi/2)\ R_{x1}(\pi)\ R_{y2}(\pi/2)\ \Phi\ R_{\overline{y}2}(\pi/2)\ R_{x1}(\pi)\ R_{y2}(\pi/2)$ $= R_{x1}(\pi)\ \Phi\ R_{x1}(\pi)$. Note that single qubit rotations acting on different qubits commute. Thus, in case 4 we get a phase gate, surrounded by two $\pi$-rotations of the internal qubit.

Section 4.2 discussed that for the implementation of a phase gate $\Phi$ we have the choice between three different methods. To implement the Deutsch-Jozsa algorithm we decided to use the composite pulse technique for $\Phi$. Remember that for the vibrational qubit here the qubit identification $|n = 1\rangle \equiv |0\rangle$ and $|n = 0\rangle \equiv |1\rangle$ was chosen. In this basis of logic states, the composite phase gate sequence of eqn. (4.2) precisely implements the desired phase gate $\Phi$ (eqn. (2.8)) since it applies a phase factor of $-1$ to the logic state $|1, 1\rangle$ $(= |D, 0\rangle)$. The $SWAP$ operation of eqn. (4.1), however, must modified due to this particular qubit identification. A closer analysis reveals that it suffices to use *blue* instead of red sideband pulses, so that the sequence to be used here reads

$$R_{swap}(\phi_0) = R^+(\frac{\pi}{\sqrt{2}}, \phi_0)\ R^+(\frac{2\pi}{\sqrt{2}}, \phi_0 + \phi_{swap})\ R^+(\frac{\pi}{\sqrt{2}}, \phi_0).$$

A quantum circuit representation of the complete sequences is shown in Fig. 4.8 [1]. In the actual experiment the black box boundary is of course a formal construct as the experimenter knows which kind of function is being performed. In principle, however, a third party is invited into the laboratory to set the "black box" (choose the computer program) while the experimenter is not present, and after this the experimenter runs the whole algorithm by adding the two $\pi/2$ pulses to the sequence and reading out the internal qubit.

## 4.4 Quantum Computation With Two and More Ions

In a string of trapped ions *direct* spin-spin type coupling between (neighboring) internal qubits is negligible as the ions are separated by several micrometers while their individual wavefunctions extend over several nanometers only (cf. section 3.2). In order to perform a quantum gate between two internal qubits (ion 1 and ion 2) the proposal of Cirac and Zoller [34] uses one of the vibrational modes to mediate the coupling. This vibrational mode is identified as a qubit just as in the previous sections and has to be prepared in the $|n = 0\rangle$ state. The experimental protocol then reads:

- Step 1: Map the (quantum) information of ion 1 to the vibrational qubit.
- Step 2: Perform the desired gate between the vibrational qubit and ion 2.
- Step 3: Map (back) the information from the vibrational qubit to ion 1.

For the mapping of quantum information from an ion to the vibrational mode (and back), a single $\pi$-pulse on the red sideband, optically addressed on ion 1, is applied [34]; the corresponding operation is illustrated in Fig. 4.9 and will be denoted $MAP$:

$$MAP(\phi_0) = R^-(\pi, \phi_0).$$

As the mode is initially in the $|n = 0\rangle$ state, the $|D, 1\rangle$ state never becomes populated in the overall procedure and so its coupling to the $|S, 2\rangle$ state outside the computational space via the red sideband does not come into play. All experimental techniques required for step 2 have been discussed in section 4.2. Note that in contrast to section 4.2 where the vibrational qubit is fully used as an independent qubit, here it only serves as a *transfer* qubit and is therefore often referred to as the *quantum bus*. This vibrational qubit repeatedly stores and passes on quantum information, but comes back to the state $|n = 0\rangle$ after completion of a two-ion gate. Individual rotations of the vibrational qubit are not needed. A beautiful feature of the Cirac-Zoller protocol is that two-qubit gates can be performed directly between any two ions in a string of, in principle, arbitrarily many ions. Just as when the $SWAP(\phi_0)$ sequence was used for single ion quantum logic, unwanted phase factors can be avoided here by using different laser phases $\phi_0 = 0$ and $\phi_0 = \pi$ for the two surrounding $MAP$ operations. For step 2, the laser has to be addressed on ion 2, while the laser focus must be switched to ion 1 for

[1] Note that in the complete sequences given in [53] the phases $\phi$ of the carrier pulses $R(\theta, \phi)$ are different. This is because in [53] the notation $R_y$ was chosen for $\pi/2$-rotations around the $x$-axis of the Bloch sphere. This corresponds to a $z$-rotation by $\pi/2$ of the Bloch sphere of the internal qubit throughout the whole algorithm, which changes nothing on its overall performance.

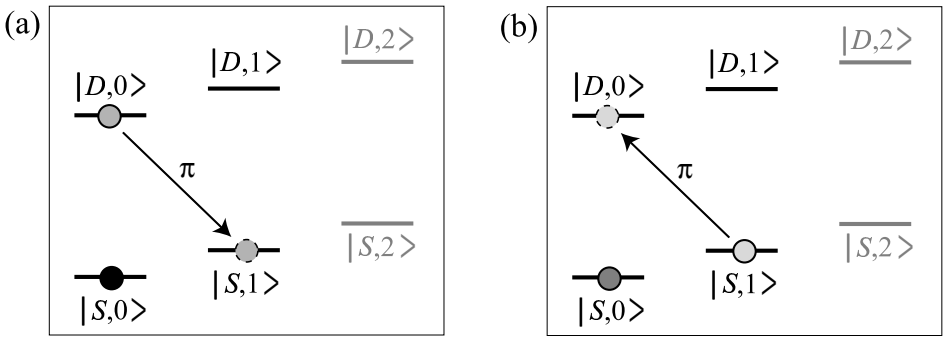


Figure 4.9: Step 1 and step 3 of the Cirac-Zoller protocol. Both figures display the internal qubit states of *ion 1* combined with the states of the vibrational mode. (a) Step 1: The mode has been prepared in $|n = 0\rangle$ while the internal qubit in general is in some superposition. Accordingly the combined system is in a superpositition of $|S, 0\rangle$ and $|D, 0\rangle$ which is indicated by a black and a grey circle. The mapping red sideband $\pi$-pulse completely transfers the $|D, 0\rangle$ population to $|S, 1\rangle$ (grey circle with dashed boundary). After this operation, the internal qubit is in the $|S\rangle$ state while the superposition is now encoded in the motional states $|n = 0\rangle$ and $|n = 1\rangle$. (b) Step 3: in the meantime (step 2) a quantum gate between the vibrational qubit and ion 2 has been performed, which in general changes the state amplitudes of the vibrational qubit, while the internal state of ion 1 remains unaffected, i.e. is $|S\rangle$. Thus the combined system is in a new superposition of $|S, 0\rangle$ and $|S, 1\rangle$, indicated by circles of different grey-scale. The red sideband $\pi$-pulse for the back-mapping transfers the $|S, 1\rangle$ population completely to $|D, 0\rangle$ (circle with dashed boundary). In this way the quantum information which was encoded in the vibrational qubit is transfered back to the internal qubit of ion 1, while the vibrational mode returns to the $|n = 0\rangle$ state.

the surrounding *MAP* gates.

Note that this procedure allows the implementation of *any* quantum gate between the two internal qubits. If this quantum gate is, for example, a *CNOT* gate, the standard method of implementing step 2 (*CNOT* between vibrational and internal qubit) is to sandwich a phase gate $\Phi$ (between vibrational and internal qubit) between two single qubit $\pi/2$-rotations on ion 2 (see section 2.2). This yields a *CNOT* controlled by the quantum bus:

$$CNOT_{\text{mode}\to 2} = R_{y2}(\pi/2)\ \Phi_{\text{mode}\leftrightarrow 2}\ R_{\overline{y}2}(\pi/2).$$

Thus the overall sequence for a *CNOT* between the two ions, where ion 1 is the control qubit, reads

$$CNOT_{1\to 2} = R_1^-(\pi, \pi)\ R_{y2}(\pi/2)\ \Phi_{\text{mode}\leftrightarrow 2}\ R_{\overline{y}2}(\pi/2)\ R_1^-(\pi, 0).$$

As in the single ion case (section 4.2), the remaining freedom lies in the method applied to implement $\Phi_{\text{mode}\leftrightarrow 2}$. In the first experiments on the two-ion *CNOT*, the composite pulse technique was employed. For the composite phase gate $\Phi'$ of eqn. (4.2), coupling on the

blue sideband is used. From an experimental point of view it is desirable to use a minimum number of different laser frequencies. Accordingly, the whole sequence is rearranged in order to comprise only blue sideband and carrier pulses. One can, for example, implement the *MAP* operations by $\pi$-pulses on the *blue* sideband $R^+(\pi, \phi_0)$ instead of the red sideband and compensate for this change by applying a *0-CNOT*$_{\text{mode}\to 2}$ instead of the $CNOT_{\text{mode}\to 2}$ gate. The latter can be realized as (see sections 2.2 and 4.2)

$$\textit{0-CNOT}_{\text{mode}\to 2} = R_{y2}(\pi/2)\ \Phi'_{\text{mode}\leftrightarrow 2}\ R_{\overline{y}2}(\pi/2)$$

The complete sequence for this two-ion *CNOT*, expressed in laser pulses, thus reads:

$$CNOT_{1\to 2} = R_1^+(\pi,\pi)\ R_{y2}(\pi/2)\ \Phi'_2\ R_{\overline{y}2}(\pi/2)\ R_1^+(\pi,0), \tag{4.6}$$

with

$$\Phi'_2 = R_2^+(\pi,\frac{\pi}{2})\ R_2^+(\frac{\pi}{\sqrt{2}},0)\ R_2^+(\pi,\frac{\pi}{2})\ R_2^+(\frac{\pi}{\sqrt{2}},0).$$

Quantum computation experiments with two (or more) ions are, in general, more difficult than with a single ion. The major reason for this lies in the reduced quantum gate speed which is explained in the following. It is outlined in Appendix A.3 that for two-ion experiments the Lamb-Dicke factor $\eta$ inevitably is smaller than in the single-ion experiments, i.e. $\eta = 1.8\%$ (compared to $\eta = 6.8\%$ in single-ion case). This is ultimately due to the need for individual addressing in the multi-ion case. According to inequality 3.33, a smaller $\eta$ corresponds to a smaller $\Omega_S$, hence a reduced gate speed.

Note that with composite pulses we have a technique at hand which allows the realization of a real *SWAP* operation. Therefore, we can, in principle, use the mode as a *complete* qubit even in the multi-ion case. This again means that with two trapped ions we could perform arbitrary three qubit quantum computations. One could even conceive of using *several* modes of a multi-ion string as additional qubits. At present, we can not fully profit from this option because with two or more ions we are forced to operate at fairly low sideband Rabi frequencies for reasons given above. Therefore, at most two *SWAP* operations are possible at present.

If a two-ion quantum gate has been implemented, a natural goal is to probe the phase coherence of the gate. This can be done by recording quantum oscillations [49, 50, 81]. This typically involves probing the quantum gate with qubit superpositions as inputs (prepared by Ramsey-type $\pi/2$ pulses) and reading out the interference pattern with additional Ramsey-type $\pi/2$ pulses added after the gate operation (the phase of which is scanned). Note that such an interferometric method [19] is conceptually equivalent to the way the operations $U_i$ are probed in the Deusch-Jozsa algorithm. By the same type of procedure, the quantum phases of an implemented gate operation can be measured, in this way performing a quantum gate tomography [82–84]. For a $CNOT$ gate, a particularly interesting case arises if the *control* ion is in a superposition at the input. For this kind of input the quantum gate produces entangled states, i.e. *Bell-States*, as an output. For example, an input state $(|S\rangle + |D\rangle)|S\rangle$ (where the first ion represents the control qubit) is transformed into the Bell state $|S,S\rangle + |D,D\rangle$ by an ideal $CNOT$ operation.

# 5 Experimental Setup

## 5.1 Design of the New Linear Trap

The first one and a half years of this PhD work used a linear ion trap which had been designed and prepared (but not yet used) by Hanns-Christoph Nägerl in his PhD [51] and it will be referred to it as the "old trap". The work and the results obtained with this trap are reported in the PhD thesis of Harald Rohde [52]. A schematic picture of the old trap is shown in Fig. 5.1. Here the end-caps were made as rings around the RF-rods. The end-cap voltage was limited by the specifications of the corresponding feed-throughs of the vacuum vessel to $V_{cap} \leq 2000$ V. At $V_{cap} = 2000$ V an axial frequency $\omega_z = 2\pi \cdot 700$ kHz was reached. From this experimental result a geometry factor $\alpha = 0.81$ can be deduced (eqn. (3.6)). Radial frequencies $\omega_r$ of up to $2\pi \cdot 1.8$ MHz were obtained with RF-drive powers of up to 5 W at a frequency $\Omega = 2\pi \cdot 16$ MHz.

A new trap design, called the "new trap", was envisaged in the year 2000 to improve on several problems encountered with the old trap. These problems and the design path towards the new trap will be elaborated in the following.

When loading a trap by ionizing Ca-atoms from an atomic oven via electron impact ionization[1], many stray electrons are deposited on electrically insulating surfaces, for example on ceramic support structures of the trap construction. Special effort to focus the ionizing electron beam well into the trap center is futile because the presence of the trapping radio-frequency fields causes a large defocussing of the beam. Deposited charges create DC fields at the trap center which must be compensated for. This is achieved by additional compensation

[1] At the time the new trap was designed, trap loading was still carried out by electron impact ionization. This method was later replaced by photoionization, see section 6.4

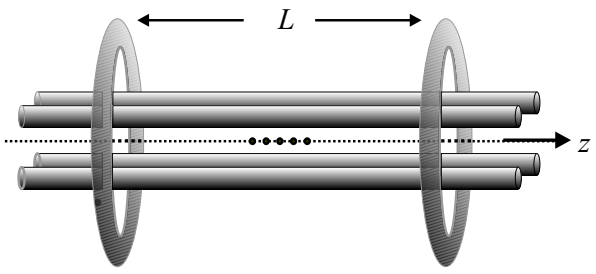


Figure 5.1: Design of the old trap. $L$ is 10 mm and $r_0$ - the shortest distance from the trap axis to the RF-rod surfaces - is 1.2 mm. The RF-rods have a diameter of 0.6 mm.

electrodes around the trap to which appropriate DC voltages are applied. Finding the right compensation voltages is a quite tedious and time consuming procedure (see also chapter 6.2). The old trap was held together by relatively large uncovered ceramic plates which collected large amounts of electrons. For the new trap design ceramic parts were to be minimized and covered by metal wherever possible.

It was found experimentally with the old trap, that the radial mode at $2\pi \cdot 1.8$ MHz as well as the axial mode at $2\pi \cdot 700$ kHz after Doppler cooling were left with mean phonon numbers $\bar{n}$ of about 45 [52] which is still relatively high. The envisaged experiments, however, require good cooling in terms of a low $\bar{n}$ for *all* vibrational modes (cf. section 7.2). A low $\bar{n}$ of a mode is most easily reached by a high mode frequency. For the radial frequencies there is essentially no limit and in a sense "the higher the better". The axial frequency, however, cannot be too high as optical single ion addressing is required. When the new trap was designed, the waist of the addressing beam at 729 nm was measured to be about 3.7 $\mu$m [52]. This limits inter-ion separations to a minimum of about 7 $\mu$m which again limits axial frequencies to not more than 700 kHz (by chance the limit of the old trap). The new trap was intended to yield axial frequencies of up to 1.5 MHz because possible future improvements of the addressing optics would then allow the operation of the trap with a stronger axial confinement. This is advantageous because it facilitates ground state cooling of the axial mode(s) and also increases the speed of quantum gates (see eqn. (3.34)).

When optimizing the trap design for higher radial frequencies several aspects must be taken into account. Firstly, the stability parameter $q$ should be clearly below 0.9. In order to avoid potential nonlinear resonances (see section 3.1) it is desirable to keep $q$ below 0.5. From eqn. (3.8) it is found, for example, that with the old trap the typical working point ($\omega_{r0} = 2\pi \cdot 1.8$ MHz, $\Omega = 2\pi \cdot 16$ MHz) was $q = 0.32$. Eqn. (3.8) also shows that with a limited $q$ the only way to increase $\omega_{r0}$ further is to go to higher drive frequencies $\Omega$. At the same time it is found (inserting eqn. (3.2) into eqn. (3.8)) that

$$\omega_{ro} \propto \frac{V}{r_0^2 \Omega} \tag{5.1}$$

which indicates that increasing $\Omega$ in the first place *decreases* the radial frequency. This must then be compensated for either by an increased RF amplitude $V$ or a decreased linear dimension $r_0$ of the trap. Increasing $V$ means increasing the RF drive power $P$, but as $V$ scales as $\sqrt{P}$ and $P$ is limited[2] to a few Watts one cannot expect to reach values of $V$ far above the ones reached with the old trap (up to about 1000 V). Therefore the only solution is to down-size the trap. When down-sizing the trap one has to worry about heating of the ions caused by nearby electrode surfaces as observed in other experiments [64] (see also chapter 6). Those experiments, with distances $r_0$ on the order of 0.1 mm, suffered serious heating problems, while at the same time experiments in Innsbruck with $r_0 = 0.7$ mm showed only negligible heating rates [4]. Consequently, a moderate size-reduction with respect to the old trap by a factor 1.5 - i.e. from $r_0 = 1.2$ mm to 0.8 mm - was envisaged.

To summarize the design guidelines for the new trap:

- Down-size the radial structure by a factor 1.5 with respect to the old trap.

[2]The RF-power is limited essentially by a heating up of the electrical feed-throughs and the trap itself (see chapter A.2).

- In order to increase the axial frequency from 700 kHz to about 1.5 MHz, i.e. by a factor of 2, according to eqn. (3.7) the distance $L$ between the end-caps has to be reduced by approximately the same factor (depending also on the new end-cap geometry, i.e. the new $\alpha$).

- All ceramic surfaces (or insulators in general) facing towards the trap should be minimized in size.

Down-sizing the radial structure and keeping the electrodes rod-like poses problems of fabrication in a machine shop, especially as a high relative accuracy is required. A blade-like construction could be fabricated with more precision at these small scales.

Finally, the design must incorporate electrodes to compensate for stray DC fields at the trap center pointing in the radial directions $x$ and $y$. These compensation electrodes must not be too close to the trap volume, as their presence may distort the trap fields. They must also leave optical access for photon counting and addressing. At the same time the compensation electrodes must be near and large enough to produce sufficiently strong DC fields at the trap center. The design guideline was that they should produce field strengths comparable to the compensation electrodes of the old trap using voltages of about 100 V. This leaves some safety margin as the overall set-up (including electrical feed-throughs) was designed to allow for voltages up to at least 3000 V. It is not possible to calculate analytically the electric field strength produced by a given compensation electrode configuration at the center of a certain trap geometry nor is it possible to analytically calculate the geometry factor $\alpha$ of a given trap. Therefore simulations of different trap configurations, including compensation electrodes were performed with the software SIMION. Demonstrative pictures of such numerical simulations are shown in Fig. 5.2. The final design of the new trap taking into account all these considerations is presented in Fig. 5.3, while Fig. 5.4 shows photographs of the complete setup including support structures and electric connections. The typical machining precision for all measures is 10 $\mu$m, down to 5 $\mu$m for critical parts. The support structures, which can be seen in the overall pictures (front view and side view) are made of Macor® ceramics. As much Macor® as possible has been milled off. Additionally, the end-caps have a 8 mm diameter base plate which covers most of the central Macor® surface. As can be seen in the draft of the end-caps, this base plate is machined such that it touches the Macor® only around the center, while the outer ring of it has a 0.2 mm gap. This is because in previous experiments it has been observed that Macor® surfaces mediate voltage shorts much better than free ultra high vacuum gaps. In fact, the outer edge of the base plates come as close as 1.5 mm to the blades and voltages of around 3000 V between them occur when the trap is operating. The blades, as well as the compensation electrodes, are made of stainless steel. Molybdenum was used for the end-caps. The blades were machined by a wire erosion technique which ensures very high precision, in particular for the holes which run through the whole length of 30 mm.

The trap is suspended in the vacuum chamber on four steel rods. In fact, Fig. 5.4 shows upside-down views. Note that the RF-blades are connected to the helical resonator by OFHC copper braids, while all DC connections are coaxially shielded steel wires. Chapter 7 shows that the performance of the real trap is very close to what is expected from the simulations (e.g. to within 5% in terms of trap frequencies).

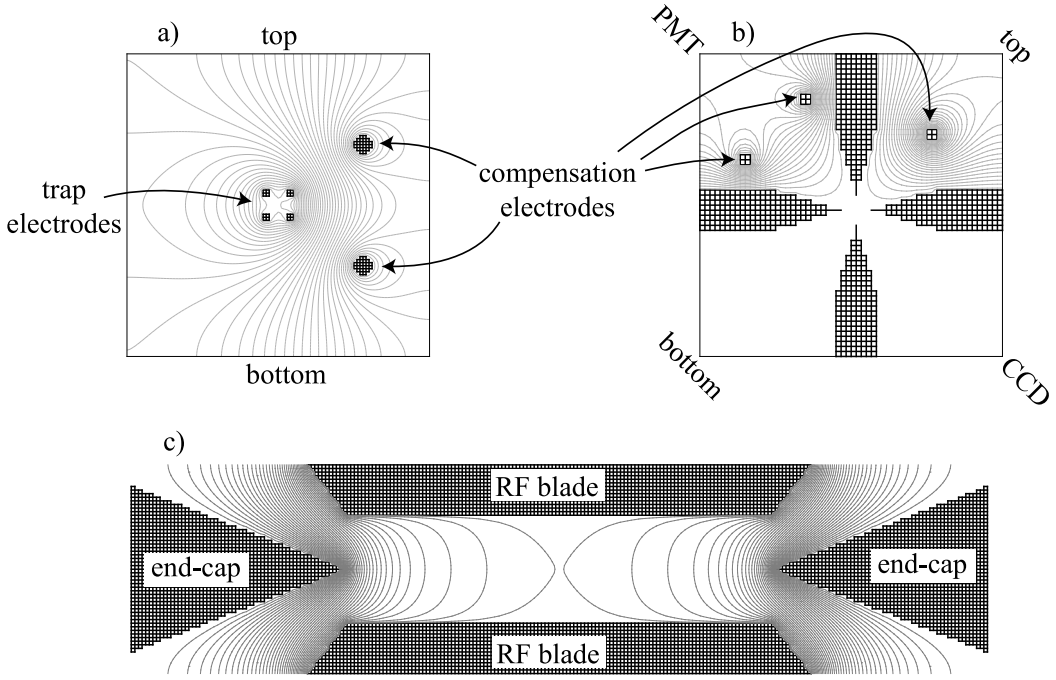


Figure 5.2: a) Simulation of the compensation electrode set-up of the old trap as a cross-check for the simulation procedure. In the center: the four RF-electrodes of the trap. The two other rods are connected to the same potential and form one electrode for horizontal compensation. Vertical compensation is performed by another rod pair which is not included here. b) Compensation electrodes of the new trap (approximation of the final design). The electrode for horizontal compensation was split up into two rods in order to leave optical access open for fluorescence counting. For vertical compensation, a single rod was used. c) Simulation for the axial trapping strength of the new trap. The simulation is 3-dimensional, this picture showing a 2D cut along the trap axis. This geometry, which is close to the final design, yielded an axial frequency of about 1.5 MHz for an end-cap voltage of 2000 V in the simulation.

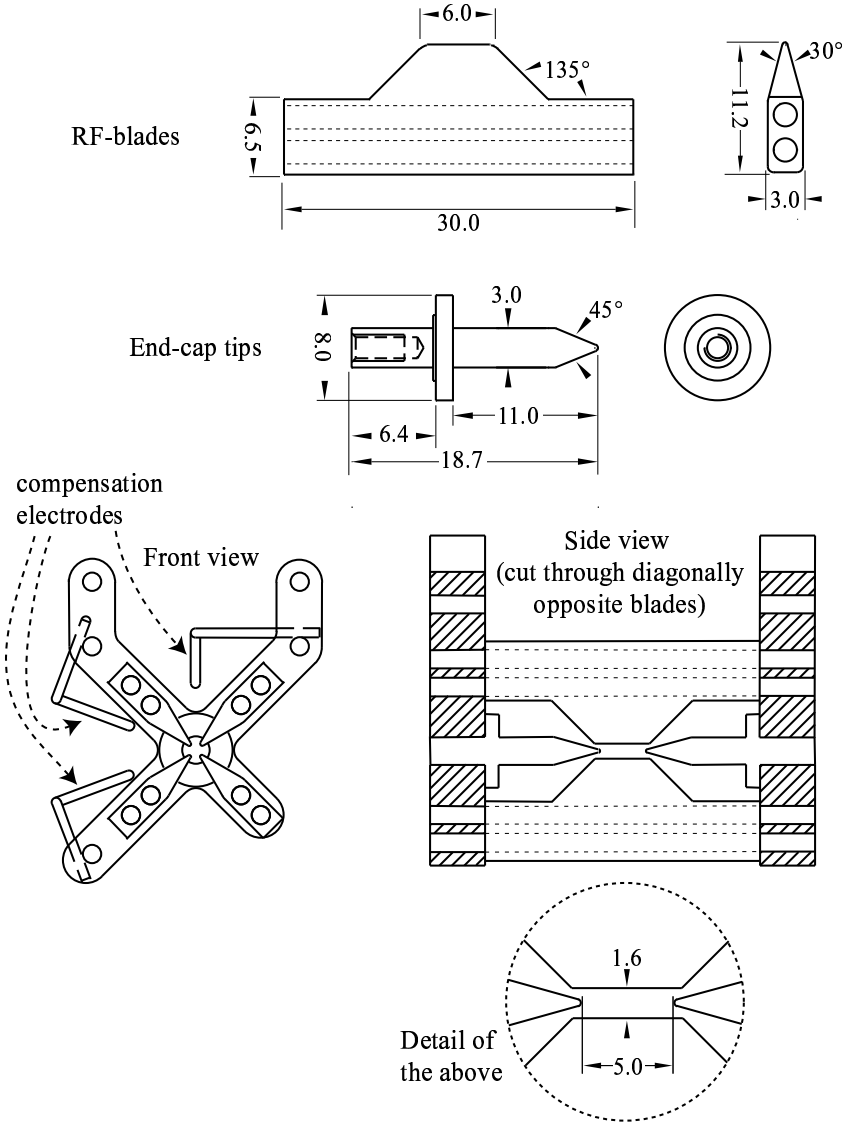


Figure 5.3: Construction of the new trap. Numbers without units are in millimeters.

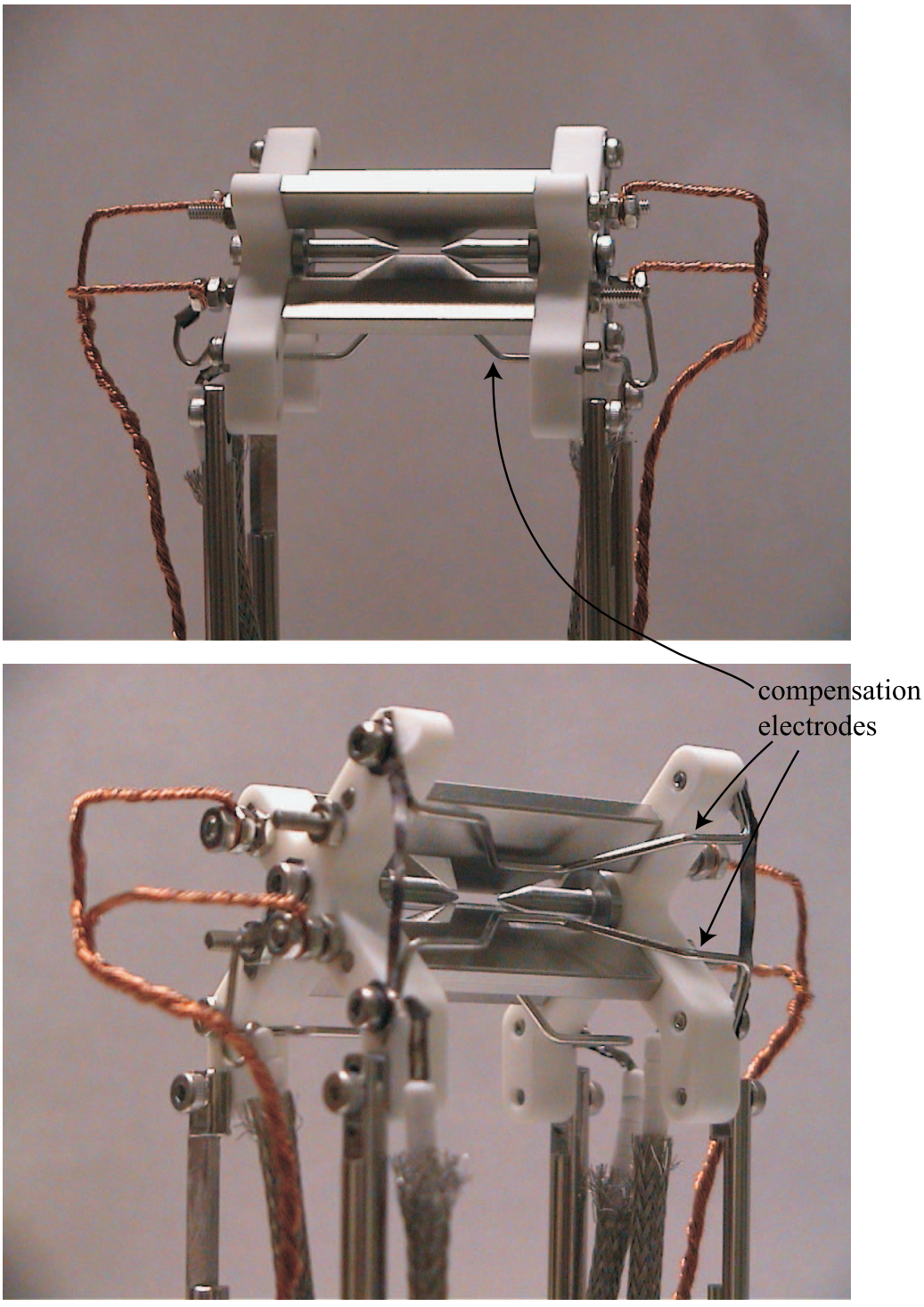


Figure 5.4: Photographs of the new trap setup. Top: sideview. Bottom: space diagonal view from the other side; note the compensation electrodes.

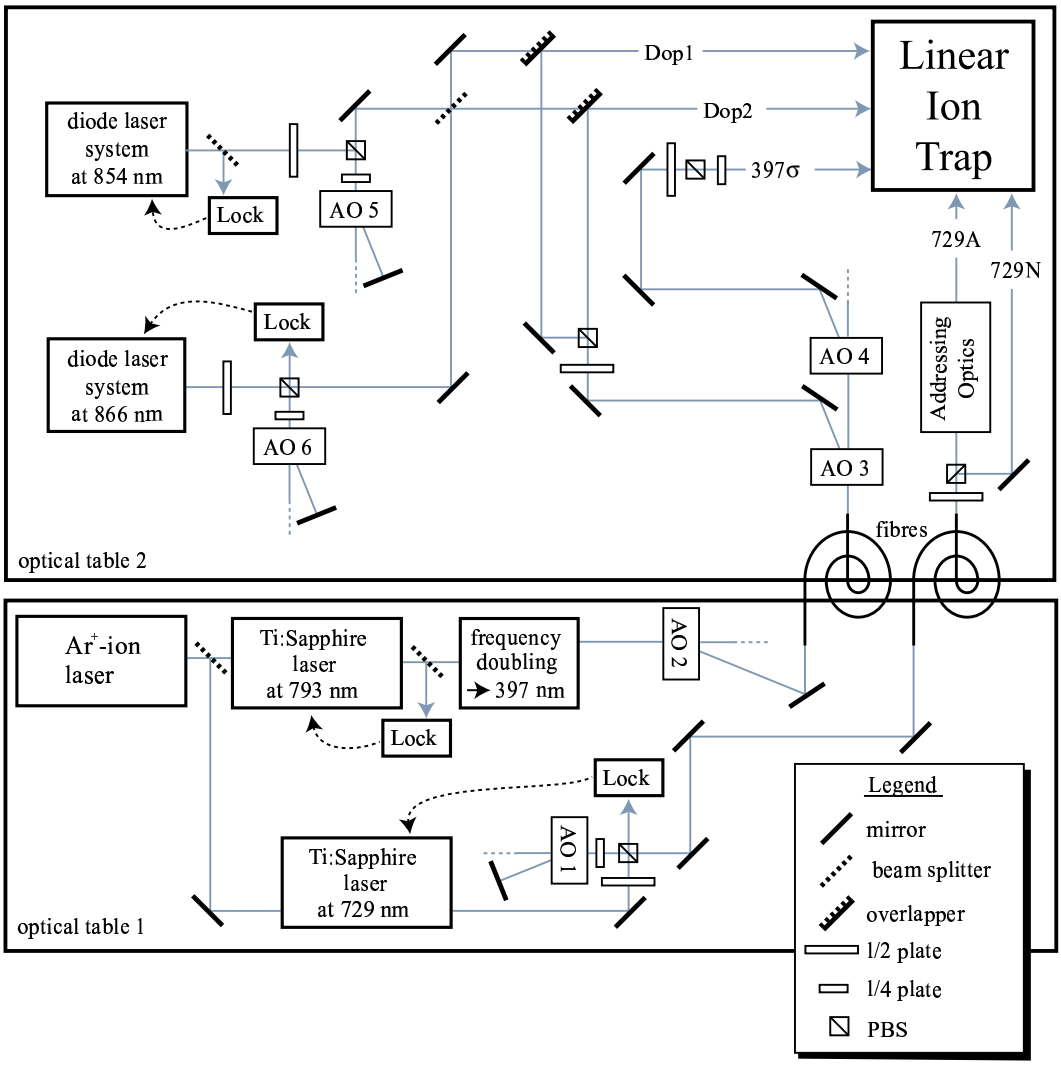


Figure 5.5: General setup, in particular laser sources. The individual elements are discussed in the text.

## 5.2 Laser Systems for $^{40}Ca^{+}$

The experiments presented here use lasers at 397 nm, 729 nm, 866 nm and 854 nm (cf. section 3.3.1). An overview of the optical setup is given in Fig. 5.5. Only the essential optical elements are shown. The experimental setup is spread over two tables. Optical table 2, along with all laser sources and a CCD camera for ion observation, is shared with our calcium cavity-QED experiment. The ion trap setup will be explained in the next section. Each laser is frequency locked to its individual optical reference cavity using the Pound-Drever-Hall method [85]. Every reference cavity is placed in a temperature stabilized vessel. The vessels for the 729 nm and the 866 nm lock consist of two layers inside each other, each one

being independently temperature stabilized. The cavity for the 729 nm laser is additionally placed in a vacuum chamber and made of ultra low thermal expansion material. Details of the specific lasers and their frequency locks have been presented in previous PhD theses on the Innsbruck calcium experiments [51], [4], [52]. No principal changes have been made since, although most components - including optics, lasers and electronics - have been improved or replaced by better versions during the last two years.

The optical element labelled "overlapper" in Fig. 5.5 is a glass substrate with high reflectivity coating for 397 nm on one side while both sides are anti-reflection coated for light around 860 nm. This allows superimposing laser beams at 866 nm and 854 nm onto a 397 nm beam. A single 50:50 beam splitter is used to split the laser beams at 866 nm and 854 nm and at the same time overlap the resulting beams. Subsequently each of these double wavelength infrared beams is overlapped with a 397 nm beam. The resulting triple wavelength beams are called Dop1 and Dop2.

It can also be seen that each laser beam can be switched on and off with either a single or a double pass acousto-optical modulator (AOM) labelled AO1...AO6. AO2, AO3, AO4 and AO5 are driven at fixed frequencies (either 80 or 270 MHz) and are used for switching and light intensity control. Frequency tuning of the corresponding lasers at 397 nm, and 854 nm is achieved by scanning the length of their reference cavities using piezos. The reference cavities for 866 nm and 729 nm do not feature piezos - and consequently are not scannable - in order to achieve minimum linewidth and frequency drift, in particular for the 729 nm light. Their frequencies are tuned with the help of the double pass setups by controlling the RF drive frequencies of AO1 and AO6. For the optical channel called $397\sigma$ circularly polarized light is produced and then shone in parallel to the magnetic field vector at the position of the trap center in order to provide $\sigma^-$ polarized 397 nm light. AO2 represents an additional switch to provide optimum cancelling of 397 nm light during periods of coherent manipulation on the 729 nm transition. Residual 397 nm light would otherwise broaden the $S_{1/2}$ ground state(s) significantly and thus destroy coherence on the qubit transition at 729 nm.

In addition to what is shown in Fig. 5.5, small fractions from all wavelength sources are sent to home built wavemeters, allowing for coarse wavelength measurements with an accuracy of about $10^{-6}$.

The light at 729 nm is either sent to the 729A or the 729N channel, while the respective other channel is then blocked. The 729A light passes through a special optics producing a tightly focussed beam at the trap center designed to address individual ions of a chain (see section 7.4). The 729N light is focussed onto the ions by single lens producing a comparatively large laser waist of about 20 $\mu$m. Lasers in the channels Dop1, Dop2 and $397\sigma$ are also focussed by just a single lens. The corresponding laser waists at the trap center are on the order of 50 $\mu$m for all 397 nm beams and about 300 $\mu$m for the 854 nm and 866 nm beams.

## 5.3 Frequency and Phase Control at 729 nm

The quantum computation protocols presented in chapters 2 and 4 require not only a precise laser power and frequency but also special phase control, in particular for the application of composite pulse operations (cf. 4.2). A complete quantum gate protocol in our experiment typically requires at least five different laser frequencies at 729 nm for ground state cooling

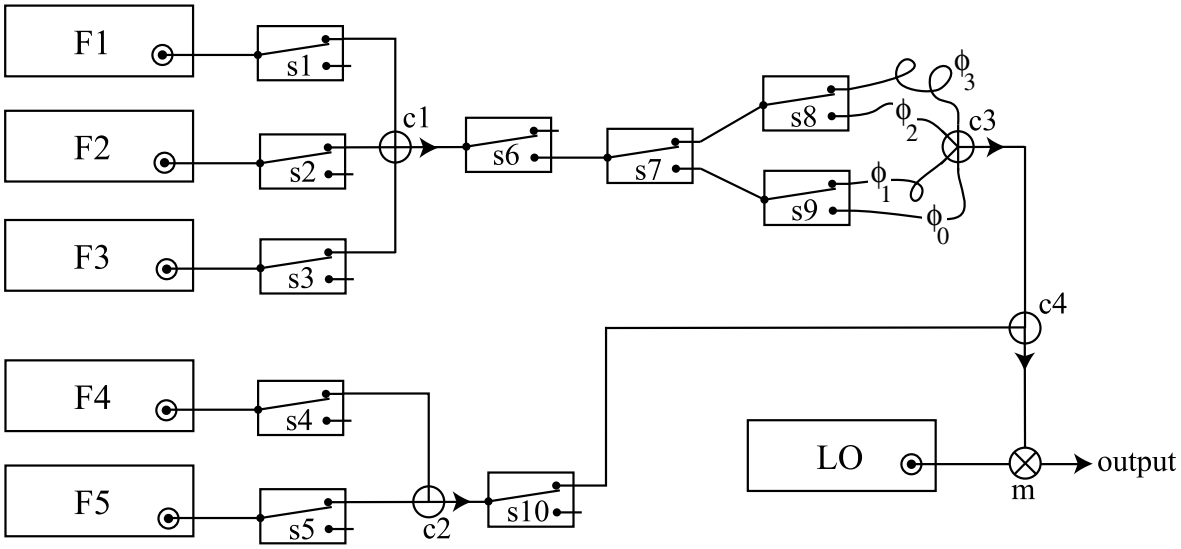


Figure 5.6: Network for laser power, frequency and phase control at 729 nm. The elements F1-F5 are signal generators running at constant frequency and power during one data acquisiation scan; s1-s10 denote TTL controlled RF switches, c1-c4 are power combiners and m is a mixer. The local oscillator LO is operated at $\sim$ 600 MHz and the sources F1-F5 at around 370 MHz. The output frequency is thus $\sim$ 230 MHz (the sum frequency of $\sim$ 1 GHz is strongly suppressed by the following RF amplifiers and the 729 nm AOM).

and coherent manipulations. Composite pulse operations can be simplified but even then require several well defined switchable laser phases at certain frequencies. The manipulation of 729 nm light in the experiment is achieved by applying suitable pulse sequences in the RF range around 230 MHz to the corresponding double pass AOM (AO1 in Fig. 5.5). The ultimate tool for the required timing, power and frequency control would be a single RF pulse source, which has just one output channel and can be computer controlled. Such an instrument would need to be specially designed and produced for the particular application, nevertheless in the long term the experiment will require such a device.

For the experiments presented here we have built a radio-frequency network which solves these problems for the time being. Fig. 5.6 shows the network and should be seen as a *generic* representation. The real setup is subject to continual modifications to meet the requirements of each individual experiment. The resonances in the $S_{1/2} \leftrightarrow D_{5/2}$ spectrum are very stable with respect to each other, typically better than 1 kHz. The only change arises from the drift of the 729 nm reference cavity. Therefore we use frequency mixing to produce the output signal. The advantage is that the frequency sources F1-F5 can be fixed, while the overall drift is compensated for by the local oscillator (LO) alone. F4 and F5 are used for sideband

cooling. Laser phases are controlled by switching between different signal paths using the switches s7-s9. The lengths of the cables denoted $\phi_0$-$\phi_3$ are carefully tailored to implement the desired phases, which depend on the experiment to be performed. Hence for a certain experimental protocol preparation of the appropriate set of cables $\phi_0$-$\phi_3$ is required. This method has served as an interim solution of the phase switching problem for the experiments presented in this thesis. Custom-made phase switching devices for the required radiofrequency range are commercially available, but feature long delivery times. The network of phase-cables and switches (between s6 and c4) is currently being replaced by such a (single) device[3].

## 5.4 Vacuum Vessel and Optical Access

The different laser beams discussed in the previous chapter are directed to the trap center at various angles with respect to the trap axes and the magnetic field. Fig. 5.7 shows the geometry of the vacuum chamber. The linear trap is at the center of the vessel construction, i.e. of the $x'$-$y'$-$z'$ coordinate system, and is indicated by two solid bars. Note that this coordinate system differs (by a rotation) from the $x$-$y$-$z$ coordinate system employed to describe the trap itself (cf. section 3.1). The trap axis ($z$) is horizontal, i.e. it lies in the $x'$-$y'$ plane, and is represented by a dash-dotted line. The RF electrode blades are at 45° with respect to the $x'$-$y'$ plane. It can be seen that the trap axis is tilted with respect to the $x'$-axis by an angle $\alpha = 22.5°$. The reason for this is that in our present scheme the 729A beam must address individual ions but at the same time have some projection along the trap axis in order to couple to sidebands of axial motion (see also Appendix A.3).

For the experiments we need a well-defined magnetic field to split the Zeeman-sublevels of the $S_{1/2} \leftrightarrow D_{5/2}$ transition. The circularly polarized 397$\sigma$ light drives $\sigma$ transitions and thereby provides optical pumping into one magnetic sublevel of the $S_{1/2}$ state. For this the laser beam must point along the magnetic field axis. In the experiments presented here, two different magnetic field configurations have been used (the motivation for this is detailed in Appendix A.3). In the first configuration, which was used for single ion experiments, the magnetic field points along the $x'$-axis (B1) and is produced by the coil[4] Cx. The other coils are used to null all external magnetic fields perpendicular to $x'$. Accordingly, the 397$\sigma$ light was directed along the 397$\sigma$1 channel. For two-ion experiments, another configuration (B2), where the magnetic field points along a 45° diagonal axis in the $x'$-$y'$ plane, was used. The field B2 is produced by the coil Cd. Perpendicular fields were compensated for with the help of the vertical coils (Cz1&Cz2) and Cy. The latter has a contribution along the Cd axis, which slightly complicates the magnetic field compensation procedure. In this configuration, the 397$\sigma$2 channel is used for optical pumping.

One arm of the vessel is used for all equipment related to the vacuum. The different elements are "IGP"- ion getter pump, "TSP"- titanium sublimation pump, "VG"- pressure gauge[5] and "V"- full metal corner valve. The latter was used to connect a turbo pump for the bake-out.

In a first design, some of the vessel's conventional viewports were replaced by quartz substrates of high optical quality and anti-reflection coated for 397 nm. The purpose of this

[3] LORCH Microwave, digital phase shifter.
[4] For notational simplicity, the prime is not used in labels, writing, for example, Cx instead of Cx′.
[5] Varian UHV-24 Ionization Gauge

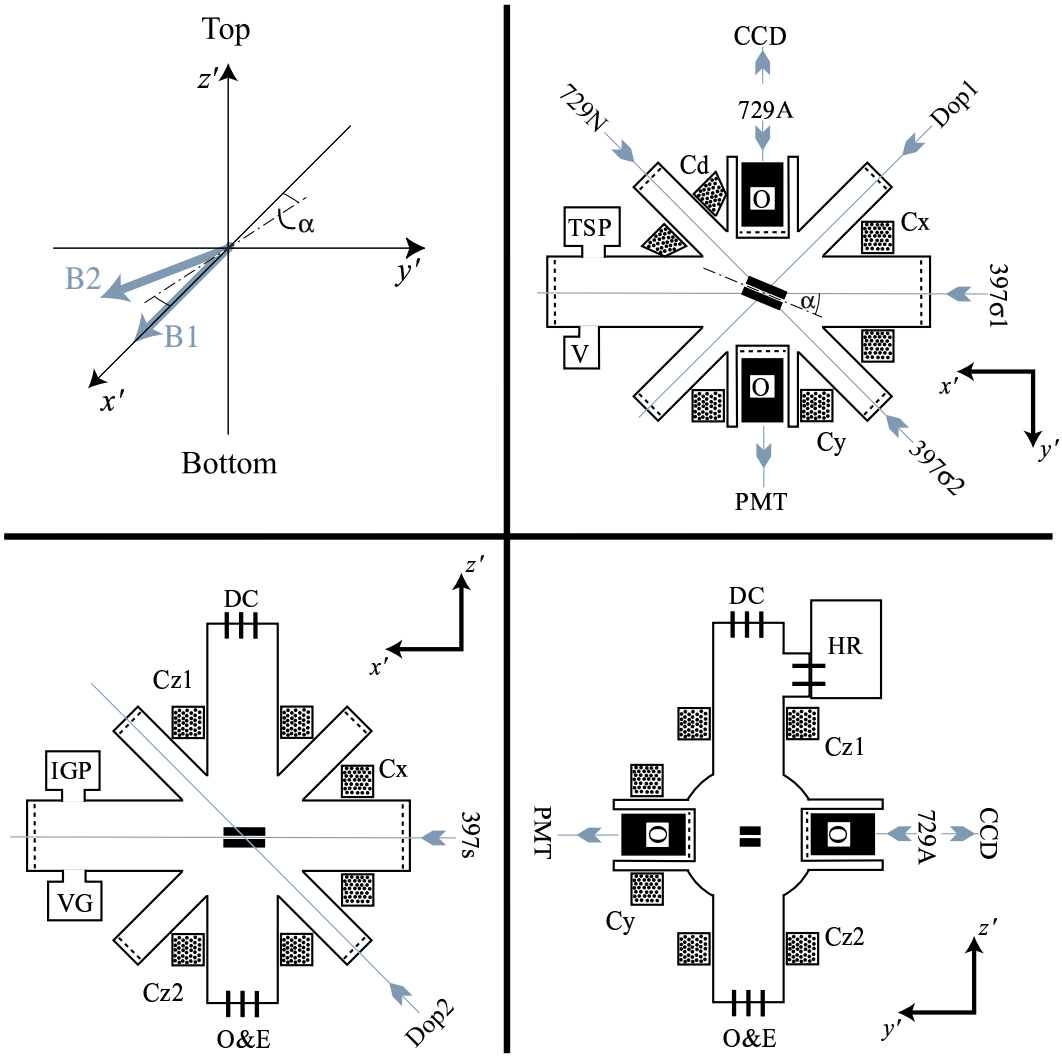


Figure 5.7: Schematic of the vacuum vessel and laser channels. Dashed lines indicate optical viewports while all other ports are used as electrical feed-throughs.

was to reduce stray light when the ions' fluorescence is detected and thus speed-up the qubit read-out. Helicoflex® seals were used for this purpose. Unfortunately, most of those windows were carved in by the sharp blades of the seals and broke during bake-out. Probably suitable seals could be fabricated but we found the personnel of Helicoflex®, respectively its distributors, fairly unwilling to consider the case. Consequently, these windows were replaced by conventional quartz viewports anti-reflection coated for 397 nm.

With the old trap we observed that at background pressures of several $10^{-10}$ mbar even permanently cooled ions sometimes spontaneously left the trap, while at $1 \cdot 10^{-10}$ mbar (which was the best achieved) this happened only rarely. However, even at $1 \cdot 10^{-10}$ mbar, ions would still get lost within about 15 minutes when left uncooled. We conclude that pressures in the

$10^{-11}$ mbar range are recommendable and make experimental work easier.

Therefore, special care was taken in the design and bake-out of the new setup in order to achieve a good vacuum. The vessel was baked out at 320°C for four days with the quartz viewports replaced by blanks as they are only specified to a maximum temperature of 200°C. All baking out was carried out in a self-built computer-controlled 1 m×1 m×1 m oven which has been optimized for a homogeneous temperature distribution. Furthermore, temperatures were always ramped up or down slowly at ±7°C per hour. Next, the quartz-viewports were installed. During this procedure, the vessel was permanently vented with nitrogen at a slight overpressure in order to exclude ambient air. In a second session the vessel was then baked out at 200°C for four days.

The final pressure is below the range of the pressure gauge, i.e. below $2 \times 10^{-11}$ mbar. No background-pressure-related loss of ions has ever been observed during permanent laser cooling. The trapping stability of uncooled ions has not been studied systematically. However, sometimes trapped ion samples were left uncooled for several (up to eight) hours, without ion loss. It has thus been possible to work up to 100 hours continuously with the same ion sample.

The drive voltage for the Paul trap is generated using a helical $\lambda/4$-resonator, denoted "HR". Helical resonator design is discussed in Appendix A.2. Unlike earlier vessel designs, a separate feed-through was used for the connection of the helical resonator to the trap in order to avoid possible RF pick-up on the DC-voltage leads through capacitive coupling in a common feed-through. For the same reason, the leads for DC-voltages from the feed-through ("DC") to the trap were coaxially shielded (cf. Fig. 5.4).

The ovens and the electron guns (two of each) are mounted directly onto their feed-through ("O&E"). Each oven consists of a thin-walled 1.8 mm diameter stainless steel tube which is heated by sending an electric current through and which is directed towards the trap center. The atomic calcium beam is screened by an additional, short 4 mm diameter tube placed over the end of the oven tube. This produces a beam with an angular divergence of 17°. The screening tube has a distance of 1.5 cm from the trap center, where the atomic beam then has a diameter of 6 mm. Oven designs are discussed in more detail in the diploma thesis of Daniel Rotter [86].

The elements denoted "O" in Fig. 5.7 are microscope objectives[6]. They have a working distance of about 65 mm and are therefore mounted into inverted viewports to place them close enough to the trap center. One objective collects fluorescence for the photomultiplier[7] (PMT). The trap center region is imaged to a focal plane about 45 cm from the objective. At that point in front of the PMT the image is spatially filtered by a diaphragm consisting of four individually adjustable blades. In this way the rectangular aperture can be adjusted for maximum fluorescence and minimum scattered light at 397 nm. Ideally, only light at 397 nm is to be detected. In particular, addressing light at 729 nm which hits the PMT head-on must be suppressed. The bialkali photo cathode by itself already strongly suppresses light above 650 nm and below 300 nm, while at 397 nm it has a specified quantum efficiency of 28%. Additionally, the PMT window is covered by stained glass filters, type BG39 and BG3. In order to reduce reflective losses all filters have been anti-reflection coated for 397 nm.

[6] Nikon MNH-23150 ED Plan 1.5x
[7] Electron Tubes, PMT type 9111.

The BG39 filter strongly suppresses light above 650 nm, while most light in the visible range (480-680 nm) is filtered out by the BG3 glass. The latter is used to allow for working on the experiment with some normal room light on.

The other objective images the ions onto the CCD camera[8]. In previous experiments the camera was always read out continuously. It served only for the experimenters to monitor the ion crystal. We recently started to read out the camera locally at the ion positions (see section 7.4), gate the read-out and synchronize it with pulsed experiments. This is important when conditional dynamics and quantum algorithms are performed with two or more ions. It is likely that the read-out of pixel arrays associated with different ions will eventually replace the PMT.

## 5.5 Addressing Optics

To address the ions with 729 nm light we use the same viewport and objective as for imaging the 397 fluorescence light onto the CCD. As can be seen in Fig. 5.8, we use a telescope-like imaging system consisting of two lenses, L1 (f=25 mm) and L2 (f=500 mm), and an electro-optic deflector[9] (D) to tailor the 729 nm beam and to steer the focus at the ion position. The

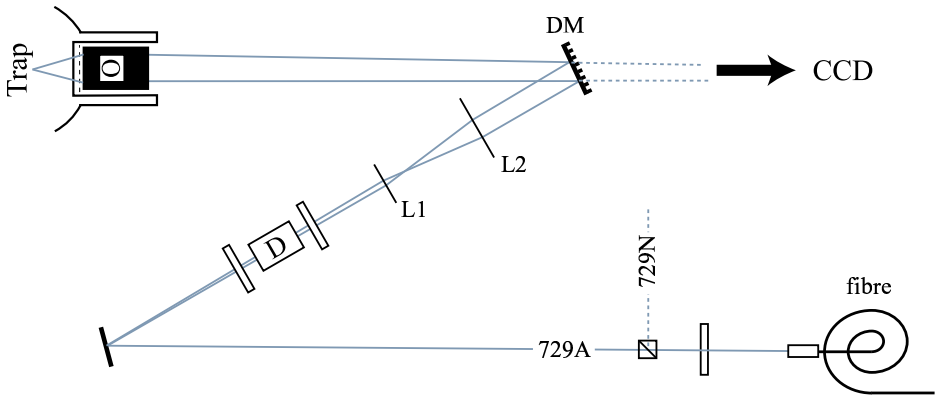


Figure 5.8: Addressing optics setup. For a legend see Fig. 5.5, cf. also Fig. 5.7. DM is a dichroic mirror which has a high reflectivity at 729 nm and a high transmission for 397 nm light.

quality of the focus profile at the ions is determined by the aberrations of all optical elements. This includes the lenses, the objective, the viewport window, the deflector, mirror surfaces and the $\lambda/2$ plates. These aberrations typically lead to a deviation from a Gaussian focus profile. While a large fraction of the light still goes into the Gaussian center part, the rest forms a more weakly focussed and often irregular background. It is this background which typically limits the quality of our addressing. The present system leaves some room for improvement. Some of this improvement, however, will involve major changes like an objective placed inside the vacuum chamber.

[8]Princeton Instruments I-PentaMAX
[9]Laser Components, ED 2-730

Another issue besides optimizing the quality of the optics is the question, how many ions can be addressed in principle by such a setup. An analysis of the ideal (aberration free and diffraction limited) system has been performed. One interesting result is that all parameters of the imaging system drop out of the equations. This includes the fiber collimator, the telescope and the objective as well as their spatial arrangement. The crucial equation for the displacement $d_F$ of the ion focus per voltage applied to the deflector is

$$d_F = \frac{\pi}{\lambda} w_D w_F \alpha, \tag{5.2}$$

where $\alpha$ is the angle (per voltage applied) by which the deflector bends a beam; $w_D$ is the waist of the beam where it passes through the deflector, while $w_F$ is the waist of the laser focus at the ion position (trap center). $w_D$ is limited by the aperture $a$ of the deflector. Looking at the specifications of our (and other) deflector type(s), one finds that for different models, $a \cdot \alpha$ is essentially a constant which is determined by the type of deflector crystal. Apart from better electro-optical crystals, which may be developed in the future, this sets an upper limit of $w_D \cdot \alpha \approx 4\ \mu\text{m}\cdot\text{kV}^{-1}$. Substituting this value into eqn. (5.2) one finds that for a given wavelength $\lambda$, $d_F$ is proportional to $w_F$. This, however, means that the number of ions which can be individually addressed with such a system is independent of how close the ions are (there is, of course, a limit because $w_F$ can not be smaller than the absolute diffraction limit $\lambda/2$). If we assume that for reasonable addressing, the distance $\triangle_i$ between two neighboring ions[10] should be four times $w_F$, one finds with $\lambda = 729$ nm, that

$$\frac{d_F}{\triangle_i} = 2.2\ \text{kV}^{-1}.$$

The requirement of fast switching, as well as the electric breakdown specifications of the deflector set a limit of about $\pm 1$ kV to the deflector voltage. Thus this type of system allows for the addressing of about five ions. Deflectors with larger aperture permit higher voltages. Optimizing the system with present day technology would probably enable the addressing of up to 10 ions. Thus for the near future, the experiment is not limited here.

[10] In reality the ions in a linear crystal are not exactly equidistant (cf. section 3.2.1) but the assumption is valid here.

# 6 Operating the Trap

This chapter describes the typical procedures of loading the ion trap and adjusting the trap parameters, in particular the compensation of stray electric fields. For the first two and a half years of this Ph.D. work, ions were produced by bombarding an atomic Ca beam with an electron gun, as in essentially all other experiments (cf. section 6.4). It will become clear in sections 6.1 to 6.3 that the electron impact ionization method has several disadvantages, for example a charging up of surfaces near the trap center, causing severe experimental problems. To cure these problems, a setup for resonant photoionization was developed consisting of two diode lasers, see section 6.4. This development has allowed for efficient trap performance, without which the experiments presented here would not have been possible. In fact, loading by photoionization was used for all experiments presented in this thesis. Electron beam ionization is nevertheless discussed in the following chapters in order to make clear where its disadvantages lay.

## 6.1 Trap Loading

Calcium ions produced in the trapping volume are cooled by the Doppler laser beams and crystallize into their equilibrium positions. Ion numbers of several hundreds have been crystallized in the new trap and various three dimensional crystal structures were observed. The experiments detailed in this thesis focus on (linear) crystals of up to three ions. CCD pictures of ion crystals are shown in Fig. 6.1.

RF-drive powers of up to 15 W were used resulting in radial trap frequencies $\omega_{r0}$ of up to 5.0 MHz. At these relatively high input powers, the whole resonator (including the trap) heats up. As a consequence, the resonance frequency of the system drifts down from 23.505 MHz (at low drive powers $< 2$ W) to 23.450 MHz (at 15 W). This process extends over about 40 minutes. A second effect of the heating-up is that the position of the trap center is shifted, which can be clearly observed by a displacement of the ion image on the CCD camera. The main shift of about 80 $\mu$m occurs on the same time scale as the $\lambda/4$ resonance shift. The trap center (hence the ion), however, keeps moving at a rate of approximately 1 $\mu$m per 15 minutes for a few hours before being stable. This long term process is probably due to a very slow heat transfer from the RF-electrodes to the ceramic support structure and from there to the stainless steel rods on which the trap is suspended. Precision experiments that require individual ion addressing can only be carried out after such thermal drifts have subsided since the focus of the addressing laser is as small as 2.5 $\mu$m.

According to eqn. (3.8), if a radial trap frequency $\omega_{r0}$ of 5.0 MHz is obtained at a RF drive frequency of $\Omega/2\pi = 23.5$ MHz, the stability parameter is $q = 0.60$. We have observed that at drive powers higher than 15 W the trapping of a single ion appears to become unstable.

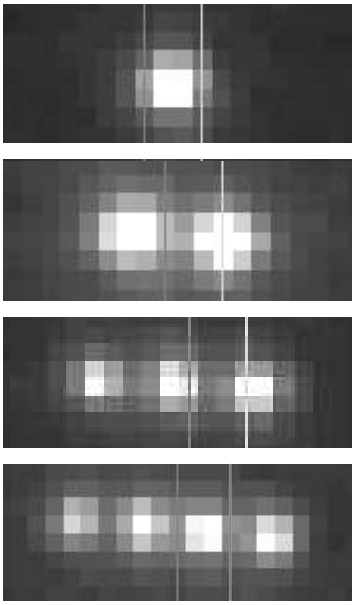

Figure 6.1: Fluorescence images on the CCD camera of a single trapped ion as well as a linear two-, three- and four-ion crystal taken with an exposure time of about two seconds. The axial trap frequency $\omega_z$ was $2\pi \cdot 1.01$ MHz (end-cap voltage $V_{cap} = 700$ V), corresponding to ion distances $\triangle z_{min}$ (cf. section 3.2.1) between 4 $\mu$m and 6 $\mu$m (characteristic length $l = 4.4$ $\mu$m). On the CCD camera the ions appear closer since they are observed under an angle of 67.5° with respect to the trap axis, cf. section 7.4.

For two ions, these instabilities already begin at a drive power of 13 W. Instabilities appear as an occasional melting-up of the ion-crystal. Re-crystallization of the ions is then difficult with the ions sometimes even leaving the trap. These effects are accounted for by trapping instabilities due to nonlinear resonances (cf. section 3.1).

When loading the trap by electron impact, in principle all atoms and molecules present in the trap volume - including those from the background gas or impurities in the atomic Ca-beam - can be ionized and trapped. These impurity ions can be seen as dark spots in the ion crystal and have been observed in the new as well as in all previous setups [51].

It was also observed that the new trap was particularly stable compared to other Ca-traps previously used in Innsbruck, like the old linear trap or ring traps [4]. This manifests in long storage times and is, at least partially, due to the improved vacuum (cf. section 5.4). It is also possible that the different trap construction (end-caps made as tips instead of rings around the RF electrodes) contributes to the improved performance. Further analysis of this assumption would require numerical simulations. The enhanced trapping stability represent a significant advantage since it takes about an hour to reload the trap and re-adjust all parameters. Moreover, for reloading the trap with electron impact ionization, the drive power must be reduced significantly. This is probably due to trapping instabilities (cf. section 3.1) leading to a reduced volume of stable trapping at strong RF drive. The momentum transferred to an

ion by the ionizing electron impact may kick the ion out of the stable trapping volume. In practice ions had to be loaded into a weak trap of about 500 kHz radial and 200 kHz axial frequency. Subsequently, the trapping potential is ramped up and several hours of waiting are required before thermal drifts of the trap have completely subsided.

## 6.2 Compensation of Micromotion

If, on top of the RF quadrupole field, electric DC fields in the radial direction are present at the trap center, then those DC fields will shift the ions from the RF-node into a region of enhanced RF-drive. This results in enhanced micromotion which, via the Doppler effect, modulates the coupling of the ion to the laser fields. This has several negative effects [4], [52], for example, an effective broadening of the Doppler cooling transition resulting in an increased cooling limit temperature.
There are two different origins for radial stray fields and these can be distinguished as:

- "charge fields" which are created by localized surface charges on trap electrodes and support structures.
- "geometric fields" which are due to geometric imperfections of the trap construction, in particular a misalignment of the end-caps with the trap axis (as defined by the RF-electrodes).

There are two major differences between these two sorts of unwanted fields:

First, charge fields are independent of the trap voltages while geometric fields have a contribution proportional to the end-cap voltage. This effect is shown in Fig. 6.2 where the voltages necessary to compensate for vertical and horizontal stray fields are plotted versus end-cap voltage. Methods to determine the appropriate compensation voltages are described below. Even geometric fields are independent of the RF amplitude as the nodal line of the RF quadrupole field remains unchanged if the RF amplitude is varied.

Second, geometric fields are reproducable whilst charge fields change between two experimental runs or even within one experimental session. This is due to the deposition of new charges on insulating surfaces in the trap loading process by electron impact ionization and slow migrations of these charges which we have observed to take place on the time scale of hours. Accordingly, the compensation procedure had to be renewed several times after electron impact ionization. At first, one might assume that charges deposited on the metallic surfaces of the trap electrodes will immediately be conducted away. There are, however, small patches of oxides even on thoroughly cleaned steel or molybdenum surfaces where electrons can be localized [87]. Moreover, oxides can form from metallic calcium depositions within a few days even in a vacuum environment of $10^{-11}$ mbar [88].

There are four different methods that have been used in the presented experiments to *compensate micromotion* (see also [4]):

- *Position compensation.* Here, the position of an ion, viewed on the CCD camera, is observed while the strength of the RF potential is varied. If the micromotion compensation is good, i.e. there are no DC fields at the trap center, then the position of the ion remains the same under this variation of RF power. If not, the ion moves away from the

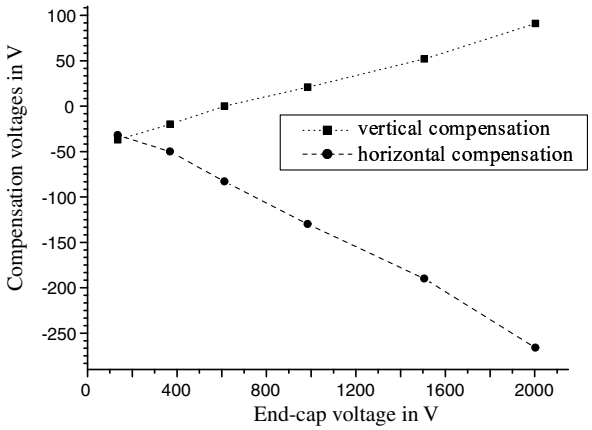


Figure 6.2: Compensation protocol of one ramping-up procedure of the trap. The two sets of voltages were fitted linearly like $V_{comp} = V_{offset} + cV_{end-cap}$. The results are $V_{offset} = -44.5$ V, $c = 0.0667$ and $V_{offset} = -7.7$ V, $c = -0.126$ for the vertical and horizontal compensation, respectively. The $c$-values, related to geometric fields, are constant as long as the trap geometry is stable, while the $V_{offset}$, related mostly to charge fields, change with every trap loading procedure.

trap center in the direction of the DC field as the radial potential is lowered and vice versa. Starting from the strongest possible RF potential and marking the position of the ion, the radial potential is subsequently lowered and at each step the ion is pushed back to the marked position with the help of appropriate voltages on the compensation electrodes.

- *Linewidth compensation.* The width of the $S_{1/2} \leftrightarrow P_{1/2}$ transition at 397 nm is broadened by micromotion sidebands. The corresponding method of compensation is to tune the laser at 397 nm to the red side of the resonance fringe (by slightly more than half a linewidth) and to optimize the compensation voltages for *minimal* fluorescence at this point. The underlying effect is that narrowing the linewidth increases the fluorescence rate on resonance but decreases fluorescence on the outer fringe whilst the total line strength remains constant. The laser at 397 nm must be desaturated otherwise the linewidth is dominated by power broadening.

- *Correlation compensation.* The back and forth movement of an ion with the drive frequency $\Omega$ causes the scattering rate to be modulated at the same frequency via the Doppler effect. The compensation method works best where the photon scattering rate depends strongly on the detuning of the laser, i.e. if the laser at 397 nm is tuned to the point of the steepest gradient of the fluorescence curve. Once again, saturation broadening of the transition must be avoided. The signal is obtained in form of a histogram of photon counts with respect to the RF phase. Although the total scattering rate, being $\sim$ 60 MHz at that point of the fluorescence curve, is larger than the RF frequency of 23.5 MHz, the average number of photons collected in one RF period is much smaller than 1 as only about 1/2000 of all scattered photons are collected and

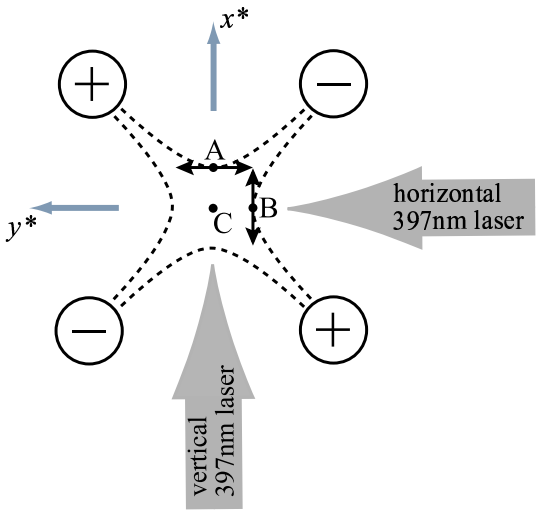


Figure 6.3: Cross section of a linear rod trap. The dashed lines respresent the quadropole field along which micromotion takes place. C is the the trap center. A and B are vertically and horizontally displaced ion positions caused by stray fields pointing in the same respective directions.

detected. Therefore a time counting method is applied in which a time interval counter[1] is triggered by the arrival of a count pulse from the photomultiplier and stopped by a pulse synchronized to the RF drive frequency. From 10000 measurements, each obtained from a single photon count, a histogram of time intervals is built up. A reasonable signal, i.e. a visible modulation in this histogram, is obtained only if the stray light background is at least five times smaller than the fluorescence count rate. If a signal is observed, i.e. the histogram is not flat, one tries to minimize this modulation in the histogram by tuning the compensation voltages.

- *Micromotion sideband reduction.* On the $S_{1/2} \leftrightarrow D_{5/2}$ transition at 729 nm, motional sidebands (including micromotion sidebands at a frequency $\Omega$ away from the carrier) can be resolved. The method consists in minimizing these sidebands by tuning the compensation voltages.

Position compensation is the crudest method, linewidth compensation is more sensitive whilst correlation compensation and micromotion sideband reduction are the most sensitive techniques. They allow the compensation voltages to be determined to within about 1%.

Two important features of stray field enhanced micromotion shall be discussed:
1) *A radial stray field pointing in some direction $\overrightarrow{e_s}$ will, in general, lead to micromotion in some different direction $\overrightarrow{e_m}$.* Fig. 6.3 illustrates a typical situation: the directions $x^*$ and $y^*$ open for optical access are tilted by 45° with respect to the connection lines between diagonally opposite electrodes. A *vertical* stray field displaces an ion in the same direction, for example to position A, where it undergoes *horizontal* micromotion. Hence in this case the two

[1] SR620, Stanford Research Systems

directions $\overrightarrow{e_s}$ and $\overrightarrow{e_m}$ are actually perpendicular to each other. This horizontal modulation will now be "seen" best by the horizontal laser. For the laser-based compensation methods (linewidth compensation, correlation compensation and micromotion sideband reduction) this means that a signal obtained with a *horizontal laser* illuminating the ion(s) is associated with the *vertical stray field component* and accordingly has to be corrected with the vertical compensation electrode.
2) *In order to increase the amplitude of micromotion caused by some stray field, the RF-drive power has to be decreased.* An increased amplitude, i.e. an enhanced micromotion modulation is particularly desirable in the case of correlation compensation, where we found that a good correlation signal could only be obtained by turning down the RF-drive significantly. For example from the typical working parameters of the new trap - 15 W RF power and 600 V end-cap voltage leading to axial and radial trap frequencies of 1 MHz and 5 MHz respectively - the RF power had to be turned down to about 1.5 W in order to see any correlation signal. The fact that the RF-modulation amplitude goes *up* when the RF drive is turned *down* is counterintuitive and therefore a short derivation of this effect is given here: The spring constant associated with the *macromotion*, i.e. the secular motion at a frequency $\omega_{r0}$ is proportional to $1/\omega_{r0}^2$. From eqns. 3.8 and 3.2 it follows that $\omega_{ro} \propto V$, the amplitude of the RF voltage. This means that a given constant force $\mathbf{F} = e\mathbf{E_s}$ caused by some radial stray field $\mathbf{E_s}$ displaces the ion radially from the trap axis by

$$r_d \propto \frac{1}{V^2} \; . \tag{6.1}$$

The amplitude $A(r)$ of the ion's *micromotion* at some distance $r$ from the trap center is proportional to the amplitude $E_Q(r)$ of the quadrupole field at this distance. The amplitude of the quadrupole field is simply the gradient of the quadrupole potential of eqn. (3.1) and it is straightforward then to derive that

$$E_Q(r) \propto rV \; . \tag{6.2}$$

Hence, a given stray field $\mathbf{E_s}$ causes a displacement $r_d$ which leads to enhanced micromotion of amplitude (eqn. (6.1) into (6.2))

$$A(r) \propto \frac{1}{V} \propto \frac{1}{\sqrt{P}} \; .$$

This means that to *increase the micromotion modulation* caused by a given stray field one has to *decrease the RF-drive power* $P$.

## 6.3 Patch effects

It was found after the first few months of good operation of the new trap (using electron gun ionization) that charge fields became increasingly dominant. At first, micromotion compensation became more and more difficult and time consuming as after every loading stray fields were completely different in an arbitrary way. Soon stray fields were so large that they could not be nulled any more, even with compensation voltages of up to 2000 V. Observation of ion motion on the CCD camera under variation of the axial and radial trap frequencies (just as in position compensation) allows a quite accurate estimate of the magnitude of those stray fields. With this method it was found at some point that in order to compensate the given stray fields, compensation voltages of several ten thousand volts would have been necessary. It should be mentioned that such effects are not particular to our setup but have occurred in other experiments [64, 89] and caused serious problems there, in some cases even bringing the experiment to a complete halt.

The ceramic support structures of the new trap are further away from the trap center than the compensation electrodes and their surface is greatly reduced with respect to the old trap. This led to the conclusion that such strong stray fields could not be produced by charges on the ceramics but must stem from charges on surfaces much closer to the trap center, i.e. on the RF electrodes or on the end-caps. The fact that the trap had been operating nicely over the first months and that the background pressure of the vacuum chamber had always been as good as $10^{-11}$ mbar suggested that the patches on which charges were localized had to be (oxidized) depositions of material from the oven beam. An optical port (beam channel Dop2) was used to observe the trap from below, where the oven beam hits the RF electrodes. There was indeed a 6 mm diameter round patch of of (grey) calcium deposit visible, distributed over two blades and just touching the tips of the end-caps. Evaporating this patch by laser heating was the only option to solve the problem without opening up the vacuum system. For this, the argon ion laser was used. The laser beam was used unfocussed with a diameter of about 2 mm in order not to produce too much local heat which might melt the steel. A CCD camera was installed to monitor the beam position on the trap. The light power was ramped up in steps until an increase in vacuum pressure was observed indicating the evaporation of material. Bursts of gas were observed at several discrete light power levels, on the order of a few Watts, probably corresponding to the evaporation of different types of material. The beam was scanned slowly over all patched areas at each of these power levels. The maximum laser power applied was 10 W. After that, all visible depositions were gone. It was found in the next experimental run that, indeed, the patches had been evaporated successfully and that the trap could be operated normally again. Before storing ions again, however, a setup for resonant photoionization to replace electron impact ionization was prepared in order to avoid patch problems in the future. This setup is presented in the following section.

## 6.4 A New Trap Loading Scheme by Photoionization

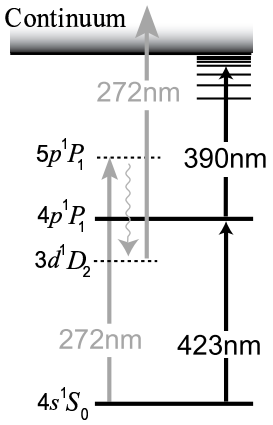


Figure 6.4: Atomic Ca.

Resonant photoionization can cure many experimental problems as described in the previous sections of this chapter: There is essentially *no charging up* of surfaces due to the loading process as the number of free electrons produced is negligible compared to the number necessary for ionization by electron impact. *No more impurity ions* are produced as, due to the resonant nature of the process, only atomic calcium will be ionized. In fact, our photionization scheme is even isotope selective, as will be shown below. Essentially, *no patches* of material from the oven beam are deposited *on the electrodes*. The reason for this is that photoionization is so much more efficient than ionization by electron impact that the atomic calcium flux could be greatly reduced (see below). The levels of atomic calcium relevant for the resonant photoionization are shown in Fig. 6.4. In fact, photoionization for loading a Paul trap has been demonstrated previously by Kjærgaard *et al.* [65] (grey arrows in Fig. 6.4). These authors use a resonant transition at 272 nm followed by a spontaneous decay and an excitation with the same light at 272 nm far into the continuum. In our scheme (black arrows in Fig. 6.4), the resonant excitation from the $4s^1S_0$ ground state to the $4p^1P_1$ state ($\Gamma_{nat} = 34.7$ MHz) at 422.791 nm (vacuum wavelength, from tables in [90]) is directly followed by an excitation with light at about 391 nm to Rydberg states from where the atom is field-ionized by the varying electric fields present in the trap volume at any given time. The primary advantage of this scheme is that the wavelengths are accessible to room temperature laser diodes which have been commercially available for two years[2]. The setup consists of two laser diodes in Littrow configuration. Details are presented in [86, 91]. The laser light at 272 nm in the experiment of Kjærgaard *et al.* had to be produced by a frequency doubled argon ion laser pumped dye laser which requires significant cost and maintenance as compared to diode lasers[3].

For the second step the exact wavelength from the $4p^1P_1$ level to the continuum threshold is 389.808 nm - again taken from the tables in [90]. Exciting high lying Rydberg levels which are subsequently field ionized can yield a higher ionization cross section than direct excitation into continuum [92]. Moreover, the efficiency of direct excitation into continuum decreases even more the further the exciting laser aims above continuum threshold. For the electric fields present in the trapping volume which are on the order of 1000 V/cm, the highest ionization efficiencies were expected roughly around 391 nm [92], which corresponds to the excitation of Rydberg states with principal quantum number $n \approx 30$ [86]. The strongly varying fields in the trap "wash out" all resonant structures hence the wavelength of the second step laser is expected not to be critical within $\pm 0.5$ nm around 391 nm.

In the test phase of this scheme, a variety of calcium crystals and clouds ranging from single to several thousands of ions were loaded into the trap. After optimizing the wavelength of

[2] Nichia Co., Japan.

[3] It should be mentioned that in the experiments of [65] the laser system for 272 nm was available anyhow because light in that wavelength range is used in the Aarhus labs for magnesium spectroscopy.

the first step (423 nm) laser for maximum ion production, the wavelength was measured with the wavemeter. The measured value of 422.792(2) nm (vac.) is in very good agreement with the value reported in literature (see above). The other laser was varied between 390.5 and 391.4 nm with ionization occurring at any wavelength.

Quantitative measurements of the ion yield [86, 91] show that photoionization is over five orders of magnitude more efficient than the electron bombardment method, hence patch effects can be greatly reduced. Due to this and the negligible amount of stray electrons the introduction of photoionizationis has lead to considerably more stable stray field compensation voltages, see [86] for a detailed account.

There is a peculiar feature of photoionization which has never been observed with electron gun loading: Ions only appear on the camera and photomultiplier one after the other over the course of minutes after the ionization lasers are blocked. This suggests that ions are produced in higher orbits (corresponding to certain electric field strengths) where they are outside the Doppler cooling beams hence do not fluoresce. Ions produced by electron impact do not seem to be stable in such higher orbits, probably due to the larger momentum absorbed in the ionization process. In addition, photoionization allows direct loading into a tight trap which is most likely also due to the smaller momentum transfer in the ionization process.

Working with a well compensated crystal of two or more ions is impossible with electron gun ionization. This is because in order to achieve a high micromotion modulation (hence a good compensation signal) the RF drive of the trap has to be turned *down* significantly (see section 6.2). Doing so with two ions it shows that at the onset point of, for example, a correlation signal the radial trap frequency has become so weak, that the ions flip into a configuration where they are placed perpendicular to the trap axis. In this configuration, the ions encounter strong RF fields of opposite phases, thus the correlation signal disappears. The only solution is then to determine the compensation voltages with one ion in the trap and then load two ions. This is possible with photoionization while with electron impact ionization the new loading would make the just determined compensation values obsolete.

At every loading run we have only ever seen pure crystals, never any non-fluorescing ions. In a separate experiment [86] an atomic Ca beam was illuminated with 423 nm light. The emitted fluorescence was observed with a photomultiplier while the laser at 423 nm was tuned over the resonance, see Fig. 6.4. Five clearly resolved resonances, each corresponding to a different calcium isotope ($^{40}$Ca, $^{42}$Ca, $^{43}$Ca, $^{44}$Ca, $^{48}$Ca), were observed [86,91], which proves the ability of isotope selective photoionization. Consequently, isotopes other than $^{40}$Ca can be loaded into the trap, even if they have a somewhat low abundance in the oven sample. This option is particularly interesting for $^{43}$Ca which is a promising future qubit candidate, cf. chapter 9.

# 7 Experimental Results: Prerequisites

## 7.1 Spectroscopy on the Qubit Transition

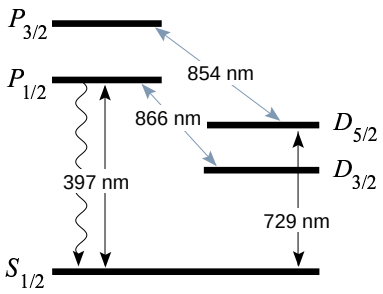


Figure 7.1: Optical transitions of interest in $^{40}Ca^{+}$.

Fig. 7.1 recalls the $^{40}Ca^{+}$ level scheme and the transitions driven by lasers in the experiment. In an experimental run, the lasers for Doppler cooling (397 nm and 866 nm) as well as the lasers at 729 nm and 854 nm are first adjusted for optimum spatial overlap with the ion(s), spectral detuning and light power. This is done in a continuous fluorescence observation mode. The procedures have been discussed in the theses of Hanns-Christoph Nägerl [51], Christian Roos [4] and Harald Rohde [52]. In contrast to continuous excitation, coherent manipulations on the qubit transition $S_{1/2} \leftrightarrow D_{5/2}$ are done in a pulsed mode. Fig. 7.2 shows a generic pulse sequence used to interrogate this transition. The sequence starts with 2 ms of Doppler cooling. At the end of this period, a short pulse of 397 nm $\sigma^-$ polarized light is applied which prepares the ion(s) in the Zeeman sublevel $S_{1/2}, m = -1/2$. Following next is the period of coherent manipulations on the $S_{1/2} \leftrightarrow D_{5/2}$ quadrupole transition. The series of pulses at 729 nm applied in this period will be referred to as the "probe sequence". During this time, all other lasers are off, with the exception of 866 nm light. This is allowed, as the latter does not couple

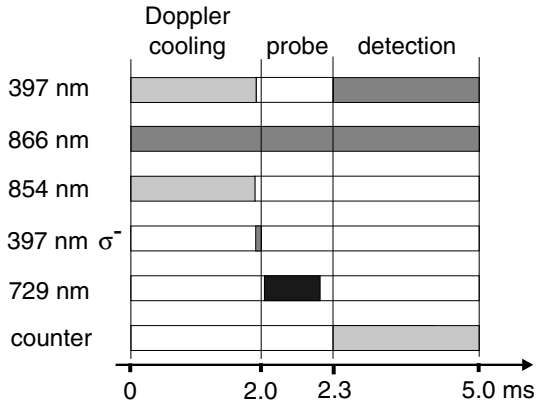


Figure 7.2: 5 ms pulse sequence for coherent dynamics. Different grey scales for the same laser indicate different laser powers.

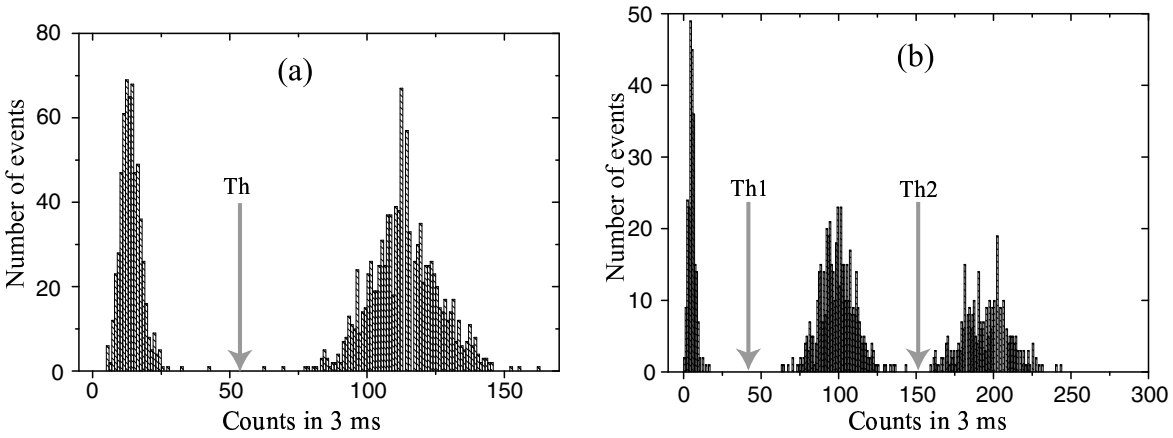


Figure 7.3: Fluorescence histograms of (a) a single ion and (b) a two-ion crystal. The grey arrows indicate where thresholds would be set for fluorescence discrimination. The average count rate per ion in (a) is slightly larger than in (b) because the 397 nm laser was detuned closer to resonance. In (b), above Th2 both ions fluoresce, thus are in the $S_{1/2}$ state. Between the two thresholds only one ion fluoresces, while the other is dark (thus in $D_{5/2}$). Below Th1 finally, both ions are in the $D_{5/2}$ and only scattered light is detected.

to the quadrupole transition (cf. section 7.3).

The overall sequence finishes with the detection period where the electron shelving technique (cf. section 3.3.1) is applied to determine the quantum state of the ion. For this, the $S_{1/2} \leftrightarrow P_{1/2}$ dipole transition is again driven. This way the ion is either projected into the $D_{5/2}$ state or cycles on the $S_{1/2} \leftrightarrow P_{1/2}$ transition. In the first case, the ion is dark to the laser radiation and hence only stray light at 397 nm is collected on the PMT, with count rates of approximately 2 kHz. If, however, the ion cycles on the $S_{1/2} \leftrightarrow P_{1/2}$ transition, a flourescence rate of 35 to 40 kHz (per ion) is obtained. This yields a very good discrimination ($> 99\%$) between "ion fluoresces"($\Leftrightarrow S_{1/2}$) and "ion dark"($\Leftrightarrow D_{5/2}$) within the 2.7 ms of detection time. Fig. 7.3(a) shows a single ion histogram of photomultiplier counts collected over many experimental sequences. In this case, the ion was excited resonantly at 729 nm during the probe period. A threshold Th is set between fluorescence ON and fluorescence OFF.

We typically perform 100 such experiments with the same parameters to record one data point. The latter is calculated as the fraction of fluorescence OFF events. It represents the $D_{5/2}$ state probability and will be denoted $P_D$ in the following. Note that in the Doppler cooling period, 854 nm light is on. This is done to repump a possible $D_{5/2}$ state population (from the previous sequence) to $S_{1/2}$.

The short 5 ms pulse sequence has the advantage that recording one data point only takes about 700 ms, including the setting of various devices and their communication with the control computer. It is used as long as motional ground state cooling is not required. Moreover, as it is not synchronized to the power line frequency of 50 Hz, the effective magnetic field fluctuations (during the probe periods) are somewhat larger if line synchronous fluctuations

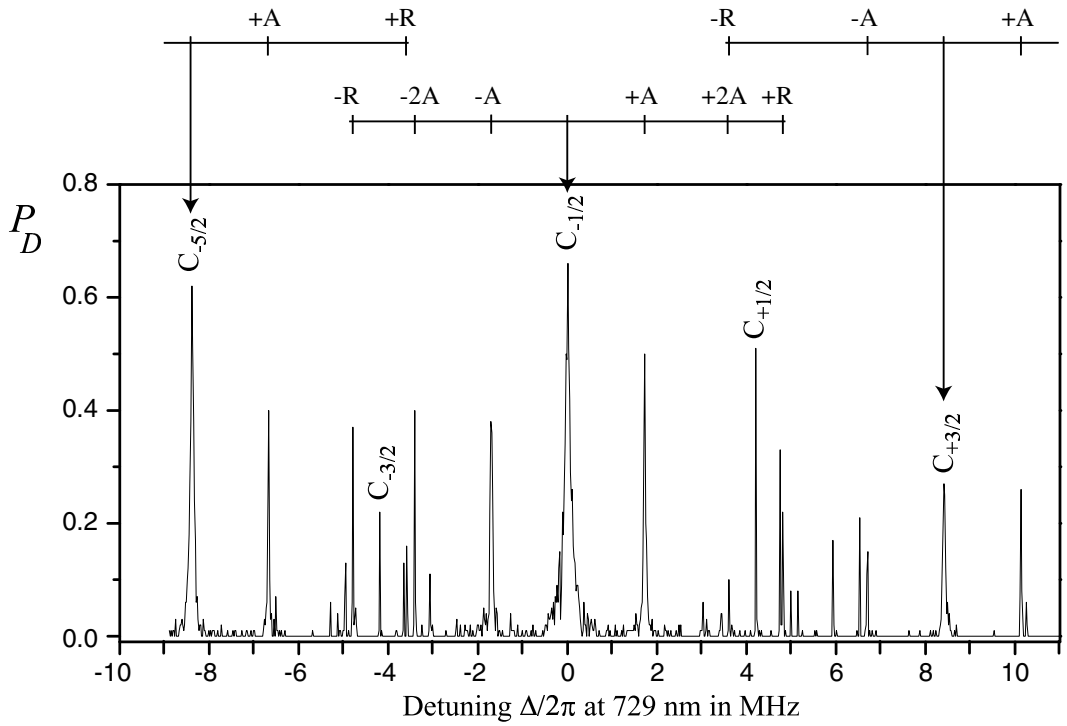


Figure 7.4: Single ion excitation spectrum on the quadrupole transition. The five carrier transitions $S_{1/2}(m = -1/2) \leftrightarrow D_{5/2}(m')$ are denoted by $C_{m'}$, where $m' = \{-5/2, -3/2, -1/2, +1/2, +3/2\}$. They are split by a magnetic field of 2.50 Gauss. Axial sidebands are labeled by A, radial sidebands by R; + signs indicate blue sidebands while − signs refer to red sidebands. For this scan, the axial frequency was tuned to $\omega_z = 2\pi \cdot 1.715$ MHz by applying an end-cap voltage of $V_{cap} = 2000$ V. On the strongest carrier $C_{-1/2}$ also higher order axial sidebands ($\pm$2A) can be seen. The radial trap frequency is $\omega_r \simeq 2\pi \cdot 4.9$ MHz. The transitions $C_{-3/2}$ and $C_{+1/2}$ which should be forbidden by geometrical selection (see text) are indeed rather weak, hence motional sidebands cannot be seen; residual excitation of these transitions is due to slight imperfections in the beam geometry (direction and polarization).

are present (see section 7.3). A line synchronous pulsed spectroscopy requires a minimum length of 20 ms, see section 7.2.2 for a generic pulse sequence.

The simplest type of a *probe* sequence is a *single pulse* at 729 nm, which is characterized by its duration $t$, its frequency $\omega_l$ and the light intensity. Two generic types of scans can then be recorded: In a *frequency scan*, $t$ is kept constant and $\omega_l$ is scanned, while in a *pulse length scan* we scan $t$ at constant $\omega_l$.

A *frequency scan* yields an *excitation spectrum* of the $S_{1/2} \leftrightarrow D_{5/2}$ transition. An example of a single ion excitation spectrum over the whole Zeeman-manifold is shown in Fig. 7.4. Only five of the ten transitions appear as, prior to each excitation, the ion has been prepared in the

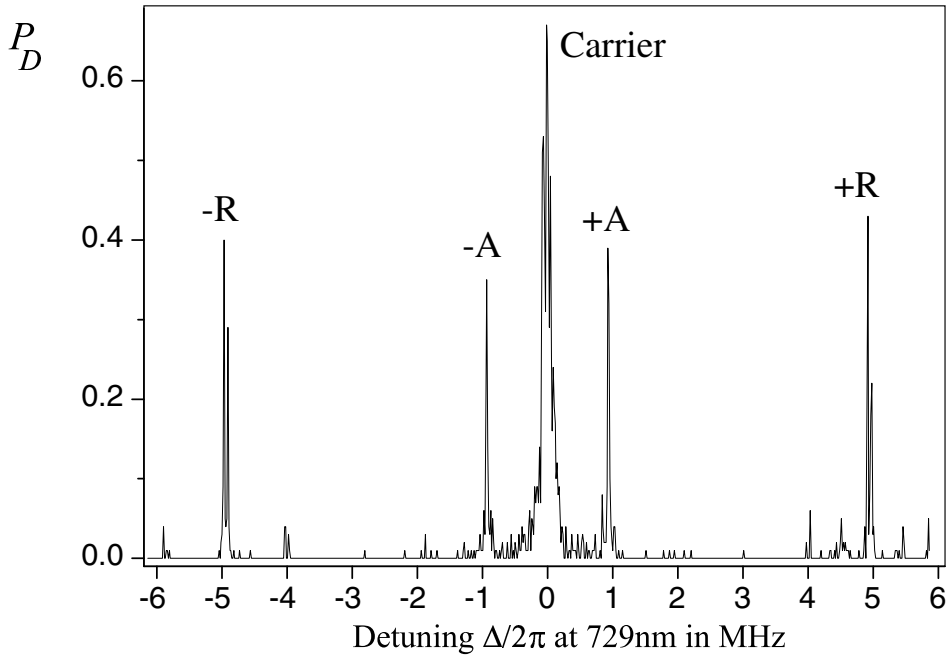


Figure 7.5: Single ion spectrum of motional sidebands around the $S_{1/2}(m = -1/2) \leftrightarrow D_{5/2}(m' = -5/2)$ transition. R and A denote axial and radial and axial sidebands, respectively. The axial trap frequency is $\omega_z = 2\pi \cdot 960$ kHz. Note that the radial sidebands at $\omega_r \simeq 2\pi \cdot 4.95$ MHz are two-fold with a splitting of $\simeq 2\pi \cdot 70$ kHz. This is a result of a slight geometric imperfection of the trap lifting degeneracy in radial direction. The defocussing effect of the radial frequency due to the axial confinement (see eqn. (3.1)) is rather small in this case as $\omega_z$ was much smaller than the "pure" radial trap frequency $\omega_{r0} \simeq 2\pi \cdot 5.05$ MHz.

$S_{1/2}, m = -1/2$ state, eliminating 5 possible transitions. In addition, here the $\phi = 45°, \gamma = 0°$ configiration (see section 3.3.5) was chosen for the geometry between 729 nm laser and magnetic field, which allows only $\triangle m = 0$ and $\triangle m = \pm 2$ transitions. Note that the 729 nm laser detuning is calculated as twice the drive frequency of the corresponding double-pass AOM (see section 5.3) which, at first, yields frequencies on the order of $2\pi \cdot 460$ MHz. For 729 nm laser frequency scans (such as excitation spectra) displayed in this thesis, the frequency axis is recalibrated such that its origin (zero detuning) coincides with one (typically the strongest) carrier resonance.

Fig. 7.5 shows a better resolved scan (taken with weaker excitation compared to Fig. 7.4) around one of the carriers, revealing details of the motional sideband structure. The same type of scan with two ions and slightly different trapping parameters is shown in Fig. 7.6. In general we evaluate two-ion fluorescence data by setting two thresholds for photomultiplier counts, see Fig. 7.3. The $D_{5/2}$ state probability $P_D$ is then calculated by weighting events below Th1 with a factor 1, events between the two thresholds with 0.5 and events above Th2 with a factor 0. The excitation probability calculated like this has a maximum value of 1

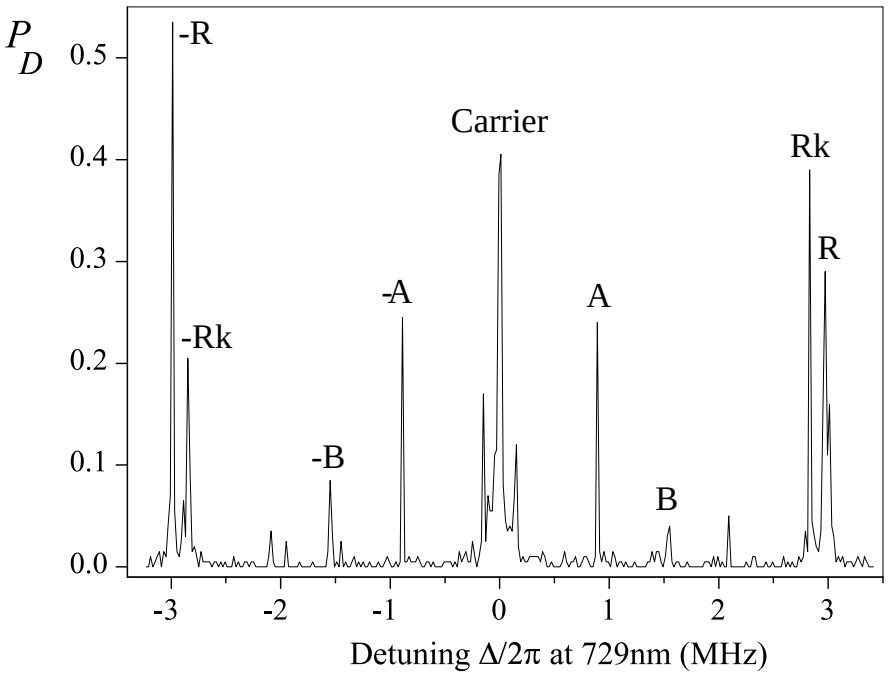


Figure 7.6: Two-ion spectrum around the $S_{1/2}(m = -1/2) \leftrightarrow D_{5/2}(m' = -5/2)$ transition. The various sidebands correspond to different vibrational modes (see section 3.2.2): A=axialCOM, B=Breathing, Rk=rocking, R=radialCOM. The axial parameters are again $\omega_z = 2\pi \cdot 960$ kHz, $V_{cap} = 600$ V while the radial frequency was $\omega_r \simeq 2\pi \cdot 3.0$ MHz. The radial splitting is hardly visible because the step size of the scan is too coarse.

which corresponds to *both* ions being in the $D_{5/2}$ state. The axial sidebands, in particular those of the breathing mode, are rather weak in this scan, as the exciting pulse was applied through the optical channel 729A (cf. 5.4), which has a quite small projection onto the trap axis direction. This results in small Lamb-Dicke parameters, thus weak coupling to the axial modes. Three-ion sideband scans will be shown in section 7.4 in the context of addressing.

With two ions and for events between the two thresholds, with a PMT it cannot be distinguished which of the ions fluoresces and which is dark. For two-ion quantum computation experiments, however, it is indispensible to discriminate between $|S, D\rangle$ and $|D, S\rangle$. In this case we need to read out the fluorescence of each ion individually, which can only be done on the CCD camera. The CCD readout procedure will be presented section 7.4.

If, in contrast to such exciation spectra, we perform *pulse length scans*, *Rabi oscillations* are observed. For the latter we typically set $\omega_l$ to one of the lines of the excitation spectrum, driving in this way the corresponding transition resonantly. In the experiments presented here, we avoid off-resonant excitations (cf. section 3.3.6) of other transitions as much as possible by keeping the coupling (i.e. the light power) sufficiently small. Examples of Rabi oscillations are shown in the following section.

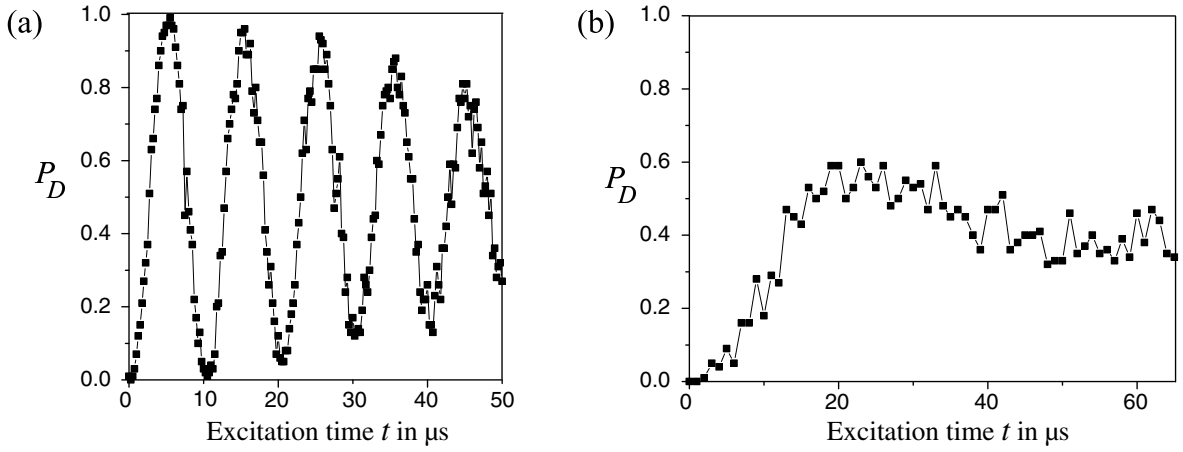


Figure 7.7: Pulse length scans using a 5 ms sequence (Doppler cooling only) with a single ion trapped at a radial frequency of 5 MHz and an axial frequency of 960 kHz. (a) shows Rabi oscillations on the $S_{1/2}(m = -1/2) \leftrightarrow D_{5/2}(m' = -5/2)$ carrier, while in (b) the laser frequency was set to the red axial sideband. From a comparison of (a) and (b), a thermal state with $\overline{n} \approx 20$ is estimated for the axial mode.

## 7.2 Laser Cooling

### 7.2.1 Doppler Cooling

An important feature of the new trap is the stronger confinement by a factor of about two in terms of trap frequencies. It is to be expected that this reduces the mean phonon numbers $\overline{n}$ in the vibrational modes after Doppler cooling by roughly the same factor, down to values $\overline{n}$ between 10 and 20. These values are well in the Lamb-Dicke regime for our trap frequencies, see Fig. 3.6. In this regime, the carrier Rabi frequencies depend only weakly on $n$. Therefore *pulse length scans* on a carrier transition after Doppler cooling are expected to show a oscillatory behaviour with a frequency close to $\Omega$ (i.e. the carrier Rabi frequency when starting from the motional ground state). An example is shown in Fig. 7.7(a). Our standard method to characterize the quality of Doppler cooling consists of comparing such carrier oscillations with pulse length scans on a sideband transitions, performed with the same laser intensity. Sideband Rabi frequencies depend strongly on the motional quantum number $n$, even in the Lamb-Dicke regime. We therefore expect the observed Rabi oscillations to damp out quickly as long as only Doppler cooling is performed; an example scan is shown in Fig. 7.7(b). Fits to both carrier and sideband Rabi-oscillations yield the mean thermal occupation number $\overline{n}$ of the corresponding mode (here: axial mode). A detailed description of the evaluation method is given in ref. [4]. Here, the assumption is made that Doppler cooling results in a thermal probability distribution over the motional states. We find from such scans, that at typical axial and radial trap frequencies of about 1 MHz and 5 MHz, respectively, we achieve Doppler cooling to mean phonon numbers of $\overline{n}_{\mathrm{ax}} \simeq 15$ for the axial mode(s) and $\overline{n}_{\mathrm{rad}} \simeq 4$ for the radial mode(s). To within the precision of this method, we find that this holds equally for single

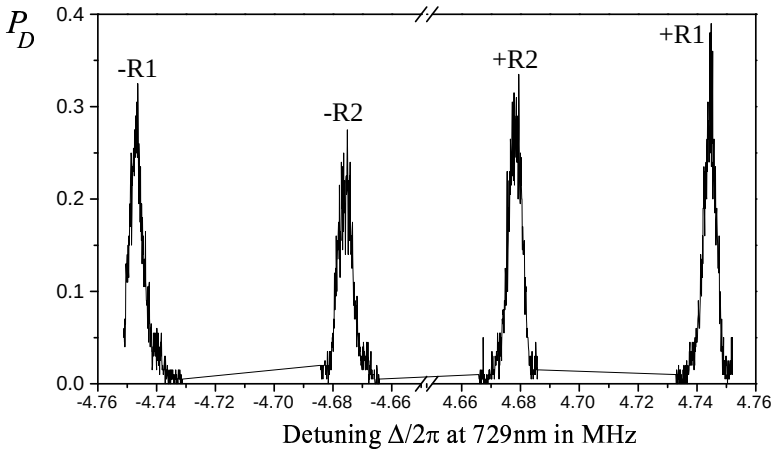


Figure 7.8: Fine scan over the radial COM modes of a single ion using 5 ms experimental sequences. Note the break in the $x$-axis. The outer mode R1 has a frequency of $2\pi \cdot 4.7456(2)$ MHz, while the inner one R2 is at $2\pi \cdot 4.6767(2)$ MHz, which means that the radial degeneracy is lifted by $2\pi \cdot 68.9(2)$ kHz. The R2 sidebands are slightly weaker, which suggests that the exciting laser beam at 729 nm has a somewhat better geometric projection onto the direction of R1. In both cases, the red sideband (-) is weaker than the blue (+) by a factor of about 0.83.

and for two-ion crystals. These values are even more than a factor of two better than what has been achieved with the old trap, in particular for the radial cooling. One reason for this is that we have improved on Doppler cooling by varying different parameters like intensity and polarization of the Doppler beams, for example. In particular, we found that the lowest temperatures are reached by strongly desaturating the Doppler cooling transition. In this way, power broadening of the resonance is avoided, resulting in a narrower line and thus in a lower Doppler cooling limit. Best conditions were reached by desaturating the Doppler cooling light at 397 nm down to about one third of the peak fluorescence. For the detection period in the experimental sequence we want stronger fluorescence on the $S_{1/2} \leftrightarrow P_{1/2}$ in order to be able to discriminate between $S_{1/2}$ and $D_{1/2}$ within the shortest time possible. Therefore we use a somewhat higher laser power at 397 nm (at the same detuning) in that period (dark grey shading in Fig. 7.2).

In general the line strength of a red sideband is smaller than of the corresponding blue sideband, because the $n = 0$ population does not contribute to the red sideband. This effect becomes detectable only in the low temperature range $\overline{n} \lesssim 8$. The radial modes are in that range after Doppler cooling and therefore we have performed comparison scans as shown in Fig. 7.8. The strength of a resonance is proportional to the (fitted) area under the corresponding line. In order to detect the small imbalance which is to be expected, the statistical error was minimized by accumulating 1000 instead of 100 experimental sequences per data point. In addition, the scan step size was reduced to 100 Hz for high resolution. In can be seen that for both sidebands R1 and R2, the blue one is slightly stronger than the red. A $\overline{n}$ of $5 \pm 1$ can be derived from this imbalance. We have recorded Rabi oscillations on the

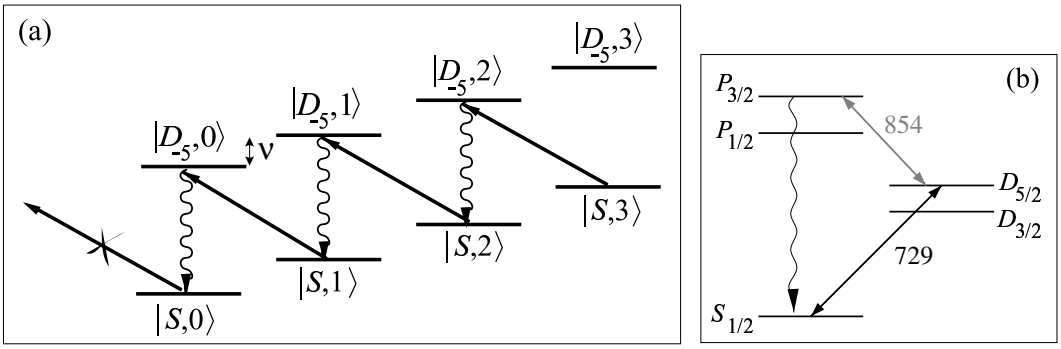


Figure 7.9: Principle of sideband cooling. (a) Ladder of states (introduced already in section 2.1 in the context of quantum computation) visualizing the combined system of the internal quasi-two-level system $|S\rangle \leftrightarrow |D_{-5}\rangle$ and a vibrational mode. Cooling is achieved by absorption on the red sideband followed by spontaneous decay on the carrier. (b) For a sufficient cooling rate, the $|D_{-5}\rangle \rightarrow |S\rangle$ decay is effectively enhanced by a quenching laser which drives the dipole transition at 854 nm.

radial sidebands and the carrier under the same conditions and compared them according to the method explained above. This analysis yielded $\overline{n} = 7 \pm 1$ which is fair agreement with the line strength comparison method.

### 7.2.2 Sideband Cooling

For the quantum computation protocols outlined in chapter 4, motional ground state cooling represents an indispensible requirement. Sideband cooling under our experimental conditions has been previously discussed in detail [4] and the general procedures are the same for the experiments presented here. The principle of sideband cooling is depicted in Fig. 7.9. For sideband cooling of a mode, the 729 nm laser is tuned to the corresponding red sideband of a Zeeman-subtransition of the $S_{1/2} \leftrightarrow D_{5/2}$ manifold. More precisely, the $S_{1/2}(m = -1/2) \leftrightarrow D_{5/2}(m' = -5/2)$ transition is chosen as it offers a nearly closed cooling cycle (see below). As in section 3.3.6, the $D_{5/2}(m' = -5/2)$ state is denoted $|D_{-5}\rangle$ here, see Fig. 7.9.

The sideband transition is resolved only if the trap frequency is large compared to the laser linewidth and the decay rate of the excited state, which is clearly the case in our system. If the decay takes place vertically, that is without change in phonon number $n$, then each excitation to the upper level is accompanied by a reduction of $n$ by 1. The requirement of preferably vertical decay is fulfilled in the Lamb-Dicke regime, namely for $\eta^2(2n+1) \ll 1$ (cf. section 3.3.3). Note that in our experiment after Doppler cooling the ions are in the Lamb-Dicke regime. Hence essentially every cycle of absorption followed by spontaneous emission takes one motional quantum out of the system until the ion reaches the ground state of motion which is decoupled from the laser radiation, see Fig. 7.9(a). In a real system, cooling always competes with heating rates caused by the environment. Using the 729 nm quadrupole transition alone would yield a decay-limited cooling rate of only 1 Hz, which is much too slow for practical purposes. In order to increase the cooling rate, the $D_{5/2}$ state is quenched with laser radiation

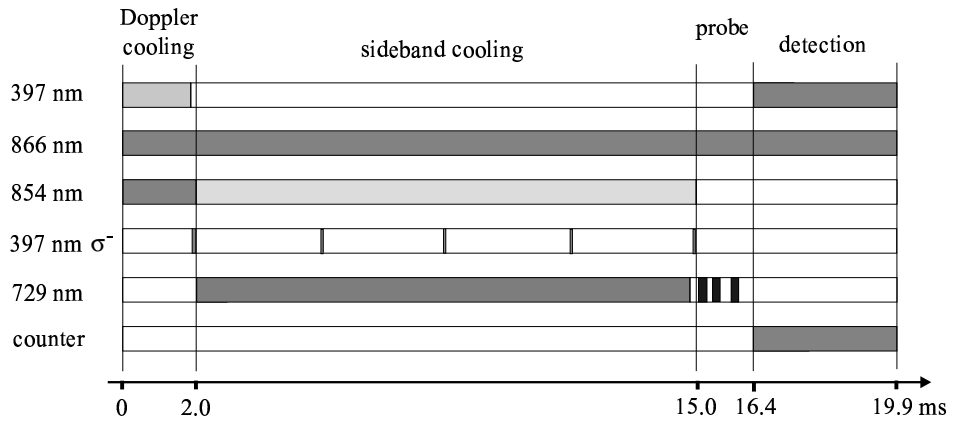


Figure 7.10: Generic 20 ms pulse sequence for coherent dynamics. Different grey scales for the same laser indicate different laser powers and/or detunings.

at 854 nm, see Fig. 7.9(b).

There is a certain probability for the ion to decay into the $S_{1/2}(m = +1/2)$ state (instead of $S_{1/2}(m = -1/2)$) and hence to be withdrawn from the cooling cycle. This probability is minimal if the $S_{1/2}(m = -1/2) \leftrightarrow D_{5/2}(m' = -5/2)$ transition is selected for sideband cooling [4]. Then the ion ends in $S_{1/2}(m = +1/2)$ after 80-160 cycles on the average, the exact value depending on the polarization of the 854 nm quenching laser. As described in section 7.2.1, the axial modes (which are to be sideband cooled) start from phonon numbers on the order of 15 due to previous Doppler cooling. Consequently, in most cases the ion never leaves the cooling cycle before the motional ground state is reached. In order to repump a possible $S_{1/2}(m = +1/2)$ population to $S_{1/2}(m = -1/2)$ in the other cases, a few short $\sigma^-$ polarized pulses at 397 nm are applied during sideband cooling, see Fig. 7.10.

Sideband cooling requires additional time in the experimental sequences. Therefore we work with a 20 ms pulse sequence, shown in Fig. 7.10, if sideband cooling is required. One way to probe the efficiency of ground state cooling is to compare red and blue sideband of the vibrational mode which is being cooled, see Fig. 7.11(a). In the motional ground state, the red sideband disappears completely. Probing the red sideband resonantly is used as an online method to tune the various parameters, namely power and detuning at 729 nm and 854 nm, for minimal red sideband excitation, hence optimum cooling. From such measurements we find that we achieve reliable cooling to ground state probabilities $p_{n=0}$ of 98% or higher for any mode of a single or two-ion crystal and for all trap frequencies in the range of our experiments. Typical ground state cooling times are on the order of 5 ms.

In order to probe the motional heating after ground state cooling, a waiting time between cooling and probe pulse is introduced. The results are shown in Fig. 7.11. A motional heating rate on the order of 140 ms per phonon is derived from these measurements. It will be shown in section 7.3 that at present coherent manipulations are restricted to a duration of about 600 $\mu$s by laser and magnetic field fluctuations leading to internal decoherence. On this time scale the experimental performance is thus not limited by motional heating.

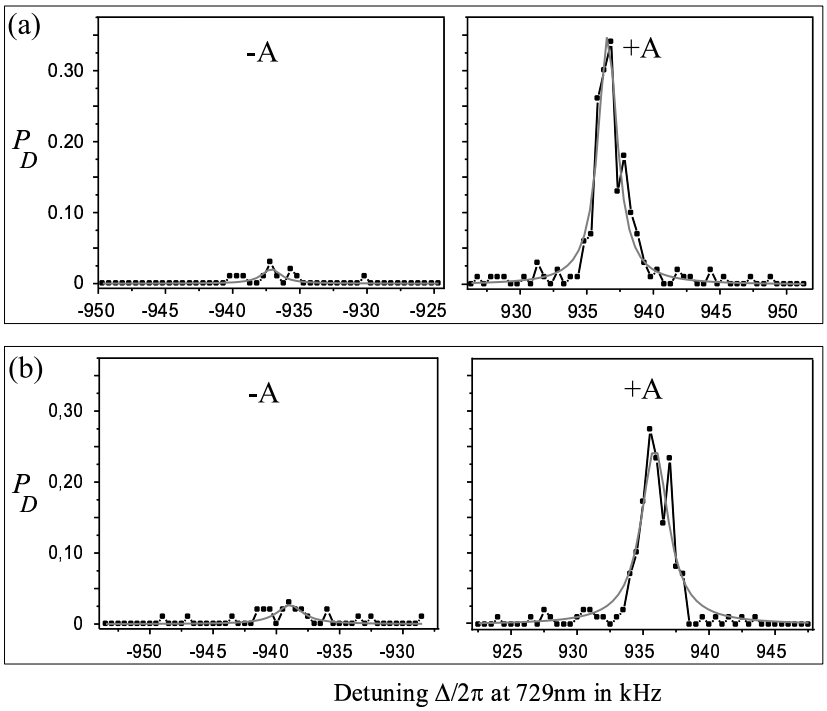


Figure 7.11: Probing the quality of sideband cooling on a single ion by a comparison of red and blue axial sideband. The radial modes at $2\pi \cdot 4.9$ MHz are only Doppler cooled, while additional sideband cooling is applied on the axial mode for 6 ms. In (a), the sideband cooling period finished immediately before detection. An axial ground state probability $p_{n=0}$ of 94% is derived from the difference in line strength between -A and +A. In (b), a waiting time of 7 ms between sideband cooling and detection was introduced and the scans were performed immediately after (a) with the same experimental parameters. For (b) the comparison of -A and +A yields $p_{n=0} = 89\%$. Consequently the axial mode has heated up by 0.05 phonons in 7 ms, which corresponds to a heating rate of 1 phonon per 140 ms.

Rabi oscillations with ground state cooled ions do not suffer from damping due to the occupation of higher phonon number states as has been observed after Doppler cooling only (Fig. 7.7). Examples of Rabi oscillations where the axial mode is sideband cooled, are shown in Fig. 7.12. In this case, the radial mode had a mean phonon number $\overline{n} \simeq 6$ due to Doppler cooling. It can be seen that the damping due to this thermal occupation is negligible for Rabi oscillations on the carrier and on the axial sideband. Based on quantum dynamics simulations performed by Hartmut Häffner, we estimate that the quality of these Rabi oscillations would be noticeably affected for mean radial phonon numbers $\overline{n} \gtrsim 10$. Axial sideband Rabi oscillations are very sensitive to any population in states of the axial mode with $n > 0$. The scans shown in Figs. 7.12(b)&(c) prove that the motional ground state probability was as high as $p_{n=0} = 99 \pm 1\%$ in this case.

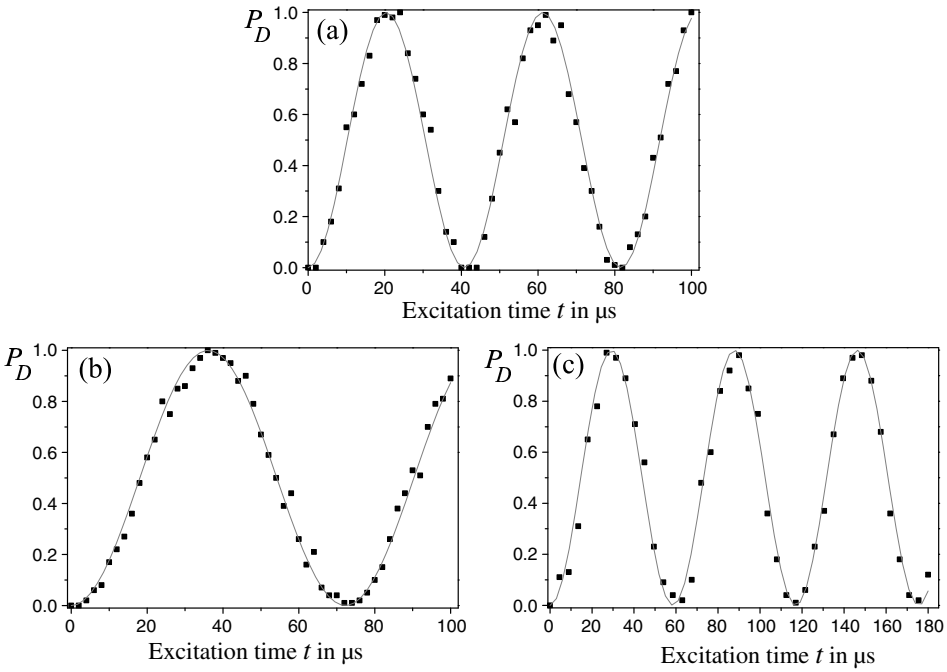


Figure 7.12: Rabi oscillations with a single ion at $\omega_r = 2\pi \cdot 4.9$ MHz and $\omega_z = 2\pi \cdot 1.7$ MHz. The radial mode is Doppler cooled while additional 6ms of sideband cooling are applied on the axial mode. (a) shows carrier oscillations, while in (b) and (c) the laser frequency was set to the blue axial sideband. Solid lines are fits with the function $\sin^2(\pi t/w)$, which assumes a motional ground state probability of 100% and zero decoherence. The excellent agreement of the data with the fits confirms these assumptions. The fit parameter $w$ corresponds to the $2\pi$ period of the Rabi oscillation ($w = 2\pi/\Omega$) and the results are (a) $w = 40.8$ $\mu$s, (b) $w = 72.2$ $\mu$s, (c) $w = 58.5$ $\mu$s.

## 7.3 Coherence on the Qubit Transition

The first and fundamental coherence limit in our quantum computational schemes is set by the lifetime of the $D_{5/2}$ state, which is 1.17 ms [61] in case of an unperturbed $^{40}Ca^+$ ion. We recently observed that in our experiment this lifetime is slightly shortened by the effect of residual 854 nm light during coherent manipulations (probe period), which is due to insufficient switching-off of the RF power going to the 854 nm double-pass AOM. Even weak light at 854 nm is sufficient to quench the $D_{5/2}$ level(s) via the $D_{5/2} \leftrightarrow P_{3/2}$ dipole transition. In order to quantify this effect, $D_{5/2}$ state lifetime measurements were carried out recently. The experiments were supported by Axel Kreuter from the $^{40}Ca^+$ cavity QED experiment of our group and the experimental method was copied from there. The measurement result was a lifetime of 750 ms. It has been verified in the $^{40}Ca^+$ cavity QED experiment (which uses the same laser sources) that this lifetime shortening is indeed due to light from the 854 nm diode laser. This was done by greatly reducing the RF power going to the RF switch for the 854 nm

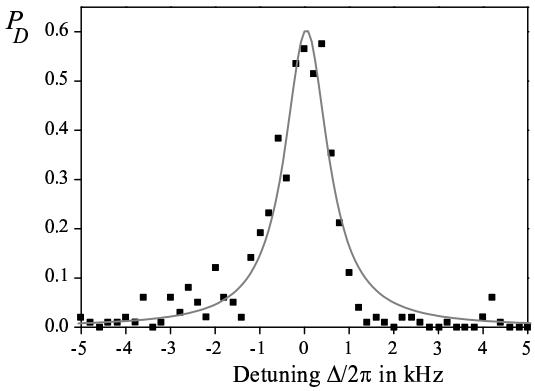


Figure 7.13: Excitation spectrum of the $S_{1/2}(m = -1/2) \leftrightarrow D_{5/2}(m' = +3/2)$ carrier resonance (data points). The pulse at 729 nm had a duration of 1 ms. A Lorentzian fit (solid line) yields a linewidth of $\triangle\omega = 2\pi \cdot 1.17(7)$ kHz.

double-pass AOM. The result was a measured lifetime equal to the value reported in [61] (to within the error bars of about 30 ms). Note that under these (weak RF) conditions the ion can still be repumped from the $D_{5/2}$ at the beginning of a sequence but that the 854 nm power is then insufficient for the quenching necessary for sideband cooling. A better RF switch will cure the problem.

Note that all experiments presented in this thesis were carried out with the present setup corresponding to an effective $D_{5/2}$ state lifetime of 750 ms. It will, however, become clear in the following that this is long enough for the performance of our experiment only to be slightly affected (cf. section 7.4).

The coherence on the qubit transition is additionally limited by fluctuations of both the 729 nm laser light and the magnetic field, the latter leading to fluctuations of the electronic energy levels. These two effects both lead to phase noise and an effective broadening of the transition frequency and are therefore difficult to distinguish in a typical experiment. We have recently installed an active AC magnetic field compensation system[1] which has improved the coherence on the qubit transition. The following begins with a description of the performance of our system *without* active compensation of magnetic field fluctuations. Next, the benefits of this compensation will be discussed.

A type of experiment which probes the frequency broadening of the qubit transition is a direct linewidth measurement as shown in Fig. 7.13. The $S_{1/2}(m = -1/2) \leftrightarrow D_{5/2}(m' = +3/2)$ transition has the strongest magnetic field dependence, namely a relative $g$-factor of 2.8, see Fig. 3.7, and is therefore strongly broadened if magnetic field fluctuations are present. Such measurements were carried out on various carriers of the Zeeman manifold and at different delays of the probe pulse with respect to the power line phase. The $S_{1/2}(m = -1/2) \leftrightarrow D_{5/2}(m' = -1/2)$ transition has the weakest magnetic field dependence, namely a relative $g$-factor of 0.4, which is seven times smaller than for the $S_{1/2}(m = -1/2) \leftrightarrow D_{5/2}(m' = +3/2)$

[1] GATAN FCS12 Field Cancelling System.

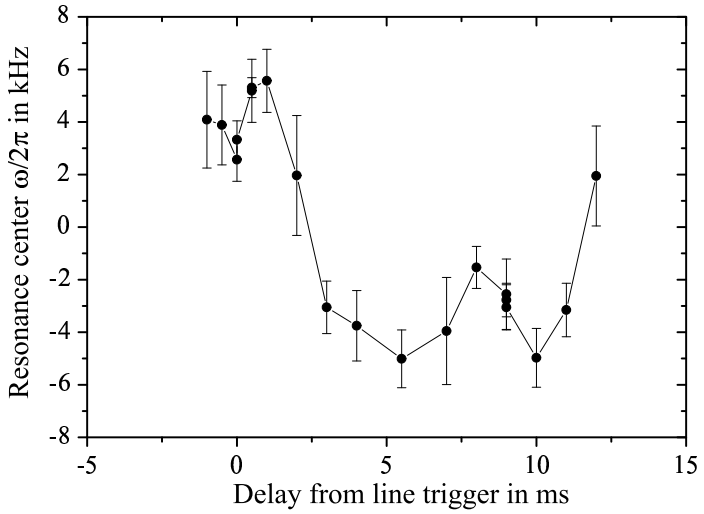


Figure 7.14: Line center of the $S_{1/2}(m = -1/2) \leftrightarrow D_{5/2}(m' = -5/2)$ resonance (data points) and corresponding linewidths (bars) at different delays of the exciting 729 nm probe pulse (duration 1 ms) with respect to the power line phase. The origin of the $y$-axis represents the average of all data points. Note that error bars on the line centers are smaller than the linewidths, namely by a factor of about three. The $S_{1/2}(m = -1/2) \leftrightarrow D_{5/2}(m' = -5/2)$ transition was chosen here as its spectral position depends strongly on the magnetic field (relative $g$-factor 2).

transition. If laser fluctuations were negligible, hence if the lines were broadened uniquely by magnetic field fluctuations, a seven times narrower line (linewidth $2\pi \cdot 170$ Hz) would be expected for the $S_{1/2}(m = -1/2) \leftrightarrow D_{5/2}(m' = -1/2)$ resonance. We observe, however, a linewidth of about $2\pi \cdot 400$ Hz (for the same line trigger delay). We conclude that the $S_{1/2}(m = -1/2) \leftrightarrow D_{5/2}(m' = -1/2)$ resonance is broadened by magnetic field and laser fluctuations to almost equal parts, while for all transitions with a higher relative $g$-factor the line broadening is dominated by magnetic field fluctuations. The linewidth of a given transition depends strongly on the line trigger delay, as shown in Fig. 7.14. It can be seen that the line is particularly narrow at certain delays. It is therefore advantageous to set the trigger of our 20 ms pulse sequences such that the probe period (where coherent manipulations are performed) falls to such a delay. Unfortunately the pattern of Fig. 7.14 is not stable over long time scales as shown by similar experiments which we have carried out at intervals of a few months. Nevertheless, these experiments reveal that there are line-synchronous, periodic fluctuations present in our system.

Non line-synchronous fluctuations can be probed by Ramsey spectroscopy as explained in Fig. 7.15. It can be seen that for $\tau = 100$ $\mu$s the observed Ramsey fringes have very high (99%) contrast. The same type of scans recorded for different waiting times $\tau$ reveal the phase decoherence which leads to a loss of contrast with increasing $\tau$, see Fig. 7.16. For quantum computation experiments a minimum contrast of about 80% is required. Our experiments show that the contrast is reduced to 80% after $\tau = 450\mu$s, which accordingly sets the time

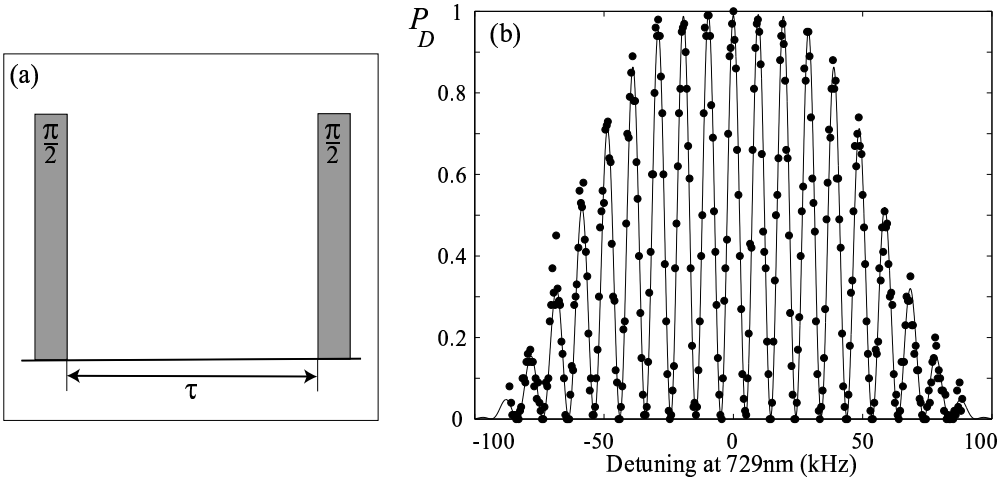


Figure 7.15: Ramsey spectroscopy. (a) The probe sequence consists of *two* identical short pulses of fixed duration at an interval of $\tau$. The light power is adjusted such that each pulse represents a $\pi/2$ rotation if the laser frequency is resonant to a certain carrier transition. For a Ramsey spectrum, the laser frequency $\omega_l$ is scanned around this carrier while all other parameters are fixed. Ideally, i.e. without phase decoherence, $P_D$ should exhibit a modulation between zero and one around the resonance. (b) Ramsey spectrum on the $S_{1/2}(m = -1/2) \leftrightarrow D_{5/2}(m' = -1/2)$ carrier. The laser detuning is given with respect to this carrier. The two pulses of length 9.5 $\mu$s were separated by $\tau = 100\mu$s.

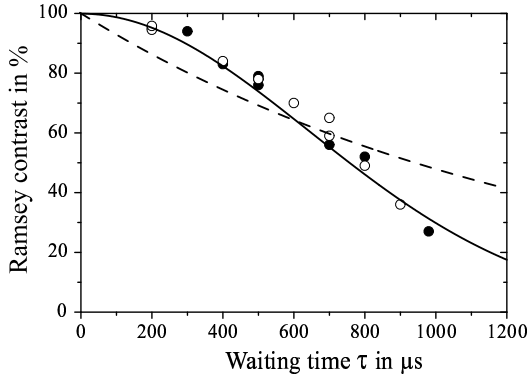


Figure 7.16: Contrast of the $S_{1/2}(m = -1/2) \leftrightarrow D_{5/2}(m' = -1/2)$ Ramsey pattern as a function of $\tau$. Solid circles: data taken without magnetic field compensation. Open circles: date taken with compensation but with a single field sensor only (see text). Solid line: Gaussian fit with $e^{-(\tau/\tau_0)^2}$ yielding $\tau_0 = 0.94(5)$ ms. Dashed line: exponential fit with $e^{-\tau/\tau_0}$ yielding $\tau_0 = 1.4(2)$ ms.

limit for coherent manipulations. Assuming a white noise model for the spectral density of frequency fluctuations, one would expect an exponential decay of contrast, $e^{-\tau/\tau_0}$, with $\tau_0 = 1/\triangle\omega$. This model predicts a Lorentzian resonance line of width $\triangle\omega$. Fig. 7.16 shows, however, that an exponential fit to our data is very poor whilst a Gaussian fit is in good agreement with the results. From this we conclude that an excess of fluctuations compared to a white noise model is present in our system for frequencies $> 1.5$ kHz.

As mentioned, an active cancellation system for magnetic field fluctuations has recently been installed on the experiment. From direct carrier scans we find that with the active compensation in use, the resonance frequencies of different carriers are essentially constant with respect to the power line delay. This has the advantage that triggering of the pulse sequences on the power line is not critical any more and that we achieve in a 5 ms pulse sequence a similar frequency stability as in a line triggered 20 ms pulse sequence. However, *linewidths* were only slightly reduced by the cancellation system. Moreover, Fig. 7.16 reveals that the contrast of Ramsey spectra as a function of the waiting time $\tau$ was essentially the same if recorded with or without the active compensation. This is attributed to a limited bandwidth of the compensation system: we have measured that the magnetic field noise suppression was sufficient only in a frequency range from 50 Hz to 1 kHz.

All experiments presented so far were carried out without magnetic field compensation or with a single magnetic field sensor for the compensation system. Due to the construction of the vacuum vessel and the size of the shielded sensor box (about 10 cm), the sensor can only be placed at a distance of about 15 cm from the trap center, hence does not pick up magnetic field fluctuation exactly where they are to be cancelled. In order to improve on this shortcoming a second sensor has been installed on the opposite position of the trap trap center. An averaged signal from the two sensors is then fed to the cancellation system. This average is expected to represent a somewhat improved measure of the actual fluctuations at the trap center. In addition, measures were taken to reduce electronic noise on the laser lock. We have observed that with these changes, the Ramsey contrast has indeed improved, being now 80% after about 700 $\mu$s. However, systematic studies on the performance of the cancellation system with two sensors have not yet been undertaken. In particular, it is not clear how important in the present setup the contribution of laser fluctuations at different frequencies of the noise spectrum is compared to magnetic field noise. Further experiments are planned to investigate these issues. For the following experiments, in particular the quantum computation experiments of chapter 8, the compensation system was used.

Most of the results presented in this section are detailed in [93]. This reference additionally discusses preliminary measurements we have carried out employing a Raman transition technique. In these experiments, Raman transitions are driven between the two magnetic sublevels ($m = \pm 1/2$) of the $S_{1/2}$ ground state. This technique allows the determination of magnetic field fluctuations alone and remains immune to laser fluctuations.

## 7.4 Individual Ion Addressing and Read-Out

One method to probe the addressing quality of the 729A channel (cf. section 5.5) is based on sweeping the laser focus over the the ions using the deflector. The ion is probed with a single pulse of fixed duration resonant to one of the $S_{1/2} \leftrightarrow D_{5/2}$ carriers. At each deflector

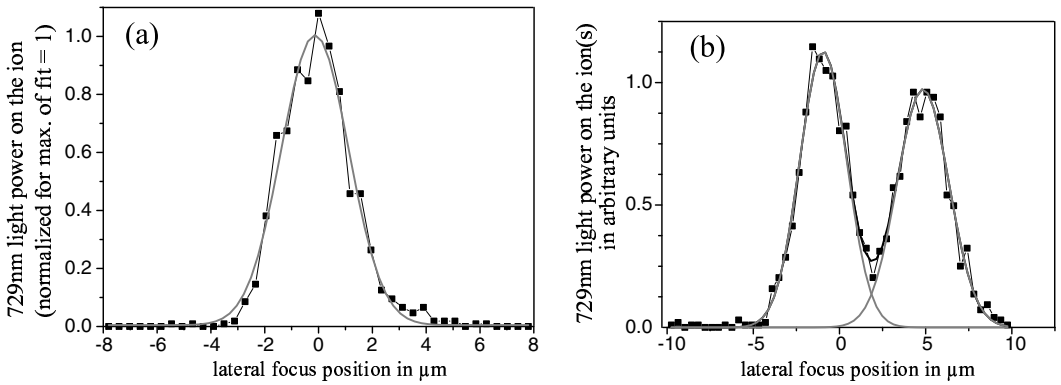


Figure 7.17: (a) Single ion deflector scan. The Gaussian fit yields a waist of 2.50(8)mum. (b) A two-ion deflector scan serves to calibrate the $x$-axes (see text). In this case, the axial trap frequency was $\omega_z = 2\pi \cdot 940$ kHz, from which an ion distance $\triangle z = 6.3$ $\mu$m is calculated; this corresponds to a projected distance $\triangle z_p = 5.8$ $\mu$m.

voltage, i.e. at each lateral focus position, the excitation probability $P_D$ is measured, which yields a profile of the laser focus. Before that, the laser focus is adjusted onto the ions by tuning the addressing optics for maximum excitation. In a second step, Rabi oscillations are recorded. For these experiments, Doppler cooling is sufficient and so a typical pulse length scan looks like Fig. 7.7(a). Following next, we select a pulse duration $t_0$ which is somewhat below the $\pi$-time of the oscillation, in case of Fig. 7.7(a), for example, $t_0 = 4$ $\mu$s. Now a *deflector scan* is performed: $\omega_l$ and $t_0$ are kept fixed while the voltage on the beam deflector is scanned. Each deflector position corresponds to a certain light intensity $I$ on the ion(s). The intensity is proportional to the Rabi frequency squared, thus $\Omega = a\sqrt{I}$ with some constant $a$ (cf. section 3.3.5). Moreover, the first oscillation of $P_D$ from zero to one (see Fig. 7.7(a)) is given by $P_D = \sin^2(\Omega t/2)$ to a very good approximation. It follows that $P_D = \sin^2(a\sqrt{I}t_0/2)$. Using this formula, the excitation probability profile can be rescaled into an intensity profile. Examples of deflector scans are shown in Fig. 7.17. If we perform such a scan with a two-ion crystal (Fig. 7.17(b)) we can calibrate the deflector voltages into lateral translations of the laser focus. To do so, the axial trap frequency $\omega_z$ is determined from an excitation spectrum; $\omega_z$ gives the distance $\triangle z$ between the ions using formulas 3.11 and 3.10. As shown in section 5.4, the trap axis is not perpendicular to the addressing beam channel 729A as the trap is tilted by 22.5°. Consequently, the effective (projected) ion distance is

$$\triangle z_p = \triangle z \cdot \cos 22.5^\circ \ . \tag{7.1}$$

From single ion deflector scans as in Fig. 7.17(a), a Gaussian focus waist of 2.5 $\mu$m is determined using this calibration. The value of 2.5 $\mu$m represents the optimum achieved by adjusting the addressing optics. This optimization is done by performing single ion deflector scans at different longitudinal positions of lens L2 of the addressing optics (see section 5.5), which corresponds to shifting the laser focus at the trap center in longitudinal direction.

Another method to characterize the addressing consists of driving carrier Rabi oscillations

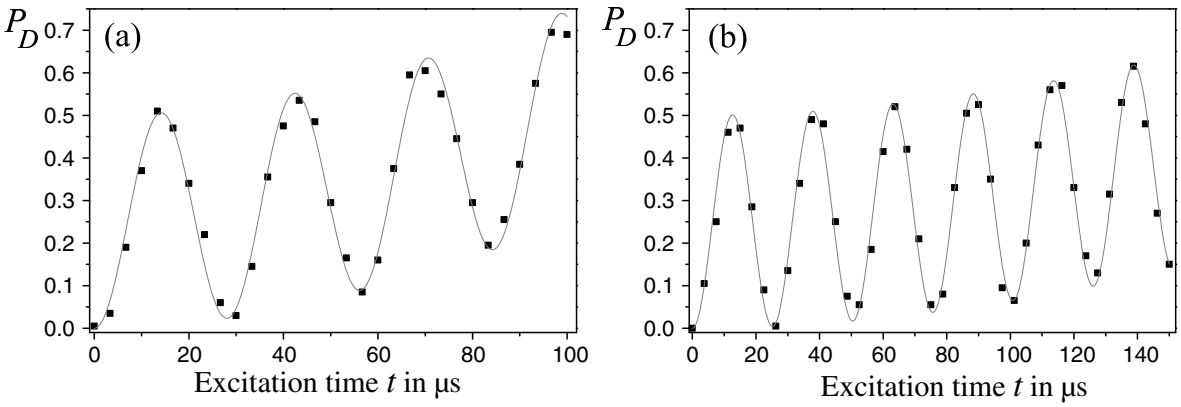


Figure 7.18: Addressed carrier Rabi oscillations performed on a two-ion crystal in a 20 ms pulse sequence including ground state sideband cooling of both the axialCOM and the breathing mode. In (a) the laser was addressed onto one of the two ions, in (b) onto the other. It can be seen that for the given adjustment of the optics, the addressing qualities differ significantly depending on which ion is addressed: (a) $\Omega_1 = 2\pi \cdot 35.5(1)$ kHz, $\Omega_2 = 2\pi \cdot 2.46(7)$ kHz, addressing quality $AQ = 6.9(1)\%$, ratio of light intensities 1:210. (b) $\Omega_1 = 2\pi \cdot 39.7(2)$ kHz, $\Omega_2 = 2\pi \cdot 1.16(5)$ kHz, addressing quality $AQ = 2.9(1)\%$, ratio of light intensities 1:1200.

in a two-ion crystal where the 729 nm laser is addressed onto one of the ions. The addressed ion will undergo oscillations with a Rabi frequency $\Omega_1$ while the other ion oscillates at a much slower frequency $\Omega_2$ due to residual light intensity at its position. In the experiment, pulse length scans are performed and the two-ion excitation probability $P_D$ is determined from the photomultiplier counts as explained in section 7.1. Exemplary scans are shown in Fig. 7.18. The data are fitted with a sum of two $\sin^2$ functions (amplitudes 0.5), the periodicities of which yield the Rabi frequencies $\Omega_1$ and $\Omega_2$. From these fit results the addressing quality $AQ$ is calculated, which we define as $AQ = \Omega_2/\Omega_1$. Note that Rabi frequencies are proportional to the electric field amplitude, hence proportional to the square root of the light intensity. Consequently, the ratio of light intensities on the two ions is given by $AQ^2$.

Aberrations of the addressing optics typically do not so much broaden the focus waist, rather lead to a background carpet of light around the Gaussian profile. In our case, this background dominates over the Gaussian behaviour at distances $> 5$ $\mu$m from the center of the focus. As a consequence, we observe that the addressing quality $AQ$ does not significantly improve for ion distances[2] $\triangle z_p > 5$ $\mu$m. This poses considerable problems in quantum computational protocols: the best addressing qualities we have achieved are on the order of $AQ = 2.9(1)\%$ as in Fig. 7.18(b). Note that this corresponds to very good addressing in terms of residual intensity on the non-addressed ion, which is smaller by a factor of 1200 (!) as compared to the addressed ion. The property of Rabi frequencies to be proportional to the

[2]For very large ion distances $\triangle x_p > 15$ $\mu$m, $AQ$ would probably eventually improve noticably. Such large distances, however, correspond to very low axial trap frequencies $\omega_z < 2\pi \cdot 200$ kHz which are not practicable for quantum computation.

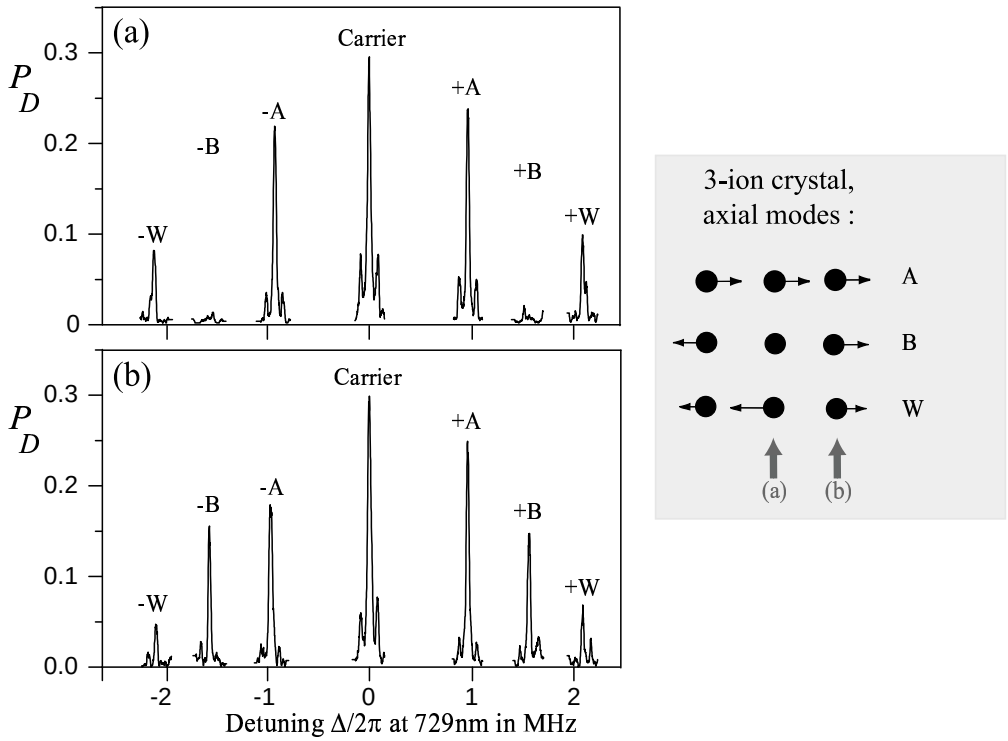


Figure 7.19: Excitation spectra of a three ion crystal around the $S_{1/2}(m = -1/2) \leftrightarrow D_{5/2}(m' = -1/2)$ resonance. The 729 nm laser was addressed on (a )the center ion, and (b) an edge ion. The axial trap frequency was $\omega_z = 2\pi \cdot 940$ kHz. Only the three axial sidebands, labeled A (axial COM mode), B (breathing mode), W (wobble mode), are visible, see also Fig. 3.4. Radial sidebands lie outside the scan range. On the right hand side, the eigenvectors of the three axial modes are depicted.

square root of the light intensity, however, leads to significant excitation of the non-addressed ion after only a few Rabi cycles of the addressed ion. This addressing error is particularly harmful on sideband transitions, where motional states with $n > 1$ may become excited in the process. Addressing errors, in principle, can be partially compensated for by additional pulses, where the light is focused onto the originally non-addressed ion and the unwanted excitation amplitude is rotated back to zero by choosing the appropriate laser phase and pulse duration. This procedure, however, requires considerably more complex pulse sequences and has not yet been tested in the experiment.

We have undertaken an additional test of the addressing with a linear three-ion crystal. As mentioned in section 3.3.4, the strength of a sideband transition, characterized by the corresponding Lamb-Dicke factor, in general depends on which ion in the string is addressed. This can be easily understood for the breathing mode of a three-ion crystal. As depicted in Fig. 7.19, the center ion does not participate in the motion of the breathing mode. Consequently, the

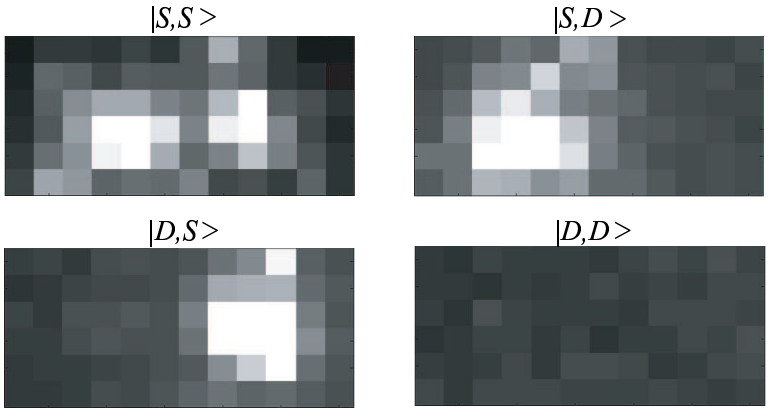


Figure 7.20: CCD camera snapshots of a two-ion crystal at an axial trap frequency $\omega_z$ of $2\pi \cdot 1.215$ MHz, corresponding to a (projected) ion distance $\triangle z_p = 4.9$ $\mu$m. Due to prior excitation of both ions with light at 729 nm, the ions (independently) are sometimes projected into the (dark) state $|D\rangle$ when illuminated with 397 nm light (electron shelving, cf. section 7.1). Consequently, in some cases both ions fluoresce (corresponding to the state $|S,S\rangle$), in others only one fluoresces ($|S,D\rangle$ or $|D,S\rangle$) and finally sometimes both ions are dark ($|D,D\rangle$).

corresponding Lamb-Dicke factor is zero if this ion alone is addressed. Hence the coupling to the breathing mode sideband transition vanishes. This is confirmed by the scan shown in Fig. 7.19(a) where the sidebands of the breathing mode disappear almost completely, the residual excitation being due to the addressing error. For a comparison, we recorded the same type of scan but now with an ion on the edge of the crystal addressed, see Fig. 7.19(b). It can be seen that now the breathing mode sidebands are clearly visible and comparable in line strength to the other sidebands.

For individual fluorescence read-out in the case of two or more ions we use the CCD camera. The fluorescence count rates achieved on the CCD are somewhat lower than on the PMT (details see below). Therefore, more time is required for a good (99%) discrimination between ON and OFF for each ion, i.e. about 10 ms instead of 3 ms on the PMT. Longer read-out times are not recommendable, because the decay probability of the $D_{5/2}$ state (effective life-time 750 ms, see section 7.3) grows by 1.3% per 10 ms, which reduces the read-out efficiency by the same amount. Fig. 7.20 shows fluorescence snapshots of a two-ion crystal where the ions have been excited on the $|S\rangle \leftrightarrow |D\rangle$ qubit transition at 729 nm into roughly a 50:50 superposition prior to illumination with dipole light at 397 nm. The pictures were taken with the same trap parameters, in particular the same $\omega_z$, at which two ion quantum computing experiments were carried out (see Appendix A.3). Compared to Fig. 6.1 these pictures look more coarse because the exposure time is considerably shorter. Note that as the imaging onto the CCD camera employs the same optical channel as the addressing, the ions appear at a reduced (projected) distance $\triangle z_p$ (see eqn. (7.1)) on the CCD.

Two regions of interest are defined, which contain an array of CCD pixels (typically 4 by

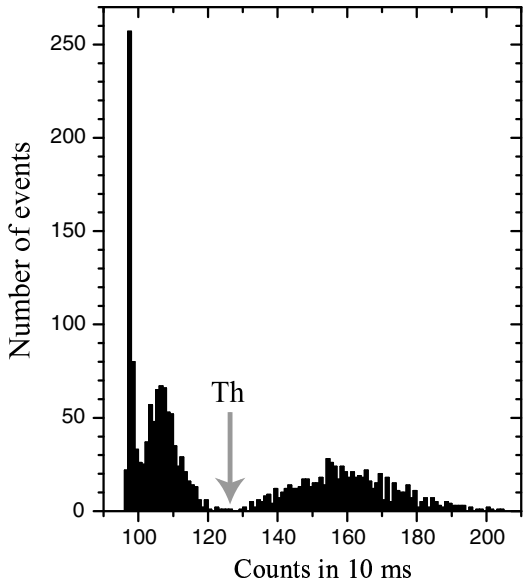


Figure 7.21: Camera histogram of fluorescence counts from a single ion in a two-ion crystal. As in Fig. 7.20, the trapping parameters were those of the two-ion standard configuration (Appendix A.3). The total number of events represented in this histogram is 1800.

4), each region corresponding to one of the ions. The two regions are read out independently. The signals from the pixels of each region are binned and taken as the fluorescence signal of the corresponding ion. A histogram of counts from one ion (one binned region) in a two-ion crystal is shown in Fig. 7.21. The histogram represents 1800 experiments, each taken in a 40 ms pulse sequence.

This is our standard sequence for two-ion experiments if individual fluorescence read-out is required. The 40 ms sequence is very similar to the 20 ms sequence of Fig. 7.10 with two modifications. First, the two-ion experiments typically require sideband cooling of both axial modes (axial COM and breathing), see section 8.3. Consequently, the sideband cooling period is divided into two parts, the first being about 4 ms of sideband cooling of the axial COM mode and the second about 8 ms of sideband cooling of the breathing (=quantum bus) mode. Second, as explained above, the fluorescence read-out on the camera requires at least 10 ms for sufficient discrimination. Consequently, the detection period extends from about 16 ms to 26 ms in the pulse sequence. The next (50 Hz) line trigger then arrives at 40 ms, where a new sequence is started. Note that this leaves a dead-time of 14 ms which is unused.

In the histogram of Fig. 7.21, there are no events with less counts than 97 and there is a sharp and high peak of events between 97 and 99 counts. The offset of 97 is because each pixel has a well defined signal offset of about 0.6 per millisecond[3]. The dark count rate (on top of this offset) per pixel is essentially zero. Moreover, scattered light at 397 nm (from the

[3]This value depends on the gain of the micro-channel plates of the camera. The value given here corresponds to the camera gain we found optimum and which was used in the experiments.

Doppler beams) is much less on the camera pixels than on the PMT as the latter integrates over a much larger surface area (about 1 $mm^2$ as compared to a CCD pixel size of about $4 \cdot 10^{-4}$ $mm^2$). Consequently, the peak between 97 and 99 counts, which corresponds to both ions being dark, is very sharp. There is an additional signal peak between 100 and 120 counts. This peak corresponds to residual fluorescence light on the pixel array attributed to the ion of interest stemming from the neighbor ion. In other words these count rates correspond to events where the ion of interest is dark, while the neighbor ion fluoresces. Finally, the peak between 130 and 200 counts corresponds to events where the ion of interest fluoresces (regardless of the state of the neighbor ion). In this case a possible fluorescence from the neighbor ion is too small to define a visibly distinguishable peak.

Just as in the experiments where the photomultiplier is used for read-out, a threshold Th is set to discriminate between fluorescence OFF and fluorescence ON (of the ion of interest). The specified quantum efficiency of the CCD is very similar to that of the PMT (close to 30%). However, a comparison of Fig. 7.21 with the PMT histograms of Fig. 7.3 shows that the effective count rate per ion (i.e. counts minus offset) is considerably smaller (remember that the counting times are different by a factor of 3.3) and therefore the discrimination is worse on the CCD. It is not yet clear, if the reason for this lies in a poor imaging of the ions onto the CCD chip (which would smear ot the ion images) or if the true quantum efficiency of the CCD at 397 nm is lower than specified. Tests are currently undertaken to clarify this issue. Note that the few events in the threshold area of Fig. 7.21 (between 120 and 130 counts) correspond mostly to cases where the ion of interest has decayed from $|D\rangle$ to $|S\rangle$ during the detection process. As mentioned above, a detection time of about 10 ms is found to be the optimum trade-off between such unwanted decay processes and the need of fluorescence discrimination. The best detection efficiency currently achieved is 99%.

## 7.5 Switching the Laser Phase

Quantum algorithms imply a complete control of the qubits' degrees of freedom, namely amplitude and phase. This, first of all requires low phase noise on the qubit states as well as on the corresponding laser at 729 nm over the time of coherent manipulations. Phase stability is, of course, intrinsically connected to frequency stability which has been discussed in section 7.3.

A quantum gate can then be realized by a set of laser pulses of certain intensities, durations and phases. Phase control entails consideration of two issues: production of laser pulses of well defined relative phase and control over AC-Stark shifts. This section details on the former while the role of AC-Stark shifts will be addressed in sections 7.6 and 7.7.

Experimental protocols as, for example, for the Deutsch-Jozsa algorithm require rather complex phase sequences. To begin with, the laser switch network (see section 5.3) and the quality of our self-made phase-defining cables were tested in a comparably simple experiment with a single ion. In this case, laser phase switching by $\pi/2$ was tested. For the experimental settings, the single ion standard configuration was used (see appendix A.3). In a first scan, Rabi oscillations on the $S_{1/2}(m = -1/2) \leftrightarrow D_{5/2}(m' = -1/2)$ carrier transition were driven resonantly at constant laser phase, see Fig. 7.22(a). In the scan shown in Fig. 7.22(b), the

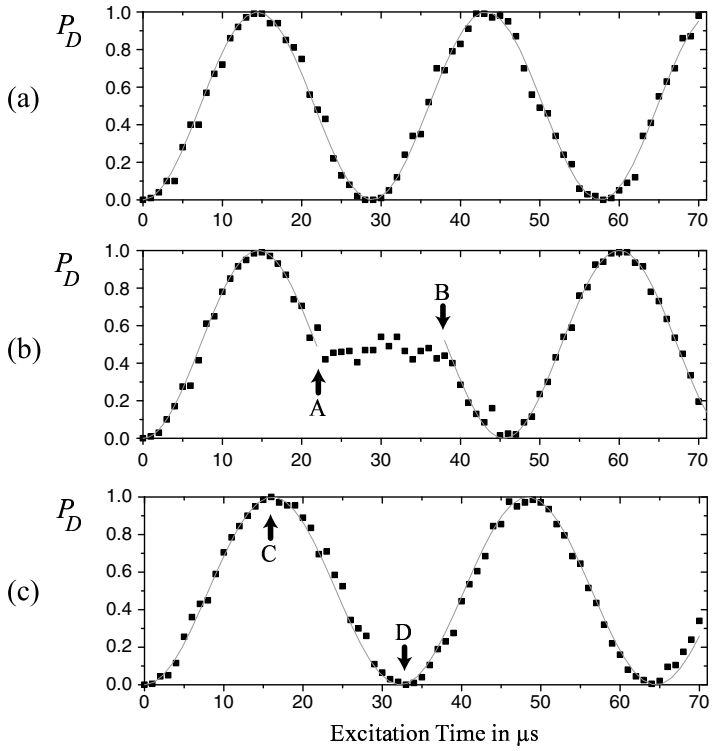


Figure 7.22: Resonantly driven Rabi oscillations on the effective two-level system formed by $S_{1/2}(m = -1/2)$ and $D_{5/2}(m' = -1/2)$. The solid lines are $\sin^2$ fits to the data. In (b) and (c), the laser phase was switched forward by $\pi/2$ (points A and C) and back to 0 (points B and D) during the excitation period. Over the course of this experiment, the laser power slowly decreased. Therefore the Rabi-frequency dropped from $2\pi \cdot 34.7$ kHz in scan (a) to $2\pi \cdot 31.0$ kHz in scan (c) (45 minutes later) which for these test experiments does not represent any problem. For the implementation of more complex dynamics as presented in the following sections and chapters, however, special care had to be taken to operate the system under more stable conditions.

laser phase was switched forward by $\pi/2$ at point A where the two-level system is in a 50:50 superposition. At this point, a laser phase jump of $\pi/2$ "locks" the Bloch vector (cf. section 2.1) on the equator of the Bloch sphere (rotating frame). The excitation probability remains at 50% although the ion is still constantly illuminated with resonant laser light! At point B the phase was switched back[4] to 0. One can see that the two-level system resumes the evolution which had been stopped at point A. In the next scan, shown in Fig. 7.22(c), the $\pi/2$-leaps forward and back were set to points where they should not disturb the sinusoidal Rabi oscillations, namely C and D. A detection scheme which is sensitive to the relative phase of the two-level system, however, would reveal that something in fact is changing at C and

[4]There is no absolute laser phase origin, so 0 is just defined by one of the cable paths, for example $\phi_0$.

D: the first excitation period from 0 $\mu$s to C rotates the Bloch vector all the way from the bottom to the top of the sphere, say about the $x$-axis. At point C the rotation axis is changed by 90° and so the vector rotates back down to the bottom of the Bloch sphere, but now about the $y$-axis. In our experiment, where only $P_D$ is measured, only the latitude so-to-say of the Bloch vector is probed and no difference (to Fig. 7.22(a)) is seen. With the phase switched back to 0 at point D, the Bloch vector resumes the original rotation about the $x$-axis. These and similar experiments confirmed that we are able to implement any phase difference with a precision of $\pm 0.05$ radians, that is $\pm 3°$.

## 7.6 AC-Stark Shift Measurement and Compensation

In section 3.3.6, equation (3.36) is derrived, which describes the relative AC-Stark shift $\delta_{AC}$ of the levels $|S\rangle$ and $|D\rangle$ induced by off-resonant light of frequency $\omega^s$. Moreover, a compensation method for AC-Stark shifts is proposed. This section features experiments in which equation (3.36) is mapped, i.e. $\delta_{AC}$ is measured as a function of $\omega^s$, and the AC-Stark shift compensation method is presented.

**Measurement Method.** In order to probe AC-Stark shifts, a Ramsey-type method is applied. The absolute positions of atomic levels can never be observed but only their relative positions, i.e. the transition frequency between some level pair. We are especially interested in the pair of levels $|S\rangle$ and $|D\rangle$, which form the internal qubit (cf. section 3.3.5). In order to measure the relative level shift $\delta_{AC}$ between these two levels (cf. eqn. (3.35)) induced by off-resonant light at frequency $\omega^s$, we apply two resonant Ramsey $\pi/2$-pulses on the $|S\rangle \leftrightarrow |D\rangle$ transition (frequency $\omega_{-1}$), see Fig. 7.23. If nothing else happens, then the two pulses add up to one $\pi$-pulse, i.e. the ion is simply excited from $|S\rangle$ to $|D\rangle$ in the overall process. If, however, in the time between the two pulses the $|S\rangle \leftrightarrow |D\rangle$ resonance frequency is shifted to $\omega_{-1} + \delta_{AC}$ by the effect of non-resonant light shone in over a duration $T$, then a *phase shift* $\varphi = T\delta_{AC}$ between the laser source and the two-level system is acquired. Consequently, the second Ramsey pulse will for example bring the system back to state $|S\rangle$ if $\varphi = \pi$ or even have no effect at all, which is the case if $\varphi = \pi/2$. The experimental method now consists of scanning the duration $T$ and measuring the excitation probability ($|D\rangle$ state probability $P_D$) at each $T$-value. The result is an excitation probability varying sinusoidally as a function of $T$ with a frequency $\delta_{AC}$. Fig. 7.23 shows an example of such a scan. Many scans for various "shifter" frequencies $\omega^s$ yield an AC-Stark shift spectrum $\delta_{AC}(\omega^s)$, thus mapping eqn. (3.36). It is assumed here, that the same experimental configuration, in particular in terms of beam geometry, is chosen, for which eqn. (3.36) has been derived, namely the *single ion* standard configuration (Appendix A.3). If we define $\Delta$ as the detuning of the shifter from the $|S\rangle \leftrightarrow |D\rangle$ resonance, namely as $\Delta = \omega^s - \omega_{-1}$, the latter equation transforms to

$$\delta_{AC}(\Delta) = \frac{\Omega_{-1}^2}{4}\left(d - \frac{a_{-5}}{\Delta + \Delta_{mag}} - \frac{2}{\Delta} - \frac{a_{+3}}{\Delta - \Delta_{mag}}\right) , \tag{7.2}$$

where

$$\Delta_{mag} = 2\pi \cdot 2.4\frac{\mu_B B}{\hbar} = 2\pi \cdot 3.36B \ \tfrac{\text{MHz}}{\text{G}}$$

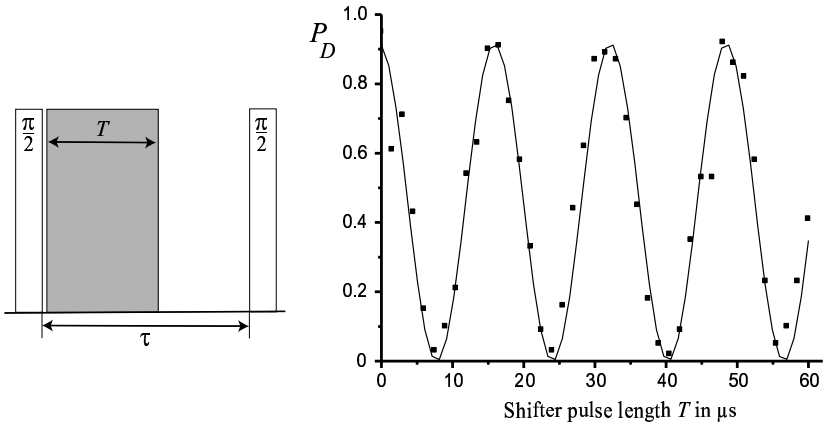


Figure 7.23: Left: Probe pulse sequence for Stark Shift measurements. Two Ramsey $\pi/2$-pulses (white) are applied on the $|S\rangle \leftrightarrow |D\rangle$ transition (duration 8 $\mu$s, separation $\tau = 200$ $\mu$s). Between the two pulses, off-resonant "shifter" light (grey) at a detuning $\Delta$ is applied for a time $T$. Right: Example of a scan recorded at a detuning $\Delta = -1.20$ MHz; the fit yields a period of 16.3(1) $\mu$s, thus $\delta_{AC} = 2\pi \cdot 61.5(5)$ kHz. The reduced contrast ($\approx 90\%$) is due to decoherence caused by laser as well as magnetic field fluctuations over the waiting time $\tau$, see section 7.3.

is the Zeeman splitting between the states $D_{1/2}(m' = -1/2)$ and $D_{1/2}(m' = -5/2)$ (respectively between $D_{1/2}(m' = +3/2)$ and $D_{1/2}(m' = -1/2)$), cf. Fig. 3.7. As mentioned, $\Delta$ (respectively $\omega^s$) should always be far enough from any carrier or sideband resonance in order to avoid population transfer. For the laser intensities used in this experiment, it was sufficient to avoid a range of $\pm 2\pi \cdot 400$ kHz around each carrier and a range of $\pm 2\pi \cdot 50$ kHz around each sideband in order to fulfill this off-resonance criterion.

**Experimental Results.** The experiments were performed in the *single ion* standard configuration (appendix A.3). The $\pi/2$ carrier pulses on the $|S\rangle \leftrightarrow |D\rangle$ transition had a duration of 8 $\mu$s. The time interval $\tau$ between them was set to 200 $\mu$s. Drifts of our reference cavity during the acquisition time result in a slightly faster or slower oscillation, depending on their sign. They can be compensated for if the drift is uniform over the time scale of acquisition (about two minutes) - which to our knowledge is a justified assumption - by doing every scan twice: once forward, scanning $T$ from zero to some suitable $T_{end}$, and then another scan from $T_{end}$ down to zero. The average of the two oscillation frequencies then represents an improved value for $\delta_{AC}$.

It is important for these measurements that the laser power is constant over all scans or at least that one keeps track of different powers. In our experiment, the 729 nm laser is actively intensity stabilized to within better than 1%. The efficiency of the double pass AOM setup which is used to switch and frequency-tune the light, however, has a certain frequency characteristic. For the Ramsey pulses this is not a problem as they remain at the same frequency, while the shifter which is scanned over as much as $2\pi \cdot 70$ MHz changes greatly in intensity

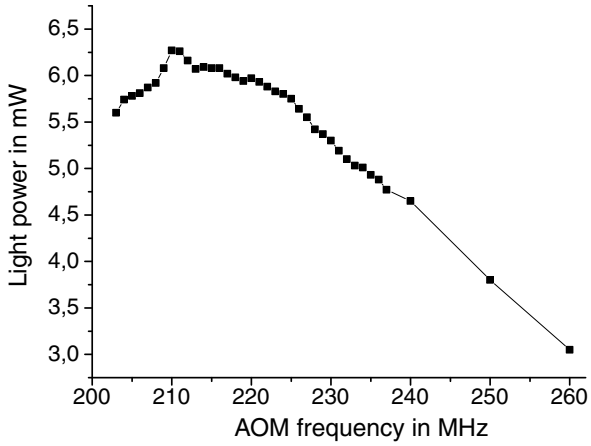


Figure 7.24: Transmitted light power through the double pass AOM setup used to tune and switch laser light at 729 nm. The $S_{1/2}(m = -1/2) \leftrightarrow D_{5/2}(m' = -1/2)$ resonance corresponds to an AOM frequency of 230 MHz. By a simple recalibration of the frequency axis, the laser power $P(\Delta)$ as a function of detuning $\Delta$ is obtained from this plot.

over this spectrum. In order to correct for this effect, the frequency dependence of the light power through the double pass AOM was recorded. This was carried out for the exact same RF drive power going to the AOM as in the experiment. The light power was measured directly in front of the ion trap to make sure that effects of different coupling out of the double pass AOM into the fibre transmitting the light to the experiment are also taken into account. The recorded curve is shown in Fig. 7.24. The $|S\rangle \leftrightarrow |D\rangle$ resonance corresponds to an AOM frequency of 230 MHz.

A total of 68 back and forth scans were recorded resulting in 34 $\delta_{AC}$ values for different $\Delta$. Additionally, Rabi oscillations on the $|S\rangle \leftrightarrow |D\rangle$ transition were recorded in order to determine the frequency $\Omega_{-1}$ of eqn. (7.2), the result being $\Omega_{-1} = 2\pi \cdot 376(7)$ kHz. All obtained $\delta_{AC}$ values were renormalized to the same laser power by dividing them by $P(0)/P(\Delta)$ (cf. Fig. 7.24). The complete data set is shown in Fig. 7.25 except for two data points at large detunings, which where omitted in order to keep the plot compact. They read $\delta_{AC} = 2\pi \cdot 5.88$ kHz and $2\pi \cdot 8.49$ kHz for detunings $\Delta$ of $2\pi \cdot 40.0$ MHz and $2\pi \cdot 60.0$ MHz, respectively.

Note that this measurement procedure only yields the modulus but not the sign of $\delta_{AC}$. The signs were attributed to the measurement results according to the theoretical curve to be expected, that is eqn. (7.2). The spectral positions of the three carrier resonances where determined directly from an excitation spectrum (cf. Fig. 7.4). From this, $\Delta_{mag}$ was determined to be $2\pi \cdot 8.40$ MHz which corresponds to a magnetic field of $B = 2.50$ G. The expected values for the relative line strengths (cf. section 3.3.6) are $a_{-5} = 0.278$ and $a_{+3} = 0.0556$.

The only complete unknown for the fit of the data with this equation was $d$. Therefore in the fitting procedure, at first only $d$ was varied and then subsequently also $\Omega_{-1}$, $a_{-5}$ and $a_{+3}$. Fig. 7.25 shows an excellent agreement of the measured values with the final fit, which yields the following values: $\Omega_{-1} = 2\pi \cdot 357(3)$ kHz, $a_{-5} = 0.318(15)$, $a_{+3} = 0.051(17)$ and

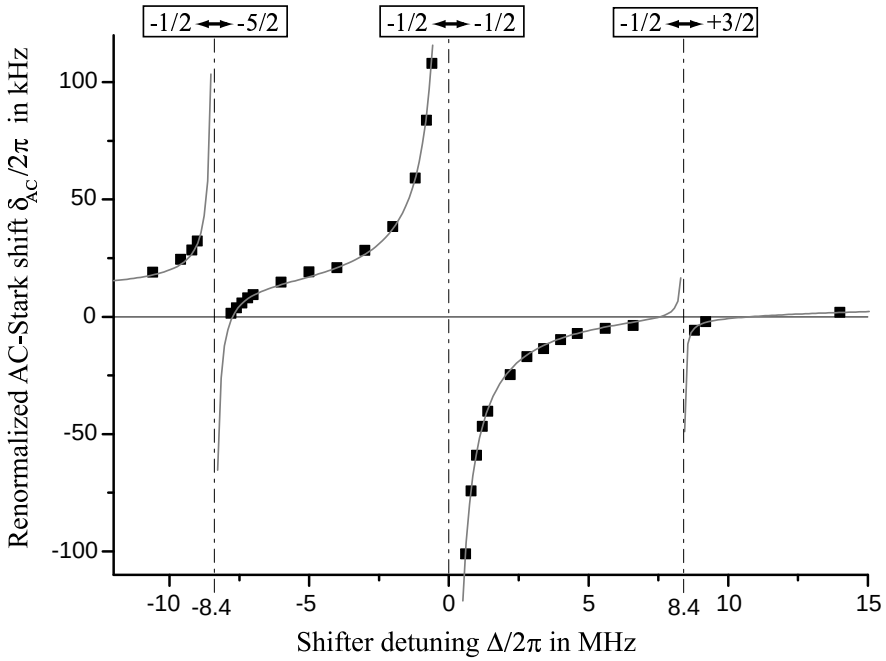


Figure 7.25: Stark shift $\delta_{AC}$ as a function of shifter detuning ($\Delta$). Data points (squares) are calculated from $T$-scans (as in Fig. 7.23) and by renormalizing the obtained $\delta_{AC}$ values to one reference laser power. The fit using eqn. (7.2) (solid line) is in very good agreement with these data.

$d = 0.224(10)/2\pi$ $(\mathrm{MHz})^{-1}$. It can be seen that the shift due to dipole transitions, in other words $d$, is relatively small. The fitted $\Omega_{-1}$ differs from the value measured by direct Rabi oscillations by 5% which is larger than the error bars of each value, which are on the order of 1-2%. This deviation could be explained by slow changes in the laser power over the course of the experiment. Such power drifts can be caused, for example, if the optical fiber transmitting the light at 729 nm slowly rotates the polarization[5] due to thermal effects. At the polarizing beam splitter after the fiber, a possible polarization rotation is directly transformed into a change in the transmitted intensity. The fit result for $a_{-5}$ lies above the theoretical value by about 10% which can be explained by a deviation from the ideal geometry on the order of 10° in beam direction or polarization. By theory the ratio between $a_{-5}$ and $a_{+3}$ is constant under *all* conditions. Thus, if $a_{-5}$ lies above the theoretical value, the same should be true for $a_{+3}$, which is not the case. However, the experimental value for $a_{+3}$ contains a large error as the coupling to the corresponding transition is very weak and only few data points have been recorded in the vicinity of the $-1/2 \leftrightarrow +3/2$ transition.

In order to cross-check the obtained values for $a_{-5}$ and $a_{+3}$, Rabi oscillations on the three carriers were recorded under the same conditions (beam geometry; single ion, sideband cooled) in a separate experiment. Light powers at 729 nm were measured for the three different (AOM) frequencies. The obtained values were used to normalize the obtained Rabi frequency values

[5]Our experience shows that such rotations occur even if fibers specified as "polarization maintaining"are used.

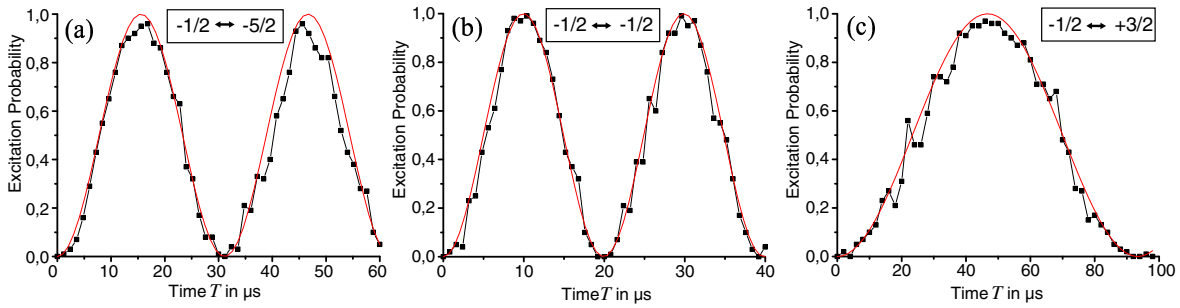


Figure 7.26: Rabi oscillations on the 3 possible carrier transitions when starting from the $S_{1/2}(m=-1/2)$ state in the beam geometry $\phi = 45°, \gamma = 0°$. The corresponding 729 nm light powers and the Rabi frequencies from the fits are (a) 158 $\mu$W $2\pi \cdot 32.15(12)$ kHz (b) 137 $\mu$W $2\pi \cdot 50.20(10)$ kHz (c) 128 $\mu$W $2\pi \cdot 10.71(6)$ kHz.

to the same light intensity. The three scans are shown in Fig. 7.26. The relative squares of the normalized Rabi frequencies yield the values $a_{-5} = 0.357(17)$ and $a_{+3} = 0.049(5)$, which are in agreement with the values obtained from the fit to the AC-Stark shift data.

**AC-Stark Shift Compensation.** The implementation of quantum algorithms in our experiment entails sequences of carrier and sideband pulses. Coupling to a carrier transition is relatively strong, which paradoxically amounts to Stark shifts induced by carrier pulses being negligible compared to the effect of sideband pulses. The reason for this is that a resonantly driven transition does *not* shift itself. When driving a sideband transition resonantly, the nearest other transition is typically a carrier, which produces strong Stark shifts. When, on the other hand, a carrier is driven then the neighboring transitions are typically sidebands. Additionally, a sideband transition in order to get, say, a full $\pi$-pulse must be driven longer by a factor $1/\eta$ if the same light power is applied. For quantum algorithms as they can be realized with our experimental parameters, this means that carrier induced AC-Stark shifts are negligible while sideband induced shifts must absolutely be compensated for.

Applying a laser on the blue axial sideband of the $|S\rangle \leftrightarrow |D\rangle$ transition ("gate laser") at a detuning of $\Delta/2\pi = +1.7$ MHz results in a negative AC-Stark shift $\delta_{AC}$. Shining in a second light field (called "compensator"in the following) at a laser detuning which yields a positive AC-Stark shift can null the overall shift. We typically set the compensator frequency to the red side of the $S_{1/2}(m=-1/2) \leftrightarrow D_{5/2}(m=-5/2)$ resonance by $2\pi \cdot 800$ kHz. At that point it produces reasonably large shifts and at the same time is too far from any resonance to induce off-resonant excitations. Our method to determine the optimum setting of the compensation laser consists of the following steps: First we detune the gate laser by $\simeq 2\pi \cdot 80$ kHz from the sideband resonance to avoid excitation into the $|D\rangle$ state (its AC-Stark effect however is still almost identical to that of a laser field resonant with the sideband). Then we minimize the total AC-Stark effect by adjusting the intensity and detuning of the compensation laser field such that the oscillations in a $T$-scan disappear. Both light fields are generated by applying two RF-frequencies simultaneously to the 729 nm double-pass AOM (AO1 in Fig.5.5). Since both light fields are derived from the same laser, intensity fluctuations do not affect

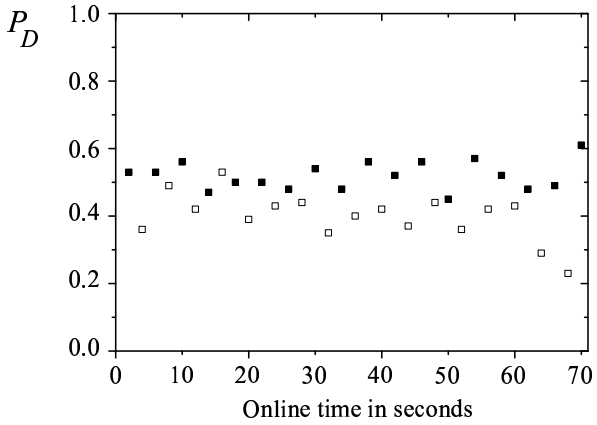


Figure 7.27: Example of online Stark shift compensation data. The time between the Ramsey-pulses was 200$\mu$s. Black squares: data points with $T_1 = 0$, white squares: data points with $T_2 = 200\mu$s.

the compensation. The accuracy to which the AC-Stark effect can be nulled is proportional to $(2\ T_R)^{-1}\ S/N$, where $T_R$ denotes the Ramsey interrogation time (here 200 $\mu$s) and $S/N$ the signal to noise ratio of the state measurement. Integrating this measurement for long times to improve $S/N$ is limited by the frequency drift of the laser source near 729 nm (typically $\leq 1$ Hz/s), since a drift of the relative phase of the Ramsey pulses mimics a residual AC-Stark effect. To overcome this problem we optimize the intensity of the compensation laser by alternating Ramsey experiments with $T_1 = 0$ and $T_2 \simeq 200\mu$s. Thus, a slow drift is discriminated against a residual phase shift due to imperfect compensation. Limited by the shot noise of $P_D(T)$, any AC-Stark effect can be cancelled to within $\simeq 2\pi \cdot 30$ Hz in 60 s. In practice, we first use quite short alternations, for example between $T_1 = 0$ and $T_2 = 20$ $\mu$s and try to minimize the difference between alternating data points by adjusting the power of the compensator. Then we step up $T_2$ and fine tune power and detuning of the compensator at each step. Starting directly with a relatively long $T_2$ of 200 $\mu$s carries the risk of adjusting the accumulated phase to some multiple of $2\pi$ rather than 0. Fig. 7.27 shows compensation data over the course of time, each data point corresponding to 100 repetitions of the experimental sequence with an acquisition time of 2 s. During the acquisition of these data no aspect of the experiment was changed in order to check the stability of the compensation.

## 7.7 Testing the $-1$ Phase of a Sideband $2\pi$ Rabi Rotation

This sections shows an example of a coherent quantum manipulation, in which the AC-Stark shift compensation method introduced in the previous section is applied.

As explained in section 2.2 a resonantly driven two-level system transforms into its initial state only by a $4\pi$ rotation. This $4\pi$ periodicity is experimentally demonstrated here. A mere $2\pi$ rotation leads to a sign change of the wavefunction. This phase shift is the central part of the Cirac-Zoller proposal [34] for quantum gates with trapped ions [?]. Similarly, Ramsey

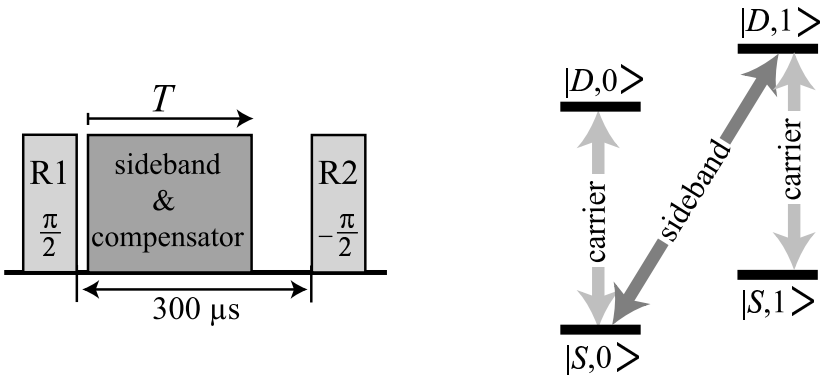


Figure 7.28: Pulse sequence and levels of interest for the "-1 phase" measurement. R1 and R2 are $\pi/2$ carrier pulses.

experiments on Rydberg atoms have been performed in the microwave regime to investigate the AC-Stark shift of the electromagnetic vacuum field [94] and to perform a tunable phase gate [95]. It will be shown how the experiment in our ion trap system deteriorates in terms of acquired phases without proper AC-Stark shift compensation.

As in the previous section, this experiment has been performed with a single ion in standard configuration (see Appendix A.3). This procedure focuses on the qubit levels $|S\rangle$ and $|D\rangle$. The probe sequence, see Fig. 7.28, looks very similar as in section 7.6, only that now the laser pulse in between the two $\pi/2$ carrier pulses is *resonant* to the *blue axial sideband*. Another minor difference is that the phase of the second carrier pulse R2 is set to $\pi$ with respect to the first so that for $T = 0$ the $D_{5/2}$-state probability $P_D$ is zero. The duration $T$ of the intermediate pulse was scanned.

What pattern does one expect from such a scan? The level scheme in Fig. 7.28 illustrates the situation. Remember that the starting point is always $|S, 0\rangle$. Let us assume that AC-Stark shifts during the sideband pulse are negligible (for example due to appropriate compensation with our "additional light" method). Then this interference experiment will yield a sinusoidal variation between 0 and 1, but with twice the oscillation period compared to just Rabi oscillations on the sideband. This behaviour can be easily understood for certain specific times $T$. If, for example, $T$ corresponds to a $2\pi$ rotation on the blue sideband, the $|S, 0\rangle$ state acquires a phase $-1$. This $-1$ sign corresponds to a phase shift of $\pi$, which compensates for the $\pi$-phase of the second carrier pulse. Consequently, R2 pulse brings all the population up to the $|D, 0\rangle$ state. Only the $4\pi$ sideband rotation leads back to the initial state.

In the experiment, first the compensation laser was set in frequency and intensity as explained in section 7.6. The setting was kept and for the rest of the experiment (unless otherwise stated) the compensation light was always on simultaneously with the blue sideband light. Next, the Rabi frequency of the sideband transition was measured under these conditions. Fig. 7.29(a) shows the corresponding Rabi oscillations, which are recorded by simply omitting R1 and R2 in the probe sequence. The solid line is a $\sin^2$ fit yielding a period (i.e. a $2\pi$ time) of 130.6(3) $\mu$s. Now R1 and R2 were inserted again and the result is presented in Fig. 7.29(b):

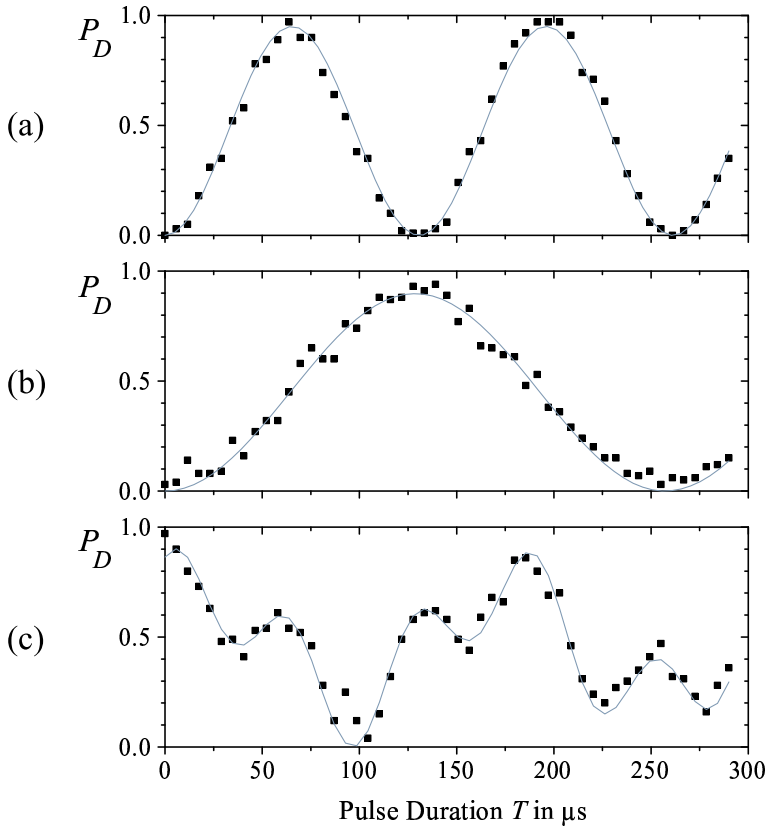


Figure 7.29: (a) Resonant Rabi oscillations on the blue sideband of the $|S\rangle \leftrightarrow |D\rangle$ transition. Period 130.6(3) $\mu$s as found from the fit. (b) Ramsey $\pi/2$ pulses on the $|S\rangle \leftrightarrow |D\rangle$ carrier transition enclose the Rabi flopping on the sideband. The phase of the $|S\rangle$ state has a full cycle period of 257(2) $\mu$s. (c) Same procedure as in (b) but with the AC-Stark shift compensation turned off.

The $2\pi$ rotation, near 131 $\mu$s interaction time, shows up as a $-1$ phase shift ($D$-state probability $\simeq 1$), while after about 260 $\mu$s a full period, corresponding to a sideband $4\pi$ rotation, is completed. The fit in this case yields 257(2) $\mu$s. The ratio of fitted periods is 1.96(3) which agrees well with the expected value of 2.

In this example, the compensation laser had to correct for an AC-Stark shift of $\delta_{AC} \approx 2\pi \cdot 3.5$ kHz. This shift alone would have resulted in an additional phase (between $|S,n\rangle$ and $|D,n\rangle$ independent of $n$, cf. section 8.1) of $\approx 0.82\pi$ in 131 $\mu$s. To show how detrimental this would be to the phase evolution, the scan of Fig. 7.29(b) was repeated, but now the compensator was simply turned off, so the blue sideband light was on alone. The $T$-scan thus obtained is shown in Fig. 7.29(c). The fit function is a weighted sum of two $\cos^2$ functions, allowing for some phase between them. It is not based on a physical picture but just serves to identify the two principle frequencies of oscillation. They come out to be $2\pi \cdot 6.41(8)$ and $2\pi \cdot 16.0(1)$ kHz. Neither of these frequencies coincide with $\delta_{AC} \approx 2\pi \cdot 3.5$ kHz or with the

sideband Rabi frequency $\omega_{sb} = 2\pi \cdot (131\ \mu\text{s})^{-1} = 2\pi \cdot 7.6$ kHz. On the other hand, this is not to be expected as by turning the compensator off the sideband transition is also shifted by $\delta_{AC}$. In the experiment, we did not not adjust the sideband laser to this change, so that it was now detuned from resonance by $\delta_{AC}$. Thus, the sideband Rabi oscillations are off-resonant. Therefore, their amplitude is expected to be 0.86 instead of 1 and their frequency $\approx 2\pi \cdot 8.2$ kHz instead of $2\pi \cdot 7.6$ kHz.

Such unwanted AC-Stark shifts and the corresponding phases could of course be reduced by working at lower Rabi frequencies. This, however, slows the algorithms down which (in view of a limited coherence time) is not desirable.

Note that there is an alternative to the compensation for AC-Stark shifts by additional light fields. Alternatively, the laser power and hence the Rabi-frequency on the sideband transition could be adjusted to a value where a sideband $2\pi$ rotation corresponds to an acquired phase due to AC-Stark shifts which is a multiple of $2\pi$. In this way AC-Stark shifts would be intrinsically cancelled. These "magic Rabi frequencies" can be predicted using the results of section 7.6. In such an experiment, the frequency of the sideband laser would have to be adjusted to the Stark-shifted sideband resonance. Quantum computing experiments employing this method of eliminating AC-Stark shifts are in preparation.

# 8 Experimental Results: Quantum Gates and Algorithms

In the first two sections of this chapter, 8.1 and 8.2, quantum operations are performed in the 2-qubit computational space, composed by a *single ion's* electronic and motional degree of freedom. In state vectors like $|S,0\rangle$ state, the right hand entry denotes the state $(n)$ of the *axial* mode. All experiments were carried out in the single ion standard configuration (see appendix A.3). The axial mode was sideband cooled to ground state probabilites of $\simeq 98\%$.

For all experiments of this chapter AC-Stark shift compensation as explained in sections 7.7 and 7.6 was an indispensable ingredient. This means that along with *every* sideband pulse, suitable light to compensate for level shifts had to be applied, even though it is not always marked in the pulse sequences or in the text.

## 8.1 Sideband Induced Stark Shifts - a Dispersive Phase Gate

The following describes experiments probing the comparably small AC-Stark shifts induced by coupling to a motional sideband. In order to detect Stark shifts due to this relatively weak transition the experiment had to be carried out in the special regime of rather small detuning $\Delta_S$ from a motional sideband. However, $\Delta_S$ must still remain large enough for the sideband coupling to produce no, or a very small amount of, population transfer. In order to detect these small level shifts, first residual AC-Stark shifts due to coupling to various other transitions have to be compensated for by the method explained in section 7.6. Light shifts induced by sideband coupling are particularly interesting as they are proportional to the motional quantum number $n$ of the mode. This feature, namely the possibility of inducing well defined state dependent level shifts, allows the implementation of a $CNOT$-type universal quantum gate in the 2-qubit space of a single trapped ion.

The probe sequence is shown in Fig. 8.1. The pulses labelled R1 and R2 are $\pi/2$ pulses on the carrier of the $|S\rangle \leftrightarrow |D\rangle$ transition with a fixed waiting time of 260 $\mu$s between them, composing a Ramsey-type spectroscopy setup. During the "AC" period, two laser fields are applied simultaneously, namely one "shifter" which is (blue-)detuned by only $\Delta_S = 60$ kHz from the blue axial sideband of the $|S\rangle \leftrightarrow |D\rangle$ transition, along with its compensator. Both laser fields, the shifter and compensator, ideally do not induce any population transfer but only level shifts.

Fig. 8.2 shows the levels of interest. Captions *below* each level indicate how the level is shifted under the action of the shifter only: On one hand, the shifter couples off-resonantly to other Zeeman-transitions (carriers) at 729 nm as well as to dipole allowed transitions. The corresponding shift is the same for all levels $|S,n\rangle$ because carrier-type coupling in the Lamb-

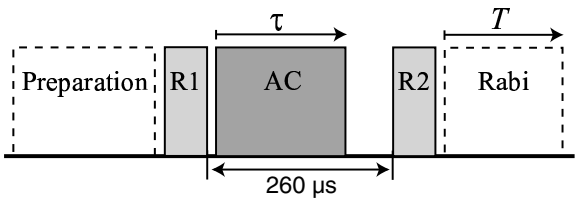


Figure 8.1: Generic probe sequence for the measurement of sideband induced Stark shifts and the implementation of a quasi-CNOT gate. The central part, in solid lines, is always applied, while the dashed sequences are used for certain measurements only.

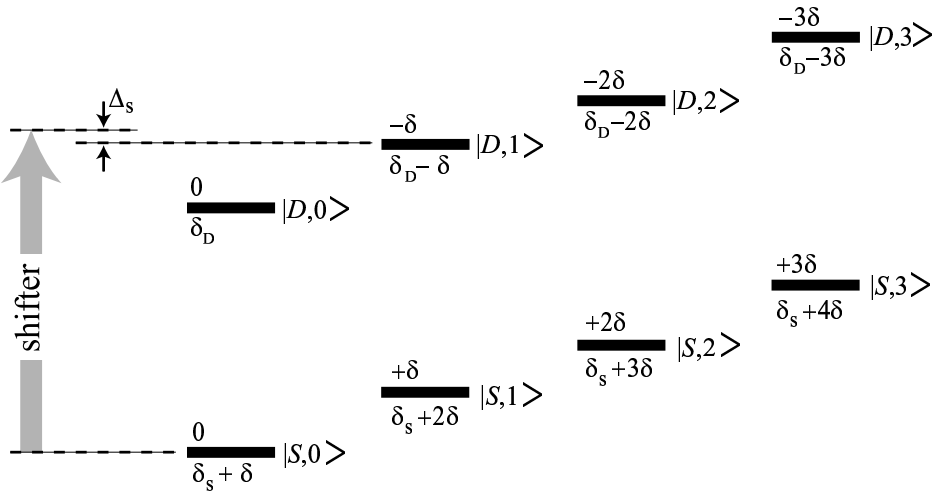


Figure 8.2: Ladder of equidistant oscillator levels $n = 0$ to $n = 3$ of the axial mode mixed with the ion's electronic degree of freedom, $|S\rangle$ and $|D\rangle$.

Dicke regime is independent of $n$. The same holds for all $|D, n\rangle$ levels. The corresponding shifts are denoted $\delta_S$ and $\delta_D$, respectively. Coupling to sideband transitions, however, strongly depends on the motional quantum number: the (resonant) Rabi frequency of the blue sideband between $|S, n\rangle$ and $|D, n+1\rangle$ is $\Omega_{n,n+1} = \sqrt{n+1}\eta\Omega_0$ (see section 3.3.3). Here $\Omega_0$ is the carrier ($|S\rangle \leftrightarrow |D\rangle$) Rabi frequency and $\eta$ the Lamb-Dicke factor of the axial mode, in this case $\eta = 6.8\%$. As discussed in section 3.3.6, the AC-Stark effect induced by off-resonant coupling to some transition shifts the upper and lower level by $-\Omega^2/4\Delta$ and $+\Omega^2/4\Delta$, respectively. Consequently, sideband coupling produces additional $n$-dependent level shifts, which are multiples of $\delta := (\eta\Omega_0)^2/4\Delta_S$, cf. Fig. 8.2.

In a first series of experiments the compensator was optimized. According to the results from section 7.6, its detuning was set to 860 kHz to the red side of the $S_{1/2}(m = -1/2) \leftrightarrow D_{5/2}(m = -5/2)$ resonance. The goal was now to adjust the intensity of the compensator such that it exactly nulls this relative shift. In general, this is only possible modulo some

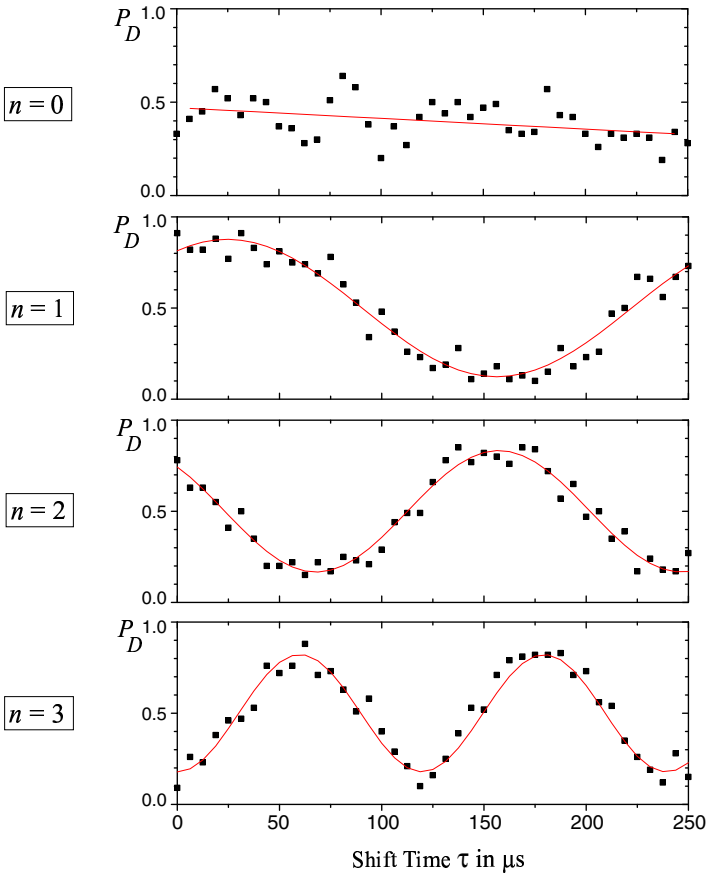


Figure 8.3: Ramsey pattern probing the relative AC-Stark shift between $|S,n\rangle$ and $|D,n\rangle$ with optimally adjusted compensator. The oscillation frequencies are expected to be $n \cdot \delta_{ac}$

offset shift common to *all* levels in Fig. 8.2. Such an overall shift, however, does not result in a relative phase between laser and ion, hence is not detectable, and therefore this overall shift will be ignored in the following. The experimental procedure now uses only the central part of the probe sequence (solid lines), where the duration $\tau$ of the AC period is scanned. Just as in section 7.6, the frequency of the resulting oscillations is exactly the relative level shift (between $|S,0\rangle$ and $|D,0\rangle$) induced by shifter and compensator applied simultaneously. The goal then is to find the compensator intensity where this frequency becomes zero, i.e. where there is no more oscillation. For this process we detune the Ramsey-pulses slightly from resonance so that with $\tau = 0$ we end up in the middle of a Ramsey-fringe, at $P_D \approx 50\%$. This regime is the most sensitive to phases acquired in the time between R1 and R2. An example scan where the compensator power is well set is shown in Fig. 8.3 at the label "$n = 0$". Residual fluctuations can be seen. These are due partially to random magnetic fields as well as laser frequency and power fluctuations. Note however, that by making 100 electron shelving experiments for one data point we always face residual statistical (shot noise limited) fluctuations of 10%. The

average excitation probability, however, only changes with a ramp of $-6(2) \cdot 10^{-4} \mu s^{-1}$ (linear fit) which gives an estimate of $\delta_{res} \leq 2\pi \cdot 180$ Hz for the residual relative level shift of this scan. As in the experiments of section 7.6, drifts of the reference cavity of the 729 nm laser are compensated for by performing every scan twice, one forward and then another scan backward from $\tau = 250$ $\mu$s down to $\tau = 0$ $\mu$s. From our data we calculate that with this method we can null the relative level shift to within $2\pi \cdot 300$ Hz. This optimum adjustment of shifter and compensator power was kept for all following experiments. The individual level shifts under these conditions are indicated in Fig. 8.2 with labels *above* each level: the compensator effectively reduces the shift of all $|S, n\rangle$ and $|D, n\rangle$ levels by $\delta_S + \delta$ and $\delta_D$, respectively.

In the next step of the experiment the ion is transferred into the $|S, 1\rangle$ state in the Preparation period, with the rest of the procedure remaining the same. This preparation is carried out by applying a resonant blue sideband $\pi$-pulse followed by a resonant carrier $\pi$-pulse, the transfer efficiencies of which are 98% and 99%, respectively. The same type of $\tau$-scans as above are performed. We now expect to actually see an oscillation with a frequency $\delta_{ac} = 2\delta$ when scanning $\tau$, as we now probe the relative phase between $|S, 1\rangle$ and $|D, 1\rangle$. For this measurement, that is for the frequency of the oscillation, it is not essential for the pulses R1 and R2 to be exactly on resonance. Consequently, slight detunings on the order of a few hundred Hz were accepted, as permanent control of the resonance condition is time consuming. Therefore the following scans do not necessarily start at $P_D = 1$. An exemplary scan is shown in Fig. 8.3 ($n = 1$). By the same method, the $|S, 2\rangle$ and the $|S, 3\rangle$ states have also been prepared by appropriate combinations of resonant blue sideband and carrier pulses, expecting frequencies of $2\delta_{ac}$ and $3\delta_{ac}$ in our $\tau$-scans. Fig. 8.3 also shows examples for these cases.

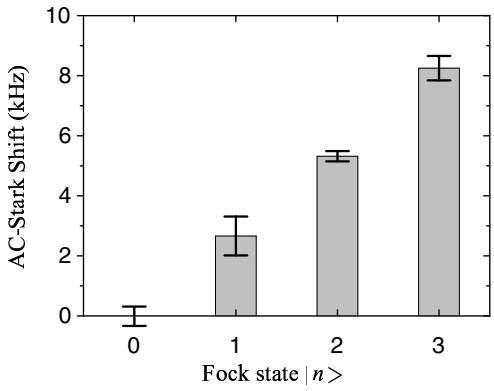


A total of 35 back and forth scans were recorded for $n = 0, 1, 2$ or 3 as input states. Fig. 8.4 shows the evaluation of the whole data set. It can be seen that the measured AC-Stark effect really is "quantized", as expected. A linear fit of this plot yields $\delta_{ac} = 2\pi \cdot 2.71(6)$ kHz.

The following will describe how this experimental scheme can be used to implement a quantum gate in the two-qubit computational space composed of the states $\{|S, 0\rangle, |D, 0\rangle, |S, 1\rangle, |D, 1\rangle\}$. The arrangement of operator matrices refers to the latter order of basis states. Let $\Phi(\tau)$ be the unitary matrix representing the action of just the shifter+compensator pulse of length $\tau$. After a suitably chosen $\tau_0$, namely such that $\delta_{ac} \cdot \tau_0 = \pi$, the states $|S, 1\rangle$ and $|D, 1\rangle$ have acquired phases of $e^{\pm i\pi/2} = \pm i$, respectively, whilst $|S, 0\rangle$ and $|D, 0\rangle$ do not acquire any phase (cf. Fig. 8.2), thus

$$\Phi(\tau_0) = \begin{bmatrix} 1 & 0 & 0 & 0 \\ 0 & 1 & 0 & 0 \\ 0 & 0 & i & 0 \\ 0 & 0 & 0 & -i \end{bmatrix}.$$

Moreover, the surrounding Ramsey pulses were from now on carefully kept on resonance to

within ±100 Hz. In a first experiment, the laser field of pulse R2 was set to have a phase of $\pi$ with respect to R1. They can therefore be seen as $R_{x1}(\pi/2)$ and $R_{\overline{x}1}(\pi/2)$ pulses. Note that the lower index 1 is used to indicate the internal qubit, see section 4.2. The corresponding matrices read

$$\frac{1}{\sqrt{2}}\begin{bmatrix} 1 & \pm i & 0 & 0 \\ \pm i & 1 & 0 & 0 \\ 0 & 0 & 1 & \pm i \\ 0 & 0 & \pm i & 1 \end{bmatrix},$$

where the + signs refer to R1= $R_{\overline{x}1}(\pi/2)$ and the − signs to R2= $R_{x1}(\pi/2)$. The main sequence then reads

$$C = R_{x1}(\pi/2) \cdot \Phi(\tau_0) \cdot R_{\overline{x}1}(\pi/2) = \begin{bmatrix} 1 & 0 & 0 & 0 \\ 0 & 1 & 0 & 0 \\ 0 & 0 & 0 & -1 \\ 0 & 0 & 1 & 0 \end{bmatrix}.$$

Except for the one minus sign, which will be discussed below, $C$ represents a *CNOT* gate where the vibrational qubit controls the internal qubit, with the more intuitive allocation $|0\rangle = |n = 0\rangle$ and $|1\rangle = |n = 1\rangle$. If R1 and R2 have the same laser phase (R1=R2=$R_{x1}(\pi/2)$), then the operation reads

$$C' = R_{x1}(\pi/2) \cdot \Phi(\tau_0) \cdot R_{x1}(\pi/2) = \begin{bmatrix} 0 & 1 & 0 & 0 \\ 1 & 0 & 0 & 0 \\ 0 & 0 & -1 & 0 \\ 0 & 0 & 0 & 1 \end{bmatrix}.$$

This is (again except for the minus sign) a *CNOT* gate with the inverse allocation $|0\rangle = |n = 1\rangle$ and $|1\rangle = |n = 0\rangle$ for the control qubit. It can, of course, also be seen as a *0-CNOT*-like gate with the intuitive allocation from above. The properties of the operation $C$ in particular the fact that it is a universal two-qubit quantum gate, have been discussed in section 2.2. The same reasoning holds for $C'$.

The fit of Fig. 8.4 gives $\tau_0 = (2{\cdot}2.71\ \text{kHz})^{-1} = 185\ \mu$s. During the running experiment $\tau_0$ was determined from a reduced set of data, the result being 200 $\mu$s. For the following experiments $\tau$ was thus *fixed* to 200 $\mu$s. We have then probed the probability truth table of the gate $C$ by subsequently preparing the 4 possible input states (again with appropriate combinations of resonant carrier and sideband $\pi$-pulses in the Preparation period) and by performing *resonant* Rabi oscillations on the blue sideband in the "Rabi" period as a state readout. The resulting scans of the "Rabi time" $T$ are shown in Fig. 8.5. The data were analysed by first performing reduced contrast sinusoidal fits to the cases A, C and D in order to determine the principal frequencies of oscillation. The results are $\omega_A = (2\pi)11.9(1)$, $\omega_C = (2\pi)12.0(2)$ and $\omega_D = (2\pi)16.95(5)$ kHz. The ratios $\omega_D/\omega_A$ and $\omega_D/\omega_C$ are expected to be $\sqrt{2}$, which is very well confirmed by the fit results: $(\omega_D/\omega_A)^2 = 2.02(4)$, $(\omega_D/\omega_C)^2 = 1.99(7)$. All four data sets were fitted again fitted taking these frequencies as fixed. This time a superposition of all four states was allowed as a final state of the gate. The applied fit function reads

$$P_D(T) = 1 - \frac{1}{2}(a_2 + a_3 + a_4 - (a_2 - a_3)\cos(\omega_1 \cdot T) + a_4 \cos(\omega_2 \cdot T)),$$

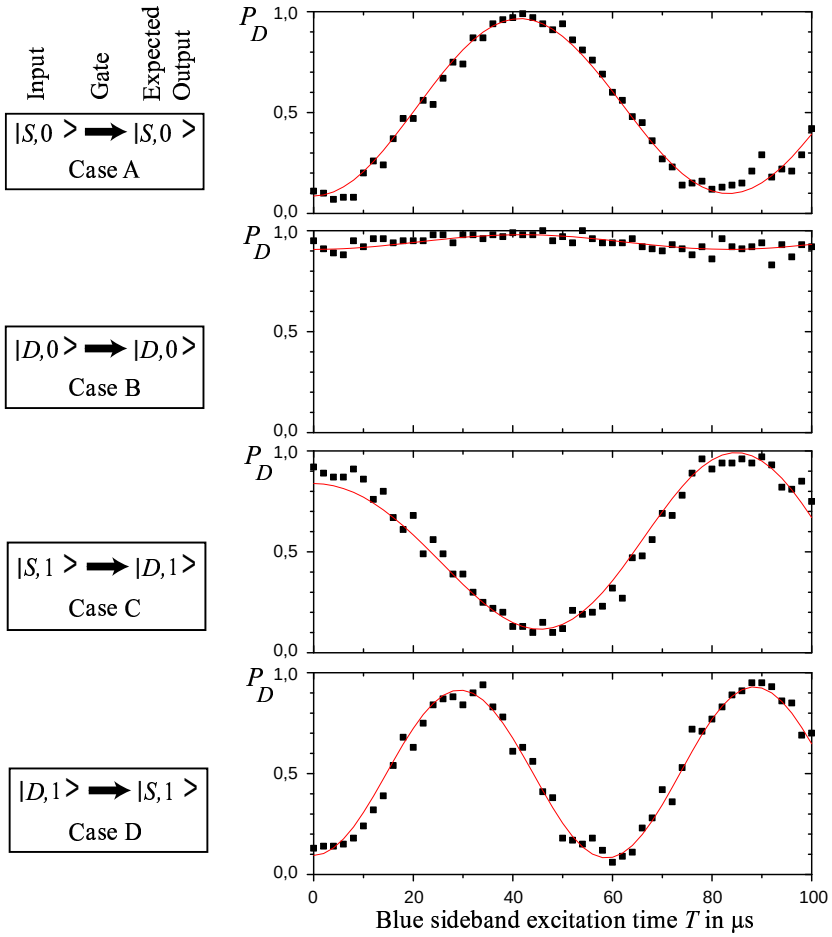


Figure 8.5: Probing the universal quantum gate $C$.

with $\omega_1 = (2\pi)12.0$ kHz and $\omega_2 = (2\pi)16.95$ kHz. The fit parameters $a_i$ are the probabilities of the four states. The function contains only the parameters $a_2$ (corresponding to $|D,1\rangle$), $a_3$ ($|S,0\rangle$) and $a_4$ ($|S,1\rangle$). The probability $a_1$ of $|D,0\rangle$ is determined from the normalization condition

$$a_1 + a_2 + a_3 + a_4 = 1.$$

The solid lines in Fig. 8.5 correspond to these fits. The following table lists the obtained $a_i$ and can be regarded as the truth table of the implemented quantum gate in terms of probabilities:

| ↓input | $\|S,0\rangle$ | $\|D,0\rangle$ | $\|S,1\rangle$ | $\|D,1\rangle$ |
|---|---|---|---|---|
| $\|S,0\rangle$ | 0.90(1) | 0.06(1) | 0.01(2) | 0.03(1) |
| $\|D,0\rangle$ | 0.09(1) | 0.89(1) | 0.00(1) | 0.02(1) |
| $\|S,1\rangle$ | 0.00(1) | 0.03(1) | 0.16(2) | 0.81(2) |
| $\|D,1\rangle$ | 0.07(1) | 0.00(1) | 0.84(2) | 0.09(2) |

In fact, by using this fit function the assumption is made that the "leakage of probability" into

"unwanted" states, i.e. the deviation from the perfect table, namely

| ↓input | $\|S,0\rangle$ | $\|D,0\rangle$ | $\|S,1\rangle$ | $\|D,1\rangle$ |
|---|---|---|---|---|
| $\|S,0\rangle$ | 1 | 0 | 0 | 0 |
| $\|D,0\rangle$ | 0 | 1 | 0 | 0 |
| $\|S,1\rangle$ | 0 | 0 | 0 | 1 |
| $\|D,1\rangle$ | 0 | 0 | 1 | 0 |

is due to *incoherent* processes. Taking unwanted coherent processes into account, would have required additional fit parameters, namely the phases acquired due to these processes as well as the ratios between coherent and incoherent leakage processes. This was not possible, as one data set as shown in Fig. 8.5 does not contain enough points for a reasonable fit with so many parameters. It should be stressed, however, that such a "perfect" fit in our case could only result in small corrections of the probability table on the order of 1%.

The $a_i$ determined above are in fact pessimistic estimates of the gate performance because they also include the imperfections of the input state preparation. If one assumes a carrier $\pi$-pulse fidelity of 99% and 98% for the sideband $\pi$-pulses of the Preparation period, one gets the following corrected probability truth table. It describes the fidelity of the quantum gate itself.

| ↓input | $\|S,0\rangle$ | $\|D,0\rangle$ | $\|S,1\rangle$ | $\|D,1\rangle$ |
|---|---|---|---|---|
| $\|S,0\rangle$ | 0.90(1) | 0.06(1) | 0.01(2) | 0.03(1) |
| $\|D,0\rangle$ | 0.08(1) | 0.90(1) | 0.00(1) | 0.02(1) |
| $\|S,1\rangle$ | 0.00(1) | 0.01(1) | 0.15(2) | 0.84(2) |
| $\|D,1\rangle$ | 0.05(1) | 0.00(1) | 0.86(2) | 0.09(2) |

In a second series of experiments, the $C'$ gate has been implemented by using equal phases for the Ramsey pulses and again with $\tau = 200$ $\mu$s fixed. The same procedure was applied, including Rabi oscillations and their fits as a state read-out. The resulting probability truth table, *not* corrected for imperfect input state preparation, reads

| ↓input | $\|S,0\rangle$ | $\|D,0\rangle$ | $\|S,1\rangle$ | $\|D,1\rangle$ |
|---|---|---|---|---|
| $\|S,0\rangle$ | 0.10(1) | 0.87(1) | 0.01(1) | 0.02(1) |
| $\|D,0\rangle$ | 0.88(1) | 0.08(1) | 0.00(1) | 0.04(1) |
| $\|S,1\rangle$ | 0.07(1) | 0.00(1) | 0.85(2) | 0.08(2) |
| $\|D,1\rangle$ | 0.02(2) | 0.04(2) | 0.14(2) | 0.80(2) |

Both gate performances (uncorrected) are depicted in Fig. 8.6 in a bar diagram representation. The fidelity of $C$ and $C'$ as they were implemented is reduced by a not perfectly chosen $\tau_0$, phase noise between the two Ramsey pulses, and off-resonant sideband excitations during the AC period which were measured to be on the order of 4%.

A nice feature of this type of gate is that it naturally conserves the computational space: the off-resonant sideband coupling in principle induces only quantum phases but no population transfer. This *dispersive* coupling is reminiscent of NMR quantum computation. In NMR, qubits are identified as nuclear 1/2-spins of neighboring atoms in a molecule. Under the conditions in which NMR quantum computing is performed today [13], namely in a liquid and when couplings are weak, the two-qubit coupling required for quantum gates has the

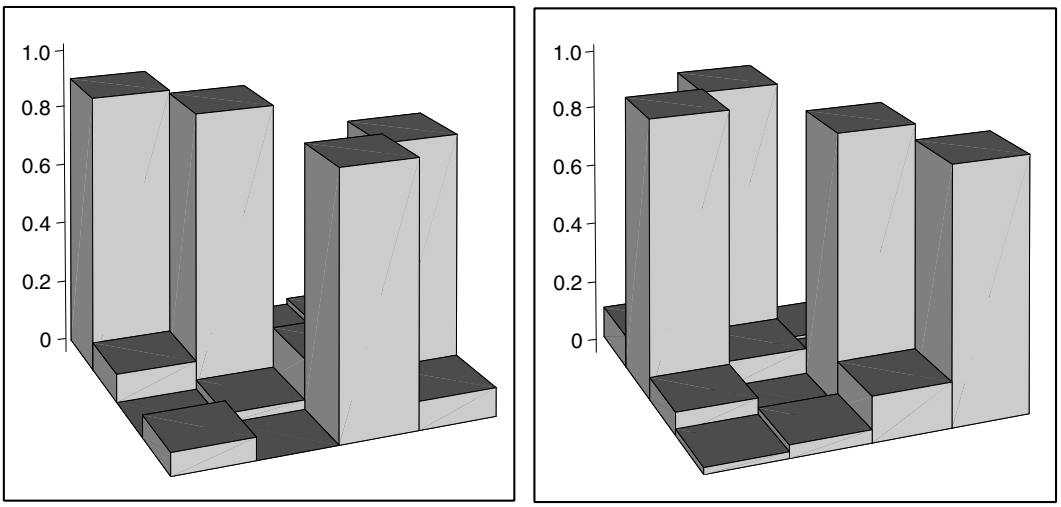


Figure 8.6: Experimentally measured probability tables for the $CNOT$-like operation $C$ (left) and the *0-*$CNOT$-like operation $C'$ (right).

form $H_{1,2}^J \simeq \frac{\hbar J}{4} Z_1 Z_2$ where $J$ denotes the coupling strength and the lower indices refer to the two neighboring spin-1/2 nuclei. Just as our off-resonant sideband interaction, the coupling $H_{1,2}^J$ does not lead to any population transfer and realizes a universal phase gate if applied for a well-defined time. The major difference is that in the case of NMR this coupling is always present. A large component of NMR quantum computing sequences is therefore required just to effectively cancel the action of $H_{1,2}^J$ at times when it is not wanted, using a technique known as refocussing [13]. In comparison, our ion trap system has the considerable advantage that the (sideband) two-qubit coupling can easily be switched on and off.

## 8.2 The Deutsch-Jozsa Algorithm

Let us first write out the complete pulse sequences $P_i$, expressed in pulse durations and phases, for the four cases, which were developed in section 4.3.2.

- $P_1 = R(\pi/2, -\pi/2)\ R(\pi/2, \pi/2)$
- $P_2 =$
  $R(\pi/2, -\pi/2) \mid R_{swap}(\pi)\ R(\pi/2, -\pi/2)\ R(\pi, \pi)\ R(\pi/2, \pi/2)\ R_{swap}(0) \mid R(\pi/2, \pi/2)$
- $P_3 = R(\pi/2, -\pi/2) \mid R_{phase} \mid R(\pi/2, \pi/2)$
- $P_4 = R(\pi/2, -\pi/2) \mid R(\pi, \pi)\ R_{phase}\ R(\pi, \pi) \mid R(\pi/2, \pi/2)$

Vertical dashes | mark the boundary of the black box operation, which in Case 1 consists just of a pure waiting time. The two-qubit operations, which are all implemented by using blue sideband pulses, read

$$R_{phase} = R^+(\pi, \frac{\pi}{2})\ R^+(\frac{\pi}{\sqrt{2}}, 0)\ R^+(\pi, \frac{\pi}{2})\ R^+(\frac{\pi}{\sqrt{2}}, 0)$$

and

$$R_{swap}(\phi_0) = R^+(\frac{\pi}{\sqrt{2}}, \phi_0)\ R^+(\frac{2\pi}{\sqrt{2}}, \phi_0 + \phi_{swap})\ R^+(\frac{\pi}{\sqrt{2}}, \phi_0).$$

In our experiment, those sideband operations represent the critical part of a sequence. This is due to the fact that our Lamb-Dicke parameter is relatively small (6.8% in this experiment). In order to avoid off-resonant carrier excitations, sideband transitions may only be driven slowly (cf. eqn. (3.33)). This makes sideband pulses long ($\pi$-times on the order of 100 $\mu$s) which soon conflicts with our coherence times on the order of[1] 400 $\mu$s. With $5.7\pi$, Case 2 is clearly the longest in terms of total sideband pulse time.

Before implementing the complete Deutsch-Jozsa sequences, the two critcal components, namely the *SWAP* operation and the phase gate $\Phi$, were tested separately. Our standard method for verification of the correct functioning of a sequence is to *trace* the complete operation in terms of $D_{5/2}$-state probability $P_D$. For this, we truncate the pulse sequence at a certain time $t$ and reveal $P_D$ equal to $\langle 1|a(t)\rangle$, see Fig. 4.7. In the experiment, the laser powers for sideband and carrier excitation must be adjusted for the desired Rabi frequencies. Moreover, AC-Stark shift compensation has to be arranged for the blue sideband excitation and used along with every pulse. Fig. 8.7 shows experimental traces of the $\Phi$ gate and of the $SWAP(\phi_0 = 0)$ operation alone. Note that in the absence of other pulses, $\phi_0$ is not well defined, but can always be set to 0 by definition. The data agree well with the calculated ideal evolution. The latter contains no fit parameters and assumes no errors (as decoherence or off-resonant excitations).

Subsequently the complete sequences of all four cases were implemented and traced by the same method, see Fig. 8.8. In a "standard" run of the Deutsch-Jozsa algorithm, $P_D$ would only be read out at the end of the sequence and ideally would be 1 in cases 3 and 4 (balanced

[1] This number corresponds to the time when we implemented the Deutsch-Jozsa algorithm. Soon afterwards, with the help of an active compensation system for magnetic field fluctuations, we were able to prolong the coherence time to 600 $\mu$s, see section 7.3.

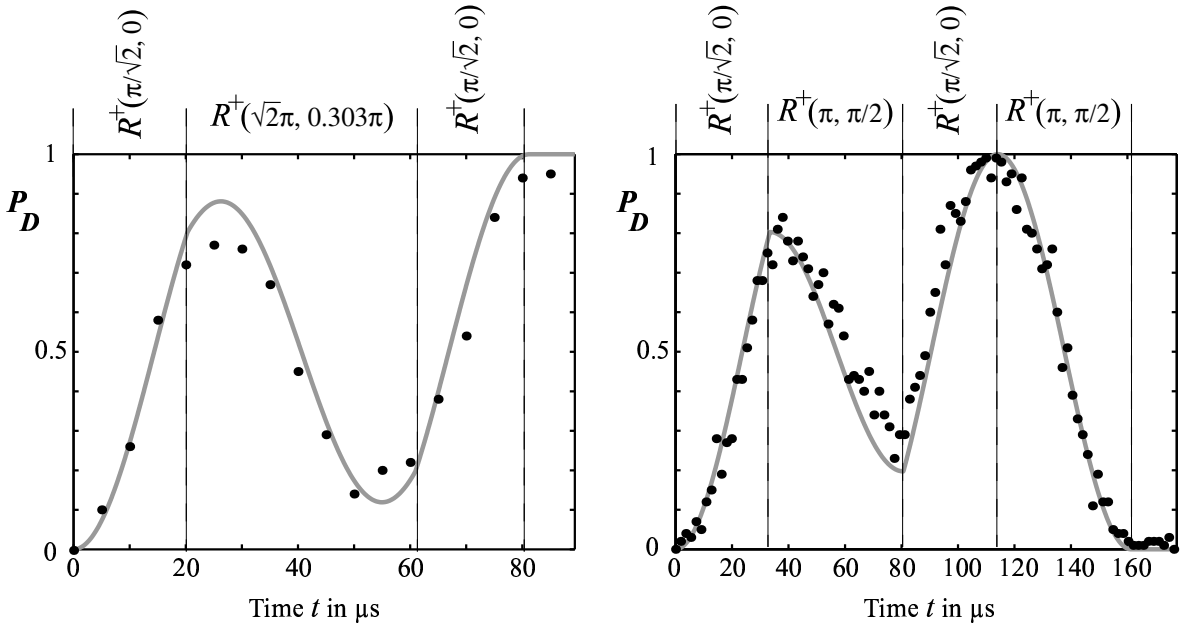


Figure 8.7: Experimental implementations of two major building blocks for the Deutsch-Jozsa algorithm. LEFT: $SWAP(0)$ operation; the laser power was adjusted for a blue sideband $2\pi$ Rabi period $T_{2\pi}^{SB}$ of 57.7 $\mu$s. RIGHT: Phase gate $\Phi$ with $T_{2\pi}^{SB} =$ 94.9 $\mu$s. The dashed lines mark the switching points of the laser phase. Solid grey lines are numerical simulations of the ideal evolution which contain no adjustable parameters.

functions) and 0 in cases 1 and 2 (constant functions). The tracing was extended somewhat beyond the end of the actual sequences (see Fig. 8.8) in order to acquire a good statistics on the output. The mean value of these final points corresponds to the readout $|\langle 1|a\rangle|^2$ of the algorithm. The results are listed in the following Readout Table:

| ↓case | expected $\lvert\langle 1\rvert a\rangle\rvert^2$ | measured $\lvert\langle 1\rvert a\rangle\rvert^2$ | expected $\lvert\langle 1\rvert w\rangle\rvert^2$ | measured $\lvert\langle 1\rvert w\rangle\rvert^2$ |
|---|---|---|---|---|
| $f_1$ | 0 | 0.019(6) | 1 | - |
| $f_2$ | 0 | 0.087(6) | 1 | 0.90(1) |
| $f_3$ | 1 | 0.975(4) | 1 | 0.93(1) |
| $f_4$ | 1 | 0.975(2) | 1 | 0.98(1) |

It can be seen that the algorithm works with good fidelity in all four cases.

In order to characterize not only the final state of the first (internal) but also that of the second (vibrational) qubit, the same method as for the AC-Stark shift based quantum gate $C$ of section 8.1 was employed: Resonant Rabi oscillations on the blue sideband were appended to the sequences. The scans are shown in Fig. 8.9. This was carried out for only the "non-trivial" cases 2, 3 and 4. The fits were performed with the same type of 4-component fuction as in section 8.1. These fits yield estimates for the individual probabilities of the four

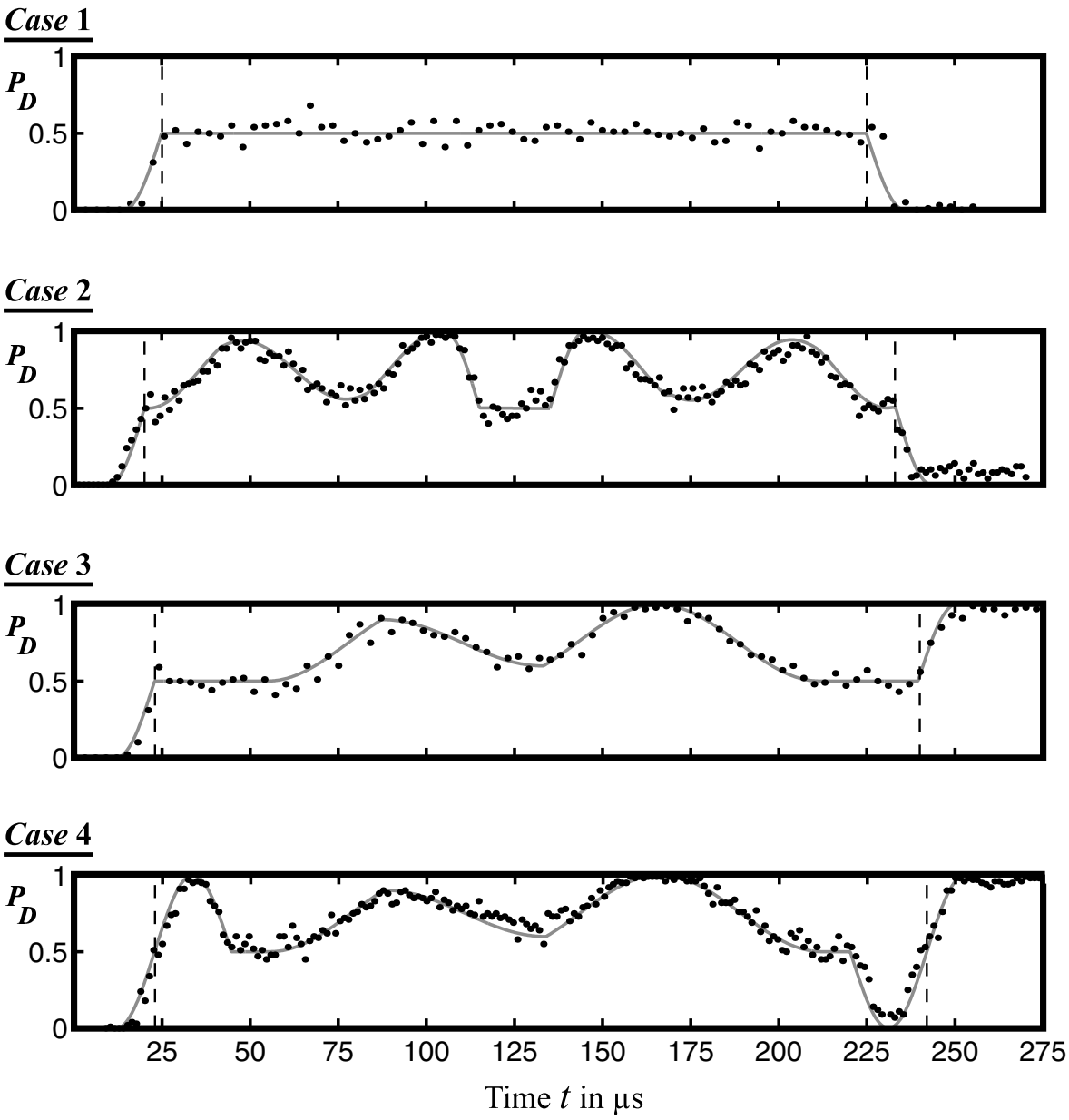


Figure 8.8: Experimental trace of all four cases of the Deutsch-Jozsa algorithm. The dashed lines mark the black box part of the sequences. Solid lines are numerical simulations of the ideal evolution which contain no adjustable parameters.

computational states at the end of the algorithm, which are listed in this table:

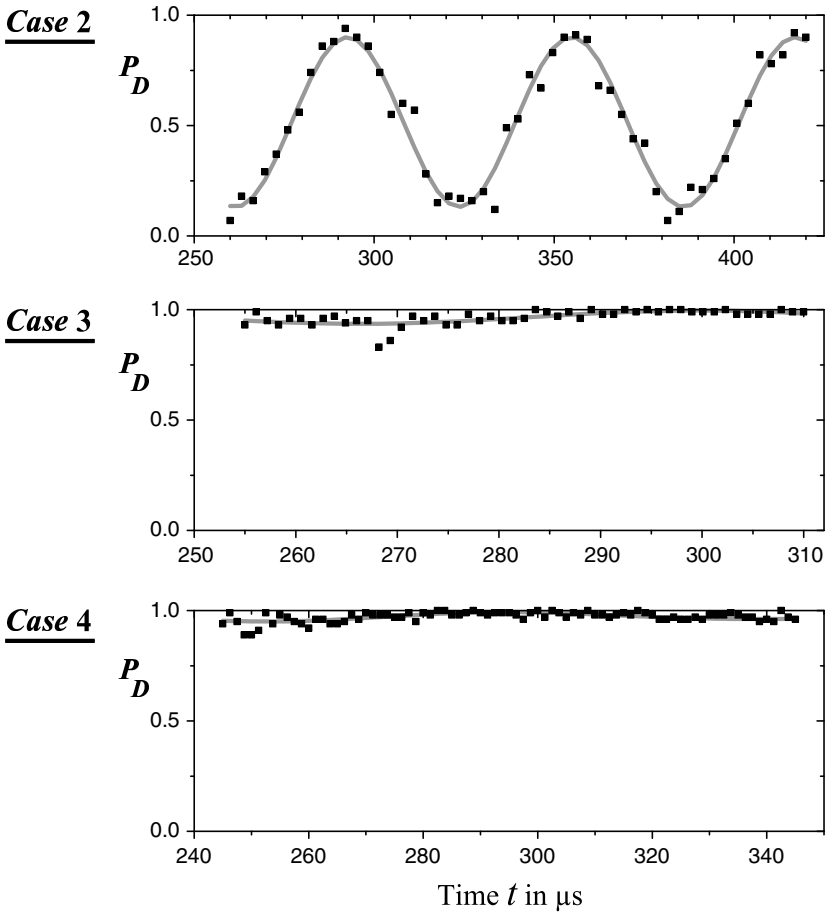


Figure 8.9: Experimental trace over the appended blue sideband Rabi oscillations for the cases $f_2$, $f_3$ and $f_4$. As expected, in cases 3 and 4 essentially no oscillation takes place, because the final state $|D, n = 0\rangle$ is dark for the blue sideband. Likewise, case 2 shows an oscillation with a Rabi frequency corresponding to the transition $|S, n = 0\rangle \leftrightarrow |D, n = 1\rangle$. For the results of the fits (solid lines), see text.

| ↓case | $\|S,0\rangle$ | $\|D,0\rangle$ | $\|S,1\rangle$ | $\|D,1\rangle$ |
|---|---|---|---|---|
| $f_2$ | 0.87(1) | 0.03(1) | 0.00(2) | 0.10(1) |
| $f_3$ | 0.00(1) | 0.93(1) | 0.06(1) | 0.01(1) |
| $f_4$ | 0.03(1) | 0.95(1) | 0.01(1) | 0.01(1) |

The sum of the probabilities of $|S, 0\rangle$ and $|D, 0\rangle$ gives the probability $|\langle 1|w\rangle|^2$ of the vibrational qubit being in the $|n = 0\rangle$ state (logic state $|1\rangle$) which is the expected output state in all four cases (see Fig. 4.8). Those values are also listed in the Readout Table above.

## 8.3 The Cirac-Zoller Gate - First Results

**First Experiments.** Work on the implementation of the Cirac-Zoller gate is in progress. First results are shown here, while the complete work will be presented in the thesis of Mark Riebe. Section 4.4 explains that there are various possibilities for the implementation of a Cirac-Zoller type quantum gate and that for the first realization we have chosen a composite pulse technique. The corresponding pulse sequence is given in eqn. (4.6) and visualized in Fig. 8.10. The grey shaded pulse P represents the preparation period in which one of the four computational basis states $|S,S\rangle, |S,D\rangle, |D,S\rangle, |D,D\rangle$ is prepared as an input state. The other pulses represent the actual gate sequence of eqn. (4.6): M labels the $MAP$ operations ($R_1^+$ pulses) which map the state of ion 1 to the bus mode and back, $\Phi$ denotes the pulse sequence of the phase gate $\Phi_2'$ (consisting of four concatenated pulses) and the two (Ramsey-type) carrier pulses on ion 2 ($R_{y2}(\pi/2)$ and $R_{\overline{y}2}(\pi/2)$) are labeled by R. The input state preparation in period P is carried out by suitable and addressed carrier $\pi$-pulses. Note that we can also prepare an arbitrary *superposition* of basis states as an input. For the bra-ket notation (ex. $|D,S\rangle$) the following convention is chosen: the control ion comes first (left) and the target ion second (right).

The experiments were carried out in the two-ion standard configuration discussed in Appendix A.3. Note that for individual ion read-out a 40 ms pulse sequence is employed as detailed in section 7.4. Switching the addressing beam from one ion to the other requires switching of the high-voltage on the beam deflector. The time required for this switching is 15 $\mu$s in the present setup. Note that in the actual gate sequence, the beam must be switched twice and that additional switching is possibly necessary in the preparation period, depending on the desired input state. In a first implementation, comparably low sideband Rabi frequencies $\Omega_S = 2\pi \cdot 5.6$ kHz were used resulting in a rather long gate sequence of about 600 $\mu$s. Results are shown in Fig. 8.11. The procedure of tracing the experimental sequence by truncating it at times $t$ is the same as, for example, in the Deutsch-Jozsa experiments of section 8.2. Note that the solid lines in Fig. 8.11 do not represent a fit but the calculated evolution of probabilities[2]. Input parameters for these calculations are the independently measured Rabi frequencies on the carrier and sideband transitions as well as the addressing error. The date agree well with the calculated ideal evolution. Deviations occur mainly at the end of the sequence where all phase errors have accumulated.

The performance of the gate operation is currently limited primarily by phase noise due to laser and magnetic field fluctuations: according section 7.3, the loss of contrast over the time of the implemented gate sequences is 15% leading to a loss of gate fidelity of the same magnitude. Other relevant error sources are laser intensity fluctuations, laser detuning er-

[2]Calculations performed by Hartmut Häffner.

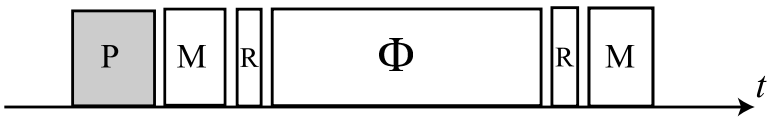


Figure 8.10: Complete pulse sequence for the implementation of a Cirac-Zoller gate.

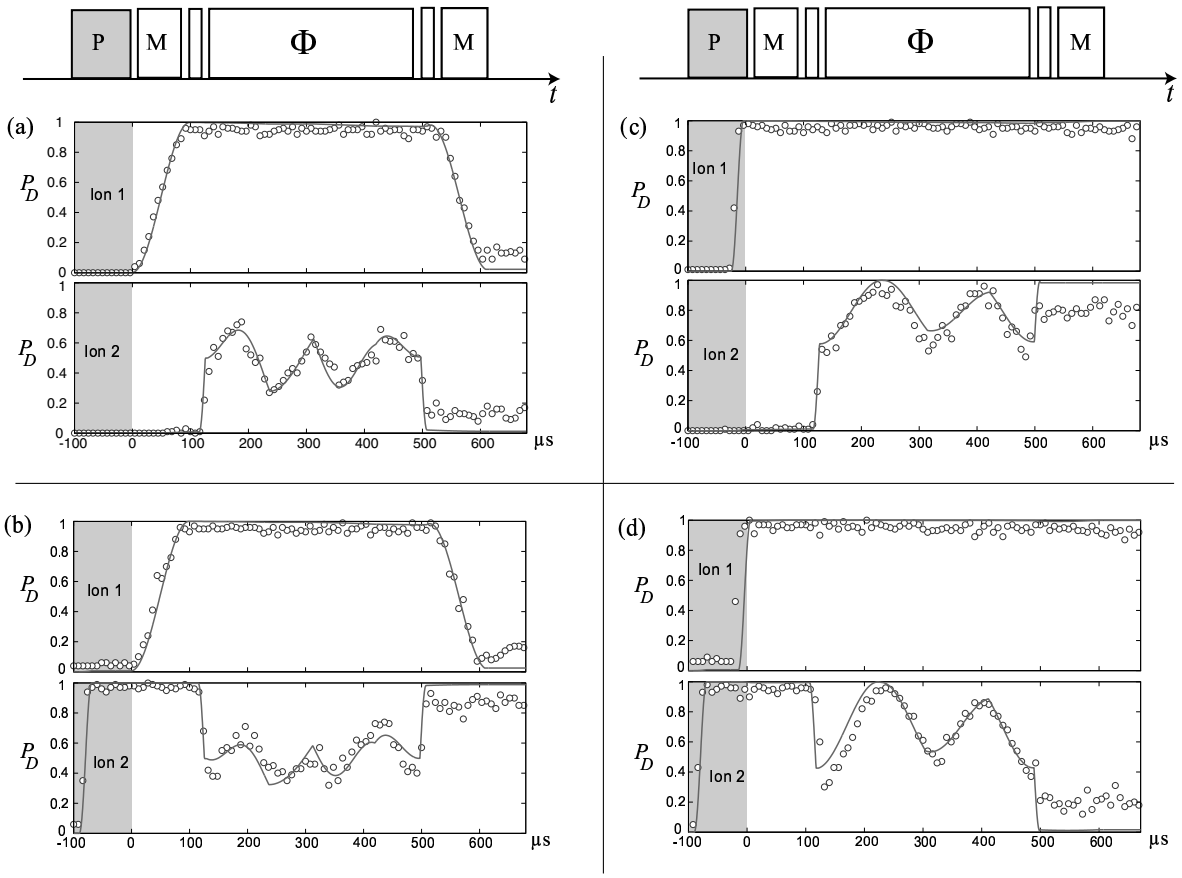


Figure 8.11: Experimental traces over the implemented Cirac-Zoller gate for different input states. The four cases correspond to the input states (a) $|S,S\rangle$, (b) $|S,D\rangle$, (c) $|D,S\rangle$, (d) $|D,D\rangle$. The fluorescence data were evaluated separately for each ion here, which yields the individual $D_{5/2}$-state probabilities $P_D$ across the sequence. The solid lines indicate the theoretically expected behaviour (see text). The input state preparation is indicated by the grey shaded areas and drawn for negative time values $t$. The actual gate sequence starts at $t = 0$.

ror, residual thermal excitation of the quantum bus mode, adressing error and off-resonant excitations, each contributing with roughly 2% to the gate fidelity reduction. Increasing the gate speed by using higher Rabi frequencies is expected to reduce the loss of phase contrast. This will, however, lead to increased off-resonant excitations so that the gate fidelity increase excpected from the use of higher Rabi frequencies is only about 5%.

**Further characterization of the implemented gate** :
Note that in each experimental sequence, 100 of which yield one data point per ion, both fluorescence values for ion 1 and ion 2 are read out. Instead of evaluating such 100 experiments for the two ions separately (as in Fig. 8.11), also the *individual* probabilities of the

four basis states, namely $||\langle\psi_o|S,S\rangle||^2$, $||\langle\psi_o|S,D\rangle||^2$, $||\langle\psi_o|D,S\rangle||^2$ and $||\langle\psi_o|D,D\rangle||^2$, can be determined. Here, $|\psi_o\rangle$ denotes the quantum state of the two ions at the output of the gate. This yields a truth table of the implemented gate operation in terms of probabilities.

Another goal is to read out the state of the quantum bus mode at the output of the gate. The bus mode is ideally expected to return to its ground state $|n=0\rangle$. This can be probed just as it has been done for the single-ion gates of sections 8.1 and 8.2, namely by appending Rabi oscillations on a sideband transition to the gate sequence.

Finally, a gate tomography as outlined in section 4.4, where quantum phases are measured, is envisaged. As explained, superpositions of the control qubit/ion are particularly interesting gate inputs because Bell states are then expected as outputs. An observation of sinusoidally varying probabilities (quantum oscillations) as a function of the phase $\phi$ of the read-out laser pulse would then also serve as a proof that the quantum state produced by the gate operation really is an entangled state and not a statistical mixture of $|S,S\rangle$ and $|D,D\rangle$. This cannot be distinguished by reading out fluorescence on the camera directly after the gate and measuring correlations.

# 9 Summary and Outlook

**The work of this thesis** started with experiments using a trap of existing design. Using the experience gained with this trap [52], a new trap was designed and built. The new trap has been shown to reliably store linear crystals of various ion numbers with a greater stability than the old setup. In previous Innsbruck experiments [4, 51, 52], motional ground state cooling and laser addressing had been demonstrated. These two prerequisites for our ion trap quantum computation schemes have been confirmed with the new trap and both have been improved. For example, due to improvements on Doppler cooling and also due to higher trap frequencies, mean phonon numbers (after Doppler cooling) of the radial modes of $\overline{n} \approx 5$ are reached, compared to $\overline{n} \approx 25$ in the old trap experiments [52]. This makes an important difference since for mean phonon numbers $\overline{n} \gtrsim 10$ of the radial modes the performance of our quantum computation schemes would be seriously affected (cf. section 7.2) and therefore additional (sub-Doppler) cooling of these modes would be required, which would complicate the experiment. The measured motional heating rates after ground state (sideband) cooling are on the order of one phonon per 140 ms which is low enough to be neglected [4]. As explained in chapter 6, when loading the trap by electron impact ionization, serious problems occur due to the large number of electrons scattered over the trap construction and due to the deposition of atomic calcium from the high oven flow that is required. These problems impeded the proper operation of the trap. As a solution, resonant photoionization was investigated and a system consisiting of two laser diodes was set up, which successfully cured the problems.

For quantum computation, additional issues needed to be addressed. AC-Stark shifts had to be taken into account and controlled. An AC-Stark shift spectrum was measured and a method based on an additional light field to compensate for unwanted AC-Stark shifts was developed. In particular for single-ion experiments, a way of using a vibrational mode as a complete qubit had to be found. Single qubit rotations of the vibrational qubit are particularly difficult to realize. The solution to this problem was to employ the technique of composite pulses. This enables, for example, the implementation of a $SWAP$ operation between internal and vibrational qubit, which makes rotations of the vibrational qubit possible. With the help of these techniques it was possible to implement the Deutsch-Jozsa algorithm, the first efficient quantum algorithm implemented on an ion trap quantum computer. The work with a single trapped ion has led to the idea of using off-resonant sideband coupling to induce motional state dependent, and therefore quantized, AC-Stark shifts. This possiblity enabled a new method of implementing a universal quantum gate, the dispersive phase gate of section 8.1. After these single-ion experiments, the experimental focus was switched to two ions. Preliminary results on the Cirac-Zoller $CNOT$ gate have been achieved. Note that the techniques developed before (AC-Stark shift compensation and the technique of composite pulses) are also very helpful for such multi-ion experiments.

**Work in progress** focuses on experimentation with the two-ion Cirac-Zoller $CNOT$ gate.

These experiments will be subject of the Ph.D. thesis of Mark Riebe [96]. It has been outlined in section 8.3 how this quantum gate may be further characterized (read-out of the probability truth table, measurement of the quantum bus mode, quantum oscillations and quantum tomography). As mentioned, a two-ion Cirac-Zoller gate produces *Bell-states* if the control ion at the gate input is in an appropriate superposition. A simpler procedure than employing a Cirac-Zoller gate exists to create Bell-states, which employs a total of only $1.5\pi$ of sideband rotations [51]. The fidelity of creating a Bell state using this method is expected to be well above 90%. Such a high quality Bell state will be a good testing ground for quantum tomography. Section 4.4 discusses that with the present experimental setup the composite pulse technique is only one out of three methods that can be used to implement a two-ion *CNOT* gate, the other two being the *auxiliary level* scheme and the *quantized AC-Stark shift* method. We are planning to implement and characterize the latter two methods for two-ion gates.

A goal for the near future is to prepare *GHZ-states* [97] of three trapped ions. Another interesting objective is the implementation of *quantum error correction* (QEC) [98]. The simplest QEC protocol involves three qubits. As mentioned in section 4.4, the use of a vibrational mode as a complete qubit turns a two-ion crystal into a *three* qubit quantum computer. A simple QEC protocol for such a three-qubit processor [99] would require an enhancement of the product "gate speed×coherence time" by a factor of two compared to the present achievements, which appears feasible.

**New experimental setups** are in preparation. Section 6.4 shows that resonant photoionization opens up the possibility to selectively load isotopes other than $^{40}$Ca into the trap such as $^{43}$Ca, for example. This option is particularly interesting as $^{43}$Ca is a promising *future qubit candidate* [68, 93]. The reason for this is that it has a hyperfine structure that offers the possibility of storing a qubit in extremely long-lived hyperfine states [100, 101]. Qubit manipulations would then be performed by Raman transitions. $^{43}$Ca provides a Raman transition from $m_F = 0$ to $m_F = 0$, going from the $F = 3$ to the $F = 4$ hyperfine ground state. These magnetic substates show only a quadratic Zeeman effect [102] and hence they are not perturbed by magnetic fields, at least for low field strengths on the order of a few Gauss, as are used in these experiments. Consequently, magnetic field fluctuations, which in the present experiments represent a major decoherence mechanism, would have no negative effects if these two states were used to encode the qubit. Experiments with $^{43}$Ca are in preparation.

Finally, the development of a *segmented linear trap* is underway; the design is being carried out by Thomas Deuschle [103]. This trap is designed to allow separation of a two-ion crystal along the trap axis into two individual potential minima, each containing one of the ions. The long term goal of this experiment is to fabricate an array of microtraps. In such an array ion qubits can be brought together in pairs for two-qubit gates, separated and then redistributed for further mutual gate operations with other ion qubits of the system [104].

# A Appendix

## A.1 Coupling Strengths on the Quadrupole Transition

D.F.V. James finds [67] for an electric quadrupole transition E2 going from a state 1 to a state 2 with total angular momenta $j$ and $j'$ and magnetic quantum numbers $m$ and $m'$, respectively, a Rabi frequency

$$\Omega = \left| \frac{eE_0}{2\hbar} \sqrt{\frac{15A}{c\alpha k^3}(2j'+1)} \sum_{q=-2}^{2} \begin{pmatrix} j & 2 & j' \\ -m & q & m' \end{pmatrix} c_{ij}^{(q)} \epsilon_i n_j \right| , \tag{A.1}$$

where the normal vector $\mathbf{n}$ indicates the direction of the wave vetctor $\mathbf{k}$; $c$ is the speed of light and $\alpha$ the fine structure constant. The total decay rate $A$ of state 2 takes into account the decay channels to all $m$-substates of the lower lying state 1. The five different $3 \times 3$ tensors $c^{(q)}$ are listed in ref. [67]. The term containing six numbers in round brackets is not a matrix but a so-called Wigner 3-j symbol, representing a number. It is related to the Clebsch-Gordan coefficients by the equation [105]

$$\langle j_1; j_2; m_1; m_2 \| j_3; m_3 \rangle = (-1)^{j_1 - j_2 + m_3} (2j_3+1)^{1/2} \begin{pmatrix} j_1 & j_2 & j_3 \\ m_1 & m_2 & -m_3 \end{pmatrix} .$$

In our case, state 1 and 2 are magnetic sublevels of the $S_{1/2}$ ground state and the metastable $D_{5/2}$ state, respectively, in other words $j = 1/2$ and $j' = 5/2$. With this, and by replacing in eqn. (A.1) the Wigner 3-j symbols by Clebsch-Gordan coefficients, taking into account that a $\pm 1$ sign in our case makes no difference because in the end the modulus is taken, we get:

$$\Omega = \frac{eE_0}{2\hbar} \sqrt{\frac{15A}{c\alpha k^3}} \sum_{q=-2}^{2} \left| \left\langle \frac{1}{2}; 2; -m; q \middle\| \frac{5}{2}; -m' \right\rangle \right| c_{ij}^{(q)} \epsilon_i n_j . \tag{A.2}$$

A property of the Clebsch-Gordan coefficients is that they differ from zero only if $m_3 = m_1 + m_2$. This condition, reading $q = \Delta m := m - m'$ in our case, makes the sum over $q$ in eqn. (A.2) obsolete, as the only non-zero term in the sum is:

$$\Lambda(m, m') c_{ij}^{(\Delta m)} \epsilon_i n_j$$

with the "specific" Clebsch-Gordan coefficients

$$\Lambda(m, m') := \left\langle \frac{1}{2}; 2; -m; \Delta m \middle\| \frac{5}{2}; -m' \right\rangle .$$

The $\Lambda(m, m')$ of interest here are (see for example tables in ref. [106]):

| $m$ | 1/2 | 1/2 | 1/2 | 1/2 | 1/2 |
|---|---|---|---|---|---|
| $m'$ | 5/2 | 3/2 | 1/2 | -1/2 | -3/2 |
| $\Lambda(m,m')$ | 1 | $\sqrt{4/5}$ | $\sqrt{3/5}$ | $\sqrt{2/5}$ | $\sqrt{1/5}$ |

Only the cases with $m = 1/2$ are listed as the $\Lambda(m,m')$ are invariant under the inversion $(m \to -m;\ m' \to -m')$, so that the $m = -1/2$ set can be easily derived by symmetry.

The geometry-dependent part is contained in the quadratic form

$$g^{(q)} := \left| c_{ij}^{(q)} \epsilon_i n_j \right| .$$

The polarization and the wave vector can be parametrised by the angle $\phi$ between the laser beam and the magnetic field and by the variable $\gamma$ describing the angle between the polarization and the magnetic field vector projected into the plane of incidence. Choosing $\mathbf{B} = B_0(0,0,1)$ one obtains $\boldsymbol{k} = k(\sin\phi, 0, \cos\phi)$[1] and $\boldsymbol{\epsilon} = (\cos\gamma\cos\phi, \sin\gamma, -\cos\gamma\sin\phi)$. The functions $g^{(q)}$ depend only on the modulus of $q$ and are given by:

$$\begin{aligned} g^{(0)} &= \tfrac{1}{2} \left|\cos\gamma \sin(2\phi)\right| \\ g^{(\pm 1)} &= \tfrac{1}{\sqrt{6}} \left|\cos\gamma\cos(2\phi) + i\sin\gamma\cos\phi\right| \\ g^{(\pm 2)} &= \tfrac{1}{\sqrt{6}} \left|\tfrac{1}{2}\cos\gamma\sin(2\phi) + i\sin\gamma\sin\phi\right| . \end{aligned}$$

Taking all these results and notations into account, eqn. (A.2) can be written as

$$\Omega = \frac{eE_0}{2\hbar}\sqrt{\frac{15A}{c\alpha k^3}}\Lambda(m,m')g^{(\Delta m)}(\phi,\gamma) .$$

## A.2 Radio-frequency trap drive

The drive voltage for the Paul trap is generated by connecting one RF-electrode pair to the open end of a helical resonator [107] (quality factor $\approx 200$) driven at its resonance frequency, thus enhancing the RF amplitude. The unloaded resonator is shown in Fig. A.1. The other blade pair of the trap is connected to the ground of the resonator setup. The input power is produced by a signal generator[2] and an RF amplifier[3]. A variable attenuator allows one to change the trapping frequencies continuously by adjusting the RF power. The helical resonator is mounted on top of the vacuum chamber inside a metal shield that prevents the electronics, for example the diode lasers, from picking up the drive frequency. All other electric connections exiting the vacuum system are low-pass filtered for the same reason. The power going into the resonator as well as the reflected power are measured[4]. The resonance frequency is adjusted by minimizing the reflected power.

The design of a helical resonator for the new trap posed considerable problems compared to other traps that have been used in our group through the last years. The usual procedure was to build a bare resonator with a resonance frequency slightly higher than the desired one

[1] The y-component of $\boldsymbol{k}$ can be chosen to be zero due to cylindrical symmetry.
[2] Marconi 2019A.
[3] Mini Circuit LZY-1. Maximum power 50 W, low distortion up to 20 W.
[4] Power meter Daiwa CN-410M.

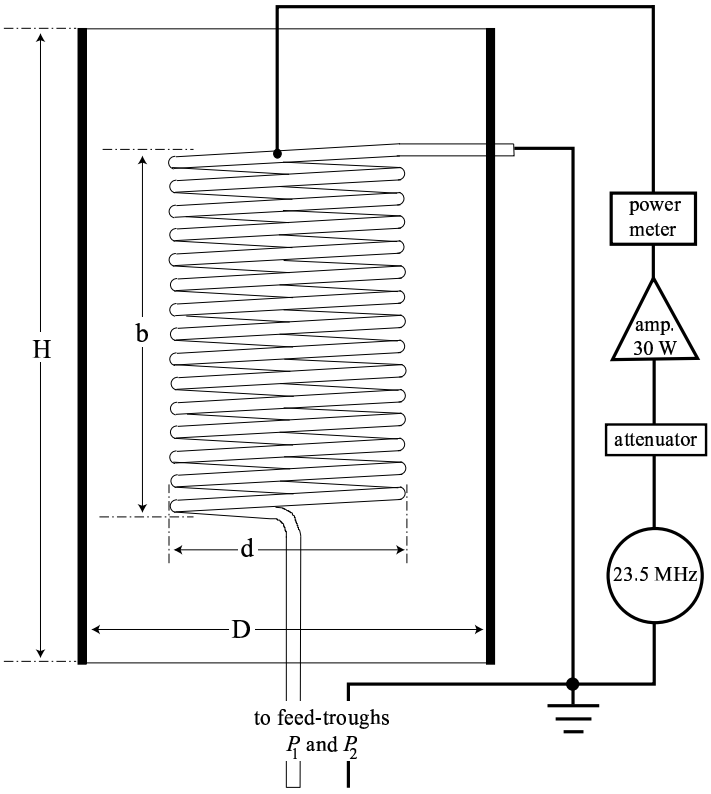


Figure A.1: Helical resonator. The copper cylinder and the copper helix form a quarter wave resonator.

(typically 15 MHz). Connecting it to the trap shifted the resonance down by values of only 2 MHz or less. For the new trap, a somewhat higher drive frequency of about 24 MHz was aimed for (cf. section 5.1). Following the above procedure, a helical resonator with a bare resonance frequency of 28 MHz was built. However, when connected to the trap, the resonance of the overall system was as low as 18 MHz. As building a helical resonator can be quite time consuming, this observation suggested to first develop a model for the combined system and to design the resonator according to this model. In the following, such considerations concerning helical resonator design are discussed.

As an *ansatz* to describe the *helical resonator without load* the following assumptions are made [107]:

- The setup behaves like a coaxial conductor with the coil as the core and the cylinder as the shield.
- The resonance frequency is determined by a $\lambda/4$-condition just like in a conventional coaxial quarter wave resonator.

The (phase) velocity along the coil is given by $v = \sqrt{\mathcal{LC}}$, where $\mathcal{L}$ and $\mathcal{C}$ are its inductance and capacitance per unit length, respectively. The $\lambda/4$ resonance condition reads $b = \lambda/4 = v/4f_0$,

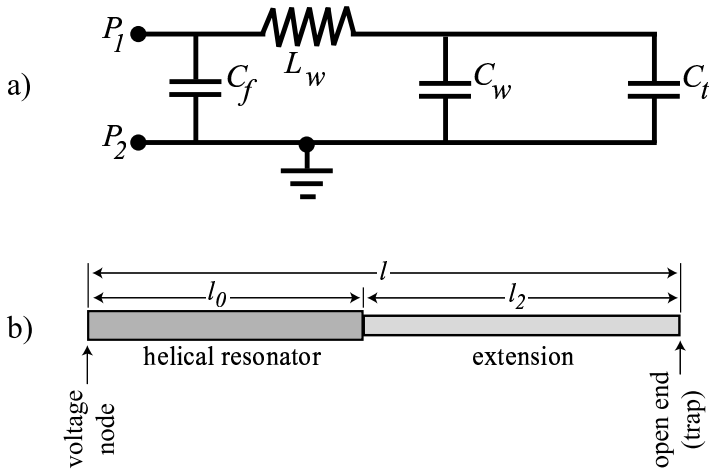


Figure A.2: a) Simple circuit diagram for the "extension" comprising the trap its radio frequency connection. It shows the capacitances of the feed-trough ($C_f$), the wire ($C_w$) and the trap ($C_t$) as well as the inductance of the wire ($L_w$). $P_1$ and $P_2$ are the pins of the electrical feed-through to the vacuum vessel. The ground line in reality consists of the whole vacuum vessel as well as everything which is grounded inside. b) Loaded resonator. Its resonance frequency $f$ is defined by $l = \lambda/4$. The grey scales represent different phase velocities

where $f_0$ is the resonance frequency. Formulae for $\mathcal{L}$ and $\mathcal{C}$ are derived in ref. [107]. In that paper, a dimensional ratio $d/D = 0.55$ is suggested for an optimum (high) Q factor. Taking this into account and putting all formulae together, one finds the simple relation

$$f_0 = \frac{2670}{N \cdot d}\ \text{MHz} \cdot \text{cm}, \tag{A.3}$$

where $N$ is the total number of windings of the helix. Note, that now $D \approx d/0.55$ is essentially fixed with the choice of $d$. The Q of the resonator is now determined by all resistive losses in the system. The use of high conductivity materials, in particular for the helix, yields high Q values. For the same reason, scaling up the setup enhances Q as it reduces the total (surface) resistance. In order to keep the whole setup compact, a compromise was chosen using a copper cylinder with $D = 10$ cm for the outer conductor. Consequently, the coil was wound with a diameter $d \simeq 5.5$ cm. In ref. [107], an optimum range $1 < b/d < 4$ for the ratio between height and diameter of the coil is given. Thus, a coil height $b \simeq 2d = 11$ cm was envisaged. Given these dimensions, in particular $d$, eqn. (A.3) determines the parameter $N$ for a desired $f_0$.

What is now the *resonance frequency $f$ of the combined system*, i.e. the helical resonator with the trap as a load? When the trap is connected to the open end, it simply represents an extension of the resonator. The entire lead from the end of the helix to the trap can be viewed as a transmission line and can be represented in a lumped circuit diagram as in Fig. A.2a). It is assumed that the wavelength of the RF signal traveling along that line (for the frequency range of interest) is much larger than all individual pieces of the circuit. Its

elements can therefore be regarded as continuously distributed. In other words the line has a length $l_2$ and an inductance and capacitance per unit length of $\mathcal{L}_2 = L_2/l_2$ and $\mathcal{C}_2 = C_2/l_2$, respectively. $L_2$ and $C_2$ are the sums of all individual inductances and capacitances in this system. This includes lumped elements, for example the capacitance of the trap, as well as more continuously distributed elements such as the inductance of the leads through the vacuum vessel to the trap electrodes. The extension by itself can thus be treated in the same way as the helical resonator above and its own $\lambda/4$ resonance could be calculated according to $f_2 = \sqrt{\mathcal{L}_2\mathcal{C}_2}/4l_2$, if $\mathcal{L}_2$ and $\mathcal{C}_2$ were exactly known. The Q value would be determined by electrical resistances to ground or along the line (which are omitted in Fig. A.2a) for the sake of simplicity). Fig. A.2b) represents a simplified picture of the loaded helical resonator. For the $\lambda/4$ resonance of the overall system one finds:

$$\frac{1}{f} = \frac{1}{f_0} + \frac{1}{f_2}.$$

This formula can be interpreted in our context: As long as $f_2$ is much higher than $f_0$, connecting the trap to the helical resonator will not change the resonance frequency considerably, as has been the case in former setups used in our group. For the new trap, two things were different: the desired final frequency was higher than before and at the same time $f_2$ was apparently lower, probably due to the higher capacitance $C_t$ of the trap. From the above mentioned observation (the loaded resonance $f$ was 18 MHz for $f_0 = 28$ MHz) an $f_2$ of about 50 MHz was calculated. As the desired $f$ was 24 MHz, the new helical resonator was now designed for $f_0 \approx 46$ MHz.

According to eqn. (A.3), this requires a coil with $N \simeq 11$ windings. Ref. [107] suggests that the clearing between two coil windings should be roughly equal the diameter of the coil wire. If only 11 windings are to be distributed over $b = 11$ cm, this requires a wire diameter of as much as 5 mm, which in fact was used for the new helical resonator. The latter turned out to have a bare resonance of $f_0$ of 41 MHz. When connected to the trap setup, it resulted in a final frequency $f$ of 23.5 MHz (which is in rather good agreement with the circuit model made).

## A.3 Standard Configurations of the Experiment

Note that we have to use an axial mode for the vibrational qubit. The use of radial modes (radial or rocking for instance) is not possible in a standard linear trap, which is radially symmetric. This means that the radial trap structure has a four-fold symmetry which leads to degenerate radial modes. There are *two* orthogonal, degenerate radial modes and likewise two rocking modes[5]. Using a radial mode would therefore correspond to a motional qubit distributed over *two* quasi-two-level systems in a rather uncontrolled way, which is undesirable. Consequently, we have to use (one of) the axial mode(s).

There is a large number of setup parameters which can be varied in the experiment. These include, for example

- the magnitude of the magnetic field;

[5] In the real trap this degeneracy is lifted (see section 7.1), which, however, changes essentially nothing about these considerations as the splitting of the radial frequency is very small ($\approx 1\%$).

- the relative directions of magnetic field, 729 nm beam and its polarization (angles $\phi$ and $\gamma$, see section 3.3.5);
- the trap parameters, namely RF drive power $P_{rf}$ and end-cap voltage $V_{cap}$ ;
- the angle $\beta$ between the 729 nm beam and the trap axis.

Over the course of this PhD work, many different combinations of these parameters have been used and tested. As a matter of fact, however, only two different configurations have been employed to achieve the major results of this thesis - one for single ion and the other for two-ion experiments.

In both cases we found the combination $\{\boldsymbol{\phi = 45°, \gamma = 0°}\}$ most useful, because the transition with the weakest magnetic field dependence, namely $S_{1/2}(m = -1/2) \leftrightarrow D_{5/2}(m' = -1/2)$ is maximally strong. The latter is then used to encode the qubit. At the same time, the $S_{1/2}(m = -1/2) \leftrightarrow D_{5/2}(m' = -5/2)$ transition in this setting is still strong enough to be used for sideband cooling. The differences of the two settings are discussed in the following:

**Single-ion standard configuration** Cooling in terms of the mean occupation number of a vibrational mode becomes easier the higher the frequency of the mode. In addition, a high axial trap frequency is recommended for fast gate operations (eqn. (3.34)). Therefore, in a single-ion experiment where individual addressing is not an issue, we turn the trap parameters as high as possible. This is in our case[6] $P_{rf} = 13 - 15$ W and $V_{cap} = 2000$ V, resulting in radial trap frequencies $\omega_r$ of $2\pi \cdot 4.4 - 4.7$ MHz and an axial frequency

$$\omega_z = 2\pi \cdot 1.715 \text{ MHz} .$$

Moreover, we want the best projection possible of the 729 nm $k$-vector onto the trap axis in order to have maximum coupling ($\eta$) to the axial mode, which is used for the motional qubit. The smallest angle $\beta$ between 729 nm beam and the trap axis in our setup is achieved by using the optical channel 729N (cf. section 5.4), namely $\beta = 22.5°$. This yields a Lamb-Dicke parameter

$$\eta = 6.8\%$$

for the axial mode. The angle $\phi = 45°$ between 729 nm beam and the magnetic field is then achieved by applying the magnetic field in $x$-direction (B1 of Fig. 5.7). A magnetic field of 2.50 G is applied. The 729 nm polarization is rotated into the $x$-$y$ plane in order to provide $\gamma = 0°$. All experiments were performed in a 20 ms line triggered pulse scheme, including sideband cooling of the axial mode to ground state probabilities greater than 98 %.

**Two-ion standard configuration** In the multi-ion case we obviously need to choose a direction of the 729 nm laser with respect to the trap axis which allows for individual addressing. The optimum for this is of course perpendicular to the ion string ($\beta = 90°$). This, however, corresponds to $\eta = 0$ for the axial modes which would make it impossible

[6] We could, in principle, work with slightly higher values, but this would very soon deteriorate the trapping stability.

to drive sideband transitions and encode a vibrational qubit into one of these modes. Consequently, a compromise must be made. In our present setup, the angle between the addressing 729 nm channel (729A) and the trap axis is $\beta = 67.5°$, which is defined by the construction of the vacuum vessel. In order to comply with $\phi = 45°$ we apply the magnetic field diagonally with the help of coil Cd (B2 of Fig. 5.7). Just as in the single ion standard configuration, the 729 nm polarization lies in the $x$-$y$ plane ($\gamma = 0°$). A magnetic field of 3.0 G is applied. As discussed in section 6.1, with a two-ion crystal the RF trap drive power had to be reduced to $P_{rf} = 12$ W for stable trapping. For the same reason it was advantageous to reduce the end-cap voltage to $V_{cap} = 1000$ V. These values yield an axial COM frequency $\omega_z$ of $2\pi \cdot 1.215$ MHz (as expected from the $\sqrt{V_{cap}}$ scaling) and a radial COM frequency $\omega_r$ of $2\pi \cdot 4.35$ MHz. Note that in our trap the degeneracy between the two radial COM modes is lifted. The $\omega_r$ values given here represent average values. At any rate, the precise position of the radial modes is not relevant for our experiments.
As outlined in section 3.3.6, it is advantageous to use the vibrational mode of highest possible frequency as the quantum bus, see eqn. (3.34). At the same time, it has been argued above that only axial modes are allowed. Consequently, the highest axial mode will be chosen for the quantum bus, which in the two-ion case is the *breathing mode* at a frequency $\omega_b = \sqrt{3}\omega_z$, hence

$$\omega_b = 2\pi \cdot 2.104 \text{ MHz} .$$

According to eqn. (3.30) the Lamb-Dicke factor of the breathing mode for an excitation through the addressing channel is then

$$\eta = 1.8\% .$$

Note, that this value is considerably smaller than in single-ion experiments (6.8%). This is due to the higher mass of the ion crystal as well as the larger angle $\beta$.
We have previously observed that sideband cooling of a vibrational mode heats up the other modes by roughly one phonon each [52]. For our quantum computation experiments, optimum ground state cooling (near 100%) is required only for the quantum bus, hence for the breathing mode. For all other modes, mean phonon numbers of up to $n = 10$ are tolerable (cf. section 7.2.2). Therefore, in the pulse sequence sideband cooling was first performed on the axial COM mode for 4 ms yielding a motional ground state probability of about 90%. Next, sideband cooling on the breathing mode was applied for 8 ms resulting in a ground state probability greater than 98 %. As mentioned, this heats the axial COM mode to $\overline{n} \approx 1$. Note that the radial modes (radial COM, rocking) are at $\overline{n} \approx 5$ due to Doppler cooling.

# Bibliography


[1] A. Pais. *Inward bound: of matter and forces in the physical world.* Oxford University Press (1986).

[2] A.E. Siegman. *Lasers.* Univ. Science Books (1986).

[3] S.M. Sze. *Physics of semiconductor devices.* Wiley (1981).

[4] C. Roos. *Controlling the quantum state of trapped ions.* Ph.D. thesis, Universität Innsbruck (2000).

[5] *Special issue: Quantum state preparation and measurement.* J. Mod. Opt. **44**(11/12), 2021 (1997).

[6] G.J. Milburn. *Schrödinger's Machines: the Quantum Technology Reshaping Everyday Life.* W.H. Freeman, New York (1997).

[7] G.J. Milburn. *The Feynman Processor: Quantum Entanglement and the Computing Revolution.* Perseus Books, Reading, Mass. (1998).

[8] R.P. Feynman. *Simulating physics with computers.* Int. J. Theor. Phys. **21**, 467 (1982).

[9] R.P. Feynman. *Quantum mechanical computers.* Foundations of Physics **16**, 507 (1986).

[10] D. Deutsch. *Quantum theory, the Church-Turing principle and the universal quantum computer.* Proc. R. Soc. London A **400**, 96 (1985).

[11] D. Deutsch. *Quantum computational networks.* Proc. R. Soc. London A **425**, 73 (1989).

[12] C.H. Bennett and G. Brassard. *Public key distribution and coin tossing.* Proc. IEEE Inter. Conf. on Computers, Systems and Signal Processing pages 175–179 (1984).

[13] M.A. Nielsen and I.L. Chuang. *Quantum Computation and Quantum Information.* Cambridge University Press (2000).

[14] D. Bouwmeester (ed.). *The Physics of Quantum Information.* Springer, Berlin (2000).

[15] D.P. DiVincenzo. *Quantum computation.* Science **270**, 255 (1995).

[16] D.P. DiVincenzo. *The physical implementation of quantum computation.* Fortschr. d. Phys. **48**, 771 (2000).

[17] D.P. DiVincenzo. *Two-bit gates are universal for quantum computation.* Phys. Rev. A **51**, 1015 (1995).

[18] D. Deutsch and R. Josza. *Rapid solution of problems by quantum computation*. Proc. R. Soc. London A **439**, 553 (1992).

[19] R. Cleve, A. Ekert, C. Macciavello, and M. Mosca. *Quantum algorithms revisited*. Proc. R. Soc. London A **454**, 339 (1998).

[20] L. Grover. *A fast quantum mechanical algorithm for database search*. Proc. 28th Annual ACM Symposium on the Theory of Computing, page 212 (1996).

[21] P.W. Shor. *Algorithms for quantum computation: Discrete logarithms and factoring*. Proc. 35th Annual Symposium on Foundations of Computater Science (1994).

[22] R.L. Rivest, A. Shamir, and L.M. Adleman. *A method of obtaining digital signatures and public-key cryptosystems*. Comm. ACM **21**, 120 (1978).

[23] C. Pomerance. In *Discrete Algorithms and Complexity*, Proc. Japan-US Joint Seminar. Academic Press (1986).

[24] D.S. Abrams and S. Lloyd. *Simulation of many-body Fermi systems on a universal quantum computer*. Phys. Rev. Lett. **79**, 2586 (1997).

[25] I.L. Chuang and Y. Yamamoto. *Simple quantum computer*. Phys. Rev. A **52**, 3489 (1995).

[26] E. Knill, R. Laflamme, and G.J. Milburn. *A scheme for efficient quantum computation with linear optics*. Nature **409**, 46 (2001).

[27] P. Domokos, J.M. Raimond, M. Brune, and S. Haroche. *Simple cavity-QED two-bit universal quantum logic gate: The principle and expected performances*. Phys. Rev. A **52**, 3554 (1995).

[28] Q.A. Turchette, C.J. Hood, W. Lange, H. Mabuchi, and H.J. Kimble. *Measurement of conditional phase shifts for quantum logic*. Phys. Rev. Lett. **75**, 4710 (1995).

[29] Y. Nakamura, Y.A. Pashkin, and J.S. Tsai. *Coherent control of macroscopic quantum states in a single-Cooper-pair box*. Nature **398**, 786 (1999).

[30] J.E. Mooij, T.P. Orlando, L. Levitov, L. Tian, C.H. van der Waal, and S. Lloyd. *Josephson persistent-current qubit*. Science **285**, 1036 (1999).

[31] P.M. Platzman and M.I. Dykman. *Quantum computing with electrons floating on liquid helium*. Science **284**, 1967 (1999).

[32] D. Loss and D.P. DiVincenzo. *Quantum computation with quantum dots*. Phys. Rev. A **57**, 120 (1998).

[33] B. Kane. *A silicon-based nuclear spin quantum computer*. Nature **393**, 133 (1998).

[34] J.I. Cirac and P. Zoller. *Quantum computations with cold trapped ions*. Phys. Rev. Lett. **74**, 4091 (1995).

[35] J.A. Jones, M. Mosca, and R.H. Hansen. *Implementation of a quantum search algorithm on a quantum computer*. Nature **393**.

[36] I.L. Chuang, N. Gershenfield, and M. Kubinec. *Experimental implementation of fast quantum searching*. Phys. Rev. Lett. **80**, 3408 (1998).

[37] L.M.K. Vandersypen, M. Steffen, G. Breyta, C.S. Yannoni, M.H. Sherwood, and I.L. Chuang. *Experimental realization of Shor's quantum factoring algorithm using nuclear magnetic resonance*. Nature **414**, 883 (2001).

[38] W.S. Warren, N. Gershenfeld, and I. Chuang. *The usefulness of NMR quantum computing*. Science **277**, 1688 (1997).

[39] S.L. Braunstein, C.M. Caves, R. Jozsa, N. Linden, S. Popescu, and R. Schack. *Separability of very noisy mixed states and implications for NMR quantum computing*. Phys. Rev. Lett. **83**, 1054 (1999).

[40] R. Schack and C.M. Caves. *Classical model for bulk-ensemble NMR quantum computation*. Phys. Rev. A **60**, 4354 (1999).

[41] N. Linden and S. Popescu. *Good dynamics versus bad kinematics: Is entanglement needed for quantum computation?*. Phys. Rev. Lett. **87**, 047901 (2001).

[42] A. Sørensen and K. Mølmer. *Quantum computation with ions in thermal motion*. Phys. Rev. Lett. **82**, 1971 (1999).

[43] A. Sørensen and K. Mølmer. *Entanglement and quantum computation with ions in thermal motion*. Phys. Rev. A **62**, 022311 (2000).

[44] D. Jonathan, M.B. Plenio, and P.L. Knight. *Fast quantum gates for cold trapped ions*. Phys. Rev. A **62**, 042307 (2000).

[45] L.-M. Duan, J.I. Cirac, and P. Zoller. *Geometric manipulation of trapped ions for quantum computation*. Science **292**, 1695 (2001).

[46] J.I. Cirac and P. Zoller. *A scalable quantum computer with ions in an array of microtraps*. Nature **404**, 579 (2000).

[47] T. Pellizari, S. A. Gardiner, J.I. Cirac, and P. Zoller. *Decoherence, continuous observation, and quantum computing: a cavity QED model*. Phys. Rev. Lett. **75**(21), 3788 (1995).

[48] B.E. King W.M. Itano C. Monroe, D.M. Meekhof and D.J. Wineland. *Demonstration of a fundamental quantum logic gate*. Phys. Rev. Lett. **75**, 4714 (1995).

[49] Q.A. Turchette, C.S. Wood, B.E. King, C.J. Myatt, D. Leibfried, W.M. Itano, C. Monroe, and D.J. Wineland. *Deterministic entanglement of two ions*. Phys. Rev. Lett. **81**, 3631 (1998).

[50] C.A. Sackett, D. Kielpinski, B.E. King, C. Langer, V. Meyer, C.J. Myatt, M. Rowe, Q.A. Turchette, W.M. Itano, D.J. Wineland, and C. Monroe. *Experimental entanglement of four particles*. Nature **404**, 256 (2000).

[51] H. C. Nägerl. *Ion strings for quantum computation*. Ph.D. thesis, Universität Innsbruck (1998).

[52] H. Rohde. *Experimente zur Quanteninformationsverarbeitung in einer linearen Ionenfalle*. Ph.D. thesis, Universität Innsbruck (2001).

[53] S. Gulde, M. Riebe, G.P.T. Lancaster, C. Becher, J. Eschner, H. Häffner, F. Schmidt-Kaler, I.L. Chuang, and R. Blatt. *Implementation of the Deutsch-Jozsa algorithm on an ion-trap quantum computer*. Nature **421**, 48 (2003).

[54] T. Sleator and H. Weinfurter. *Realizable universal quantum logic gates*. Phys. Rev. Lett. **74**, 4087 (1995).

[55] S. Lloyd. *Almost any quantum logic gate is universal*. Phys. Rev. Lett. **75**(2), 346 (1995).

[56] A. Barenco. *A universal two-bit gate for quantum computation*. Proc. R. Soc. Lond. A **449**, 679 (1995).

[57] D. Deutsch, A. Barenco, and A. Ekert. *Universality in quantum computation*. Proc. R. Soc. Lond. A **449**, 1937 (1995).

[58] W. Paul, O. Osberghaus, and E. Fischer. *Ein Ionenkäfig*. Forschungsberichte des Wirtschafts- und Verkehrsministeriums Nordrhein-Westfalen 415, Westfälischer Verlag (1958).

[59] P. K. Ghosh. *Ion traps*. Clarendon Press (1995).

[60] R. March and J. Todd (eds.). *Practical aspects of ion trap mass spectrometry, Volume I*. CRC Press (1995).

[61] P.A. Barton, C.J.S. Donald, D.M. Lucas, D.A. Stevens, A.M. Steane, and D.N. Stacey. *Measurement of the lifetime of the 3d* $^2D_{5/2}$ *state in* $^{40}Ca^+$. Phys. Rev. A **62**, 032503 (2000).

[62] H. Rohde, S.T. Gulde, C.F. Roos, P.A. Barton, D. Leibfried, J. Eschner, F. Schmidt-Kaler, and R. Blatt. *Sympathetic ground state cooling and coherent manipulation with two-ion-crystals*. J. Opt. B **3** (2001).

[63] M.C. Raizen, J.C. Bergquist, J.M. Gilligan, W.M. Itano, and D.J. Wineland. *Linear trap for high-accuracy spectroscopy of stored ions*. J. Mod. Opt. **39**, 233 (1992).

[64] Q.A. Turchette, D. Kielpinski, B.E. King, D. Leibfried, D.M. Meekhof, C.J. Myatt, M.A. Rowe, C.A. Sackett, C.S. Wood, W.M. Itano, C.Monroe, and D.J. Wineland. *Heating of trapped ions from the quantum ground state*. Phys. Rev. A **61**, 063418 (2000).

[65] N. Kjaergaard, L. Hornekaer, A.M. Thommesen, Z. Videsen, and M. Drewsen. *Isotope selective loading of an ion trap using resonance-enhanced two-photon ionization*. Appl. Phys. B **71**, 207 (2000).

[66] M. Drewsen and A. Brøner. *Harmonic linear Paul trap: Stability diagram and effective potentials*. Phys. Rev. A **62**, 045401 (2000).

[67] D. F. V. James. *Quantum dynamics of cold trapped ions with application to quantum computation*. Appl. Phys. B **66**, 181 (1998).

[68] A. Steane. *The ion trap quantum information processor*. Appl. Phys. B **64**, 623 (1997).

[69] D.G. Enzer, M.M. Schauer, J.J. Gomez, M.S. Gulley, M.H. Holzscheiter, P.G. Kwiat, S.K. Lamoreaux, C.G. Peterson, V.D. Sandberg, D. Tupa, A.G. White, R.J. Hughes, and D.F.V. James. *Observation of power-law scaling for phase transitions in linear trapped ion crystals*. Phys. Rev. Lett. **85**, 2466 (2000).

[70] J.P. Schiffer. *Phase transitions in anisotropically confined ionic crystals*. Phys. Rev. Lett. **70**, 818 (1993).

[71] C. A. Blockley, D. F. Walls, and H. Risken. *Quantum collapses and revivals in a quantized trap*. Europhys. Lett. **17**, 509 (1992).

[72] J.I. Cirac, A.S. Parkins, R. Blatt, and P. Zoller. *Non-classical states of motion in ion traps*. Adv. Atom. Molec. and Opt. Phys. **37**, 237 (1996).

[73] R. Loudon. *The quantum theory of light*. Oxford University Press, second edition (1983).

[74] D.S. Weiss, B.C. Young, and S. Chu. *A precision measurement of h/MCs based on photon recoil using laser cooled atoms and atom interferometry*. Appl. Phys. B **59**, 217 (1994).

[75] K. Sengstock, U. Sterr, V. Rieger, D. Bettermann, J.H. Müller, and W. Ertmer. *Optical Ramsey spectroscopy on laser trapped and thermal Mg-atoms*. Appl. Phys. B **59**, 99 (1994).

[76] M. Niering, R. Holzwarth, J. Reichert, P. Pokasov, Th. Udem, M. Weitz, T.W. Hänsch, P. Lemonde, G. Santarelli, M. Abgrall, P. Laurent, C. Salomon, and A. Clairon. *Measurement of the hydrogen 1s-2s transition frequency by phase coherent comparison with a microwave cesium fountain clock*. Phys. Rev. Lett. **84**, 5496 (2000).

[77] A. Kaplan, M.F. Andersen, and N. Davidson. *Suppression of inhomogeneous broadening in rf spectroscopy of optically trapped atoms*. Phys. Rev. A **66**, 045401 (2002).

[78] M.H. Levitt. *Composite pulses*. Prog. NMR Spectroscopy **18**, 61 (1986).

[79] A.M. Childs and I.L. Chuang. *Universal quantum computation with two-level trapped ions*. Phys. Rev. A **63**, 012306 (2001).

[80] Calculations carried out by Hartmut Häffner.

[81] D.J. Wineland J.J. Bollinger, W.M. Itano and D.J. Heinzen. *Optimal frequency measurements with maximally correlated states*. Phys. Rev. A **54** (1996).

[82] J.F. Poyatos, J.I. Cirac, and P. Zoller. *Complete characterization of a quantum process: The two-bit quantum gate*. Phys. Rev. Lett. **78**, 390 (1997).

[83] U. Leonhardt and H. Paul. *Measuring the quantum state of light*. Prog. Quant. Electron. **19**, 89 (1995).

[84] I.L. Chuang and M.A. Nielsen. *Prescription for experimental determination of the dynamics of a quantum black box*. J. Mod. Opt. **44**, 2455 (1997).

[85] R.W.P. Drever, J.L. Hall, F.V. Kowalski, J. Hough, G.M. Ford, A.J. Munley, and H. Ward. *Laser phase and frequency stabilization using an optical resonator.*. Appl. Phys. B **31**, 97 (1983).

[86] D. Rotter. *Diplomarbeit*. University of Innsbruck (2003).

[87] Dietrich Leibfried. Private communication.

[88] Rainer Blatt. Private communication.

[89] R.G. DeVoe and C. Kurtsiefer. *Experimental study of anomalous heating and trap instabilities in a microscopic $^{137}Ba$ ion trap*. Phys. Rev. A **65**, 063407 (2002).

[90] A.A. Radzig and B.M. Smirnov. *Reference Data on Atoms, Molecules and Ions*. Springer-Verlag, Berlin (1985).

[91] S. Gulde, D. Rotter, P. Barton, F. Schmidt-Kaler, R. Blatt, and W. Hogervorst. *Simple and efficient loading of ions for precision ion-trapping experiments*. Appl. Phys. B **73**, 861 (2001).

[92] Wim Hogervorst. Private communication.

[93] F. Schmidt-Kaler, S. Gulde, M. Riebe, T. Deuschle, A. Kreuter, G. Lancaster, C. Becher, J. Eschner, H. Häffner, and R. Blatt. *The coherence of qubits based on single $Ca^+$ ions*. J. Phys. B **36**, 623 (2003).

[94] M. Brune, P. Nussenzveig, F. Schmidt-Kaler, F. Bernardot, A. Maali, J.M. Raimond, and S. Haroche. *From Lamb shift to light shifts: Vacuum and subphoton cavity fields measured by atomic phase sensitive detection*. Phys. Rev. Lett. **72**, 3339 (1994).

[95] A. Rauschenbeutel, G. Nogues, S. Osnaghi, P. Bertet, M. Brune, J.M. Raimond, and S. Haroche. *Coherent operation of a tunable quantum phase gate in cavity QED*. Phys. Rev. Lett. **83**, 5166 (1999).

[96] M. Riebe. Ph.D. thesis, in preparation.

[97] D.M. Greenberger, M.A. Horne, A. Shimony, and A. Zeilinger. *Bell's theorem without inequalities*. Am. J. Phys. **58**, 1131 (1990).

[98] A. M. Steane. In *The Physics of Quantum Information*, eds. D. Bouwmeester, A. Ekert, A. Zeilinger. Springer, Berlin (2000).

[99] A. M. Steane. Private communication.

[100] C. Monroe, D. M. Meekhof, B. E. King, S. R. Jefferts, W. M. Itano, D. J. Wineland, and P. Gould. *Resolved-sideband Raman cooling of a bound atom to the 3D zero-point energy*. Phys. Rev. Lett **75**, 4011 (1995).

[101] D. M. Meekhof, C. Monroe, B. E. King, W. M. Itano, and D. J. Wineland. *Generation of nonclassical motional states of a trapped atom*. Phys. Rev. Lett. **76**, 1796 (1996).

[102] C. Cohen-Tannoudji, B. Diu, and F. Laloë. *Quantum Mechanics, Vols. I & II*. Wiley-Interscience (1977).

[103] T. Deuschle. Ph.D. thesis, in preparation.

[104] D. Kielpinski, C.R. Monroe, and D.J. Wineland. *Architecture for a large-scale ion-trap quantum computer*. Nature **417**, 709 (2002).

[105] R.D. Cowan. *The Theory of Atomic Structure and Spectra*. University of California Press, Berkeley (1981).

[106] E.U. Condon and G.H. Shortley. *The Theory of Atomic Spectra*. Cambridge University Press (1953).

[107] W.W. Macalpine and R.O. Schildknecht. *Coaxial resonators with helical inner conductor*. Proc. *IRE* **47**, 2099 (1959).

An dieser Stelle möchte ich mich bei allen bedanken, die zum Gelingen dieser Arbeit beigetragen haben.

Mein Dank gilt zuallererst Prof. Rainer Blatt für die Aufnahme in seine Arbeitsgruppe und für seine Unterstützung bei meiner Doktorarbeit.

Des weiteren gebührt mein ganz besonderer Dank Ferdinand Schmidt-Kaler, der mir stets mit Optimismus und enormem Fachwissen zur Seite gestanden ist. Auch allen anderen, die im Laufe meiner Arbeit zusammen mit mir experimentiert haben, bin ich zu großem Dank verpflichtet. Da wären zunächst alle diejenigen zu nennen, die direkt am linearen Fallenexperiment mitgewirkt haben, namentlich Hartmut Häffner, Mark Riebe, Gavin Lancaster, Paul Barton, Daniel Rotter, Christian Roos, Harald Rohde und Liv Hornekaer. Das Experiment ist eng verbunden mit unserem Kalzium-Cavity-QED-Experiment und daher möchte ich mich auch bei Axel Kreuter und Andreas Mundt für die schöne Zusammenarbeit bedanken. Axel Kreuter hat sich nicht nur als hervorragender Bürokollege erwiesen sondern auch als sehr guter Freund. Philipp Spitzer danke ich für seine Unterstützung beim Aufbau des Photoionisations-Lasersystems und für das großzügige Ausleihen von prima Rennrodeln.

Die Mitarbeiter unserer feinmechanischen Werkstatt, Anton Schönherr und Stefan Haslwanter, hatten stets ein offenes Ohr für mich und gute Einfälle zur Lösung meiner Konstruktionsprobleme. Stefan Haselwanter gebührt mein besonderer Dank für sein Engagement beim Entwurf und der Fertigung der linearen Ionenfalle, mit der diese Experimente durchgeführt wurden.

Ich bedanke mich bei Felicity Splatt, Alex Wilson und Gavin Lancaster für das Korrekturlesen verschiedener englischer Texte inclusive dieser Arbeit. Allen Mitgliedern der Kochgruppe danke ich für gutes Essen, interessante Gespräche und für die Erweiterung meiner Allgemeinbildung (obwohl die genaue Lage von Vitaminen in bzw. an Kartoffeln ungeklärt blieb...). Ich bedanke mich bei allen Mitarbeitern der Arbbeitsgruppen Blatt und Grimm, auch den nichtwissenschaftlichen, für die angenehme Arbeitsatmosphäre.

Meiner Freundin Rosemarie danke ich ganz herzlich für die Aufmunterungen in Zeiten, als am Experiment alles schief ging, und für ihre Freude, wenn es dann endlich funktionierte. Schließlich möchte ich mich bei meinen Eltern und meiner übrigen Familie für ihre Unterstützung und ihr Interesse bedanken. Abschließend kein Dank, sondern ein Ausdruck der Freude darüber, dass mein Patenkind Rebekka jetzt wieder gesund ist.